Ultracold bosons in tilted optical lattices – impact of spectral statistics on simulability, stability, and dynamics

Hannah Venzl

Ultracold bosons in tilted optical lattices – impact of spectral statistics on simulability, stability, and dynamics

vorgelegt von

Hannah Venzl

aus Starnberg

2011

Betreuer der Arbeit: Prof. Dr. Andreas Buchleitner
In Zusammenarbeit mit: Dr. Moritz Hiller

Dekan: Prof. Dr. Kay Königsmann
Referent: Prof. Dr. Andreas Buchleitner
Koreferent: Prof. Dr. Thomas Filk

Tag der mündlichen Prüfung: 29. 04. 2011

Zusammenfassung

In der vorliegenden Dissertation werden wechselwirkende ultrakalte Bosonen in gekippten optischen Gittern untersucht. Dabei handelt es sich um ein Paradigma komplexer Vielteilchen-Quantensysteme. Unsere Analyse basiert auf dem gekippten Bose-Hubbard Modell, welches Tunnelübergänge zwischen benachbarten Gitterplätzen, Wechselwirkung zwischen Teilchen sowie ein statisches Feld berücksichtigt. Das konkurrierende Verhalten dieser Beiträge bedingt die Komplexität des Systems, welche sich auf spektraler Ebene in einer chaotischen Statistik der Eigenwerte ausdrückt. Wir untersuchen sowohl, wie sich dieses spektrale Chaos auf die Systemdynamik auswirkt, als auch welche Informationen wir aus der Dynamik des Systems über sein Vielteilchenspektrum ableiten können.

Unter Verwendung von Methoden aus der Theorie der Zufallsmatrizen analysieren wir zunächst den regulären und den chaotischen Spektralbereich des Hamiltonoperators und bestimmen außerdem das Skalierungsverhalten der Bereichsgrenzen. Im Hauptteil der Arbeit gehen wir sodann der obigen Fragestellung aus drei verschiedenen Richtungen nach: Erstens untersuchen wir wie die Statistik der Energieeigenwerte die Simulierbarkeit des Systems beeinflusst, wobei wir einen Zusammenbruch der Simulationseffizienz beim Übergang vom regulären zum chaotischen Bereich beobachten. Zweitens analysieren wir die Stabilität der Eigenzustände des Hamiltonoperators im chaotischen Spektralbereich und identifizieren robuste Zustände, die gegenüber Störungen dynamisch stabil sind. Drittens untersuchen wir den schnellen und irreversiblen Zerfall der Bloch-Oszillationen im chaotischen Bereich. Dabei entwickeln wir eine Methode, die auf einer statistischen Analyse des Geschwindigkeitsoperators beruht, und weisen einen charakteristischen Übergang im Zerfallsverhalten der Bloch-Oszillationen nach, welcher wiederum an der Grenze zwischen regulärer und chaotischer Eigenwertstatistik auftritt.

Abstract

In this thesis, we study interacting ultracold bosons in tilted optical lattices, a paradigm for complex many-body quantum systems. Our analysis is based on the tilted Bose-Hubbard Hamiltonian which incorporates inter-site tunneling, inter-particle interaction, and a static field. The competition between the three contributions induces the system's complexity which, on the spectral level, is reflected in chaotic level statistics. We address the question how this spectral chaos influences the dynamical behavior of the system and, vice versa, which information we can infer from the system's dynamics on its many-body spectrum.

Employing methods from random matrix theory, we first perform a detailed analysis of the Hamiltonian's regular and chaotic spectral regimes and determine their borders by means of a scaling analysis. In the main part of the thesis, we tackle the question raised above from three different perspectives: Firstly, we investigate how the Hamiltonian's level statistics affects the simulability of the system and find a breakdown of the simulation efficiency at the crossover from the regular to the chaotic regime. Secondly, we analyze the stability of the Hamiltonian's eigenstates within the chaotic spectral regime and identify robust states that are dynamically stable against perturbations. Thirdly, we study the fast and irreversible decay of the Bloch oscillations in the chaotic regime. We develop an approach that is based on a statistical analysis of the velocity operator and find a characteristic crossover in the Bloch oscillations' decay, once again right at the transition from regular to chaotic level statistics.

Many people have contributed to this work in some way and this thesis would not have been possible without them. I would now like to take the opportunity to thank them here.

First of all, I thank Andreas Buchleitner for giving me the opportunity to do my PhD in his group. The present thesis emerged under his supervision and I am thankful for many helpful discussions and suggestions.

My deepest gratitude goes to Moritz Hiller. Our countless discussions, his critical feedback, and careful proofreading of the manuscript were of inestimable value for me. Thanks also for guiding me through the many challenges and the ongoing advice and support.

I would also like to thank Florian Mintert for many intense discussions and the long and fruitful collaboration. It was a pleasure to work with you and join your barbecues at any time of the year.

Moreover, I thank Andrew Daley, Bartłomiej Oleś, and Tobias Zech for stimulating discussions and fruitful collaborations.

Many thanks go to all members of the group Quantum Optics and Statistics. *I truly enjoyed the international, stimulating and loyal atmosphere and want to thank all colleagues from the Max-Planck Institute in Dresden and from the ninth floor of the physics high-rise in Freiburg for making this possible.*

A big thank goes to my friends Carola and Susi for all the laughter and distraction, for the shared wines and salads, and all the great times we spent together. I thank all the mums and kiddies for the shared breakfasts, lunches and cakes sessions and all friends who stayed in touch even though it was hard to ever catch me on the phone. I also want to thank Klaudia for the mentoring, all the fascinating new impressions, and the ongoing support in finding my own way.

Above all, I truly thank my family for the everlasting support: Mum, I thank you for the times you spend with us in Freiburg in order to support me when the daycare facility was closed and for always being there for me. Dad and Aresu, thanks for the coaching and all the helpful discussions. I also thank you for pushing me, when I thought there was no way to succeed. Katha and Tilman, thanks for all the babysitting and the willingness to always help us out. I have no idea how I could have handled all this without your help.

Thomas, thanks for always believing in me and for supporting me and my plans throughout all these years. Lenja, I thank you so much for reminding me everyday of what matters most in life.

Contents

1 Motivation and overview

The realization of Bose-Einstein condensation of interacting ultracold atoms in optical lattices [4, 32, 138] was among the most fascinating experimental achievements of the last years. These systems allow for a rapid and precise tuning of the dynamical control parameters, like the inter-atomic interaction, the inter-site tunneling coupling, and, if desired, additional potential gradients or the degree of disorder [77, 125, 134]. At the same time, an almost perfect screening from the environment leads to extremely long coherence times [17]. This precise control has sparked the experimental investigation of a plethora of physical phenomena: On the one hand, it enabled the realization of well-known effects from solid-state physics, like the superfluid to Mott-insulator transition [78, 167, 170], Anderson localization [6, 15, 154], the Bose-glass phase [63], the Josephson effect [32], and Bloch oscillations, that arise under the influence of a static tilt [4, 46, 133]. On the other hand, ultracold atoms in optical lattices have also been used for the high-precision determination of fundamental constants [37] as well as for technological applications, like, *e.g.*, atomic clocks [1, 173] and atom lasers [4, 7, 86, 132]. The latest experimental developments even allow to monitor and manipulate single atoms in optical lattices [10, 11, 165, 200] and render the system a celebrated candidate for potential implementations in quantum computing [17, 69, 136]. The rapid experimental advance is paralleled by thriving theoretical research that combines ideas and techniques developed in areas as diverse as statistical, mathematical, atomic, and solid-state physics and has led to a profound theoretical understanding, see, *e.g.*, [26, 51, 99, 207].

The above examples demonstrate that ultracold bosons in optical lattices constitute a paradigm of complex many-body quantum systems. The complexity, which emerges from the inter-atomic interaction, can basically be controlled at will by properly adjusting the control parameters [77, 78, 99, 100, 125, 134]. It is, among others, reflected in the appearance of chaotic spectral structures [168] that can be characterized by universal distributions [74]. The latter are found in various branches of physics, ranging from mesoscopics [104], and photonics [169, 208] to nuclear [74] and atomic physics [128].

In the present thesis, we focus on the impact of many-body complexity, manifest in spectral chaos [19, 28, 34, 47, 53, 92, 93, 110, 115, 116], on the behavior of ultracold bosons in tilted optical lattices. Specifically, we investigate how the spectral structure of the underlying Hamiltonian affects the possibility to accurately describe the system with manageable numerical effort, the system's stability under perturbations, and its dynamics. Our studies,

in turn, provide means to infer spectral properties from the dynamics of the bosons.

The work is structured as follows:

In *Chapter two*, we introduce the fundamental concepts and basic physics of ultracold bosons in optical lattices. We present the main aspects of Bose-Einstein condensation and of the trapping of atoms in optical lattices, before turning to the mathematical description of the system that relies on the many-body (tilted) Bose-Hubbard Hamiltonian.

In *Chapter 3*, we give a short introduction to universal spectral statistics. We identify the borders of the chaotic regime of the Bose-Hubbard Hamiltonian and elaborate on their dependence on the control parameters and particle number. This knowledge forms the basis to study the impact of spectral chaos on the system's dynamics, what is the topic of the following chapters.

The rapid growth of the Hilbert-space dimension with the number of atoms renders efficient simulation techniques quintessential in order to accurately describe the time evolution of ultracold atoms in optical lattices. In *Chapter four*, we investigate the system's simulability in the different spectral regimes of the Hamiltonian, based on the time-dependent density matrix renormalization group algorithm. The latter is a numerical method that is widely spread in the field and we introduce it at the beginning of the chapter.

While, in general, the inter-atomic interaction induces complex behavior of the bosons in the lattice, it can also lead to the appearance of robust structures that persist well in the chaotic regime of the Bose-Hubbard Hamiltonian. In *Chapter five*, we identify and characterize such robust structures and, in particular, discuss their stability under driving of the tilted lattice.

In *Chapter six*, we study the influence of interactions on the experimentally well-studied phenomenon of Bloch oscillations. Our key focus lies on the irreversible and fast decay of the oscillations in the chaotic regime of the Bose-Hubbard Hamiltonian. We start with a general introduction to the theory of Bloch oscillations and discuss different experimental realizations. In the main part, we pursue two different approaches to relate the spectral properties of the many-body Hamiltonian to the decay of the oscillations: The first one is well-known from the adiabatic theory of driven quantum systems, while the second approach, which we develop in this thesis, relies on a statistical analysis of the velocity operator.

2 Ultracold bosons in optical lattices

Ultracold atoms in optical lattices offer unique possibilities to investigate fundamental questions of quantum physics. In this chapter, we introduce the fundamental concepts and basic physics of these systems what supplies us with the instruments necessary to obtain the results presented throughout this thesis. We will first revise the basic aspects of Bose-Einstein condensation that occurs at temperatures close to the absolute zero. Next, the trapping of atoms in optical lattices will be presented. This leads to the mathematical description of ultracold bosons in (tilted) optical lattices, the Bose-Hubbard Hamiltonian.

2.1 Ultracold bosons

Bose-Einstein condensation was predicted by Einstein in 1924 [59, 60] for a gas of particles obeying Bose statistics [22]. This phase transition can be understood from the fundamentally distinct behavior of a dilute gas of identical bosonic atoms in different temperature regimes, as depicted schematically in Fig. 2.1: Whereas, at high temperatures, the atoms behave like "billiard balls", *i.e.*, classical particles, at low temperatures, the rules of quantum mechanics come into play, and the atoms have to be described as wave packets. Their extension is given by the thermal de Broglie wavelength

$$\lambda_{dB} = \sqrt{\frac{2\pi\hbar^2}{mk_BT}}, \tag{2.1}$$

where m is the mass of the atoms, T is the temperature and k_B is Boltzmann's constant. Lowering the temperature even further leads to a condensation of a macroscopic fraction of the bosons into the lowest quantum state at a certain critical temperature T_c. At this temperature, λ_{dB} is comparable to the mean interparticle distance $d = \rho^{-1/3}$, where ρ is the density of the gas, and the quantum mechanical wave packets that represent the individual particles start to overlap. The system then undergoes a phase transition to a Bose-Einstein condensate and can be described by a single macroscopic wave function $\psi(x)$, also referred to as *order parameter*. At zero temperature, the thermal cloud disappears: All particles occupy the ground state and thereby form a "giant matter wave".

The cooling of atoms to temperatures close to the absolute zero, in order to obtain the necessary phase-space density, was the main challenge for an experimental realization of
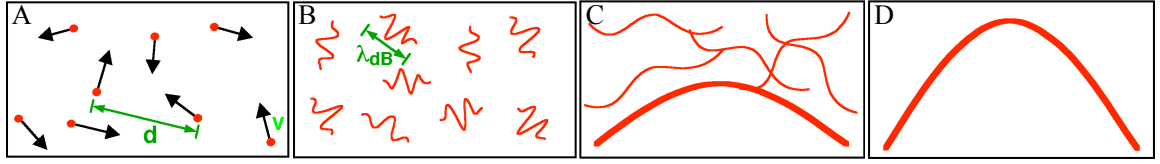
Figure 2.1: Schematic sketch of a gas of identical bosons at different temperatures (adapted from Ref. [103]). (A) At high temperatures, the atoms behave like "billiard balls", *i.e.*, classical particles. (B) For sufficiently low temperatures, the atoms have to be described as wave packets obeying the rules of quantum mechanics. (C) When the thermal de Broglie wavelength λ_{dB} is comparable to the mean interparticle distance d, a phase transition to a BEC occurs. (D) At zero temperature, all particles occupy the lowest quantum state and form a "giant matter wave".

Bose-Einstein condensation [134]. This obstacle was partially overcome with the advent of *laser cooling*, which was proposed in the 1980's and resulted in a Nobel prize in 1997 [36, 43, 146]. The technique takes advantage of the Doppler effect in order to slow down the atoms that are typically held in a magneto-optical trap. Laser cooling yields temperatures of about a few hundred microkelvin which is, however, still too high for Bose-Einstein condensation. Thus, the next step is to apply *evaporative cooling*, that relies on the escape of the hottest, *i.e.*, most energetic, atoms when slightly decreasing the potential barriers of the trap. Then, at temperatures in the nanokelvin regime, a Bose-Einstein condensate is created. For the first time, this was achieved in a cloud of alkali atoms in 1995 [5, 23, 52] and shortly after led to the second Nobel price in the field of ultracold atoms within four years: the Nobel prize for Bose-Einstein condensation in 2001 [44, 103].

   In order to avoid the formation of a solid or a liquid during the generation of a Bose-Einstein condensate, the gas must be sufficiently dilute [50]. Therefore, the particle density is kept very low during the cooling process, at typically $10^{13-15} cm^{-3}$ in experiments with alkali atoms [144]. The interactions within the condensate are then dominated by elastic binary collisions and can be treated by scattering theory. Due to the extremely low temperatures, the only relevant contribution is s-wave scattering, that is solely characterized by the s-wave scattering length a_s. It fulfills the *dilute gas condition* $a_s \ll \rho^{-1/3}$ [122]. Whereas a Bose-Einstein condensate is stable for repulsive interactions ($a_s > 0$), the condensate becomes unstable for attractive interactions ($a_s < 0$) if the number of bosons n in the condensate exceeds a critical value.

   In the last decades, numerous fascinating experiments involving Bose-Einstein condensates of various atomic species have been performed in laboratories all over the world [177]. Depending on the particular experiment, different trapping potentials are used to manipulate the atoms before probing the properties of the condensate. In this respect, periodic poten-
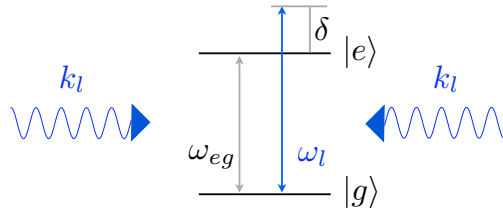
Figure 2.2: Schematic diagram of a two-level atom that interacts with an optical standing wave formed by two counter-propagating laser beams. The internal states of the atom $|g\rangle$ and $|e\rangle$ are separated in energy by $\hbar\omega_{eg}$ and the lasers have frequency ω_l and wave number k_l. The (in this case blue) detuning from resonance is given by $\delta = \omega_l - \omega_{eg}$.

tials are exceptionally interesting since they enable us to investigate fundamental questions of solid state physics and also mesoscopic phenomena. They are typically realized with the help of optical lattices as will be explained in the following.

2.2 Optical lattices

The idea of trapping atoms with the help of a standing light wave dates back to 1986 [124] and the first experimental realization was achieved in 1987 for a classical gas of Cesium atoms [159]. The rich physics of such systems allows to mimic standard as well as exotic solid-state Hamiltonians where the parameters defining the dynamics can, in principle, be experimentally controlled at will, as we describe below [77, 125, 134]. The excellent isolation from the environment, which offers the possibility of coherent dynamics on long timescales, also renders the system a promising candidate for technological applications, like, *e.g.*, ever more accurate atomic clocks [1, 173] or potential implementations in quantum computing [17, 69, 136].

2.2.1 Periodic potential

The interaction of a neutral atom with a light field can be split into a conservative and a dissipative part. Whereas the former can be used for the creation of optical potentials like optical lattices and other optical traps (*dipole traps*) [80], the latter leads to a scattering of atoms by atom-photon interactions and is also used for laser cooling [146].

In order to illustrate the basic physics, we consider the interaction of a two-level atom with classical, single-mode laser light of frequency ω_l, as schematically shown in Fig. 2.2. The atom is assumed to be initially in the electronic (ground) state $|g\rangle$ which is coupled

by the laser to the (excited) state $|e\rangle$. The energy difference between the states is given by $\hbar\omega_{eg}$. We can apply this two-level approximation as long as the frequency ω_l is sufficiently far from frequencies required to couple $|g\rangle$ to other internal states. The oscillating electric field $\mathbf{E}(\mathbf{x},t)$ then induces a dipole moment [42, 144]

$$\mathbf{D}(\mathbf{x},t) = \alpha(\omega_l)\mathbf{E}(\mathbf{x},t), \tag{2.2}$$

where $\alpha(\omega)$ is the atomic polarizability that exhibits a resonance at ω_{eg}. In the dipole approximation, the interaction of this induced dipole with the electric field leads to a complex energy shift of the atomic level $|g\rangle$ by

$$\begin{aligned}\Delta E_g &= -\frac{1}{2}\alpha(\omega_l)\left\langle \mathbf{E}(\mathbf{x},t)^2\right\rangle_t \\ &= V_g - i\hbar\Gamma_{sc}/2,\end{aligned} \tag{2.3}$$

where $\langle\cdot\rangle_t$ denotes a time average. The real, *i.e.*, conservative, part corresponds to the so-called ac Stark shift

$$V_g = -\frac{1}{2}Re(\alpha(\omega_l))\left\langle \mathbf{E}(\mathbf{x},t)^2\right\rangle_t \propto \frac{I(\mathbf{x},t)}{\delta}, \tag{2.4}$$

where $\delta = \omega_l - \omega_{eg}$ is the detuning and $I(\mathbf{x},t)$ is the laser intensity. The imaginary, *i.e.*, dissipative, part leads to a finite lifetime of the state $|g\rangle$ due to photon absorption and subsequent emission with scattering rate

$$\Gamma_{sc} \propto \frac{I(\mathbf{x},t)}{\delta^2}. \tag{2.5}$$

For red detuning $\delta < 0$, the induced dipole $\mathbf{D}(\mathbf{x},t)$ is in phase with the electric field and the atoms are attracted to regions of high intensity. On the contrary, for blue detuning $\delta > 0$, the atoms are attracted to the dark regions where the light intensity, and thus the loss rate, is lowest. It is therefore favorable to work at the largest possible blue detuning to minimize dissipative effects[1] and to obtain a conservative potential for the atoms.

In order to create a one-dimensional (1D) optical lattice[2] one can superimpose two identical, counter-propagating laser beams that will form a standing light wave. For wave number $k_l = 2\pi/\lambda_l$, this leads to a periodic potential

$$V(x) = V_0\sin^2(k_l x), \tag{2.6}$$

with lattice spacing $d = \lambda_l/2$, amplitude $V_0 \propto I_P/\delta$, and I_P the peak intensity of the laser. In practice, optical lattices are realized by retro-reflecting a laser beam with a high-quality

---

[1]In principle, spontaneous emission leads to decoherence of many-body states due to heating of the bosonic atoms, see for example Refs. [118, 147].

[2]From now on, we restrict the description to the 1D case since we only consider 1D lattices in this work. The 3D case can, however, be described analogously, see for example Ref. [134].

mirror and precisely controlling the beam intensity in order to tune the depth of the lattice. Alternatively, one can use two counter-propagating phase-coherent laser beams. A frequency shift $\Delta \nu_l$ between the two laser beams, that can be introduced by using, *e.g.*, an acousto-optic modulator [134], causes the formerly stationary lattice to move at the velocity $v_{lat} = d\Delta \nu_l$. If, in addition, $\Delta \nu_l$ is varied in time, the lattice will be accelerated, resulting in a force acting on the atoms in the rest frame of the lattice. For $\Delta \nu_l \propto t$, the resulting force has the form of a static field (see also Sec. 2.4), effects of which will be studied in detail in Chapters 5 and 6.

2.2.2 Band structure

On timescales where spontaneous emission can be neglected ($t \ll 1/\Gamma_{sc}$), the dynamics of a single atom in the optical lattice can be described by the Hamiltonian

$$\hat{H} = \frac{\hat{p}^2}{2m} + V_0 \sin^2(k_l x). \tag{2.7}$$

The eigenstates $|\phi_q^{(\eta)}\rangle$ of this periodic Hamiltonian in position representation, *i.e.*, $\langle x|\phi_q^{(\eta)}\rangle = \phi_q^{(\eta)}(x)$, are Bloch waves and can be written as [9]

$$\phi_q^{(\eta)}(x) = e^{iqx} u_q^{(\eta)}(x), \tag{2.8}$$

where the functions $u_q^{(\eta)}(x) = u_q^{(\eta)}(x+d)$ have the same periodicity as the lattice. The eigenstates and the corresponding eigenenergies $E_q^{(\eta)}$ are labeled by the *quasimomentum* $q \in [-\pi/d, \pi/d]$ and the *band index* η.

Fig. 2.3 shows the band structure of a 1D optical lattice for different lattice depths V_0. For $V_0 = 0$, the energy bands express the dispersion relation of a free particle (the energy-momentum parabola) reduced to the first Brillouin zone. Increasing the lattice depth leads to the appearance of energy gaps and a flattening of the bands, and also reduces the mobility of the bosons on the lattice.

2.2.3 Wannier functions

So far, we have only considered the single-particle case. In the following, we will, however, mainly be interested in many-body phenomena, taking into account short-range interactions between the particles. For the description of such systems it is convenient to use Wannier functions

$$w_\eta(x - x_l) = \sqrt{\frac{d}{2\pi}} \int\limits_{-\pi/d}^{\pi/d} dq\, u_q^{(\eta)}(x) e^{-iqx_l}, \tag{2.9}$$
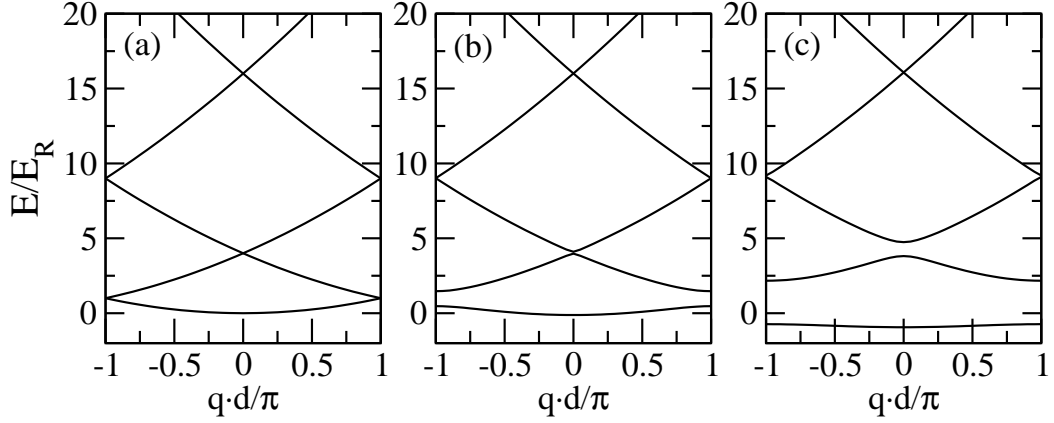
Figure 2.3: Band structure of a 1D optical lattice for different potential depths V_0. Shown are the band energies $E_q^{(\eta)}/E_R$ as a function of the quasimomentum q within the first Brillouin zone for (a) $V_0/E_R = 0$, (b) 2, and (c) 6. Here, $E_R = \hbar^2 k_l^2/(2m)$ is the photon recoil energy.

which are localized on a particular lattice site x_l. When interpreting $u_q^{(\eta)}$ as a function of the quasimomentum q, the Wannier function $w_\eta(x - x_l)$ is thus the Fourier transform of $u_q^{(\eta)}$ evaluated at the point x_l. Accordingly, the Bloch functions in the ηth band can be expressed as a Fourier series of Wannier functions

$$u_q^{(\eta)}(x) = \sqrt{\frac{d}{2\pi}} \sum_{x_l} w_\eta(x - x_l) e^{iqx_l} . \tag{2.10}$$

2.3 Microscopic description: Bose-Hubbard Hamiltonian

A mathematical description of interacting ultracold bosons in optical lattices is given by the Bose-Hubbard Hamiltonian [99]. This Hamiltonian is well-known in solid state physics and is valid for deep lattices since it relies on the restriction of the dynamics to the lowest band of the underlying optical lattice. The Bose-Hubbard Hamiltonian provides the simplest nontrivial model describing a bosonic many-body system that cannot be mapped to a single-body problem. It is of major importance in situations where quantum fluctuations are crucial, *i.e.*, when the number of atoms per lattice site is small and particle correlations have to be taken into account. In the following, we will show how the Bose-Hubbard Hamiltonian can be derived in second quantization and discuss its validity and properties.

2.3.1 Derivation of the Bose-Hubbard Hamiltonian

In second quantization, the many-body Hamiltonian describing interacting bosonic particles in an external potential $V(x)$ is given by [50, 99]

$$
\begin{aligned}
\hat{H} = & \int dx \, \hat{\psi}^\dagger(x) \left(-\frac{\hbar^2}{2m} \nabla^2 + V(x) + V_{add}(x) \right) \hat{\psi}(x) \\
& + \frac{1}{2} \int \int dx \, dx' \, \hat{\psi}^\dagger(x) \hat{\psi}^\dagger(x') U(x-x') \hat{\psi}(x') \hat{\psi}(x),
\end{aligned}
\tag{2.11}
$$

where $\hat{\psi}(x)^{(\dagger)}$ are the bosonic field operators that annihilate (create) a particle at the position x, and $V_{add}(x)$ accounts for a possibly present additional potential that is slowly varying along the lattice. The latter condition guarantees that the lattice, which is described by $V(x)$, is not considerably modified and different sites can be treated analogously. Whereas the first three terms in the Hamiltonian are single-particle contributions, the last term describes the binary inter-atomic interaction and thus accounts for the many-body properties. Assuming that the latter results only from s-wave scattering [122] we can apply a contact-interaction pseudopotential approximation,

$$
U(x-x') = \frac{4\pi a_s \hbar^2}{m} \delta(x-x'),
\tag{2.12}
$$

with the *s*-wave scattering length a_s. This assumption is fulfilled for very low particle densities and temperatures, both of which is the case in ultracold atom experiments, as discussed in Sec. 2.1. The Hamiltonian then reads

$$
\begin{aligned}
\hat{H} = & \int dx \, \hat{\psi}^\dagger(x) \left(-\frac{\hbar^2}{2m} \nabla^2 + V(x) + V_{add}(x) \right) \hat{\psi}(x) \\
& + \frac{1}{2} \frac{4\pi a_s \hbar^2}{m} \int dx \, \hat{\psi}^\dagger(x) \hat{\psi}^\dagger(x) \hat{\psi}(x) \hat{\psi}(x).
\end{aligned}
\tag{2.13}
$$

For sufficiently deep lattices, as considered throughout this thesis, the bosonic operators $\hat{\psi}(x)$ can be expanded in the basis of Wannier functions $w_0(x-x_l)$ of the lowest band (*tight-binding approximation*)

$$
\hat{\psi}(x) = \sum_l \hat{a}_l w_0(x-x_l),
\tag{2.14}
$$

where $\hat{a}_l$ annihilates a particle in the Wannier function $w_0(x-x_l)$, localized at the *l*th lattice site. Here, sufficiently deep means that all the energies involved in the system dynamics are small compared to excitation energies to the second band. The many-body Hamiltonian $\hat{H}$, Eq. (2.13), then reduces to the Bose-Hubbard Hamiltonian

$$
\hat{H} = -\frac{J}{2} \sum_l (\hat{a}_{l+1}^\dagger \hat{a}_l + h.c.) + \frac{U}{2} \sum_l \hat{n}_l(\hat{n}_l - 1) + \sum_l \varepsilon_l \hat{n}_l.
\tag{2.15}
$$

The bosonic annihilation and creation operators $\hat{a}_l$ and $\hat{a}_l^\dagger$ fulfill the canonical commutation relation

$$[\hat{a}_l, \hat{a}_j^\dagger] = \delta_{l,j}, \tag{2.16}$$

and the operator $\hat{n}_l$, that counts the number of atoms at lattice site l, is defined as

$$\hat{n}_l = \hat{a}_l^\dagger \hat{a}_l. \tag{2.17}$$

The parameters J, U, and ε_l correspond to the *tunneling coupling* (hopping) between neighboring sites[3], the *onsite interaction strength*, and a local energy offset at each site, respectively, and are given by

$$J = -2 \int dx\, w_0(x) \left(-\frac{\hbar^2}{2m} \nabla^2 + V(x) \right) w_0(x-d), \tag{2.18}$$

$$U = \frac{4\pi a_s \hbar^2}{m} \int dx\, |w_0(x)|^4, \tag{2.19}$$

$$\varepsilon_l = \int dx\, V_{add}(x) |w_0(x)|^2. \tag{2.20}$$

Numerical calculations show that both, next-nearest neighbor coupling and nearest-neighbor interaction are typically two orders of magnitude smaller than J and U and can thus be neglected [99].

Qualitative insight into the dependence of the parameters on the lattice geometry is obtained via a harmonic approximation around the minima of the potential wells:

$$V_{ho}(x) = \frac{1}{2} m \omega_T^2 x^2. \tag{2.21}$$

Here, $\omega_T = 2\sqrt{V_0 E_R}/\hbar$ is the trapping frequency and $E_R = \hbar^2 k_l^2/(2m)$ is the photon recoil energy. The spacing between the lowest and the first excited Bloch band is then given by $\Delta E = \hbar \omega_T$. The oscillator ground state wave function of a single atom trapped in one of the minima of the potential has a Gaussian profile with width $a_G = \sqrt{\hbar/(m\omega_T)}$. Consistency of the Bose-Hubbard model then requires $a_s \ll a_G \ll d$ and $U \cdot n_l(n_l - 1)/2 \ll \Delta E$ for all lattice sites l. Whereas the former follows from the contact-interaction pseudopotential approximation and the requirement of a large energy separation from the second band, the latter expresses the requirement that the onsite interaction must be much smaller than the excitation energy to the next band. Moreover, the interaction energies have to be small compared to the single-particle ground state energy since otherwise the single-particle wave function would have to be adjusted to account for the (mean-field) interaction [126]. All requirements are readily satisfied in the experiment [48, 99].

---

[3]Note that in the original definition [99], the tunneling coupling is given by J instead of $J/2$.

As mentioned above, when realized within an optical lattice, the parameters of the Bose-Hubbard Hamiltonian can, in principle, be experimentally controlled at will [134]: Both tunneling coupling and onsite interaction can be varied by adjusting the depth of the lattice, *i.e.*, the intensity of the lasers. Whereas in a deep lattice [207] the hopping strength is given by $J = \Delta_0/2$, where Δ_0 is the width of the lowest band, and decreases exponentially with V_0, $J \propto \exp\left(-2\sqrt{V_0/E_R}\right)$, the interaction increases algebraically[4] like $U \propto (V_0/E_R)^{1/4}$. In addition, external magnetic fields can be used to independently adjust the value of U by changig the s-wave scattering length a_s via Feshbach resonances [96, 122]. It is thus possible to enter the strong coupling regime, where the interaction energy is of the order of the kinetic energy, and simulate otherwise intractable systems in condensed matter physics, what provides us with new insight in the physics of many-body systems [100, 134].

In the following, we will consider the Bose-Hubbard Hamiltonian (2.15) to be dimensionless, *i.e.*, the parameters J and U, and the energy are always given in units of the photon recoil energy E_R. Likewise, actions are measured in units of $\hbar$ (*i.e.*, $\hbar \equiv 1$). In order to see how this translates to laboratory units, we consider the experimental parameters of Ref. [83] where the authors investigate the dynamics of a Bose-Einstein condensate of Cesium atoms in a vertically oriented optical lattice. The laser used for the generation of the lattice has a wavelength of $\lambda = 1064\,nm$, what results in a photon recoil energy of $E_R = k_B \cdot 64\,nK$, and the lattice depth is $V_0 = 7.9\,E_R$. Consequently, the tunneling amounts to $J = 0.0385\,E_R$, while the onsite interaction can be tuned with the help of a Feshbach resonance from $a_s = -2a_0$ to $a_s = 300a_0$, where a_0 is the Bohr radius. For example, for $a_s = 25a_0$ and $a_s = 100a_0$, this results in $U = 0.114\,E_R$ and $U = 0.458\,E_R$, respectively.[5]

2.3.2 Properties of the Bose-Hubbard Hamiltonian

The physics of the Bose-Hubbard Hamiltonian is characterized by the interplay of tunneling and onsite interaction. On the one hand, the tunneling coupling J tends to distribute the atoms over the lattice. As a consequence, for dominant tunneling, $U \ll J$, the eigenstates are Bloch states that are completely delocalized on the lattice. On the other hand, the repulsive inter-atomic interaction U localizes the single atoms on individual sites of the lattice. For strong onsite interaction, $U \gg J$, the eigenstates of the Bose-Hubbard Hamiltonian are thus given by Wannier states with a well-defined particle number on every lattice site. That is, they are (Wannier-) Fock states of the form

$$|\mathbf{n}\rangle = |n_1\rangle \otimes |n_2\rangle \otimes \cdots \otimes |n_L\rangle \equiv |n_1, n_2, ..., n_L\rangle, \tag{2.22}$$

---

[4]In general, one finds $U \propto (V_0/E_R)^{\mathcal{D}/4}$, where $\mathcal{D}$ is the dimensionality of the lattice [153].

[5]Note that the values for J and U are obtained from the equations for a deep lattice [207] and thus have to be treated with care. In order to obtain the exact numbers, one would have to directly evaluate Eqs. (2.18) and (2.19).

where n_l is the number of particles on the lth site, L is the number of lattice sites, and $n = \sum_{l=1}^{L} n_l$ is the total number of bosons in the system. However, when the tunneling and the onsite interaction terms have comparable magnitude, there exists no natural basis and thus the system shows features of quantum chaos [19, 34, 47, 53, 92, 93, 110, 116], as will be discussed thoroughly in Sec. 3.2.1.

Whilst we are mainly interested in the impact of chaos in the excitation spectrum of the Bose-Hubbard Hamiltonian, the properties of the ground state have been studied in detail in the last decades, see for example [207]. Under this perspective, the system undergoes a quantum phase transition between a *superfluid* and a *Mott insulating state*, controlled by the relative strength of onsite interaction and tunneling strength U/J [71]. In contrast to the classical analog, *quantum* phase transitions are driven by quantum (not thermal) fluctuations [157] and thus occur at zero-temperature. In the limit $(U/J) \to 0$, the Bose-Hubbard ground state is superfluid and can be written as

$$|\Psi_{SF}\rangle = \left(\frac{1}{\sqrt{L}} \sum_{l=1}^{L} \hat{a}_l^\dagger \right)^n |0\rangle, \tag{2.23}$$

where $|0\rangle = |0, \ldots, 0\rangle$ is a Fock state that contains zero particles. For $n, L \to \infty$ and constant filling factor n/L, this tends to a locally coherent state, *i.e.*, a coherent state at each lattice site l,

$$|\Psi_{SF}\rangle = \bigotimes_{l=1}^{L} \left[\exp\left(\sqrt{\frac{n}{L}} \hat{a}_l^\dagger \right) |0\rangle_l \right], \tag{2.24}$$

with Poissonian number statistics [207]. Here $|0\rangle_l$ is a local Fock state on site l that contains zero particles. The state $|\Psi_{SF}\rangle$, Eq. (2.24), represents an ideal Bose-Einstein condensate where all particles are in the Bloch state $|\phi_{q=0}^{(\eta=0)}\rangle$.

Increasing the ratio U/J makes it less favorable for the atoms to tunnel between neighboring sites and for $(U/J) \to \infty$ the fluctuations of the particle number on a particular site are completely suppressed. For integer filling $n/L \in \mathbb{N}$, this leads to the Mott insulating state

$$|\Psi_{MI}\rangle = \bigotimes_{l=1}^{L} \left[\left(\hat{a}_l^\dagger \right)^{n/L} |0\rangle_l \right], \tag{2.25}$$

which is a product of local Fock states with particle number $n_l = n/L$ at each site. In 1D, the quantum phase transition occurs at the critical value[6] [207] $(U/J)_c = 7.68$, for $n/L = 1$, and at $(U/J)_c = 4.4 \cdot n/L$, for $n/L > 1$. It was first observed, in 3D, in 2002 [78], subsequently, in 1D, in 2004 [170], and in 2D in 2007 [167].

---

[6]Note that due to the the choice of the tunneling coupling as $J/2$ instead of J, the shown values deviate from the ones given in Ref. [207] by exactly the factor of 2.
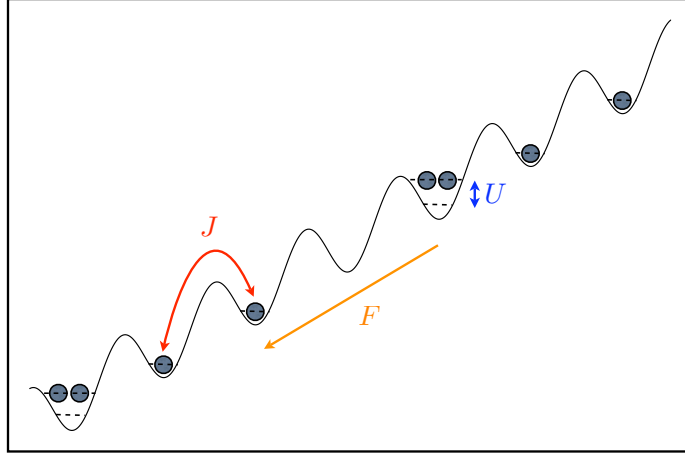
Figure 2.4: Schematic diagram of ultracold bosons in the lowest band of a tilted optical lattice described by the tilted Bose-Hubbard Hamiltonian $\hat{H}$, Eq. (2.26). The parameters J, U, and F denote the strength of tunneling coupling, onsite interaction, and tilt, respectively.

2.4 The tilted Bose-Hubbard Hamiltonian

Similar to solid state systems, where an electric field induces a potential gradient along a crystal [9], we can apply an additional static field to the optical lattice, as schematically depicted in Fig. 2.4. Experimentally, a global tilt can be realized by introducing a time-dependent frequency shift between the lasers used for the generation of the lattice potential [12, 133], or by tilting the lattice into the direction of the gravitational field [65, 83].

Mathematically, this amounts to choosing $\varepsilon_l = F\tilde{l}$ in the Bose-Hubbard Hamiltonian, Eq. (2.15), which then reads

$$\hat{H} = \underbrace{-\frac{J}{2}\sum_{l=1}^{L-1}(\hat{a}_{l+1}^{\dagger}\hat{a}_l + h.c.)}_{\hat{H}_J} + \underbrace{\frac{U}{2}\sum_{l=1}^{L}\hat{n}_l(\hat{n}_l - 1)}_{\hat{H}_U} + \underbrace{F\sum_{l=1}^{L}\tilde{l}\hat{n}_l}_{\hat{H}_F} \ . \tag{2.26}$$

Here, L is the finite number of lattice sites and we chose $\tilde{l} = -L/2 - 1 + l$, for even L, and $\tilde{l} = -(L+1)/2 + l$, for odd L, what corresponds to tilting around the central lattice site but has no further physical implications. The tilting strength F includes the lattice spacing via $F = fd$, where f is the static field, and, without loss of generality, we assume $F \geq 0$ in the following.

The tilting of the lattice introduces a new energy scale to the system and can induce excitations to higher Bloch bands, via Landau-Zener tunneling [121, 203], with the transition probability [94]

$$|T|^2 = \exp\left(-\frac{\pi^2}{8}\frac{\Delta E^2}{F}\right).$$

(2.27)

This effect has been studied both theoretically and experimentally in much detail, see for example [46, 94, 102, 137, 174] and references therein. However, in order to guarantee the validity of the single-band approximation that was employed in the derivation of the Bose-Hubbard Hamiltonian, see Sec. 2.3.1, such transitions have to be negligible. We thus find that for $V_0 = 10$ the field strength has to be restricted to $F < 30$ [75, 112]. In the experiment, lattice depths of $V_0 > 20$ can easily be realized [78], what allows for even stronger tilts without compromising the single-band approximation.

The global tilt is at the heart of this thesis and leads to interesting physical phenomena, like the appearance of Bloch oscillations (for further details see Chapter 6). It also strongly influences the spectral statistics, as we discuss in Chapter 3.

Note that the static field term induces a constant offset between the potential at adjacent lattice sites and thus breaks the translational invariance of the Bose-Hubbard Hamiltonian, which holds for $\varepsilon_l = 0$ in Eq. (2.15). In the Hamiltonian (2.26), it is therefore not possible to apply periodic boundary conditions, that are frequently used in solid state physics, in order to avoid finite size, *i.e.*, boundary effects [9]. We rather have to require Dirichlet boundary conditions such that the state vector vanishes on the boundaries of the finite lattice. A possibility to adjust the Hamiltonian such that periodic boundary conditions can be applied, will be discussed in the following section.

2.4.1 Time-dependent Bose-Hubbard Hamiltonian and periodic boundary conditions

The dynamics of a quantum system is dictated by the Schrödinger equation

$$i\partial_t|\psi(t)\rangle = \hat{H}|\psi(t)\rangle,$$

(2.28)

where $|\psi(t)\rangle$ is the state vector of the system and $\hat{H}$ is the Hamiltonian, in our case given by the tilted Bose-Hubbard Hamiltonian $\hat{H} = \hat{H}_J + \hat{H}_U + \hat{H}_F$, Eq. (2.26). In order to transform to the interaction representation with respect to the static field term $\hat{H}_F$, we apply the gauge transformation [75, 114]

$$|\psi(t)\rangle = e^{-i\hat{H}_F t}|\tilde{\psi}(t)\rangle.$$

(2.29)

This results in

$$i\partial_t|\tilde{\psi}(t)\rangle = \hat{\tilde{H}}(t)|\tilde{\psi}(t)\rangle$$

(2.30)

and

$$\hat{\bar{H}}(t) = e^{i\hat{H}_F t}(\hat{H}_J + \hat{H}_U)e^{-i\hat{H}_F t} = e^{i\hat{H}_F t}\hat{H}_J e^{-i\hat{H}_F t} + \hat{H}_U. \tag{2.31}$$

The transformed Hamiltonian

$$\hat{\bar{H}}(t) = -\frac{J}{2}\sum_{l=1}^{L-1}(\hat{a}_{l+1}^{\dagger}\hat{a}_l\, e^{iFt} + h.c.) + \frac{U}{2}\sum_{l=1}^{L}\hat{n}_l(\hat{n}_l - 1) \tag{2.32}$$

is now periodically time-dependent, with the Bloch period[7]

$$T_B = \frac{2\pi}{F}, \tag{2.33}$$

and reminiscent of the Hamiltonian of periodically driven systems.

The gauge transformation applied above does not yet affect the boundary conditions. However, the transformed Hamiltonian $\hat{\bar{H}}(t)$ no longer contains a constant potential offset, but a time-dependent phase factor between adjacent lattice sites, that is independent of the considered sites. The translational invariance, previously broken by the additional static field, is thus recovered in the new representation. Consequently, we can enforce periodic boundary conditions by adding the coupling term $-J/2\,(\hat{a}_1^{\dagger}\hat{a}_L\, e^{iFt} + h.c.)$ between lattice sites L and 1. This amounts to

$$\hat{\bar{H}}_p(t) = -\frac{J}{2}\sum_{l=1}^{L}(\hat{a}_{l+1}^{\dagger}\hat{a}_l\, e^{iFt} + h.c.) + \frac{U}{2}\sum_{l=1}^{L}\hat{n}_l(\hat{n}_l - 1), \tag{2.34}$$

where we identify $\hat{a}_{L+1}^{(\dagger)} = \hat{a}_1^{(\dagger)}$. Note that, compared to (2.32), the sum in the tunneling term now runs up to L, instead of $L-1$.

One ought to keep in mind, however, that this transformed system with periodic boundary conditions is no longer simply the interaction representation of the initial Hamiltonian with respect to the static field. This is immediately evident when back-transforming the Hamiltonian $\hat{\bar{H}}_p(t)$ via $e^{-i\hat{H}_F t}\hat{\bar{H}}_p(t)e^{i\hat{H}_F t}$ what results in

$$\hat{H}_p(t) = \hat{H}_J - \frac{J}{2}(\hat{a}_1^{\dagger}\hat{a}_L e^{itFL} + h.c.) + \hat{H}_U + \hat{H}_F, \tag{2.35}$$

and we find that the Hamiltonian is time dependent even in the rest frame of the lattice. The transformed Hamiltonian with periodic boundary conditions $\hat{\bar{H}}_p(t)$, Eq. (2.34), and, accordingly, the back-transformed Hamiltonian $\hat{H}_p(t)$, Eq. (2.35), thus describe a different physical system, *e.g.*, bosonic particles trapped on an accelerated ring structure [3].

Periodic (Born-von Karman) boundary conditions are frequently used on grounds of mathematical convenience in solid state physics [9]. This choice is justified in cases where

---

[7]The Bloch period T_B fixes the periodicity of the *Bloch oscillations* which will be discussed in detail in Chapter 6.

the system under consideration is large and boundary effects are irrelevant, since the finiteness of the lattice would be manifest only on very large timescales. More precisely, periodic boundary conditions mimic a periodic, infinite system where the primitive cell is given by the original system. Furthermore, it can be numerically advantageous to use periodic boundary conditions as will be discussed below.

We thus have to address the question under which circumstances the different systems, that correspond to the different choices of boundary conditions described by the Hamiltonians (2.26) and (2.34), coincide. Or, in other words, when do the boundaries actually affect the quantities under consideration, *e.g.*, when are the boundaries probed by the dynamics? Obviously, this strongly depends both, on the particular realization of the system and on the quantities of interest. For example, in the limit of very small tunneling strength $J \ll U$, the exact form of the boundary conditions is essentially irrelevant, since the particles barely move and thus hardly ever reach the boundaries of the lattice. Consequently, if we study dynamical quantities, like, *e.g.*, the velocity or the center of mass of the bosons on the lattice, the influence of the boundary conditions will depend on the initial state and on the values of the parameters J, U and F: The amplitude of the Bloch oscillations, for example, is proportional to $1/F$. This leads to a high sensitivity on the choice of boundary conditions for small values of the tilting strength, where the bosons actually hit the edges of the lattice and reflections can occur (see Chapter 6 for more details). For large values of the tilt F and an initial wave packet that is localized in the middle of the lattice, the boundary conditions though do not matter significantly. Whether or not results obtained either from Hamiltonian $\hat{H}$, Eq. (2.26), or from Hamiltonian $\hat{\tilde{H}}_p(t)$, Eq. (2.34), can be carried over to the other system therefore has to be checked depending on the specific problem at hand.

2.4.1.1 Quasimomentum basis

The translational invariance of $\hat{\tilde{H}}_p(t)$, Eq. (2.34), leads to the appearance of a new quantum number, the quasimomentum κ, which can be used to construct a new set of basis vectors that reveals the symmetry of the Hamiltonian, as we will see in the following. Note that, as opposed to Secs. 2.2.2 and 2.2.3, where we referred to the *continuous* quasimomentum as q, here we choose κ instead, in order to stress that in a finite lattice it can only take a finite number of *discrete* values.

Starting from an arbitrary Fock state $|\mathbf{s}\rangle$ of the form (2.22), the *shift operator* $\hat{S}$, defined via

$$\hat{S}|n_1, n_2, ..., n_L\rangle = |n_L, n_1, n_2, ..., n_{L-1}\rangle \,, \tag{2.36}$$

can generate at most L distinct Fock states. Using those states $|\mathbf{s}\rangle$ which cannot be transformed into each other with the help of $\hat{S}$ and are referred to as *seed states*, a new set of

basis vectors [114]

$$|\mathbf{s}, \kappa\rangle = \frac{1}{\sqrt{M(s)}} \sum_{l=1}^{M(s)} e^{i\kappa l} \hat{S}^l |\mathbf{s}\rangle \,, \tag{2.37}$$

can be constructed. Here, the cyclicity $M(s)$ is the number of different Fock states that can be generated from $|\mathbf{s}\rangle$ under the action of the shift operator $\hat{S}$, and the quasimomentum takes the values $\kappa = 2\pi \cdot (j-1)/M(s)$ with $j = 1, \ldots, M(s)$.

By construction, each basis state $|\mathbf{s}, \kappa\rangle$ is completely delocalized over the lattice. As a consequence, any localized state is a superposition of different states $|\mathbf{s}, \kappa\rangle$. For example, a Fock state $|\mathbf{n}\rangle = |\ldots, 0, n, 0, \ldots\rangle$ with all particles on one particular site of the lattice is a superposition of different states $|\mathbf{s}, \kappa\rangle$ with distinct values of quasimomentum κ, where $|\mathbf{s}\rangle$ is the seed state from which $|\mathbf{n}\rangle$ can be constructed.

With the help of this new set of basis vectors, the Hamiltonian $\hat{\bar{H}}_p(t)$, Eq. (2.34), becomes block diagonal and decomposes into the direct sum

$$\hat{\bar{H}}_p(t) = \oplus_{j=1}^{L} \hat{\bar{H}}_p^{(\kappa_j)}(t), \tag{2.38}$$

where each operator $\hat{\bar{H}}_p^{(\kappa_j)}(t)$ corresponds to one possible value of quasimomentum κ, given by $\kappa_j = 2\pi \cdot (j-1)/L$ with $j = 1, \ldots, L$. Note that, in general, the blocks have different size, since not every seed state contributes to every block of quasimomentum.

The decomposition (2.38) is important for the spectral analysis of the system, as will become clear in Sec. 3.1. Moreover, since the dimension[8]

$$\mathcal{N} = \frac{(n+L-1)!}{n!\,(L-1)!} \tag{2.39}$$

of the Bose-Hubbard Hamiltonian's Hilbert space grows exponentially, both with the boson number n and the number L of lattice sites, this decomposition can lead to an enormous numerical advantage in the simulation of the system dynamics: Each of the sub-Hamiltonians $\hat{\bar{H}}_p^{(\kappa_j)}(t)$ acts on a Hilbert space of dimension $\mathcal{N}_{\kappa_j} \approx \mathcal{N}/L$.

2.4.2 Floquet operator

The time-evolution operator generated by the time-dependent Hamiltonian $\hat{\bar{H}}_p(t)$ is given by [79]

$$\hat{U}(t) = \mathcal{T} \exp\left(-i \int_0^t \hat{\bar{H}}_p(t) dt \right), \tag{2.40}$$

---

[8]The dimension of the Hilbert space that corresponds to the Bose-Hubbard Hamiltonian arises from combinatorics by placing $L-1$ boundaries (between the lattice sites) between n particles where both boundaries and particles are indistinguishable.

where $\mathcal{T}$ denotes time ordering. It is the formal solution of the Schrödinger equation for a time-dependent Hamiltonian and maps the state of a quantum system at time 0 to its state at time t, *i.e.*, $|\psi(t)\rangle = \hat{U}(t)|\psi(0)\rangle$.

Since the Hamiltonian is itself periodic, the Bloch period T_B defines the natural timescale for the system dynamics. For such periodic boundary conditions in time we can write [160]

$$\hat{U}(t + T_B) = \hat{U}(t)\hat{U}(T_B) \tag{2.41}$$

where the *Floquet operator*

$$\hat{U}(T_B) = \mathcal{T}\exp\left(-i\int\limits_0^{T_B}\hat{\bar{H}}_p(t)dt\right) \tag{2.42}$$

propagates the system over one period T_B of the Hamiltonian. Eq. (2.41) implies $\hat{U}(nT_B) = \hat{U}(T_B)^n$, and thus knowledge of $\hat{U}(T_B)$ is sufficient if we are not interested in fine-grained details of the time-evolution but rather in the general or long-time behavior of the system.

In the quasimomentum basis (2.37) also the Floquet operator has block diagonal form,

$$\hat{U}(T_B) = \oplus_{j=1}^{L}\hat{U}^{(\kappa_j)}(T_B), \tag{2.43}$$

where some pairs of blocks are related to each other by time-reversal symmetry [114].

2.5 Mean-field description: Discrete Gross-Pitaevskii equation

An alternative approach to describe ultracold bosons in optical lattices can be formulated for large filling factors $n/L \gg 1$. In this regime, atom number fluctuations are negligible, and a mean-field approach, as first developed by Bogoliubov for the homogeneous case of a Bose-Einstein condensate in a single trap [20], is applicable. Since, in the present work, we focus on the regime where the number of atoms per lattice site is small, $n/L \approx 1$, we only give a short recollection here. For a thorough discussion see for example Refs. [50, 122, 134].

In the ideal case of a noninteracting gas of bosons at temperature $T = 0$, all n particles are described by identical single-particle wave functions $\phi(x)$. The wave function of the condensate is then given by $\psi(x) = \sqrt{n}\phi(x)$, which can be related to the superfluid state $|\Psi_{SF}\rangle$, Eq. (2.24), where all particles are in the Bloch state $|\phi_{q=0}^{(\eta=0)}\rangle$. Including nonuniform and time-dependent configurations, one can generalize Bogoliubov's original theory by rewriting the bosonic field operators as [122]

$$\hat{\psi}(x,t) = \psi(x,t) + \delta\hat{\psi}(x,t), \tag{2.44}$$

where $\psi(x,t) = \langle \hat{\psi}(x,t) \rangle$ is a classical field, also referred to as *macroscopic wave function* or *order parameter*. The atom density is $\rho(x,t) = |\psi(x,t)|^2$, and the wave function is normalized such that $\int dx \rho(x,t) = n$. The quantum fluctuations are given by $\delta\hat{\psi}(x,t)$ and lead to a depletion of the condensate mode by population of excited modes.

For a dilute, weakly-interacting gas with $\rho a_s^3 \ll 1$, and upon neglect of the fluctuations, the above ansatz together with Eq. (2.13) leads to the well-known *Gross-Pitaevskii equation* [81, 82, 149]

$$i\hbar\partial_t\psi(x,t) = \left[-\frac{\hbar^2}{2m}\nabla^2 + V(x) + V_{add}(x) + \frac{4\pi a_s \hbar^2}{m}|\psi(x,t)|^2 \right]\psi(x,t). \qquad (2.45)$$

It has proven useful for the description of certain condensate properties,[9] like, *e.g.*, the interference between condensates [7], but cannot explain quantum features, like, *e.g.*, the superfluid to Mott insulator transition [71, 78].

For sufficiently deep lattices, again, a tight-binding approximation can be applied. Analogously to the quantum description, see Sec. 2.3.1, the condensate wave function is expanded in the basis of Wannier functions of the lowest band:

$$\psi(x,t) = \sqrt{n}\sum_l A_l(t)w_0(x - x_l). \qquad (2.46)$$

Taking into account only onsite interaction and nearest-neighbor coupling, one obtains the *discrete Gross-Pitaevskii equation* [134]

$$i\partial_t A_l(t) = -\frac{J}{2}\left(A_{l+1}(t) + A_{l-1}(t) \right) + Un|A_l(t)|^2 A_l(t) + \varepsilon_l A_l(t), \qquad (2.47)$$

for the complex amplitudes $A_l(t)$, where the parameters J, U, and ε_l are given by Eqs. (2.18) to (2.20). This equation is also referred to as *discrete nonlinear Schrödinger equation* [166, 175]. Furthermore, (2.47) is a special form of the *discrete self-trapping equation* [58], which is not restricted to nearest-neighbor coupling and is frequently used in quantum chemistry to describe bond excitations of small molecules.

Alternatively, Eq. (2.47) can be derived as the semiclassical limit (see for example [90]) of the Bose-Hubbard Hamiltonian (2.15), by assuming $Un = const.$ and $n \to \infty$. In this approach, the annihilation (creation) operators $\hat{a}_l^{(\dagger)}$ are replaced by the scaled operators $\hat{c}_l^{(\dagger)} = \hat{a}_l^{(\dagger)}/\sqrt{n}$, in order to scale out the global dependence of the energy on the particle number n. For $n \gg 1$, the commutators $[\hat{c}_l, \hat{c}_j^\dagger] = \delta_{l,j}/n$ vanish and the $\hat{c}_l^{(\dagger)}$ can be substituted by c-numbers, what corresponds to neglecting the quantum fluctuations and leads to the equations of motion (2.47).

---

[9] The Gross-Pitaevskii equation (2.45) is also used in nonlinear optics to describe wave-propagation through single-mode Kerr fibers [13, 70].

Eq. (2.47) can be regarded as a set of L nonlinear oscillators that are linearly coupled. Consequently, the system has L degrees of freedom. Alike the Bose-Hubbard Hamiltonian, it has two constants of motion, namely the energy E and the total number of atoms, where the latter condition translates into $\sum_l |A_l|^2 = 1$. Hence, for $L > 2$ lattice sites and appropriate values of the control parameters, the dynamics can become chaotic [90].

The different dynamical regimes of (2.47) have been thoroughly studied in various branches of physics, ranging from nonlinear optics to microcantilever arrays and Bose-Einstein condensates in optical lattices. For a review see [57].

3 Spectral statistics

The key target of the present thesis is to determine the impact of spectral chaos on the dynamical behavior of ultracold bosons in tilted optical lattices. More precisely, we want to understand how simulability, stability under perturbations, and dynamics of such systems depend on the spectral structure of the underlying Hamiltonian. We thus need adequate tools to differentiate chaotic and regular spectral regimes.

Classically, chaotic systems are distinguished by the fact that small deviations in the initial conditions grow exponentially as time elapses [127, 139]. As opposed to the *regular* (or *integrable*) case, such systems have less constants of motion than degrees of freedom. In quantum mechanics, chaos can either be characterized by semiclassics (periodic orbit theory) [85, 168], or by *random matrix theory* [130]. The latter is a statistical approach that covers *universal* features of the system under consideration, *i.e.*, characteristics that are independent of the specific Hamiltonian at hand, but rather result from global symmetry properties [74, 85, 139, 168]. In the following, we will give a short introduction to universal spectral statistics. Thereafter, we will apply the theory to the (tilted) Bose-Hubbard Hamiltonian in order to identify its chaotic parameter regime.

3.1 Introduction to universal spectral statistics

It was Wigner who first introduced the idea that the energy level spectra of complicated systems could be treated statistically [196, 197] and that they should have similar properties as the spectra of ensembles of random matrices [130]. Originally, the theory was developed to understand complex nuclei. However, the "*universality of the laws of level fluctuations*" has been conjectured to be applicable to the spectra of classically chaotic dynamical systems by Bohigas, Giannoni, and Schmidt in 1984 [21]. Since the energy spectrum is one of the best accessible quantities of a quantum system, random matrix theory is by now well established in nuclear [74] and atomic physics [128], mesoscopics [104], and photonics [169, 208].

Without any detailed knowledge on the system, random matrix theory predicts statistical properties, such as, *e.g.*, the distribution $P(s)$ of the normalized level spacings

$$s_i = \frac{E_{i+1} - E_i}{\Delta(E)} \tag{3.1}$$

between neighboring energy levels E_i of a system. Here the E_i are sorted in ascending order and $\Delta(E)$ is the local mean level spacing obtained from averaging over a few spacings in the vicinity of E_i. The division by $\Delta(E)$ is also called *unfolding* of the spectrum and serves to eliminate system specific properties.[1] As evident from Fig. 3.1, the level-spacing distribution $P(s)$ is identical for a large variety of classically chaotic systems with a discrete excitation spectrum, and follows the random matrix theory prediction (solid line). Whereas Sinai's billiard (a), a hydrogen atom in a strong magnetic field (b), and an excited NO_2 molecule (c) represent quantum systems, the acoustic resonance spectrum of a Sinai-shaped quartz block (d), the microwave spectrum of a 3D chaotic cavity (e), and the vibration spectrum of a quarter-stadium shaped plate (f) have classical origin. All these systems are described by some sort of wave equation with a discrete spectral component. This means that the precise characteristics of a chaotic system are not relevant for the statistical features of the spectrum. Instead, it suffices to consider global symmetry properties, like, *e.g.*, time-reversal invariance, and one can treat the matrix elements of the Hamiltonian as independent random variables, *i.e.*, relate the spectra to ensembles of random matrices [130]. Thus, the level-spacing distribution $P(s)$ is a *universal* feature that can be used to classify a system.

3.1.1 Chaotic Wigner-Dyson statistics

In order to specify random matrix ensembles, the invariance of physical predictions under changes of the set of basis functions, and the independence of the individual matrix elements has to be required [139, 168]. This can be shown to enforce Gaussian distributions of the entries of the Hamiltonian. Depending on the behavior under time-reversal, we can distinguish three different universality classes,[2] each with a distinct, universal level-spacing distribution. Those are the *Gaussian orthogonal ensemble* (GOE) for systems with time-reversal symmetry, the *Gaussian unitary ensemble* (GUE) for systems with broken time-reversal symmetry, and the *Gaussian symplectic ensemble* (GSE) for systems with time-reversal symmetry and spin-1/2 interactions, see for example [168].

Since the Bose-Hubbard Hamiltonian is invariant under time-reversal and does not contain spin-1/2 interactions, we concentrate on the GOE ensemble in the following. In order to derive the corresponding nearest-neighbor level-spacing distribution $P(s)$, we here recall *Wigner's surmise*, that reproduces the exact distribution with less than two percent error although being based only on 2×2-matrices.[3] In this case, the Hamiltonian $\hat{H}$ is represented by a real symmetric matrix H, a property that is preserved under the orthogonal

---

[1]For a more detailed discussion of the unfolding procedure see Appendix A.

[2]Altogether, there exist ten known universality classes [61, 88, 206].

[3]The exact distribution corresponds to the limit $N \to \infty$, where N is the dimension of the matrix (see Sec. 4.4 of Ref. [85]).
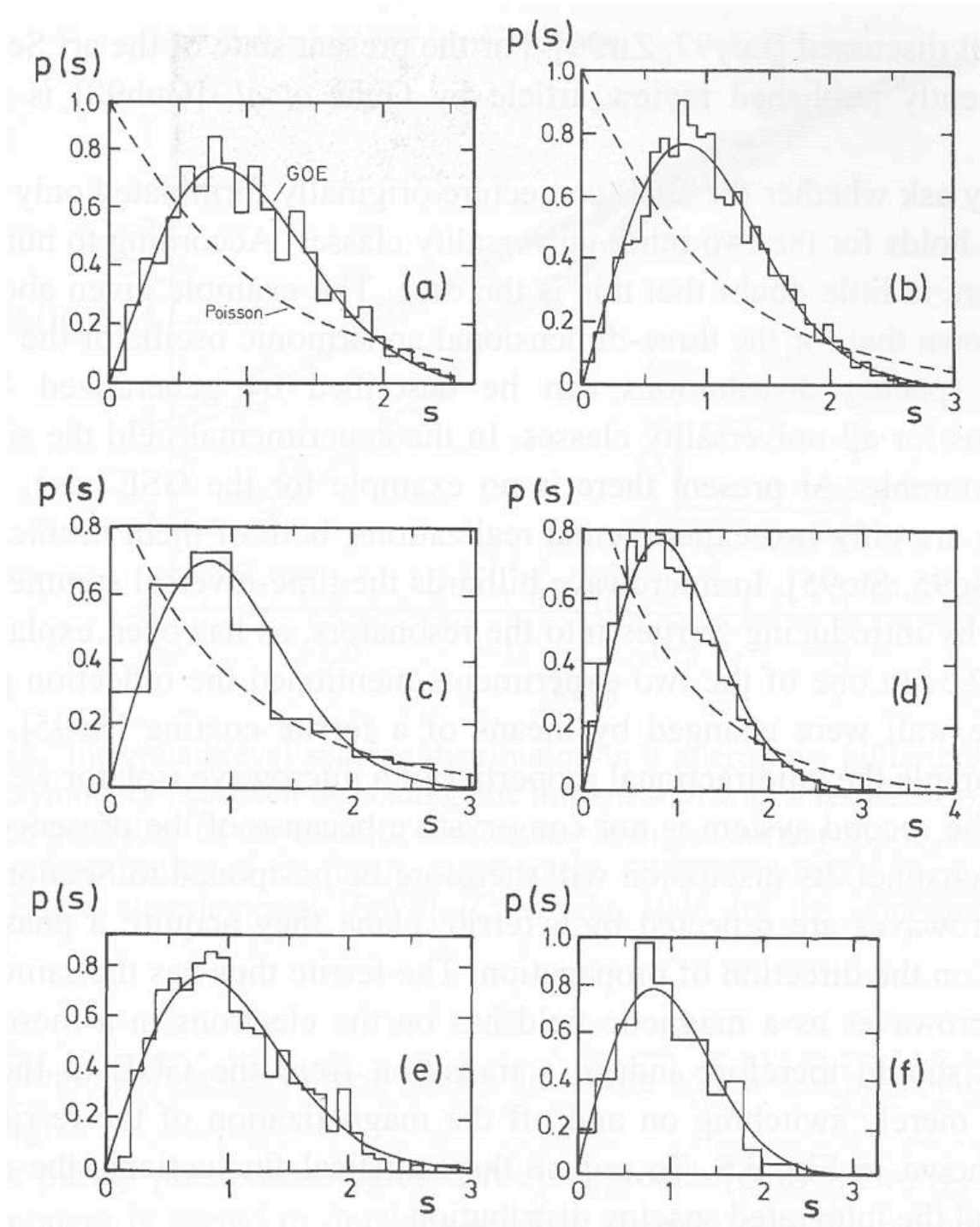
Figure 3.1: Nearest-neighbor level-spacing distribution $P(s)$ for different physical systems, taken from [168]. Shown is the distribution for a Sinai billiard (a), a hydrogen atom in a strong magnetic field (b), the excitation spectrum of an excited NO_2 molecule (c), the acoustic resonance spectrum of a Sinai-shaped quartz block (d), the microwave spectrum of a 3D chaotic cavity (e), and the vibration spectrum of a quarter-stadium shaped thin plate (f). Only the first three cases belong to quantum systems, however, in all cases a Wigner-Dyson distribution (solid lines) is found (all systems are described by some sort of wave equation [168]). The dashed lines in panels (a) - (d) correspond to the Poissonian distribution (3.11) of regular systems, compare Sec. 3.1.2.

transformation $H' = OHO^T$, where the orthogonal matrix fulfills $OO^T = 1$. We thus write

$$H = \begin{pmatrix} H_{11} & H_{12} \\ H_{21} & H_{22} \end{pmatrix} = \begin{pmatrix} a+b & c \\ c & a-b \end{pmatrix}, \quad \text{with} \quad a,b,c \in \mathbb{R}. \tag{3.2}$$

This matrix has two eigenvalues, and their level spacing is

$$s = 2\sqrt{b^2 + c^2}. \tag{3.3}$$

Assuming a Gaussian distribution $W_\sigma(b,c)$ with width σ for both, b and c, we obtain

$$\begin{aligned} P_{GOE}(s) &= \int\limits_{-\infty}^{\infty} \int\limits_{-\infty}^{\infty} db\, dc\, W_\sigma(b,c)\, \delta\left(s - 2\sqrt{b^2 + c^2}\right) \\ &= 2\pi \int\limits_{0}^{\infty} dr\, r\, \frac{1}{\sqrt{2\pi}\sigma} \exp\left(-\frac{r^2}{2\sigma^2}\right) \delta(s - 2r) \\ &= \frac{\sqrt{2\pi}}{2\sigma}\, s\, \exp\left(-\frac{s^2}{8\sigma^2}\right). \end{aligned} \tag{3.4}$$

Normalization then results in the level-spacing distribution

$$P_{GOE}(s) = \frac{\pi}{2}\, s\, \exp\left(-\frac{\pi}{4}s^2\right) \tag{3.5}$$

of the Gaussian orthogonal ensemble [130].

In particular, the GOE distribution implies that the distance between neighboring levels never vanishes, since $P(s) \to 0$ for $s \to 0$, as already observed in Fig. 3.1. Thus, in the chaotic regime, no crossings between energy levels occur under changes of a system parameter. Instead, the levels always couple and therefore *repel* each other as depicted schematically in Fig. 3.2 (b). In a large system with a high spectral density, this leads to various overlapping avoided crossings of different size what is a clear indication of quantum chaos. As opposed to that, in a regular system, typically true crossings between neighboring levels occur, see Fig. 3.2 (a). In other words, in the integrable case, the levels can be labeled by *good quantum numbers* and the character of the corresponding eigenstates is not affected by changes of the control parameter. In the nonintegrable case, however, the inter-state coupling destroys those good quantum numbers. This leads to a mixing of their properties in the interaction region and is reflected in the statistical properties of the distribution $P(s)$.

Since the distribution $P(s)$ is to some extent sensitive to the specific binning that underlies the histogram, it can be advantageous to consider the *integrated level-spacing distribution* $I(s)$ that counts the number of spacings smaller than s, and is obtained from $P(s)$ via

$$I(s) = \int\limits_{0}^{s} P(s')ds'. \tag{3.6}$$
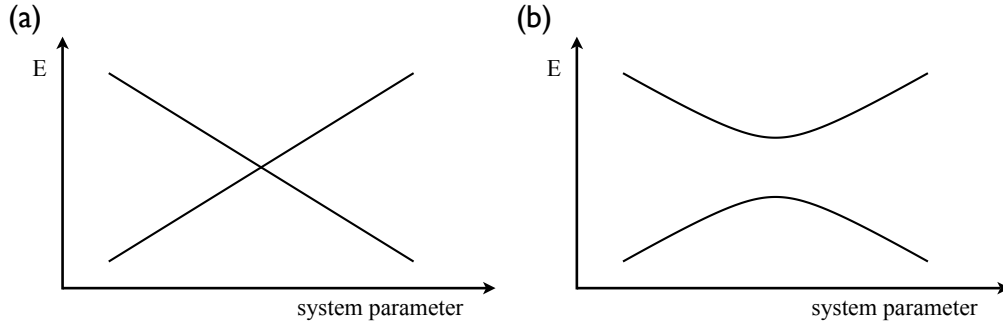
Figure 3.2: Schematic sketch of the typical behavior of two adjacent energy levels of a large system with a high spectral density, under variation of a suitable system parameter. (a) corresponds to a regular or integrable system, and (b) to a nonintegrable or chaotic system. Whereas, in the former case, the levels are completely uncorrelated and undergo a crossing, in the latter case, an avoided crossing emerges.

For the GOE it reads

$$I_{GOE}(s) = 1 - \exp\left(-\frac{\pi s^2}{4}\right). \tag{3.7}$$

3.1.1.1 Circular ensembles

In the case of time-periodic systems, one can analyze the level-spacing distribution of the eigenphases of the Floquet operator (see Sec. 2.4.2), in order to distinguish regular from chaotic dynamics. In contrast to the Gaussian ensembles, here the eigenvalues are homogeneously distributed on the unit circle and thus the corresponding ensembles, that were first introduced by Dyson [56], are called *circular*. As in the case of the Gaussian ensembles, in order to define the *circular unitary ensemble* (CUE), the *circular orthogonal ensemble* (COE) and the *circular symplectic ensemble* (CSE), the invariance of physical predictions under changes of the set of basis functions has to be required. It is, however, not necessary to impose the statistical independence of the matrix elements as an additional condition (see Sec. 4.1.2 of Ref. [168]). Yet, the according level-spacing distributions are known to be identical to the ones of the Gaussian ensembles [85, 130], and, in particular, $P_{COE}(s)$ is given by Eq. (3.5).

3.1.1.2 Symmetries

In our above reasoning, we assumed that the system under consideration is sufficiently complex, *i.e.*, it has less integrals of motion than degrees of freedom. However, any discrete symmetry, as for example translational invariance, gives rise to a new quantum number and

thus reduces the complexity of the system [168]. Mathematically, this can be expressed in the following way: If $\hat{H}$ is invariant with respect to a symmetry relation, then there is an associated operator $\hat{R}$ that fulfills

$$\left[\hat{H}, \hat{R}\right] = 0. \tag{3.8}$$

Since commuting operators can be diagonalized simultaneously, the matrix representation of $\hat{H}$ can be considerably simplified when expressed in the eigenbasis of $\hat{R}$. The Hamiltonian is then block diagonal,

$$H = \begin{pmatrix} H^{(1)} & 0 & \cdots \\ 0 & H^{(2)} & \cdots \\ \vdots & \vdots & \ddots \end{pmatrix}, \tag{3.9}$$

where each bloch $H^{(i)}$ corresponds to one eigenvalue of $\hat{R}$, *i.e.*, one good quantum number. This procedure can be repeated for any symmetry, until we obtain a matrix representation of $\hat{H}$ that cannot be further reduced. Each irreducible block then corresponds to one set of conserved quantum numbers and thus the spectrum of the Hamiltonian $\hat{H}$ (and, if periodic, of its Floquet operator) decomposes into completely uncorrelated sub-spectra.

In order to obtain meaningful results, any analysis of the spectral statistics thus has to be restricted to one of the sub-Hamiltonians. For example, the translational invariance of the time-dependent tilted Bose-Hubbard Hamiltonian with periodic boundary conditions leads to a decomposition of $\hat{\tilde{H}}_p(t)$, Eq. (2.38), (and likewise of $\hat{U}(T_B)$, Eq. (2.43)) in blocks with distinct quasimomentum κ_j, see Secs. 2.4.1, and 2.4.2. The statistical analysis therefore requires a diagonalization at fixed κ_j.

3.1.2 Regular statistics

In the case of a completely integrable system which has as many constants of motion, *i.e.*, good quantum numbers, as degrees of freedom, any eigenvalue makes up a symmetry class of its own. The energy levels can then be assumed to be completely uncorrelated and the nearest-neighbor level-spacing distribution is easily calculated [168]: The probability to find an eigenvalue at a distance between s and $s+ds$ from a given eigenvalue, but no other eigenvalue in between, is $P(s)ds$. In order to calculate the distribution $P(s)$, we divide the interval $[0, s]$ in N equal subintervals of length s/N. The probability to find no eigenvalue in any of the subintervals then reads $\lim_{N \to \infty}(1 - s/N)^N$, whereas the probability to find an eigenvalue in the interval $[s, s+ds]$ is given by ds. Combination of both leads to

$$P_P(s)ds = \lim_{N \to \infty} \left(1 - \frac{s}{N}\right)^N ds, \tag{3.10}$$
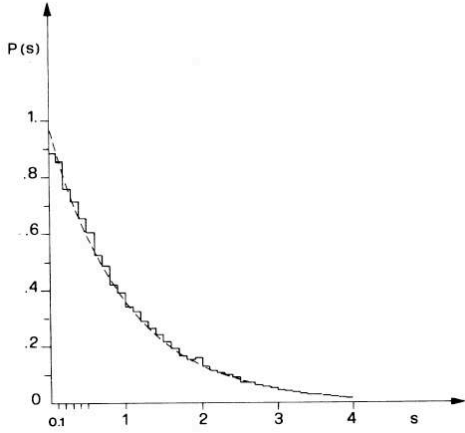
Figure 3.3: Level spacing distribution for the first 100,000 levels of a rectangular billiard, taken from [30]. The dashed line corresponds to a Poissonian distribution, Eq. (3.11).

what, after performing the limit, results in the *Poissonian distribution*,

$$P_P(s) = \exp(-s) \tag{3.11}$$

for the normalized nearest-neighbor level-spacing distribution of regular systems [14]. It has its maximum at $s = 0$ and thus clustering, as opposed to repulsion in chaotic systems, is an important signature of integrability [85]. Poissonian statistics $P_P(s)$ have been observed in a variety of regular systems, like, *e.g.*, rectangular billiards [30], see Fig. 3.3. As depicted schematically in Fig. 3.2 (a), neighboring levels in such systems typically cross under changes of a suitable system parameter. The integrated level-spacing distribution, as defined in Eq. (3.6), is then given by

$$I_P(s) = 1 - \exp(-s). \tag{3.12}$$

Although Poissonian statistics is the generic case for integrable systems [14], the number of exceptions to the expected behavior is rather large [168]. For example, the eigenvalues of the harmonic oscillator form an equidistant sequence and thus the level-spacing distribution is obviously not Poissonian. Furthermore, most physical systems are neither integrable in a strict sense nor completely chaotic. The associated classical phase space is rather mixed regular and chaotic and the nearest-neighbor level-spacing distribution interpolates between Poissonian and Wigner-Dyson statistics. Different approaches to treat such situations have been established, see for example [24, 25, 97, 98].

## 3.2 Spectral statistics of the Bose-Hubbard system

We now investigate the spectral properties of the Bose-Hubbard Hamiltonian in the different parameter regimes determined by J, U, and F, and in the following chapters relate them to the simulability, stability, and dynamics of ultracold bosons in tilted optical lattices. We shortly discuss the untilted lattice ($F = 0$) and then turn to the influence of the tilt F, which defines our main interest. The tilted system will be analyzed for both Dirichlet and periodic boundary conditions, and also its Floquet spectrum will be discussed.

In all following subsections, the mean level spacing $\Delta(E)$ – used to unfold[4] the spectra (see Eq. (3.1)) – is obtained from averaging the energy differences with a Gaussian weight. The width of the latter is chosen such that the average density of states $\bar{d}(E)$, Eq. (A.2), is sufficiently smooth. In order to obtain reliable statistics, we choose systems with a sufficiently large Hilbert space dimension $\mathcal{N}$ ($n \approx L \gtrsim 7$, $\mathcal{N} \gtrsim 1700$). For the sake of a clear presentation of crucial qualitative features, *i.e.*, in order to be able to resolve the individual levels, we, however, plot spectra of relatively small systems ($n \approx L \approx 4$, $\mathcal{N} \approx 35$). Moreover, since we are interested in the properties of the bulk of the spectrum (as will be explained in the following subsection), we neglect the states at the edges of the spectrum in our statistical analysis.

3.2.1 Spectrum of the Bose-Hubbard Hamiltonian

The spectrum of the Bose-Hubbard Hamiltonian for $F = 0$ was studied by various authors [19, 34, 47, 53, 92, 93, 110, 116]. Here, we follow the analysis presented in Ref. [116], for periodic boundary conditions. The latter renders the system translationally invariant and the Hamiltonian decomposes into a direct sum of sub-Hamiltonians with uncorrelated spectra, each belonging to one possible value of quasimomentum (see Secs. 2.4.1.1 and 3.1.1.2). Fig. 3.4 shows the entire spectrum of $\hat{H}$, Eq. (2.15), in panel (a), as well as the sub-block with fixed quasimomentum $\kappa = 2\pi/5$, panel (b), for $n = 4$ and $L = 5$, as a function of $U = 1 - J$, where $U, J \in [0, 1]$. For both limiting cases of noninteracting ($U = 0$) and immobile particles ($U = 1$), the Hamiltonian has a natural basis, as discussed in Sec. 2.3.2. Those two sets of basis states are mutually orthogonal and are given by the Bloch states ($U = 0$) and the Wannier states ($J = 0$), respectively. The regularity is reflected in the appearance of degeneracies for $U = 0$ and $U = 1$, even when considering only a single symmetry class, *i.e.*, one value of κ, as in Fig. 3.4 (b). Note that in the case of dominant interaction $U \approx 1$, the individual lattice sites decouple. As a consequence, different seed states $|\mathbf{s}\rangle$, that are related to each other by anti-cyclic permutations of the lattice sites, are degenerate and only few individual levels remain.

---

[4]The unfolding procedure is discussed in Appendix A.
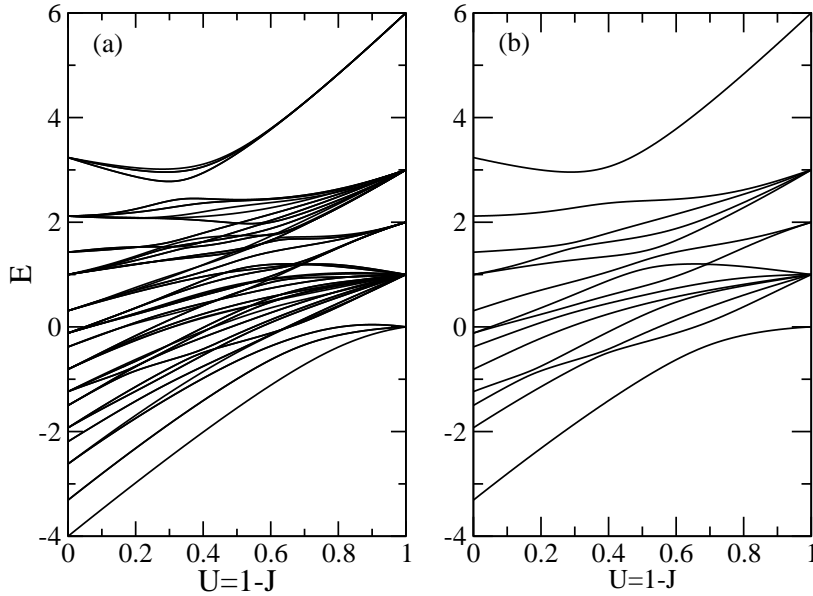
Figure 3.4: Energy spectrum of the Bose-Hubbard Hamiltonian $\hat{H}$, Eq. (2.15), with periodic boundary conditions as a function of $U = 1 - J$, where $U, J \in [0, 1]$, for $n = 4$ and $L = 5$. Due to the translational invariance, the Hamiltonian decomposes into a direct sum of sub-Hamiltonians with completely uncorrelated spectra. Shown is both, (a) the entire spectrum and (b) the sub-block with $\kappa = 2\pi/5$.

In contrast, whereas for $U \approx J$ there are many crossings between energy levels belonging to different values of the quasimomentum (Fig. 3.4, (a)), no degeneracies are left when considering only one value of κ (Fig. 3.4, (b)), what reduces the number of levels to $\mathcal{N}_{\kappa_j} \approx \mathcal{N}/L$, see Sec. 2.4.1.1. In this intermediate parameter regime, the energy levels depend sensitively on the parameter U and repel each other. The Hamiltonian thus does not have a natural basis, what is a prerequisite for quantum chaos. This leads to chaotic level statistics [110, 116], as depicted in Fig. 3.5, which shows the numerically obtained, integrated level-spacing distributions $I(s)$ of the $\kappa = 2\pi/7$ block of a larger system with $n = 6$, $L = 7$, for different interaction strengths U. That is, the distributions for $U = 0.35$ and 0.5 faithfully follow the GOE distribution. On the contrary, for $U = 0.1$ and 0.9, the level statistics exhibit level clustering what is an important signature of integrability as pointed out in Sec. 3.1.2. For $U \approx 1$, degeneracies between the energy levels predominate as discussed in the preceding paragraph (see also Fig. 3.4). Thus, the system does not represent a generic regular system and in Fig. 3.5, the numerically obtained distribution $I(s)$ lies even above the Poissonian distribution for $U = 0.9$. Moreover, we note that also for $U = 0.1$, it deviates considerably from Poissonian statistics.
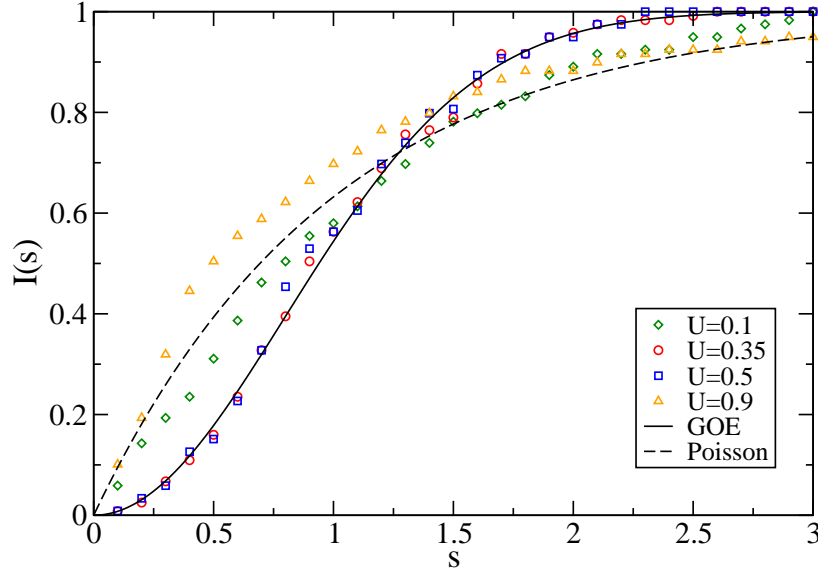
Figure 3.5: Integrated nearest-neighbor level-spacing distribution $I(s)$ of the Bose-Hubbard Hamiltonian $\hat{H}$, Eq. (2.15), with periodic boundary conditions, for $n = 6$, $L = 7$, and $U = 0.1$ (green diamonds), 0.35 (red circles), 0.5 (blue squares), and 0.9 (orange triangles), with $U + J = 1$. The spectral analysis is restricted to the sub-block of the Hamiltonian with $\kappa = 2\pi/7$, *i.e.*, $\mathcal{N}_\kappa \approx 1700$. For comparison, the GOE (solid line), Eq. (3.7), and Poissonian (dashed line), Eq. (3.12), distributions are also shown.

Note that for $U \approx J$, the sensitive dependence on the parameter U predominates for levels with intermediate energies (see Fig. 3.4 (b)), whereas the states at the edges of the spectrum do not show the same behavior. This arises from the fact that the states with the lowest energies have a large contribution from the tunneling coupling, $\langle \hat{H}_J \rangle \gg \langle \hat{H}_U \rangle$, and are rather delocalized on the lattice, while the states with the highest energies have large contributions from the onsite interaction, $\langle \hat{H}_U \rangle \gg \langle \hat{H}_J \rangle$, and correspond to localized states. Here, $\langle \cdot \rangle$ denotes the expectation value with respect to a typical eigenstate from the corresponding part of the spectrum. As a consequence, chaos is primarily developed in the spectrum's bulk. When evaluating the level statistics, we thus always neglect a few states at the edges of the spectrum, while retaining at least 90% of the spectrum. Furthermore, we numerically confirmed that the level statistics do not depend on the particular choice of the quasimomentum value κ.

From the above analysis, we infer that the untilted Bose-Hubbard Hamiltonian is chaotic in a regime where onsite interaction and tunneling coupling are comparable. In the following subsections, we investigate the influence of an additional tilt on the system's spectral properties.
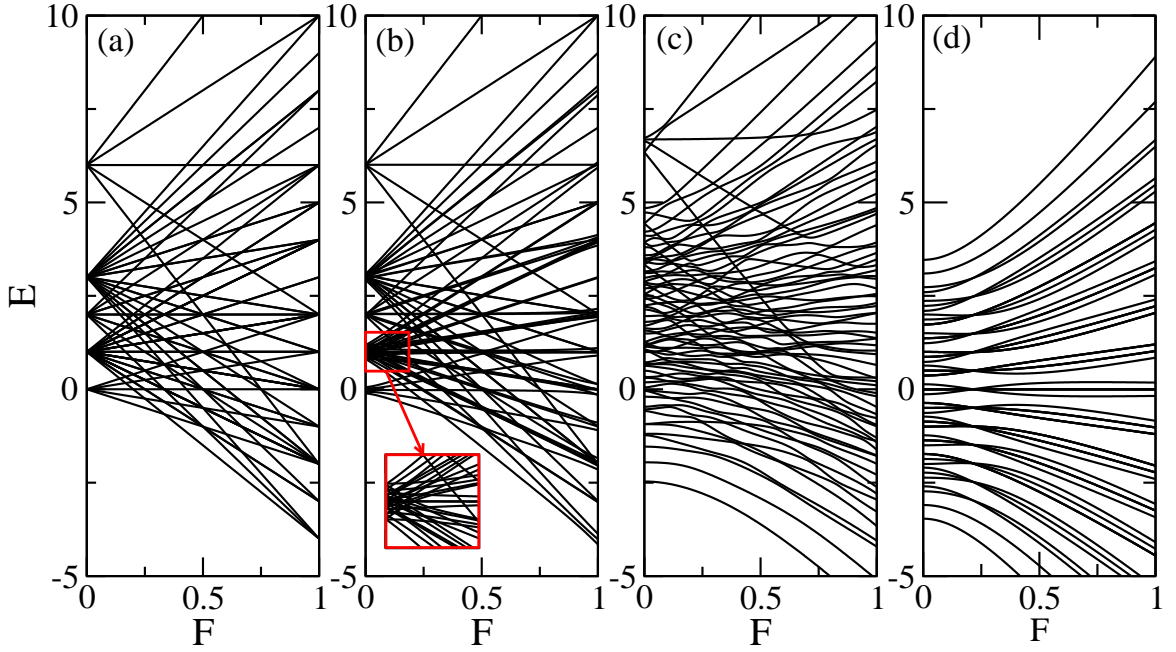
3.2.2 Spectrum of the tilted Bose-Hubbard Hamiltonian

We now analyze the spectrum of the Bose-Hubbard Hamiltonian $\hat{H}$, Eq. (2.26), with an additional static field term. Here, the translational invariance of the system is broken and periodic boundary conditions are not applicable. In the spectral analysis, we thus have to consider the entire spectrum since the Hamiltonian does not decompose into uncorrelated sub-blocks.

Fig. 3.6 shows the evolution of the energy levels of the tilted Bose-Hubbard Hamiltonian under changes of the static field strength F, which is also termed *parametric level evolution*. The individual panels belong to different values of the onsite interaction U and the tunneling coupling J, with fixed number of bosons $n = 4$ and lattice sites $L = 5$.

For (a) vanishing tunneling coupling $J = 0$, the tilted Bose-Hubbard Hamiltonian commutes with the center-of-mass operator $\sum_{l=1}^{L} \tilde{l} \hat{n}_l$, and the eigenstates do thus not change their characteristic properties under variations of the tilt F. They are given by Wannier-Fock states, with a well-defined number of particles on each site. Thus, the eigenenergies depend linearly on the tilting strength, and the slope of the levels is given by the center of mass of the corresponding eigenstate. As a consequence, the parametric spectrum consists of intersecting straight lines featuring numerous degeneracies. Furthermore, the spectrum can be split in five manifolds, each belonging to a specific class of Fock states on the lattice: The uppermost manifold corresponds to states where all n particles are located on one lattice site, *i.e.*, states of the type $|\ldots, n, \ldots\rangle$, where dots denote empty lattice sites. The second manifold represents states where $n - 1$ particles are located on one lattice site, *i.e.*, states of the type $|\ldots, 1, \ldots, n-1, \ldots\rangle$, and so on for the other spectral manifolds. The total number of manifolds that appear in the spectrum is determined by the number of distinct values of the Fock states' interaction energy, represented by the quantity

$$\alpha = \frac{1}{2} \sum_{l=1}^{L} n_l (n_l - 1).$$

(3.13)

Each manifold can thus be labeled by one particular value of α, which can also be considered a good quantum number in this regime. The different levels within one manifold arise from different realizations of positions of the bosons on the L different lattice sites, while keeping the interaction energy unchanged. For example, whereas the uppermost level corresponds to placing all bosons in the uppermost site of the lattice, the horizontal level of the energetically highest manifold corresponds to placing all bosons in the site located in the middle of the lattice. This decomposition of the spectrum implies that within one manifold all levels are degenerate for $F = 0$. Since hopping between lattice sites is forbidden for $J = 0$, no coupling between any two eigenstates occurs, and the levels perfectly cross under changes of the parameter F.

Figure 3.6: Spectrum of the tilted Bose-Hubbard Hamiltonian $\hat{H}$, Eq. (2.26), as a function of the static field strength F, for $n = 4$ and $L = 5$. The onsite interaction and the tunneling coupling are set to (a) $U = 1, J = 0$, (b) $U = 1, J = 0.1$, (c) $U = 1, J = 1$, and (d) $U = 0, J = 1$.

For small small tunneling coupling $J = 0.1$ (Fig. 3.6 (b)), the eigenstates are not Wannier-Fock states anymore, and the degeneracies start to get lifted, which is in particular visible for $F = 0$, where the $J = 0$ manifolds are broadened (see inset of Fig. 3.6 (b)). However, the regular behavior of the energy levels is still largely conserved, since there is little coupling between eigenstates, what leads to only small avoided crossings between levels of different manifolds.

For the case of comparable interaction and tunneling strengths $U = J = 1$ (Figs. 3.6 (c) and 3.7), the manifold structure is basically destroyed, and α is no longer a good quantum number:[5] As particularly evident from Fig. 3.7 (c), the previously separated groups of eigenstates overlap and couple strongly, what is reflected in numerous avoided crossings of different size between the levels.

For vanishing onsite interaction $U = 0, J = 1$ (Fig. 3.6 (d)), the Hamiltonian's eigenstates are Bloch states and the system is again regular. This is reflected in the behavior of the energy levels which exhibit many degeneracies and form basically equidistant groups.

---

[5]Note, however, the almost straight lines traversing the chaotic bulk in Fig. 3.6 (c) and Fig. 3.7 (b), respectively. The corresponding eigenstates are referred to as *solitonic* eigenstates and will be the subject-matter of Chapter 5.
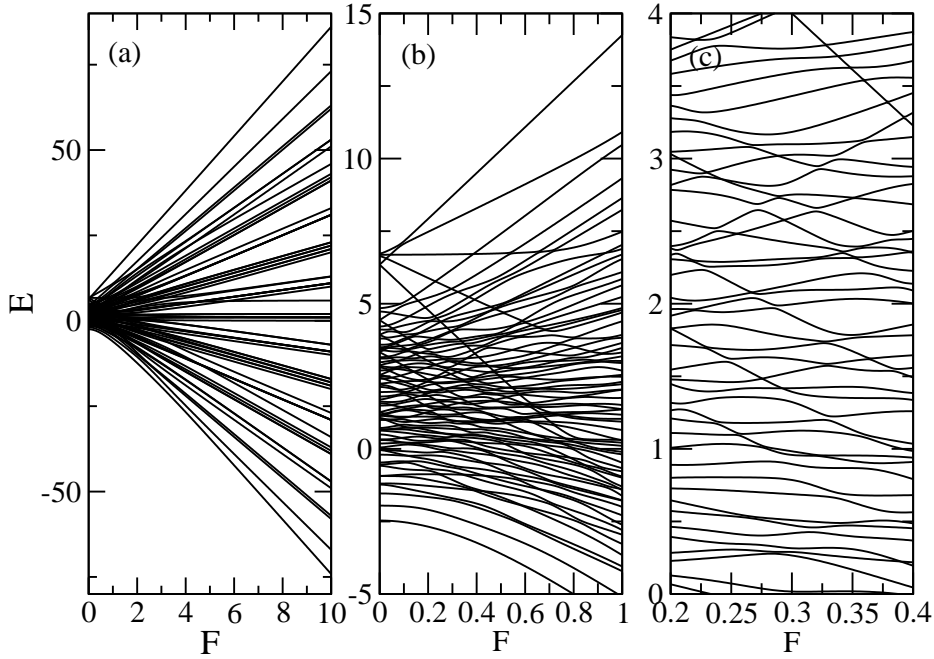
Figure 3.7: Spectrum of the tilted Bose-Hubbard Hamiltonian $\hat{H}$, Eq. (2.26), as a function of the static field strength F, for $n = 4$, $L = 5$, and $U = J = 1$ (compare Fig. 3.6, (c)). Different parts of the spectrum are shown, in order to highlight the behavior of the levels at different tilting strengths.

So far, we have only discussed the parametric level evolution for $0 \leq F \leq 1$, see Fig. 3.6. However, for large values of F, the so-called Wannier-Stark ladder [75] emerges and the system becomes regular, irrespective of U and J, see Fig. 3.7 (a). In this regime, the individual sites essentially decouple since the energy offset between neighboring sites is too large to allow for tunneling, and the eigenstates are again given by Wannier-Fock states. This suggests that, for $U = J$, the static field strength F can be used to tune between regular and chaotic level statistics. This assumption is supported by Fig. 3.8, which shows the numerically obtained nearest-neighbor level-spacing distributions for $n = 6$, $L = 7$, $U = J = 1$, and different values of F: For small and intermediate tilts, $F = 0.1$ (orange diamonds) and $F = 1$ (blue squares) (compare Fig. 3.7 (b) and (c)), the distributions closely follow the expected GOE behavior. For a large tilt $F = 3$ (red circles), however, the integrated level-spacing distribution is well approximated by Poissonian statistics, *i.e.*, the systems turns regular in the Wannier-Stark limit.

We note that we do not find GOE behavior for $F = 0$ (green triangles). The corresponding distribution rather lies between the GOE and the Poissonian distribution, what seems to contradict the observations for periodic boundary conditions, see Fig. 3.5. The reason for this mismatch is that in the limit $F \to 0$, the system is symmetric under reflections around
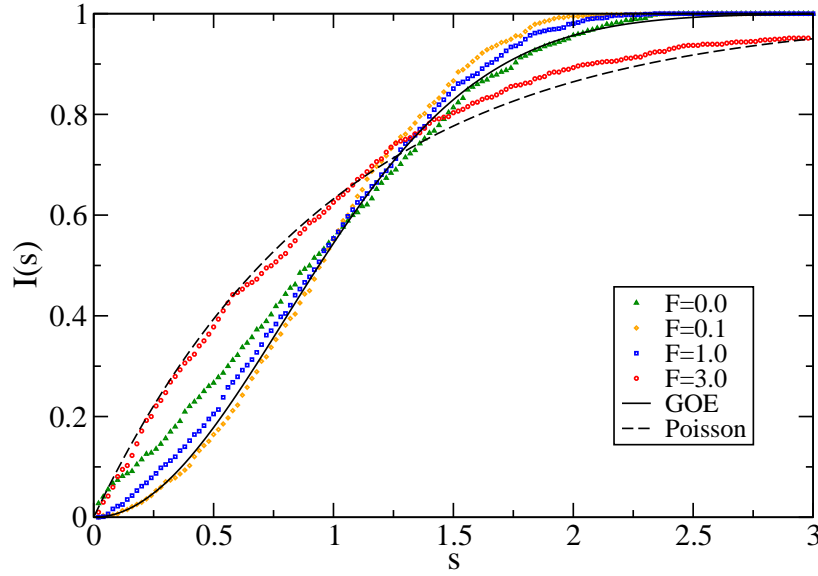
Figure 3.8: Integrated nearest-neighbor level-spacing distribution of the spectrum of the tilted Bose-Hubbard Hamiltonian $\hat{H}$, Eq. (2.26), for $n = 6$, $L = 7$, $U = J = 1$ and $F = 0$ (green triangles), 0.1 (orange diamonds), 1 (blue squares), 3 (red circles). For comparison, the GOE (solid line), Eq. (3.7), and Poissonian (dashed line), Eq. (3.12), distributions are also shown.

the central lattice site, a symmetry that was not taken into account in the statistical data analysis presented here (see also Sec. 3.1.1.2).

3.2.3 Adiabatic spectrum of the time-dependent Hamiltonian

The transformation of the Bose-Hubbard Hamiltonian to the interaction representation with respect to the static field term $\hat{H}_F$ renders the Hamiltonian $\hat{\tilde{H}}_p(t)$ time dependent and allows us to use periodic boundary conditions, see Eq. (2.34). As elaborated in Sec. 2.4.1.1, due to the translational invariance, the Hamiltonian matrix then decomposes into uncorrelated blocks of fixed quasimomentum κ, which can be diagonalized separately. Without loss of generality, we focus on the $\kappa = 0$ block in the following discussion.

The eigenenergies of the Hamiltonian $\hat{\tilde{H}}_p(t)$, at fixed t, form the so-called *adiabatic* spectrum, expressing the fact that they are time dependent and follow the temporal evolution of the Hamiltonian. The corresponding eigenstates are termed *adiabatic* or *instantaneous* eigenstates. In Fig. 3.9, the spectrum is shown as a function of the Hamiltonian's phase $\phi(t) = Ft = t/T_B$, for $n = 4$, $L = 5$, and for different values of the onsite interaction U. For $U = 0$, the corresponding eigenstates are Bloch states, since in this case the Hamiltonian solely consists of the tunneling term, $\hat{\tilde{H}}_p(t) = -\frac{J}{2} \sum_{l=1}^{L} (\hat{a}_{l+1}^\dagger \hat{a}_l \, e^{iFt} + h.c.)$. This leads to
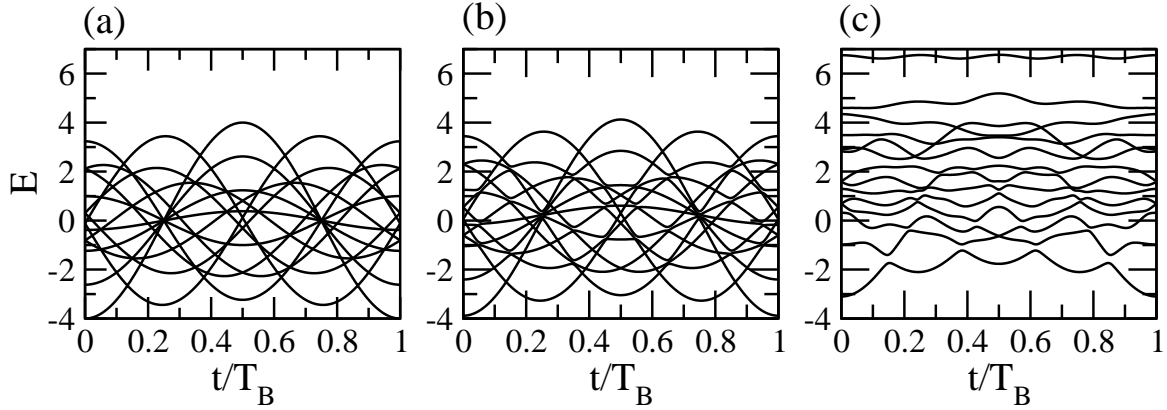
Figure 3.9: Adiabatic spectrum of the transformed, time-dependent Hamiltonian $\hat{\bar{H}}_p(t)$, Eq. (2.34), for $n = 4$ and $L = 5$, as a function of time, in units of the Bloch period T_B which fixes the periodicity of the Hamiltonian. Shown are the levels with quasimomentum $\kappa = 0$, for tunneling coupling $J = 1$ and onsite interactions (a) $U = 0$, (b) 0.1, and (c) 1.

the perfect cosine-like behavior of the individual energy levels in Fig. 3.9 (a) with perfect crossings between them. Note that all levels have the same periodicity and differ only in amplitude and phase shift. Moreover, due to the temporal symmetry of $\hat{\bar{H}}_p(t)$, the spectrum as a whole is symmetric around $t/T_B = 0.5$. For an integer ratio n/L, the Hamiltonian is periodic in time with the period T_B/L, leading to additional symmetries in the spectrum, see Ref. [114].

In the case of non-zero interaction strength $U \neq 0$, the nonlinearity induces couplings between the Bloch states what leads to avoided crossings as time elapses. For small $U = 0.1$ (Fig. 3.9 (b)), the levels thus start to repel each other and small avoided crossings open up.

Further increase of the interaction strength to $U = 1$ results in even stronger coupling of the eigenstates, and the formerly perfect cosine-like behavior of the time-dependent levels is destroyed, as evident from Fig. 3.9 (c). In this regime, the energy levels undergo numerous avoided crossings, what is a clear indication for quantum chaos as discussed in Sec. 3.1.1. Nevertheless, the symmetry of the spectrum around $t/T_B = 0.5$ is not affected, since the Hamiltonian's temporal symmetry is conserved.

Note that the adiabatic spectrum does not depend on the strength of the static field, since F merely enters in $\hat{\bar{H}}_p(t)$ via a time-dependent phase factor and the time-axis has been scaled with the Bloch period $T_B = 2\pi/F$. However, when considering the system's dynamics, the static field strength F determines the velocity with which the adiabatic spectrum is traversed. In order to study the influence of the parameter F on the level statistics of the transformed, time-dependent system, one thus has to investigate the Floquet operator

$\hat{U}(T_B)$, Eq. (2.42), as will be done in the following subsection.

The set of eigenvalues and corresponding eigenvectors that form the adiabatic spectrum can be interpreted as belonging to a set of fictitious classical particles moving in one dimension as time elapses [85, 135, 141]. Thus, the parametric level evolution is sometimes also referred to as *level dynamics*. An initial excitation of one eigenstate, *i.e.*, in a particular level, will then spread through the system as a function of time. This spreading depends on the interaction between the fictitious particles, *i.e.*, the coupling between the energy levels, and the strength of some external driving. Whereas in the noninteracting case $U = 0$, Fig. 3.9 (a), the excitation will stay localized due to the perfect crossings, for nonzero interaction $U \neq 0$, Fig. 3.9 (b), (c), it will, in general, be distributed amongst the levels. For very slow driving rates, this concept can also be applied to explain energy diffusion in a system where, in the present case, the driving is given by the static field F. This approach will be discussed in Sec. 6.3.

3.2.4 Floquet spectrum

We now turn to the Floquet operator $\hat{U}(T_B)$, Eq. (2.42). In the case of dominant interaction $U \gg J$, which implies regular level statistics of the Hamiltonian (see Sec. 3.2.2), we can neglect the tunneling coupling and approximate the Floquet operator by

$$\hat{U}(T_B) \approx \mathcal{T} \exp\left(-i \int_0^{T_B} \hat{H}_U dt\right). \tag{3.14}$$

Since the interaction part $\hat{H}_U$ of the Hamiltonian is time independent, the operator's eigenvalues are [114]

$$\exp\left(-iET_B\right) = \exp\left(-i\alpha U T_B\right) = \exp\left(-i\alpha U \frac{2\pi}{F}\right), \tag{3.15}$$

where the factor α, Eq. (3.13), is determined by the interaction energy of the basis states. In the regime of dominant interaction, we thus expect the eigenphases to be linear functions of $1/F$, with slope proportional to α, which, in this regime, can also be regarded as a good quantum number. In the following, we will investigate the eigenphases' parametric evolution as a function of $1/F$. Due to the translational invariance of $\hat{\tilde{H}}_p(t)$, the statistical analysis again requires a diagonalization at fixed quasimomentum, and, without loss of generality, we choose $\kappa = 0$ here.

Fig. 3.10 shows the eigenphases of the Floquet operator for $n = 3$, $L = 4$ with fixed onsite interaction $U = 1$, and different values of the tunneling coupling J, in units of π, *i.e.*, $ET_B/\pi = 2E/F$, as a function of $1/F$. Since we consider three particles on a lattice
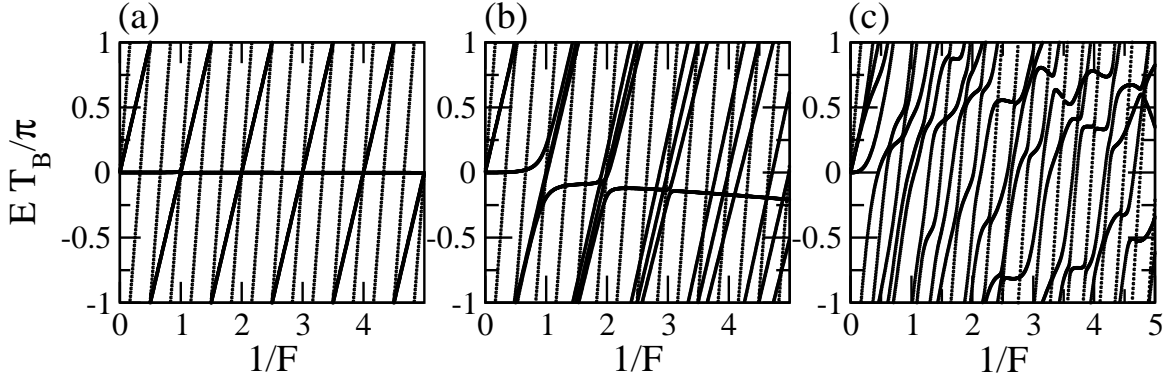
Figure 3.10: Spectrum of the $\kappa = 0$ block of the Floquet operator $\hat{U}(T_B)$, Eq. (2.42), for $n = 3$ and $L = 4$ plotted in units of π versus $1/F$. The onsite interaction is set to $U = 1$ and the tunneling coupling is (a) $J = 0.01$, (b) 0.1, and (c) 1.

of four sites, the factor α can take three different values $\alpha = 0, 1, 3$. For $J = 0.01$ (a), the spectrum consists of three sets of basically perfectly crossing straight lines. Increasing the tunneling strength to $J = 0.1$ (b) leads to avoided crossings between levels with distinct slope and lifts the degeneracies between levels with identical slope in the small-J limit. For comparable tunneling coupling and interaction strength $J = U = 1$ (c), the spectrum features various avoided crossings of different size. This is a clear indication for quantum chaos [114, 115] as we will confirm by an analysis of the spectral statistics: Fig. 3.11 shows the nearest-neighbor level-spacing distribution of the Floquet operator's eigenphases for the $\kappa = 0$ bloch of a larger system with $n = 8$, $L = 9$, *i.e.*, Hilbert-space dimension $\mathcal{N}_{\kappa_0} = 1430$, and $U = J = 1$. Here, the appropriate random matrix ensemble is the COE. As pointed out in Sec. 3.1.1, the corresponding level-spacing distribution is identical to the one of the GOE. In agreement with the analysis of the time-independent Bose-Hubbard Hamiltonian in Sec. 3.2.2, the tilt F can induce a transition from the chaotic to the regular regime.

To illustrate the influence of the Hilbert-space dimension on the numerically obtained statistics, in Fig. 3.11 we also plot the level-spacing distribution for the $\kappa = 0$ block of a smaller system with $n = 6$ and $L = 7$, *i.e.*, $\mathcal{N}_{\kappa_0} = 133$. While the system is still chaotic, the smaller Hilbert-space dimension induces deviations from the expected behavior which are manifest in fluctuations around the universal distributions.
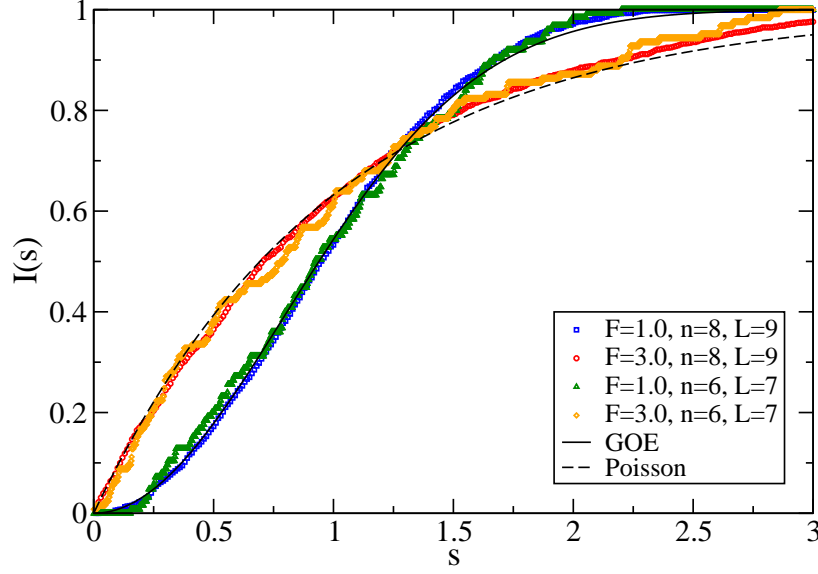
Figure 3.11: Integrated nearest-neighbor level-spacing distribution $I(s)$ of the Floquet operator's eigenphases of the $\kappa = 0$ block with $n = 8$, $L = 9$, $U = J = 1$, and $F = 1$ (blue squares) and 3 (red circles). The corresponding Hilbert-space dimension is given by $\mathcal{N}_{\kappa_0} = 1430$. In order to illustrate the influence of the Hilbert-space dimension on the numerically obtained statistics, the distribution of a smaller system with $n = 6$, $L = 7$, $\mathcal{N}_{\kappa_0} = 133$, and again $F = 1$ (green triangles) and 3 (orange diamonds) is also shown. For comparison, we also plot the GOE (solid line), Eq. (3.7), and Poissonian (dashed line), Eq. (3.12), distributions.

3.3 The chaotic regime of the tilted Bose-Hubbard Hamiltonian

The preceding analysis has demonstrated that the tilted Bose-Hubbard Hamiltonian $\hat{H} = \hat{H}_J + \hat{H}_U + \hat{H}_F$, Eq. (2.26), exhibits chaotic spectral statistics, whenever the contribution from onsite interaction and tunneling coupling are comparable in magnitude, *i.e.*,

$$\langle \hat{H}_J \rangle \approx \langle \hat{H}_U \rangle , \tag{3.16}$$

where $\langle \cdot \rangle$ is the expectation value with respect to a typical state from the bulk of the spectrum. Moreover, we have seen that a tilting of the lattice can induce regular spectral statistics (see Figs. 3.7 and 3.8) and, consequently, we have to require that the contribution from the tilt $\langle \hat{H}_F \rangle$ does not dominate the system. In the following, we map out the chaotic regime by the dependence of the spectral structure on the parameters J, U, F, n, and L.

We hitherto merely considered systems with approximately one atom per site, *i.e.*, with filling factors $n/L \approx 1$. Since the three terms in Eq. (2.26) depend differently on the boson

number n and on the lattice size L, we perform a scaling analysis with respect to those two parameters. Under the assumption that $\langle \hat{n}_l \rangle \approx n/L$, we find that

$$\left\langle \hat{H}_J \right\rangle \propto J \cdot n/L, \tag{3.17a}$$

$$\left\langle \hat{H}_U \right\rangle \propto U \cdot (n/L)^2, \tag{3.17b}$$

$$\left\langle \hat{H}_F \right\rangle \propto F \cdot L \cdot (n/L). \tag{3.17c}$$

Together with condition (3.16), this suggests that the system should be chaotic for

$$J \approx U \cdot n/L, \tag{3.18}$$

as long as $F \cdot L$ is smaller than some critical value that remains to be determined.

In order to facilitate the differentiation between regular and chaotic spectral regimes, we use the normalized mean square deviation

$$\Delta^2 = \frac{1}{N} \int\limits_0^\infty ds \, (f(s) - I(s))^2, \tag{3.19}$$

which quantifies the difference between the numerically obtained distributions $I(s)$ and the universal distributions $f(s)$ as introduced in Sec. 3.1. The normalization factor N is chosen such that the deviation between chaotic Wigner-Dyson and regular Poissonian universal statistics equals unity. In the following, we consider the deviation of $I(s)$ from Wigner-Dyson, $f(s) = I_W(s)$, Eq. (3.7), and Poissonian, $f(s) = I_P(s)$, Eq. (3.12), statistics as a function of the static field strength F and of the scaled static field strength $F \cdot L$, respectively. Pragmatically, we consider the point of transition from chaotic to regular spectral statistics to be that value F_{tr}, or equivalently $(F \cdot L)_{tr}$, where the two lines that correspond to the deviation from GOE and Poissonian statistics intersect. We then regard all systems to be chaotic for $F < F_{tr}$ (or equivalently $F \cdot L < (F \cdot L)_{tr}$), and as regular for $F > F_{tr}$ (or equivalently $F \cdot L > (F \cdot L)_{tr}$).

Fig. 3.12 shows representative plots of Δ^2 as a function of the static field strength F for different values of the filling factor n/L and of the interaction strength U, at fixed tunneling coupling $J = 1$. We consider filling factors $n/L = 0.5$, 1, and 2, with $n = L = 5$ (black solid lines), $n = 5$, $L = 10$ (red dotted lines), and $n = 10$, $L = 5$ (blue dashed lines), respectively. We start our analysis with $U = 1$, where the transition from chaotic to regular level statistics was found in the interval $1 < F_{tr} < 3$, for six bosons in seven lattice sites, *i.e.*, $n/L \approx 1$ (compare Fig. 3.8). This is consistent with the behavior for $n/L = 1$ (see black solid lines in Fig. 3.12 (a)), where the transitions occurs at $F_{tr} \approx 1.7$. The transition points of the three individual systems considered here, however, differ strongly. In contrast, when scaling the interaction strength such that $U \cdot n/L = 1$ without changing the other parameters (see
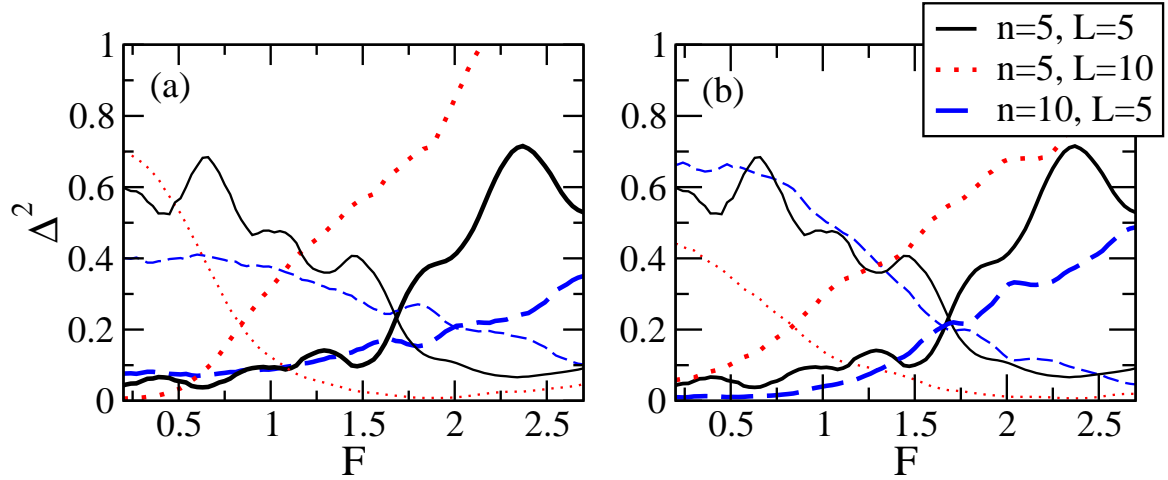
Figure 3.12: Mean square deviation Δ^2, Eq. (3.19), of the numerically obtained nearest-neighbor level-spacing distributions from GOE (thick lines) and Poissonian statistics (thin lines), as a function of the static field F. The system size is given by $n = L = 5$ (black solid lines), $n = 5$, $L = 10$ (red dotted lines), and $n = 10$, $L = 5$ (blue dashed lines), and the tunneling coupling is $J = 1$. Whereas in (a) the interaction strength is $U = 1$, in (b) we fix $U \cdot n/L = 1$.

Fig. 3.12 (b)), we find that, for the two systems with $L = 5$, chaotic level statistics emerge for practically the same values of F. Though, the chaotic regime of the system with $L = 10$ is restricted to smaller values of the static field F. Additional scaling of the abscissa with the size of the lattice L, as suggested by Eq. (3.17c), renders all three considered systems chaotic in the same range of $F \cdot L$, as spelled out by Fig. 3.13.

In order to determine whether this scaling holds in general, we now investigate the transition point from chaotic to regular spectral statistics in more detail. We plot $(F \cdot L)_{tr}$ versus the Hilbert-space dimension $\mathcal{N}$, Eq. (2.39), for several systems with $U = 1$ in Fig. 3.14 (a), and with $U \cdot n/L = 1$ in Fig. 3.14 (b). We find that the regime of chaotic spectral statistics slightly grows with $\mathcal{N}$, in both cases. Overall, for $U = 1$, the chaotic regime is smallest for $n/L < 1$ (blue circles) and largest for $n/L > 1$ (red triangles) while systems with $n/L = 1$ (black squares) lie in between. As predicted by the scaling argument (3.17a) - (3.17c), the data scatters less for $U \cdot n/L = 1$, rendering systems with comparable Hilbert space dimension chaotic within the same parameter regime.

A few data points, however, do not follow the expected scaling: In Fig. 3.14 (a) we find three systems with $n/L > 1$ that do not have a chaotic regime at all. This is indicated by the transition point $(F \cdot L)_{tr} = 0$ which here denotes that the systems are regular independent of the static field strength F, including $F = 0$. In Fig. 3.14 (b), we can identify four systems with $n/L < 1$ which also exhibit a significantly restricted range of chaotic spectral statis-
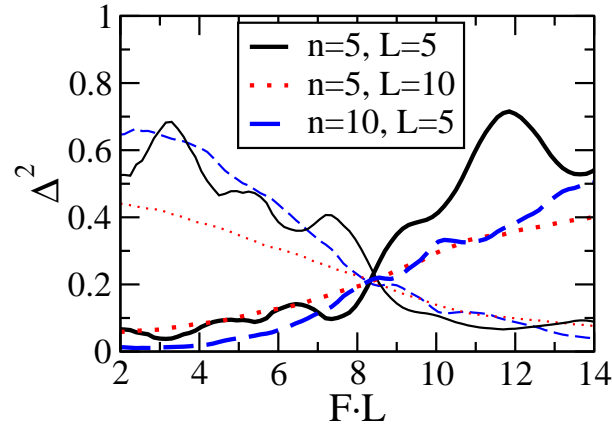
Figure 3.13: Same as Fig. 3.12 (b), but here Δ^2, Eq. (3.19), is plotted against the scaled static field $F \cdot L$.

tics. In order to understand the origin of these deviations, we plot in Fig. 3.14 (c) the filling factor n/L for all systems displayed in (a) and (b). In doing so, we find that the exceptions correspond to those systems with the largest and smallest filling factors, respectively. The first case, $n/L \gtrsim 4$ and fixed $U = 1$, corresponds to the strongly interacting regime, where the eigenstates are Wannier states and the spectrum is regular. Accordingly, if we choose $U \lesssim 0.25$ such that $U \cdot n/L = 1$, all three systems have the expected chaotic regime as evident from Fig. 3.14 (b). In the second case, the small filling factor $n/L \lesssim 0.4$, requires $U \gtrsim 2.5$ in order to achieve $U \cdot n/L = 1$. Such large values of the onsite interaction, however, lead to a suppression of the mobility of the bosons since the tunneling coupling J is effectively reduced. That is, the particles hardly move on the lattice what again induces regular spectral statistics for relatively small values of $F \cdot L$ already.

We thus confirm the predicted scaling behavior, *i.e.*, that fixed values of J, $U \cdot n/L$ and $F \cdot L$ render different systems equivalent with respect to their spectral structure. More precisely, in order to obtain chaotic spectral statistics, we have to require $J \approx U \cdot n/L$ and $F \cdot L < (F \cdot L)_{tr}$. This observation holds as long as the filling factor is not too small, *i.e.*, $n/L \gtrsim 0.4$. Moreover, the size of the chaotic regime also (weakly) depends on the Hilbert-space dimension $\mathcal{N}$, and large systems have slightly larger chaotic regions, *i.e.*, the transition point $(F \cdot L)_{tr}$ is shifted to larger values when $\mathcal{N}$ increases.

The transition from chaotic to regular spectral statistics with increasing tilt F has also been found in the analysis of the Floquet operator $\hat{U}(T_B)$, Eq. (2.42), with periodic boundary conditions, see Fig. 3.11. In this case, F enters the operator in the form of a time-dependent phase factor between neighboring lattice sites, that is identical for all pairs of adjacent sites.
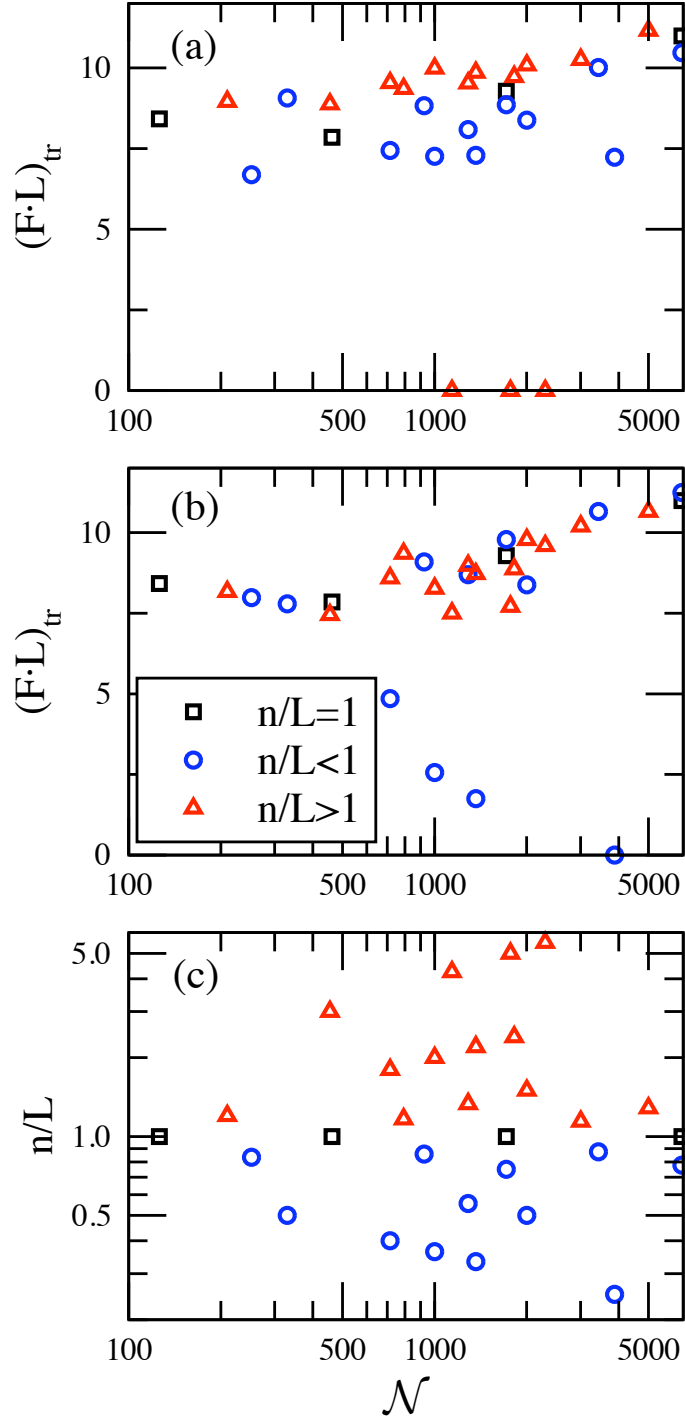
Figure 3.14: (a), (b) Point of transition $(F \cdot L)_{tr}$ from chaotic to regular spectral statistics, and (c) filling factor n/L, as a function of the Hilbert-space dimension $\mathcal{N}$, Eq. (2.39), for various systems. In panel (a) we set $U = 1$ and in panel (b) we chose $U \cdot n/L = 1$. The black squares correspond to systems with filling factor $n/L = 1$, blue circles to systems with $n/L < 1$, and red triangles to systems with $n/L > 1$.

A scaling with the number of sites L of the form $F \cdot L$ can thus not be expected. We rather find that, whereas the condition $J \approx U \cdot n/L$ still has to be satisfied, the transition from chaotic to regular statistics occurs at a point F_{tr} that is independent of L.[6] A descriptive explanation for this observation is based on the adiabatic spectrum of the transformed, time-dependent Hamiltonian: As explained in Sec. 3.2.3, here the tilt F represents the velocity with which the adiabatic spectrum is traversed as time elapses. If F is large, the chaotic structure of the spectrum as in Fig. 3.9 (c) is not resolved during time evolution. This results in perfectly regular level statistics of the Floquet operator (see Fig. 3.11). On the contrary, if F is sufficiently small, the irregular behavior of the energy levels is reflected in chaotic level statistics of the Floquet operator.

---

[6] The mean-square deviations Δ^2 from chaotic and regular universal statistics are shown for an exemplary system consisting of eight bosons in nine sites in Fig. 4.9 (a).

4 Simulability and complexity

The rapid growth of the Hilbert-space dimension $\mathcal{N}$ with the number of constituents is a generic feature of many-body quantum systems. For example, in a seemingly "small" Bose-Hubbard system of twelve bosons in a lattice of twelve sites we already have $\mathcal{N} = 1,352,078$, see Eq. (2.39). Consequently, an exact solution can in general not be found and efficient simulation techniques are needed in order to describe the resulting time evolution accurately. One such method is the time-dependent density matrix renormalisation group (t-DMRG) algorithm [163, 193, 194], that we discuss below and which is frequently used for the description of ultracold bosons in optical lattices.

The possibility to describe a system accurately with manageable numerical effort is termed *simulability*. Its natural opponent is *complexity* which is formally measured by the shortest possible length of an algorithm designed to simulate the system at hand [111]. One can also define complexity in terms of spectral quantities like the level-spacing distribution as discussed in Chapter 3. Here, we investigate how the complexity of a quantum system affects its simulability [152, 179]. We perform our analysis based on the Bose-Hubbard Hamiltonian with an additional static tilt, which serves as a paradigmatic example of a many-body quantum system where the complexity can be adjusted at will via the experimental control of the Hamiltonian.

In the following, we first introduce the basic features of the adaptive t-DMRG algorithm and then discuss the simulation of the dynamics in the different spectral regimes of the Bose-Hubbard-Hamiltonan.

4.1 The adaptive time-dependent DMRG algorithm

DMRG methods were first developed by White in 1992 [193] to determine the ground states of large 1D systems and have since then aided efficient simulation considerably. The basic idea lies in the representation of the system state in terms of significantly fewer basis states than the total dimension of the Hilbert space. In particular in perturbative regimes, where a system has a natural basis, such techniques work very successfully, and the ground states of 1D systems with Hamiltonians that incorporate only nearest-neighbor coupling are typically well represented in this form [184, 186]. DMRG techniques have also been implemented to tackle dynamics and have proven to work well for low-energy initial states

[2, 49, 186, 195]. For a generic initial state, however, they may perform well only for short times [164].

The method we apply here is based on Vidal's algorithm [186, 187], the relation of which to standard DMRG techniques was first brought forward in 2004 in Refs. [49, 195]. It can be used to integrate the many-body Schrödinger equation on an adaptively truncated Hilbert space for Hamiltonians that couple at most neighbouring sites, as will be detailed below. The algorithm is applicable only for Dirichlet boundary conditions in 1D. Other algorithms that can be generalized for periodic boundary conditions and 2D systems have also been developed [183, 185].

In this section, the main features of the adaptive t-DMRG algorithm that are necessary to understand the results presented in Sec. 4.2, will be discussed: We first introduce the specific state representation, which is based on the Schmidt decomposition and matrix product states, and discuss the von Neumann entropy as a measure for the correlations in the system. Then we explain how the simulation of the dynamics is performed. For further details on the algorithm, see for example [48, 49, 195] and references therein.

4.1.1 State representation

In order to apply DMRG methods, the Hilbert space of the system at hand must be expressed as the tensor product of local Hilbert spaces,

$$|\psi\rangle = \sum_{i_1,i_2,...,i_L=1}^{M} c_{i_1 i_2...i_L} |i_1\rangle \otimes |i_2\rangle \otimes ... \otimes |i_L\rangle. \tag{4.1}$$

Here the $|i_l\rangle$ are basis states in the local Hilbert spaces at the sites l which are assumed to be ordered in a chain-like structure. For simplicity, we also assume that the dimension M of the local Hilbert spaces is the same at all sites. In the case of the Bose-Hubbard Hamiltonian, describing n particles on a lattice of L sites, this is easily achieved if we consider as local Hilbert spaces the ones that correspond to the sites of the optical lattice, each of which has dimension $M = n + 1$, with the local basis given by the Fock basis states $|0\rangle, |1\rangle, ..., |n\rangle$, see Fig. 4.1.

4.1.1.1 Schmidt decomposition

The actual state representation is then defined in terms of the Schmidt decomposition [162] which can be derived from the singular value decomposition of matrices [136]. It defines a particular, unique representation of a state $|\psi\rangle$ of any *bipartite* system, *i.e.*, a system that consists of two subsystems A and B. For the Bose-Hubbard Hamiltonian, such a bipartite splitting corresponds to a separation of the lattice into two sublattices A and B between any
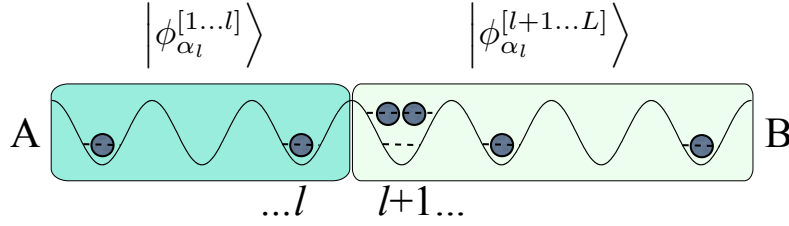
Figure 4.1: Schematic diagram of a system described by the Bose-Hubbard Hamiltonian. Each site of the lattice can be interpreted as a local Hilbert space with dimension $n+1$, where n is the number of atoms on the lattice. A bipartite splitting corresponds to a separation in the two parts left and right of the splitting between lattice sites l and $l+1$, with Schmidt eigenvectors $|\phi_{\alpha_l}^{[1...l]}\rangle$, Eq. (4.9), and $|\phi_{\alpha_l}^{[l+1...L]}\rangle$, Eq. (4.10), respectively.

two lattice sites l and $l+1$, see Fig. 4.1. The state decomposition then reads

$$|\psi\rangle = \sum_{\alpha=1}^{\chi_{AB}} \lambda_\alpha |\phi_\alpha^{[A]}\rangle \otimes |\phi_\alpha^{[B]}\rangle, \tag{4.2}$$

where $\{|\phi_\alpha^{[A]}\rangle\}$ and accordingly $\{|\phi_\alpha^{[B]}\rangle\}$ form an orthonormal basis of *Schmidt eigenvectors* for the two subsystems and

$$\langle\phi_\alpha^{[A]}|\psi\rangle = \lambda_\alpha |\phi_\alpha^{[B]}\rangle. \tag{4.3}$$

The *Schmidt rank* χ_{AB} counts the number of non-zero *Schmidt coefficients* λ_α and can be used as a measure of entanglement [136]. For example, $\chi_{AB} = 1$ implies that the state $|\psi\rangle = |\phi^{[A]}\rangle \otimes |\phi^{[B]}\rangle$ is a product state, what is tantamount to being separable. If $\chi_{AB} > 1$, the state $|\psi\rangle$ cannot be written as a product state and thus the two subsystems are entangled. Consequently, the Schmidt coefficients λ_α describe the quantum correlations between A and B. They fulfill the normalization condition $\sum_\alpha \lambda_\alpha^2 = 1$ and determine the eigenvalues of the reduced density matrices $\rho_A = \text{Tr}_B(|\psi\rangle\langle\psi|)$ and $\rho_B = \text{Tr}_A(|\psi\rangle\langle\psi|)$ of the two subsystems. Here $\text{Tr}_{A,B}$ denotes the partial trace over subsystems A, B, and we have

$$\rho_A|\phi_\alpha^{[A]}\rangle = \lambda_\alpha^2 |\phi_\alpha^{[A]}\rangle \tag{4.4}$$

and

$$\rho_B|\phi_\alpha^{[B]}\rangle = \lambda_\alpha^2 |\phi_\alpha^{[B]}\rangle. \tag{4.5}$$

The simulation of the time evolution with t-DMRG techniques relies on an approximation of the quantum state $|\psi\rangle$ by effectively decimating the system's Hilbert space. This is realized by setting an upper bound χ on χ_{AB} and thus retaining only those eigenstates with the largest Schmidt coefficients λ_α. The error in the final state is then proportional to the sum of the squares of the discarded eigenvalues $\sum_{\alpha=\chi+1}^{\chi_{AB}} \lambda_\alpha^2$.
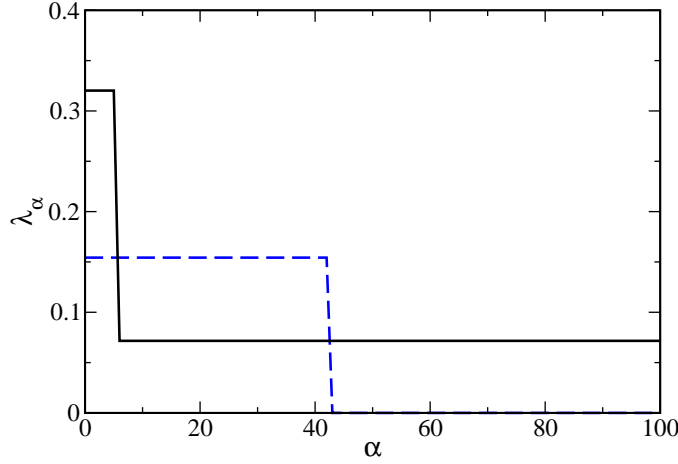
Figure 4.2: Two different distributions of Schmidt coefficients λ_α with identical von Neumann entropy $S = 5.39$, as defined by Eq. (4.6).

4.1.1.2 Von Neumann entropy

Both the entanglement between two subsystems *A* and *B* and the amount of information in one of the subsystems can be quantified with the help of the *von Neumann entropy* [136]

$$S = -\text{Tr}\left[\rho_A \log_2 \rho_A\right] = -\text{Tr}\left[\rho_B \log_2 \rho_B\right] = -\sum_{\alpha=1}^{\chi_{AB}} \lambda_\alpha{}^2 \log_2 \lambda_\alpha{}^2. \tag{4.6}$$

It provides a lower bound χ for the number of Schmidt coefficients λ_α that are required for a representation of the state under consideration via $\chi \geq 2^S$. Note, however, that fundamentally different distributions of Schmidt coefficients can have identical von Neumann entropy, as depicted in Fig. 4.2 where $S = 5.39$ for both distributions. In the case of the blue dashed distribution, taking into account $2^S = 42$ basis states, as suggested by the von Neumann entropy, describes the system's state accurately. On the contrary, in the case of the black solid distribution, this truncation implies $\sum_{\alpha=43}^{100} \lambda_\alpha^2 \approx 0.3$ and thus appreciable errors will be induced. Consequently, the von Neumann entropy only gives a first, rough estimate for the appropriateness of a basis truncation. In order to determine whether or not a truncation at a given value χ will describe the state accurately, we also have to consider the distribution of Schmidt coefficients.

As mentioned above, the von Neumann entropy (4.6) also quantifies the entanglement between the two subsystems *A* and *B*: For a separable state, we have $S_{min} = 0$ while for a maximally entangled state it takes its maximum value $S_{max} = \log_2 \mathcal{N}_{min}$, where $\mathcal{N}_{min}$ is the Hilbert-space dimension of the smaller of the two subsystems *A* and *B*.

4.1.1.3 Matrix product states

The key ingredient of the t-DMRG simulation protocol is the decomposition of the coefficients $c_{i_1 i_2 \ldots i_L}$ in Eq. (4.1) into a series of tensors [186],

$$c_{i_1 i_2 \ldots i_L} = \sum_{\alpha_1, \ldots, \alpha_{L-1}=1}^{\chi_1, \ldots, \chi_{L-1}} \Gamma_{\alpha_1}^{[1] i_1} \lambda_{\alpha_1}^{[1]} \Gamma_{\alpha_1 \alpha_2}^{[2] i_2} \lambda_{\alpha_2}^{[2]} \Gamma_{\alpha_2 \alpha_3}^{[3] i_3} \ldots \Gamma_{\alpha_{L-1}}^{[L] i_L}. \tag{4.7}$$

The corresponding states are known as *matrix product states* [49, 163, 195] or *finitely-correlated states* [64, 107]. Here, the Schmidt rank χ_l in general depends on the position l in the chain, which is why the sum in Eq. (4.7) runs up to different values χ_l for each α_l. The $\lambda^{[l]}$ are first-order tensors, while the $\Gamma^{[l]}$ are either of third order, for $l \neq 1, L$, *i.e.*, within the chain of local Hilbert spaces, or of second order, for $l = 1, L$, *i.e.*, at the edges of the chain. This stems from the application of Dirichlet boundary conditions, which we have to enforce in order to render the algorithm applicable. The strength of the state decomposition (4.7) is that the $\Gamma^{[l]}$ and $\lambda^{[l]}$ can be efficiently updated during time evolution, as will be elucidated in Sec. 4.1.2. Note that so far the representation of the state is exact and the tensors $\Gamma^{[l]}$ and $\lambda^{[l]}$ replace the M^L coefficients $c_{i_1 i_2 \ldots i_L}$ by approximately $(M \cdot \chi_{rep}^2 + \chi_{rep}) \cdot L$ coefficients, where χ_{rep} is a representative Schmidt rank for the system at hand. Whether or not this new decomposition is advantageous, depends on the scaling of χ_{rep} with the system size. More precisely, if $\chi_{rep} \propto e^L$, which is the generic case for a quantum state, we have neither gained nor lost anything. However, if χ_{rep} grows algebraically with the system size L, the state can be represented efficiently in this new form. Especially the low-energy states of 1D lattice and spin models have been found to be described efficiently in this form [163].

The tensors $\Gamma^{[l]}$ and $\lambda^{[l]}$ are constructed such that a bipartite splitting between any two local Hilbert spaces in the chain (*e.g.*, between site l and site $l+1$ as in Fig. 4.1) leads to the Schmidt decomposition

$$|\psi\rangle = \sum_{\alpha_l=1}^{\chi_l} \lambda_{\alpha_l}^{[l]} |\phi_{\alpha_l}^{[1 \ldots l]}\rangle \otimes |\phi_{\alpha_l}^{[l+1 \ldots L]}\rangle, \tag{4.8}$$

with Schmidt coefficients $\lambda_{\alpha_l}^{[l]}$ and Schmidt eigenvectors [49]

$$|\phi_{\alpha_l}^{[1 \ldots l]}\rangle = \sum_{\alpha_1, \ldots, \alpha_{l-1}=1}^{\chi_1, \ldots, \chi_{l-1}} \sum_{i_1, \ldots, i_l=1}^{M} \Gamma_{\alpha_1}^{[1] i_1} \lambda_{\alpha_1}^{[1]} \Gamma_{\alpha_1 \alpha_2}^{[2] i_2} \lambda_{\alpha_2}^{[2]} \Gamma_{\alpha_2 \alpha_3}^{[3] i_3} \ldots \Gamma_{\alpha_{l-1} \alpha_l}^{[l] i_l} |i_1\rangle \otimes \ldots \otimes |i_l\rangle \tag{4.9}$$

and

$$|\phi_{\alpha_l}^{[l+1 \ldots L]}\rangle = \sum_{\alpha_{l+1}, \ldots, \alpha_{L-1}=1}^{\chi_{l+1}, \ldots, \chi_{L-1}} \sum_{i_{l+1}, \ldots, i_L=1}^{M} \Gamma_{\alpha_l \alpha_{l+1}}^{[l+1] i_{l+1}} \lambda_{\alpha_{l+1}}^{[l+1]} \Gamma_{\alpha_{l+1} \alpha_{l+2}}^{[l+2] i_{l+2}} \ldots \Gamma_{\alpha_{L-1}}^{[L] i_L} |i_{l+1}\rangle \otimes \ldots \otimes |i_L\rangle. \tag{4.10}$$

Here $\{|\phi_{\alpha_l}^{[1 \ldots l]}\rangle\}$ and $\{|\phi_{\alpha_l}^{[l+1 \ldots L]}\rangle\}$ again form an orthonormal basis for the subsystems which are now given by all the sites left and all the sites right of the splitting, respectively.

4.1.2 Time evolution

In the following, we discuss how, based on the state representation introduced above, the many-body Schrödinger equation can be integrated. Since we consider Hamiltonians that exhibit at most nearest-neighbor coupling, only operations that act either on a single local Hilbert space or on the local Hilbert spaces of two neighboring sites need to be considered. In this context, it is convenient to express the Hamiltonian as

$$\hat{H} = \sum_{l\,even} \hat{F}_{l,l+1} + \sum_{l\,odd} \hat{G}_{l,l+1}, \qquad (4.11)$$

where $\hat{F}_{l,l+1}$ ($\hat{G}_{l,l+1}$) is the Hamiltonian that links sites l and $l+1$ for even (odd) l. Consequently, $[\hat{F}_{l,l+1}, \hat{F}_{j,j+1}] = [\hat{G}_{l,l+1}, \hat{G}_{j,j+1}] = 0 \; \forall l, j$, while $\hat{F}_{l,l+1}$ and $\hat{G}_{j,j+1}$ only commute if they do not share a site. For small time steps δt, the time-evolution operator can then be expressed as

$$\hat{U}(\delta t) = e^{-i\hat{H}\delta t} = \prod_{l\,even} e^{-i\hat{F}_{l,l+1}\delta t} \prod_{l\,odd} e^{-i\hat{G}_{l,l+1}\delta t} + O(\delta t^2), \qquad (4.12)$$

which allows us to compute the time evolution of a state by repeated application of the two-site time-evolution operators $e^{-i\hat{F}_{l,l+1}\delta t}$ and $e^{-i\hat{G}_{l,l+1}\delta t}$. Here, the error stems from neglecting the commutator $[\hat{F}_{l,l+1}, \hat{G}_{j,j+1}]$, when $\hat{F}_{l,l+1}$ and $\hat{G}_{j,j+1}$ share a site. It can be reduced by applying higher order expansions [171, 172]. For longer times $t = n \cdot \delta t$ we then have $|\psi(t = n \cdot \delta t)\rangle = \hat{U}(\delta t)^n |\psi_0\rangle$.

4.1.2.1 Single-site and two-site operations

The Hamiltonian $\hat{F}_{l,l+1}$ ($\hat{G}_{l,l+1}$) incorporates both, single-site operations U_l and two-site operations $V_{l,l+1}$, which will be discussed in the following. In the case of the Bose-Hubbard Hamiltonian, they correspond to the onsite interaction and to the tunneling coupling, respectively.

A single-site operation acts only on the local Hilbert space of one particular site l, and has the form

$$U_l = \sum_{i,j=1}^{M} U_j^i |i_l\rangle\langle j_l|. \qquad (4.13)$$

Since it generates a local, unitary time evolution that does not affect the correlations between any two subsystems, it does not have an impact on the Schmidt decompositions. Consequently, in the state decomposition (4.7) only the tensor $\Gamma^{[l]}$ has to be updated.

On the contrary, two-site operations

$$V_{l,l+1} = \sum_{k,n,i,j=1}^{M} V_{kn}^{ij} |i_l j_{l+1}\rangle\langle k_l n_{l+1}|, \qquad (4.14)$$
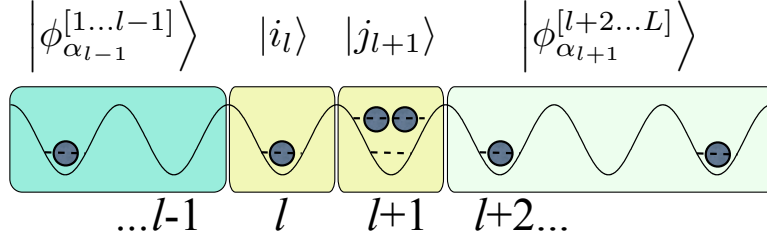
Figure 4.3: Sketch of a system described by the Bose-Hubbard Hamiltonian as in Fig. 4.1. By repeated Schmidt decompositions between sites $l-1$ and l, l and $l+1$, and $l+1$ and $l+2$, respectively, the state of the system $|\psi\rangle$ can be expressed such that an operation that acts on the two neighboring sites l and $l+1$ can be efficiently implemented as described in Sec. 4.1.2.1.

act simultaneously on the local Hilbert spaces of two neighboring sites l and $l+1$.[1] In order to identify the tensors Γ and λ that are affected under action of the operator $V_{l,l+1}$, we express the state $|\psi\rangle$ such that the two lattice sites under consideration are separated from the rest of the system. To this end, we apply three Schmidt decompositions, *i.e.*, we spilt the lattice between sites $l-1$ and l, l and $l+1$, and $l+1$ and $l+2$, respectively, as depicted in Fig. 4.3. This leaves us with the representation

$$|\psi\rangle = \sum_{\alpha_{l-1},\alpha_l,\alpha_{l+1}=1}^{\chi_{l-1};\chi_l;\chi_{l+1}} \sum_{i,j=1}^{M} \lambda_{\alpha_{l-1}}^{[l-1]} \Gamma_{\alpha_{l-1}\alpha_l}^{[l]i} \lambda_{\alpha_l}^{[l]} \Gamma_{\alpha_l\alpha_{l+1}}^{[l+1]j} \lambda_{\alpha_{l+1}}^{[l+1]} |\phi_{\alpha_{l-1}}^{[1...l-1]}\rangle \otimes |i_l\rangle \otimes |j_{l+1}\rangle \otimes |\phi_{\alpha_{l+1}}^{[l+2...L]}\rangle .$$
(4.15)

Application of the operator $V_{l,l+1}$ then leads to

$$|\psi'\rangle = \sum_{\alpha_{l-1},\alpha_{l+1}=1}^{\chi_{l-1};\chi_{l+1}} \sum_{i,j=1}^{M} \Theta_{\alpha_{l-1}\alpha_{l+1}}^{ij} |\phi_{\alpha_{l-1}}^{[1...l-1]}\rangle \otimes |i_l\rangle \otimes |j_{l+1}\rangle \otimes |\phi_{\alpha_{l+1}}^{[l+2...L]}\rangle ,$$
(4.16)

where

$$\Theta_{\alpha_{l-1}\alpha_{l+1}}^{ij} = \sum_{\alpha_l=1}^{\chi_l} \sum_{k,n=1}^{M} V_{kn}^{ij} \lambda_{\alpha_{l-1}}^{[l-1]} \Gamma_{\alpha_{l-1}\alpha_l}^{[l]k} \lambda_{\alpha_l}^{[l]} \Gamma_{\alpha_l\alpha_{l+1}}^{[l+1]n} \lambda_{\alpha_{l+1}}^{[l+1]} .$$
(4.17)

We thus find that the two-site operation $V_{l,l+1}$ only requires updating the tensors $\Gamma^{[l]}$, $\Gamma^{[l+1]}$, and $\lambda^{[l]}$, and therefore can be efficiently implemented. Note that as opposed to the case of single-site operations, here also the Schmidt coefficients $\lambda_{\alpha_l}^{[l]}$ which describe the correlations between the two subsystems are affected.

---

[1]Note that we focus on operations that do not affect the two sites at the edges of the chain, *i.e.*, we consider $l \in [2, L-2]$. The expressions for $l = 1, L-1$ are, however, analogous to the ones discussed here.

4.1.2.2 Simulation of the time evolution

As explained in Sec. 4.1.1.1, in the simulation of a quantum system's time evolution with
t-DMRG techniques, the Hilbert space is truncated by setting an upper bound χ on the χ_l
in representation (4.7). In standard t-DMRG techniques, the basis states are chosen at the
beginning of the simulation and are kept fixed during time evolution.

On the contrary, in the adaptive t-DMRG algorithm, the considered Hilbert space is dy-
namically adapted in the course of the propagation[2] by choosing the basis states $|\phi_\alpha\rangle$ ac-
cordingly. To this end, after application of a two-site time evolution operator $e^{-i\hat{F}_{l,l+1}\delta t}$ (or
$e^{-i\hat{G}_{l,l+1}\delta t}$), a new Schmidt decomposition is performed. This results in

$$|\tilde{\psi}\rangle = e^{-i\hat{F}_{l,l+1}\delta t}|\psi\rangle = \sum_{\alpha_l=1}^{\chi \cdot M} \tilde{\lambda}_{\alpha_l}^{[l]} |\tilde{\phi}_{\alpha_l}^{[1...l]}\rangle \otimes |\tilde{\phi}_{\alpha_l}^{[l+1...L]}\rangle, \qquad (4.18)$$

where the tilde indicates that in general both basis states and coefficients will have changed
due to the operation. Note that the formerly χ Schmidt coefficients $\lambda_{\alpha_l}^{[l]}$ have been replaced
by $\chi \cdot M$ Schmidt coefficients $\tilde{\lambda}_{\alpha_l}^{[l]}$. Subsequently, always those χ eigenstates with the largest
weight in the decomposition are retained and the remainder is discarded [49, 195].

The above approximation is good if, at each instance of time, the decreasingly ordered $\lambda_{\alpha_l}^{[l]}$
decay rapidly as a function of their index α_l, for every possible bipartition. It thus implicitly
relies on the assumption that the entanglement between any two parts of the system is never
too large. Or, in other words, if the entanglement grows rapidly with time, a simulation of
the system will be difficult, whereas if it is bounded during the dynamics, we can compute
the dynamics over long time periods without accumulating appreciable errors.

4.2 Simulation of the many-body dynamics

In what follows, we analyze the efficiency of the adaptive t-DMRG algorithm to simulate
the dynamics in the different spectral regimes of the tilted Bose-Hubbard Hamiltonian iden-
tified in Sec. 3.2. To this end, we monitor both the dynamically generated many-particle en-
tanglement, given by the von Neumann entropy S, Eq. (4.6), and the distribution of Schmidt
coefficients λ_α. We stress that the Bose-Hubbard system serves as a paradigmatic physi-
cal model to relate the simulability of a system to its complexity expressed by regular or
chaotic universal level statistics of the underlying Hamiltonian. Since universality means
that the specific form of the Hamiltonian is irrelevant and only global symmetry properties
have to be considered [74, 85, 168] (see also Sec. 3.1), the results presented here directly
carry over to other generic many-body quantum systems.

---

[2]Furthermore, going beyond Refs. [186, 187], conserved quantities, such as the total particle number n in
the Bose-Hubbard Hamiltonian, are taken into account in order to minimize numerical noise [48, 49].

4.2.1 Creation of many-particle entanglement

For comparable contributions of onsite interaction and tunneling coupling, the Bose-Hubbard system exhibits a transition from chaotic to regular spectral statistics when the strength of the static tilt is varied. For a filling factor $n/L \approx 1$, this translates into $J \approx U$, see Sec. 3.3. In order to analyze the applicability of the t-DMRG algorithm in the different spectral regimes, we thus simulate the dynamics for $U = J = 1$ while varying F. As a reference, we also consider dominant interaction, $U = 10$ and $J = 1$, since in this case the system is regular, irrespective of the static field strength.

The numerical data presented in the following are generated for a system that consists of $n = 8$ bosons initially placed in $m = 8$ neighboring sites, in the center of a lattice with $L = 64$ sites, and Dirichlet boundary conditions.[3] The initial states are of the form

$$|\psi_0\rangle = |n_1, n_2, \ldots, n_8\rangle, \tag{4.19}$$

i.e., they are Wannier-Fock states as given by Eq. (2.22). We consider random realizations of occupation numbers n_l on the single sites, while limiting the maximal number of bosons on one individual lattice site to two, with $\sum_l n_l = 8$. This choice guarantees that all initial states have comparable energies that lie within the bulk of the tilted Hamiltonian's spectrum. We can thus average the dynamical data over different initial configurations. Note that for the states considered here, at $t = 0$ there is no entanglement between any two subsystems and therefore the von Neumann entropy S, Eq. (4.6), vanishes for all bipartite splittings, as can be observed in Fig. 4.4. In particular, this means that all correlations, reflected by $S > 0$, are generated during the dynamics. In the simulation, the number of retained Schmidt coefficients is set to $\chi = 100$, what results in a maximal possible entropy $S_{max} = 6.64$.

The dynamically generated many-particle entanglement, measured by the average von Neumann entropy S, is plotted as a function of the static field strength F and time, in units of the Bloch period t/T_B, in Fig. 4.4. Red regions correspond to large and blue regions to small values of the entropy. We can distinguish fundamentally different regimes of entanglement growth, depending on the relative strength of the system's control parameters: On the one hand, for dominant onsite interaction, $U = 10$ (Fig. 4.4 (a)), the entanglement grows only slightly for all values of F. On the other hand, when onsite interaction and tunneling coupling are comparable, $U = 1$ (Fig. 4.4 (b)), there is a clear transition from slow to rapid entanglement growth when the strength of the static field is decreased. This means that in the former case, we expect the system to be simulable for long time periods, whereas in the latter case a simulation of the system will be difficult for small values of the tilt.

---

[3]The numerical data obtained from t-DMRG simulations was provided by Andrew Daley in the context of a collaboration, see also Ref. [179].
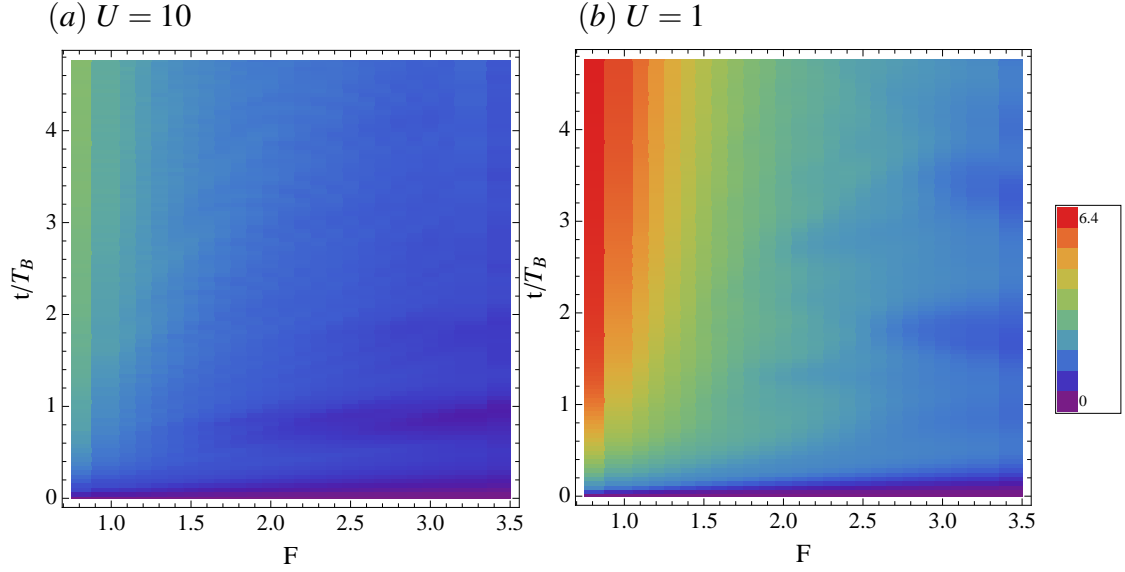
Figure 4.4: Dynamically generated many-particle entanglement measured by the average von Neumann entropy S, Eq. (4.6), as a function of F and t/T_B for $J = 1$ and (a) $U = 10$, (b) $U = 1$. Red regions correspond to large and blue regions to small values of S. The data is extracted from t-DMRG simulations of eight particles initially localized in eight neighboring lattice sites which are placed in the middle of a lattice consisting of 64 sites. The average is taken over ten different separable initial states.

For the average data shown in Fig. 4.4, we always consider that particular bipartite splitting that results in the largest entanglement entropy, as this eventually limits the efficiency of the algorithm, as discussed in Sec. 4.1. However, as evident from Fig. 4.5, other bipartitions also yield comparable results. Given that the initial states are located on lattice sites 28 through 35, we find that any splitting in the middle of the initially occupied part of the lattice yields almost the same von Neumann entropy.

In order to facilitate the identification of the entropy's asymptotic behavior, Fig. 4.6 (a) shows the von Neumann entropy S as a function of time for different values of the static field strength F. We find that for small times $t/T_B < 0.25$, S grows rapidly for all parameter sets. This behavior can be attributed to the initial states (4.19) considered here: They are not eigenstates of the Hamiltonian and thus the bosons first adapt to the particular physical situation that is determined by the values of the parameters J, U, and F. Indeed, when considering as initial state the ground state of the untilted lattice, the rapid growth of the entropy for short times does not occur. Subsequently, for dominant onsite interaction $U = 10$, the von Neumann entropy grows only little and, independently of the tilt, stays well below the maximal value $S_{max} = 6.64$ during the simulation. For $U = 1$, on the other hand,
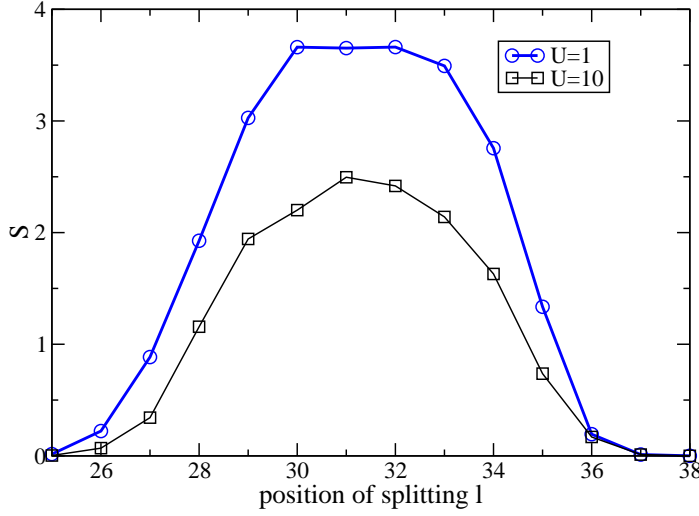
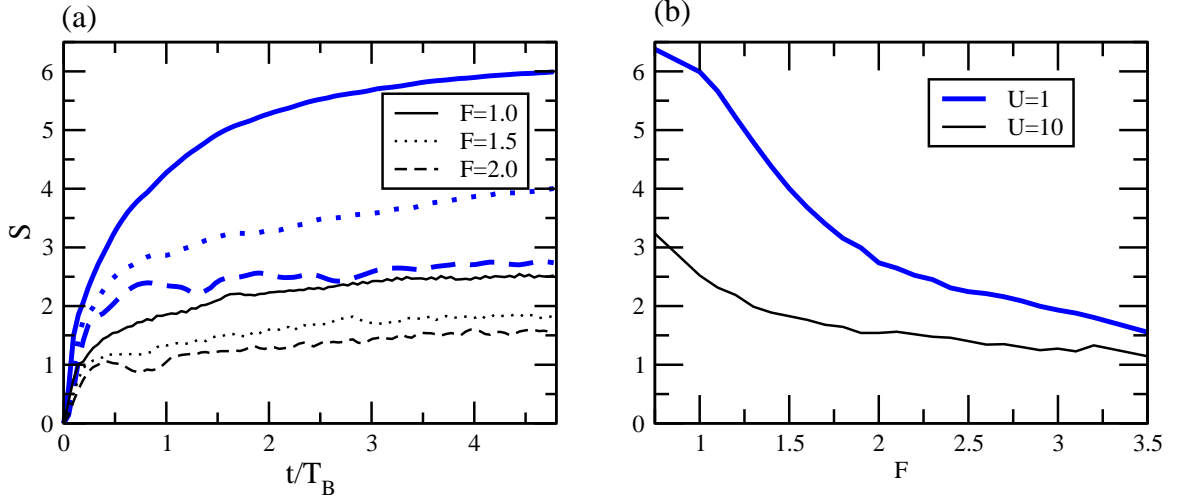**Figure 4.5:** Example of the von Neumann entropy S, Eq. (4.6), for a single initial state $|\psi_0\rangle = |1,1,0,2,0,1,1,2\rangle$, at $t/T_B = 4.8$, when the state evolution has reached its asymptotic behavior (compare Fig. 4.6 (a) and the corresponding discussion in the text). S is plotted as a function of the position l of the bipartite splitting, *i.e.*, the splitting is taken between sites l and $l+1$. The interaction strength is $U = 1$ (blue thick line), 10 (black line) and the static field is set to $F = 1.5$.

the behavior strongly depends on the strength of the static field: For a moderate value $F = 2.0$, there is only little growth, which increases for $F = 1.5$, and is largest for a small tilt $F = 1$. In all those cases where the entanglement stays small (say $S \lesssim 3$) during the simulation, the state evolution quickly reaches its asymptotic behavior, a basically constant and small slope of $S(t)$ that allows a simulation over long times. Note that for $U = F = 1$, the saturation-like behavior of S is a numerical artifact of the truncation at $\chi = 100$. In this case, the simulation only approximates the real values of S from below, *i.e.*, at a given time $t/T_B \gtrsim 1.5$, S grows when increasing χ, as we numerically confirmed by varying χ.

In Fig. 4.6 (b), we show the von Neumann entropy as a function of F at a fixed time $t/T_B = 4.8$, where the state evolution has reached its asymptotic behavior. This supports the conjecture that for dominant interaction $U = 10$, the system can be effectively represented in terms of matrix product states, independent of the static field strength. Note that the increase of S for small values of F corresponds to a regime where the von Neumann entropy has reached its asymptotic behavior, as evident from Fig. 4.6 (a), and thus efficient simulation is not hindered by this behavior. The situation would be different if we considered even smaller values of the tilt: As mentioned already in Sec. 2.4.1, then the spatial extent of the atoms' motion is larger and they travel into initially unoccupied regions. Consequently, for very small static fields, we expect simulations to be hard irrespective of U. As opposed

Figure 4.6: Average von Neumann entropy S, Eq. (4.6), (a) as a function of time, in units of the Bloch period t/T_B, and (b) as a function of the static field strength F. The system is chosen as in Fig. 4.4, with interaction strength $U = 1$ (blue thick lines) and 10 (black lines). In panel (a), the time evolution of S is plotted for different values of the static field, namely $F = 1.0$ (solid), 1.5 (dotted), 2.0 (dashed), respectively. Panel (b) shows S at time $t/T_B = 4.8$, when the state evolution has reached its asymptotic behavior for the given basis size.

to the strongly interacting case $U = 10$, for comparable strength of onsite interaction and tunneling coupling, $U = J = 1$, an accurate description of the system with t-DMRG will only be feasible[4] for $F \gtrsim 1.3$.

As detailed in Sec. 4.1.1.2, the von Neumann entropy only yields a first estimate on the simulation efficiency. A more precise measure is provided by the distribution of average Schmidt coefficients λ_α. Since we choose separable initial states $|\psi_0\rangle$, Eq. (4.19), at $t = 0$ only one Schmidt coefficient contributes. We are thus interested in the dynamically generated distributions as depicted on a semi-logarithmic scale for $t/T_B = 4.8$ in Fig. 4.7. Shown are the average values λ_α^2 as a function of their index α, sorted in descending order. They can be divided into two fundamentally different categories: For strong interaction $U = 10$, only few comparably large coefficients dominate the distribution, which shows a rapidly diminishing tail. As in the case of the von Neumann entropy, this observation is independent of the static field strength F. We can observe the same kind of peaked distribution for weak interaction $U = 1$ and medium static field strength $F = 2$. However, for $F = 1.5$, there is a transition to a broader distribution that exhibits a slowly decaying tail with many

---

[4]Note that for $U = 1$ and $F \lesssim 1.0$, the saturation in Fig. 4.6 (b) is again caused by the choice of finite $\chi = 100$ in the simulation.
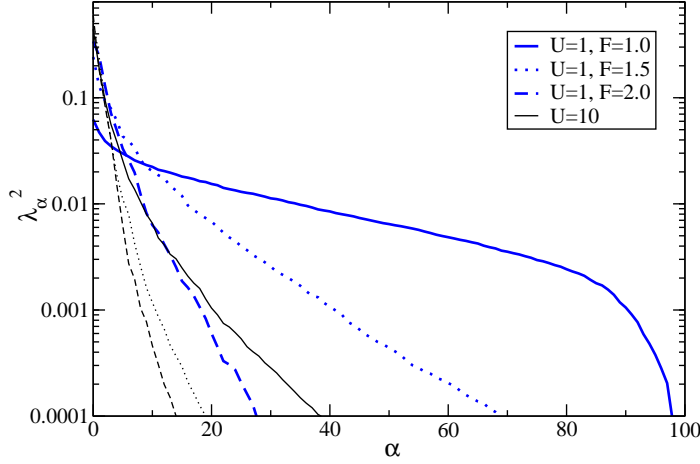
Figure 4.7: Distribution of average Schmidt coefficients λ_α as a funtion of their index α on a semi-logarithmic scale. Shown are the squares λ_α^2 of the $\chi = 100$ largest average Schmidt coefficients, sorted in descending order. The system parameters are those of Fig. 4.4, with $U = 1$ (blue thick lines) and $U = 10$ (black lines), and different values of the static tilt $F = 1$ (solid), 1.5 (dotted), 2 (dashed), at $t/T_B = 4.8$.

non-negligible coefficients. For even weaker static field $F = 1$, the distribution has changed its character completely and basically all Schmidt coefficients have the same magnitude. Analogously to the saturation of the von Neumann entropy in Figs. 4.6 (a) and (b), the rapid decrease of the Schmidt coefficients beyond $\chi = 80$ for $F = 1$ is a numerical artifact caused by the basis truncation at $\chi = 100$.

What are the implications of two such distributions on the possibility to truncate the basis? Obviously, a narrow distribution allows us to effectively reduce the Hilbert space by dropping the major portion of Schmidt basis states, and a reliable simulation by t-DMRG is feasible. On the other hand, if the distribution is broad, basically all Schmidt coefficients have to be taken into account. Dropping even a few basis states will already induce considerable errors in the simulation, and the t-DMRG algorithm will not be efficient.

4.2.2 Breakdown of simulability in the chaotic regime

The above analysis gives evidence that the efficiency of the t-DMRG method strongly depends on the control parameters of the system. In the following, we will investigate whether this behavior is reflected in the spectral properties of the underlying Hamiltonian, *i.e.*, whether the simulability of the system can be related to parameter regimes of regular and chaotic universal level statistics.

Here, we present t-DMRG simulations of eight bosons initially placed in eight neigh-
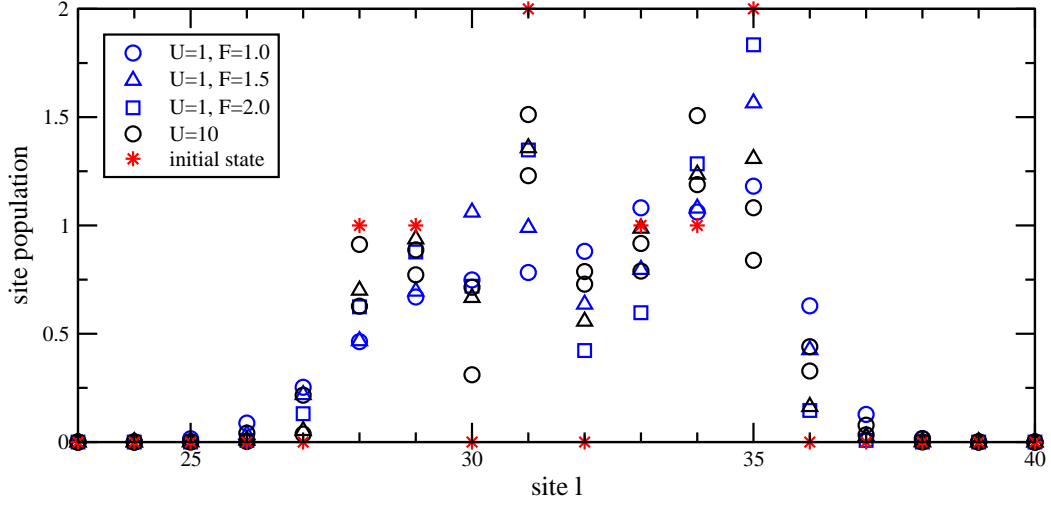
Figure 4.8: Example of the single lattice sites' populations after a simulation time $t/T_B = 4.8$, for different parameter choices. The interaction strength is $U = 1$ (blue symbols), 10 (black symbols) and the static tilt is set to $F = 1.0$ (circles), 1.5 (triangles), 2.0 (squares). The initial state $|\psi_0\rangle$ is chosen as in Fig. 4.5, and the associated site population (for $t = 0$) is depicted by red stars.

boring sites in the center of a lattice of length 64 with Dirichlet boundary conditions. One would be tempted to compare the efficiency of the dynamical simulations to the spectral properties of that very system. Instead, we investigate the spectrum of the Floquet operator[5] $\hat{U}(T_B)$, Eq. (2.42), of eight particles in nine lattice sites. Why is this comparison reasonable? First of all, we note that due to the large size of the lattice as compared to the extent of the initial states, the boundaries are not probed during the dynamics. The system is effectively infinite and thus can be mimicked by a smaller lattice with periodic boundary conditions (see discussion in Sec. 2.4.1). What is now the adequate extent of this smaller lattice such that it reflects the features of the large system faithfully? In order to answer this question, we note that for $F \gtrsim 1$, the particles hardly spread on the lattice during the considered timescale. This is evident from Fig. 4.8, where we depict the population on the single sites at $t/T_B = 4.8$ for $U = 1, 10$ and $F = 1.0, 1.5, 2.0$, for the same single initial state as in Fig. 4.5. In particular, the slight spreading is basically independent of both static field[6] F and interaction strength U. Thus, a restriction to nine lattice sites in the spectral analysis is justified in the entire parameter regime considered here.

Moreover, although the spectral statistics for a fixed set of parameters J, U, and F in

---

[5]For further details on the Floquet operator's spectrum and its spectral statistics see Sec. 3.2.4.

[6]As discussed above, this would be different if we considered also smaller values of the tilt. The resulting difficulty of efficient simulations is indicated also in Fig. 4.7, where the distribution of Schmidt coefficients gets slightly broader for $F = 1$, even when $U = 10$.

principle depend on the bosons number n and the lattice size L (see Sec. 3.3), it changes marginally for $n = 8$ and $L = 9 \pm 1$, since the filling factor n/L is only shifted by about 10%.

We now evaluate the integrated nearest-neighbor level-spacing distribution $I(s)$ (as introduced in Eq. (3.6) of Sec. 3.1) of the Floquet operator's eigenphases for $U = 1$ and 10, and fixed quasimomentum $\kappa = 0$. To this end, Fig. 4.9 (a) shows the mean square deviation Δ^2, Eq. (3.19), of the numerically obtained distributions from (chaotic) Wigner-Dyson, $I_W(s)$, Eq. (3.7), and (regular) Poissonian statistics, $I_P(s)$, Eq. (3.12), as a function of the static field strength F. For $U = 10$, the system is regular as it obeys Poissonian statistics, irrespective of the static field strength F. In agreement with the analysis of Sec. 3.3, for $U = 1$, a sudden and pronounced transition in the level statistics occurs: Whereas for $F \lesssim 1.3$, the deviation from Wigner-Dyson statistics is negligible, the spectrum turns Poissonian for $F \gtrsim 2$. In between, there is a transition region for $1.3 \lesssim F \lesssim 2$, where the level-spacing distribution changes its character.

The observed sharp transition between chaotic and regular level statistics is directly reflected in the applicability of a basis truncation, expressed by the von Neumann entropy S, Eq. (4.6), which is depicted in Fig. 4.6 (b). However, as discussed in Sec. 4.1.1.2, S only serves as a first estimate for simulabilty and we thus also consider the number of Schmidt coefficients $N(\varepsilon)$ larger than a given threshold ε, which is depicted for $\varepsilon = 0.01$ in Fig. 4.9 (b). In the regular regime ($U = 10$, and $U = 1$ with $F \gtrsim 2$) typically less than 20% of the coefficients exceed the threshold ε, whereas in the chaotic regime ($U = 1$, $F \lesssim 1.3$) essentially all of them contribute. That is, whereas the dynamics can be efficiently simulated in the regular regime, simulability breaks down in the chaotic regime since any basis truncation will rapidly lead to substantial errors in the time evolution as reflected in the saturation of $N(\varepsilon)$ for $F \lesssim 1.3$. An accurate description of the system's dynamics then requires large numerical efforts that scale exponentially, much as the system size itself.

4.3 Conclusion

The above observations have also been verified for a larger system with 20 particles initially placed in 20 lattice sites, where an exact treatment of the dynamics becomes impracticable. Moreover, also simulations with initial states that bear a finite amount of quantum correlations,[7] expressed by a non-vanishing von Neumann entropy, affirm the intricacy of simulations in the chaotic regime. An example for such states is provided by the untilted Hamiltonian's ground state. Thus, the breakdown of simulability with t-DMRG, *i.e.*, a

---

[7]Highly correlated initial states will be hard to simulate even when the Hamiltonian that generates the dynamics is regular, since right at the start of the simulation they prevent an efficient basis truncation. Examples of such states are eigenstates of the Bose-Hubbard Hamiltonian in its chaotic parameter regime.
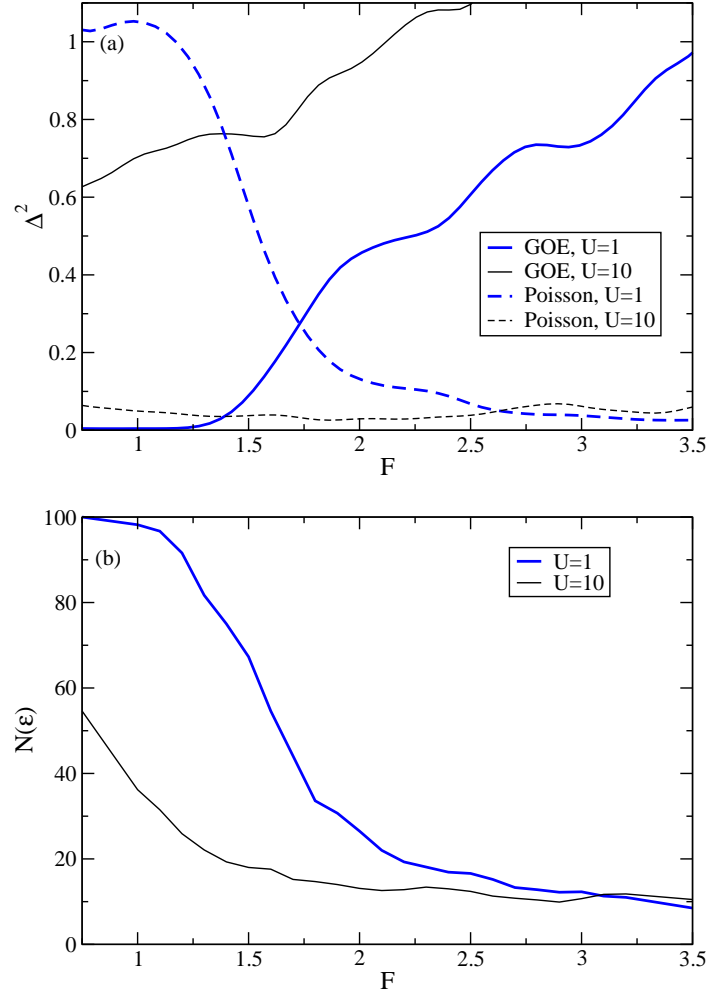
Figure 4.9: (a) Mean square deviation Δ^2, Eq. (3.19), of the distribution of spacings between neighboring eigenphases of the Floquet operator, and (b) average number of Schmidt coefficients larger than the threshold value $\varepsilon = 0.01$. Both quantities are plotted versus the static field strength F. In panel (a), the Floquet operator $\hat{U}(T_B)$, Eq. (2.42), has fixed quasimomentum $\kappa = 0$ and corresponds to eight particles on nine lattice sites with periodic boundary conditions. Depicted are the deviation from regular Poissonian (dashed lines) and chaotic Wigner-Dyson statistics (solid lines), for $U = 1$ (blue thick lines) and 10 (black lines). The data shown in panel (b) again corresponds to a simulation time $t/T_B = 4.8$. The system is chosen as in Fig. 4.4, with interaction strengths $U = 1$ and 10, respectively.

broad distribution of dynamically generated Schmidt coefficients, is an unambiguous indicator of the underlying complexity of the many-particle spectrum [179], reflected by the chaotic universal spectral statistical as shown in Fig. 4.9 (a).

That is, while t-DMRG is a powerful tool to simulate, *e.g.*, the dynamics of quantum systems in the regime of regular spectral structure, there can be parameter regimes where the spectrum of *exactly the same system* follows chaotic statistics and a faithful representation of the system state spans essentially the entire Hilbert space. Numerical simulations are then plagued by highly unfavorable scaling. More precisely, we conjecture that the distribution of dynamically generated Schmidt coefficients of typical states in spectrally regular and chaotic systems exhibits universal features[8], in close analogy to the energy level distributions of regular and chaotic quantum systems.

Furthermore, it is known that universal spectral statistics in turn imply universal properties of the associated eigenstates of generic quantum systems [85]: In the chaotic regime, they are delocalized in any generic basis and, vice versa, any generic basis state is delocalized in the eigenbasis of the Hamiltonian. This implies that generic initial states evolve to states broadly distributed in any basis, under the time evolution induced by a quantum chaotic Hamiltonian. Thus, the breakdown of simulability in the chaotic regime, which we have demonstrated for the t-DMRG algorithm, holds in general for renormalization algorithms also in higher dimensions [183].

As universality means that the specific form of the Hamiltonian is not relevant but only its global symmetry properties matter, we stress again that our results obtained via the Bose-Hubbard system can be directly carried over to generic many-body quantum systems even in more than one dimension [74, 128]. Another example from atomic physics is provided by the three body Coulomb problem of the helium atom. The accurate dynamical simulation of the latter remains a challenge even for modern computational physics [128], for the very same spectral reasons as identified here.

---

[8]An exact formula for the distribution of Schmidt eigenvalues for the so-called fixed-trace ensemble, a random matrix theory model for compound quantum systems, has been derived in Ref. [120].

5 Robust states in the chaotic regime

In the preceding chapters we repeatedly witnessed that the inter-atomic interaction can induce complex behavior in the Bose-Hubbard system, reflected in chaotic level dynamics. One important consequence for the experiment is that the resulting, sensitive dependence of the system on its control parameters renders the quantum dynamics essentially uncontrollable. However, it is also known that, in a regime of globally chaotic level dynamics, quantum mechanical systems can feature robust structures, opening new perspectives for robust control [27, 35].

Here we will identify such robust structures that persist in the chaotic regime of the tilted Bose-Hubbard Hamiltonian and find that their robustness is *induced* by the nonlinearity. The associated eigenstates exhibit strong localization properties on the lattice [182] and are dynamically stable against external perturbations [181].

5.1 Identification of robust structures

We now detect these robust structures by direct investigation of the parametric level evolution of the Bose-Hubbard Hamiltonian under changes of the applied tilt. Subsequently, we discuss their characteristic properties and explain the underlying mechanism responsible for their generation [182].

5.1.1 Parametric level evolution

In Chapter 3 we have found that the parametric level evolution of the tilted Bose-Hubbard Hamiltonian $\hat{H}$, Eq. (2.26), sensitively depends on the system parameters. Specifically, for comparable onsite interaction and tunneling coupling, $U = J$, the energy levels undergo numerous avoided crossing of different size under variation of the static field. This behavior can nicely be seen in Fig. 5.1, where we consider a system that consists of three bosons in eleven lattice sites. As already observed in Sec. 3.2.2, there are several regular structures in the spectrum, represented by almost perfect straight lines that traverse the irregular bulk. As opposed to the majority of levels from the bulk, which couple strongly, these regular structures undergo only very tiny avoided crossings and in particular do not change their slope under variations of the tilt F. In analogy to solitonic water waves that keep their
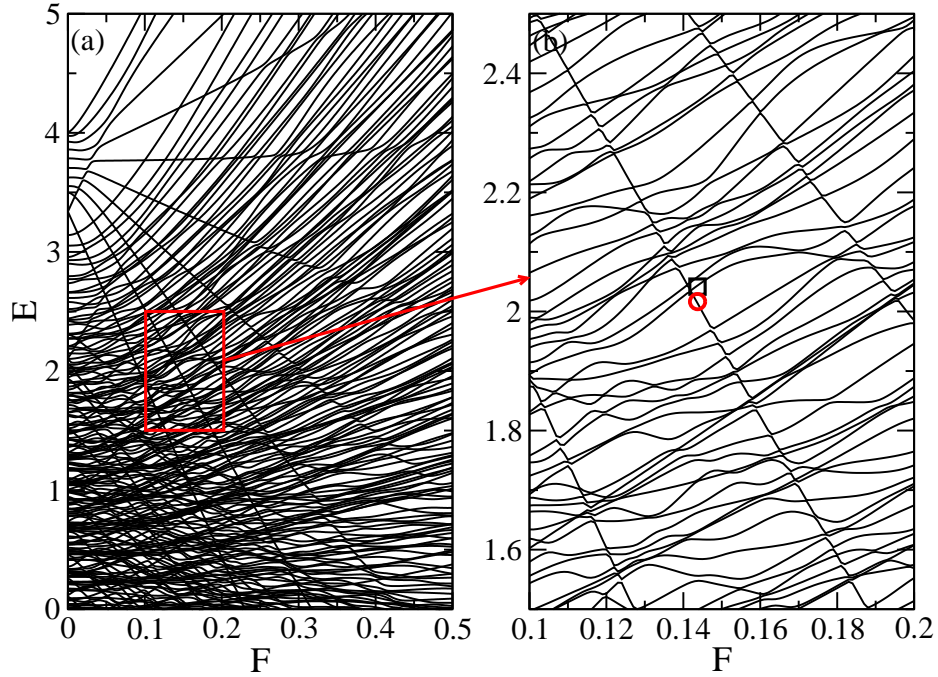
Figure 5.1: Parametric level evolution of the tilted Bose-Hubbard Hamiltonian $\hat{H}$, Eq. (2.26). Shown is the energy spectrum as a function of the tilt F for $n = 3$ bosons on $L = 11$ lattice sites for fixed onsite interaction and tunneling coupling $U = J = 1$. In (b) a magnification of the region that is marked in (a) is shown. The red circle and the black square depict the single solitonic and the single irregular state which are investigated in more detail in Fig. 5.3.

shape when running through other waves [156], we call the states corresponding to the regular structures *solitonic states*. They should however not be considered as propagating in real space, they rather propagate through the chaotic bulk of the spectrum evolving with a fictitious time given by the tilting strength F [202].

Since the system under consideration has a relatively small filling factor $n/L = 3/11$ which was not studied in detail in Sec. 3.3, we verify that it exhibits a parameter range of chaotic level structure in Fig. 5.2. We find that for $F \lesssim 0.6$, the spectrum features universal Wigner-Dyson statistics[1], *i.e.*, the solitonic states indeed emerge within the Hamiltonian's chaotic regime.

---

[1] For $F \to 0$ the system is symmetric under reflections around the central lattice site, and thus its nearest-neighbor level-spacing distribution is not given by GOE statistics in this limit, see also discussion at the end of Sec. 3.2.2.
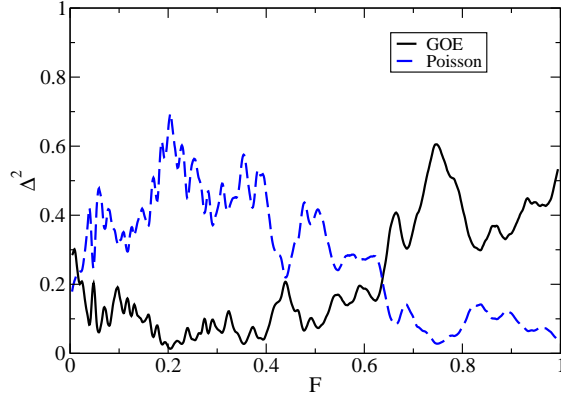
Figure 5.2: Deviation Δ^2, Eq. (3.19), of the numerically obtained nearest-neighbor level-spacing distribution from GOE and Poissonian statistics, as a function of the static field strength F. The system is chosen as in Fig. 5.1.

5.1.2 Characteristics of the solitonic eigenstates

Similar to the behavior of all energy levels in the case of vanishing coupling $J = 0$, see Fig. 3.6 (a), the energies of the solitonic states have a constant slope over a wide range of the tilt. This, according to the Hellmann-Feynman theorem [68]

$$\frac{\partial E}{\partial F} = \left\langle \frac{\partial \hat{H}}{\partial F} \right\rangle = \left\langle \sum_{l=1}^{L} \tilde{l}\hat{n}_l \right\rangle, \tag{5.1}$$

defines a constant center of mass of the many-particle wave function. Here $\langle \cdot \rangle$ represents the expectation value with respect to a single solitonic state. Consequently, we expect these states to show characteristic localization properties of the particles on the lattice, that are invariant under changes of the tilt, as we elaborate in the following.

Since the behavior of the solitonic states resembles the Hamiltonian's eigenstates for $J = 0$, we now consider the representation of the solitonic states in the Wannier-Fock basis. The modulus squared $|c_i|^2$ of the associated expansion coefficients of one such state (red), and of a typical chaotic state (black) is shown in Fig. 5.3 (a) for the same system parameters as before, and for an exemplary value of the tilt, $F \approx 0.145$. Both states are also highlighted in the spectrum in Fig. 5.1 (b). The dimension of the Hilbert space is $\mathcal{N} = 286$, and while in the chaotic case many Fock basis states contribute, in the solitonic case only few coefficients are nonzero. Here the maximal weight is given by $|c_i|^2 \approx 0.6$. It corresponds to the state where all particles are located on the single lattice site $l = 2$, *i.e.*, the Fock state $|0, 3, 0, ...\rangle$. The next two coefficients, that are already significantly smaller and have the values $|c_i|^2 \approx 0.1$ and $|c_i|^2 \approx 0.075$, belong to the states $|1, 2, 0, ...\rangle$ and $|0, 2, 1, 0, ...\rangle$, respectively. That is, the other non-vanishing coefficients belong to Fock states with a similar center of mass, while Fock states with a markedly different center of mass are not occupied. Given the above, we conjecture the solitonic states to be highly localized, both in the Fock basis and on the lattice itself. In particular, we also expect to find as many solitonic states as lattice
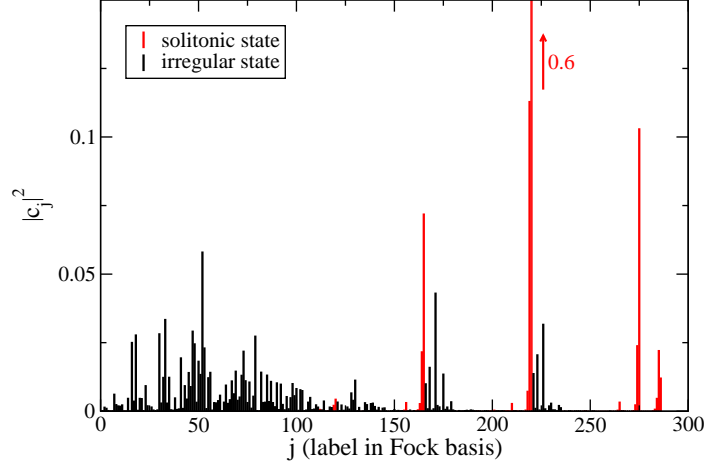
Figure 5.3: Weights $|c_i|^2$ of two eigenstates of the Hamiltonian $\hat{H}$, Eq. (2.26), in the Fock basis, at $F \approx 0.145$, for the same system parameters as in Fig. 5.1, and Hilbert-space dimension $\mathcal{N} = 286$. Shown are a solitonic state (red) and a nearby state from the chaotic bulk of the spectrum (black). Both states are also marked in the spectrum in Fig. 5.1 (b).

sites L, *i.e.*, eleven solitons in the present system.

The localization of a state $|\psi\rangle$ in a given basis $\{|b_j\rangle\}$ can be measured by the *inverse participation ratio* (IPR), see, *e.g.*, Ref. [85],

$$\text{IPR}(|\psi\rangle) = \sum_{j=1}^{\mathcal{N}} |c_j|^4 \, , \tag{5.2}$$

where $\mathcal{N}$ is again the Hilbert-space dimension and the c_j are the expansion coefficients of the state, such that $|\psi\rangle = \sum_{j=1}^{\mathcal{N}} c_j |b_j\rangle$. The IPR represents the inverse number of basis states occupied by the state $|\psi\rangle$ and thus takes the limiting values one, for a basis state, and $1/\mathcal{N}$, for superpositions of all basis states with equal weight. From Fig. 5.4, where the $L = 11$ states with the largest individual IPR in the Wannier-Fock basis are plotted in red, on top of the energy spectrum, we find that the solitonic states are indeed localized in the Fock basis.

For a quantitative comparison, the average IPRs of all solitonic and of the remaining non-solitonic states are shown in Fig. 5.5. The latter changes only little with the static field strength and features a slight increase with growing F. This is due to the onset of Stark localization, where the eigenstates are given by Fock basis states and which is expected for large tilts [28, 75]. In the case of the solitonic states, the behavior is dramatically different: For $F \lesssim 0.12$, there is an increase of the average IPR, followed by a plateau for $0.12 \lesssim F \lesssim 0.27$, and a subsequent decrease for $F \gtrsim 0.27$. Comparison with Fig. 5.4 reveals that the plateau region is identical to the region where the straight lines exist within
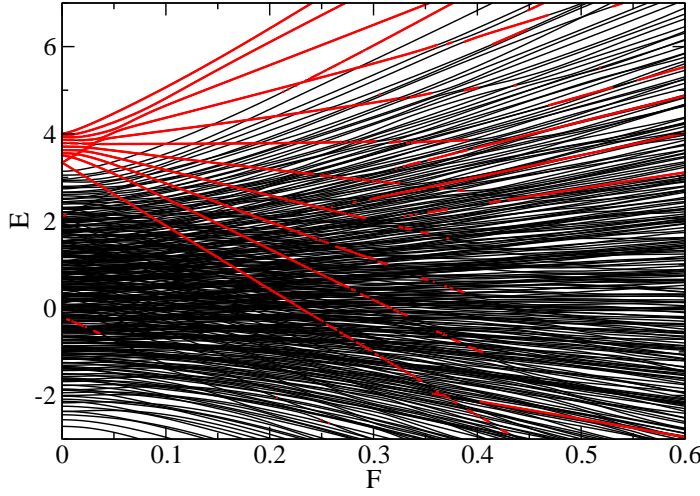
Figure 5.4: Spectrum of the Hamiltonian $\hat{H}$, Eq. (2.26), as a function of F, for the same system parameters as in Fig. 5.1 (b). The $L = 11$ eigenstates with the largest IPR, Eq. (5.2), in the Wannier-Fock basis are plotted in red.

the irregular bulk. For $F \lesssim 0.12$, their energies lie above the energies of the remaining states, and for $F \gtrsim 0.27$ they start to dissolve again. For an even stronger tilt $F \gtrsim 0.45$, the average IPR features a slight increase with growing F. Whereas this latter behavior is again compatible with Stark localization, the behavior for $F \lesssim 0.45$ can not be explained with the expected formation of well-localized Wannier-Stark states for growing F. As compared to the non-solitonic states, the average IPR is enhanced by about an order of magnitude, and thus manifests the pronounced localization of the solitons in the Fock basis.

Note that the fluctuations of the average IPR of the solitonic states in Fig. 5.5 can be attributed to the influence of the (small) avoided crossings that locally affect the levels. Due to the limited number $L = 11$ of solitonic levels, they are not washed out by the averaging. In the case of the non-solitonic states the average is taken over significantly more states, and the IPR is therefore a smooth function of F.

For a quantification of the localization of the states on the lattice, we use the average maximal population (AMP) on a single site:

$$\text{AMP} = \left\langle \frac{\max_l \langle \psi | \hat{n}_l | \psi \rangle}{n} \right\rangle. \tag{5.3}$$

Here, $|\psi\rangle$ is an eigenstate of the Hamiltonian $\hat{H}$, Eq. (2.26), and the average $\langle \cdot \rangle$ is again taken over all the solitonic and the remaining non-solitonic states, respectively. The maximum of the populations on the L individual sites of the lattice, for each basis state, is denoted by $\max_l \langle \psi | \hat{n}_l | \psi \rangle$. If all particles are located on one and the same lattice site, the
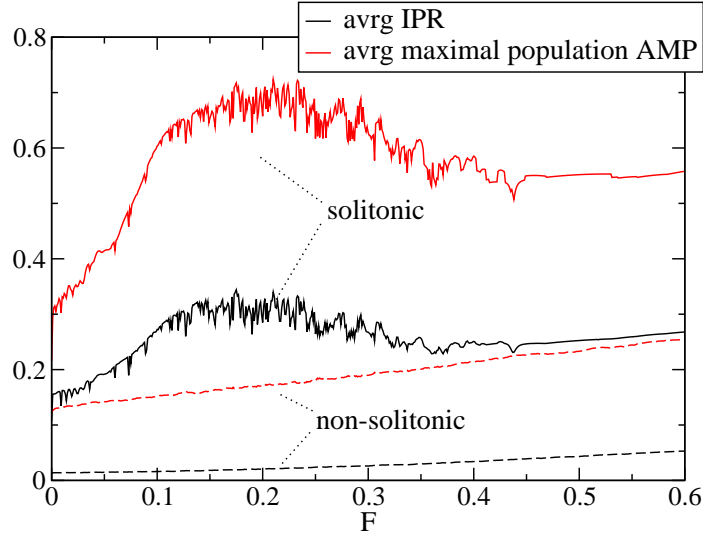
Figure 5.5: Averaged IPR in the Fock basis (black), Eq. (5.2), and AMP (red), Eq. (5.3), of the eigenstates of the Bose-Hubbard Hamiltonian $\hat{H}$, Eq. (2.26), as a function of the tilt F. Shown are the data for the $L = 11$ eigenstates with the largest individual IPR (solid lines), as well as the average over all other eigenstates (dashed lines). The system parameters are chosen as in Fig. 5.1 (b).

AMP takes its maximal value one, since we normalize with respect to the boson number n. In contrast, if the bosons are equally distributed on the lattice, the AMP is given by $1/L$, which, for the system considered here, equals approximately 0.09.

As evident from Fig. 5.5, which shows the AMP for both sets of states, in the case of the solitonic states, typically more than 60% of the atoms are located on a single lattice site.[2] Moreover, the regime where the solitonic states show an enhanced AMP exactly coincides with the regime of an enhanced average IPR. This behavior renders them very different from the non-solitonic states which do not feature the same particle clustering. Here, the particles are distributed over the lattice, and for $F \to 0$ the AMP is close to its minimum value. Note that the onset of Stark localization is again reflected in a slight increase of the curve for increasing F.

In conclusion, we find that the $L = 11$ solitonic states are indeed highly localized, both, in the Fock basis and on the lattice itself. Whereas the localization in the Fock basis alone does not allow for an immediate physical interpretation, the localization on the lattice has a clear physical meaning: The solitonic states are well localized on a specific site of the lattice, and hardly change their location under variations of the tilt. This defines a clear

---

[2]The fluctuations of the AMP of the solitonic states are again due to the small sample of states averaged over.
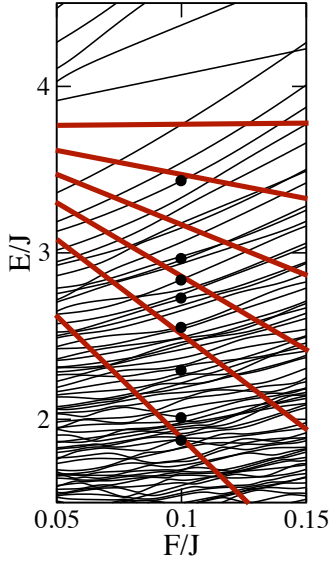
Figure 5.6: Magnification of the spectrum for $n = 3$, $L = 11$ and $U = J = 1$ as in Fig. 5.1. The energy levels belonging to the solitonic and irregular initial states $|\psi_0\rangle$, that are considered in the dynamics, are marked with red lines and black dots, respectively.

experimental signature and also helps to understand the underlying physical mechanism for their existence and robustness [182] which will be discussed Sec. 5.3.

5.2 Dynamical stability under driving

The small coupling between solitonic and irregular states, reflected by solely tiny avoided crossings between them, induces an enhanced stability under perturbations, as we will now evidence by exposing the system to a time-dependent tilt [181]. More precisely, we consider linear driving of the form

$$F(t) = F_i + Rt \tag{5.4}$$

from an initial value $F(0) = F_i$ of the tilt to a final value $F(\Delta t) = F_f$, with variable rates

$$R = \frac{F_f - F_i}{\Delta t}. \tag{5.5}$$

We consider the dynamics of both, a set of solitonic and irregular initial states $|\psi_0\rangle$, that lie in the same energy range within the bulk of the spectrum, as shown in Fig. 5.6. The stability of the two kinds of states is then characterized in terms of the average IPR, Eq. (5.2), in two different bases. That is, we consider the initial (fixed) eigenbasis, see Figs. 5.7 (a) and (c), and the instantaneous eigenbasis, *i.e.*, the Hamiltonian's time-dependent eigenbasis that follows the evolution of the static field $F(t)$, see Fig. 5.7 (b). For the initial and final values of the tilt we chose $F_i = 0.1$ and $F_f = 0.4$, thus not driving the system beyond the interval where the solitonic states exist.

When considering the IPR in the fixed eigenbasis at F_i, see Fig. 5.7 (a), we find that a large rate $R = 1$ basically corresponds to the diabatic regime, where the system cannot adapt to the modified conditions, on the timescale of the driving. Hence, the IPR does almost not change, and remains close to unity. Consequently, also a difference between solitonic and irregular initial states can hardly be observed. For smaller rates $R = 0.1$ and 0.01, the average IPR decreases for both sets of initial states. However, in the case of the solitonic states, the drop is one order of magnitude less than in the case of the irregular states. Since the IPR in the initial (fixed) basis gives a measure of how far a given state is driven away from its initial form, we find that the solitonic states are much more stable under dynamical changes of the static field.

A complementary information can be obtained from the IPR in the instantaneous basis, which measures how close, at each instance of time, the time-evolved state $|\psi(t)\rangle = \hat{U}(t)|\psi_0\rangle$ is to a system eigenstate. Here, $\hat{U}(t)$ is the time-evolution operator. That is, if there was no coupling, *i.e.*, no avoided crossings, between the system eigenstates under changes of the parameter F (as fulfilled for $J = 0$, see Fig. 3.6 (a)), the IPR would exhibit the constant value unity. Since this is not the case here, for both kinds of states a broadening of the initial preparation due to transitions to other states occurs, as can be seen in Fig. 5.7 (b). Nevertheless, there is again a striking difference between the two sets of initial states: The IPR of the irregular states decays rapidly, reflecting the sensitive dependence of the system eigenstates on any parameter, in this case the tilt F, in the chaotic regime. In contrast, the solitonic states' IPR is significantly more stable, since the levels undergo only tiny avoided crossings with other states.[3] Moreover, we find that the decay of the IPR in the instantaneous eigenbasis, as opposed to the decay of the IPR in the initial eigenbasis, is essentially independent of the rate R.

It is possible to find such scaling also in the case of the fixed basis at F_i. For short times, the inverse participation ratio

$$\text{IPR}(|\psi(t)\rangle) = \sum_{j=1}^{\mathcal{N}} |\langle \psi_j | \hat{U}(t) | \psi_0 \rangle|^4, \tag{5.6}$$

is essentially determined by the survival probability

$$P(t) = |\langle \psi_0 | \hat{U}(t) | \psi_0 \rangle|^2, \tag{5.7}$$

since, for $j \neq 0$, we have $|\langle \psi_j | \hat{U}(t) | \psi_0 \rangle|^2 \simeq 0$. According to quantum linear response theory

---

[3]Note that whereas the IPR in the initial basis, Fig. 5.7 (a), (c), is a smooth function of F, the IPR in the instantaneous basis, Fig. 5.7 (b), fluctuates rather strongly. This can be attributed to the fact that while the former corresponds to a fixed basis, the latter is evaluated in a basis that depends sensitively on the parameter F.
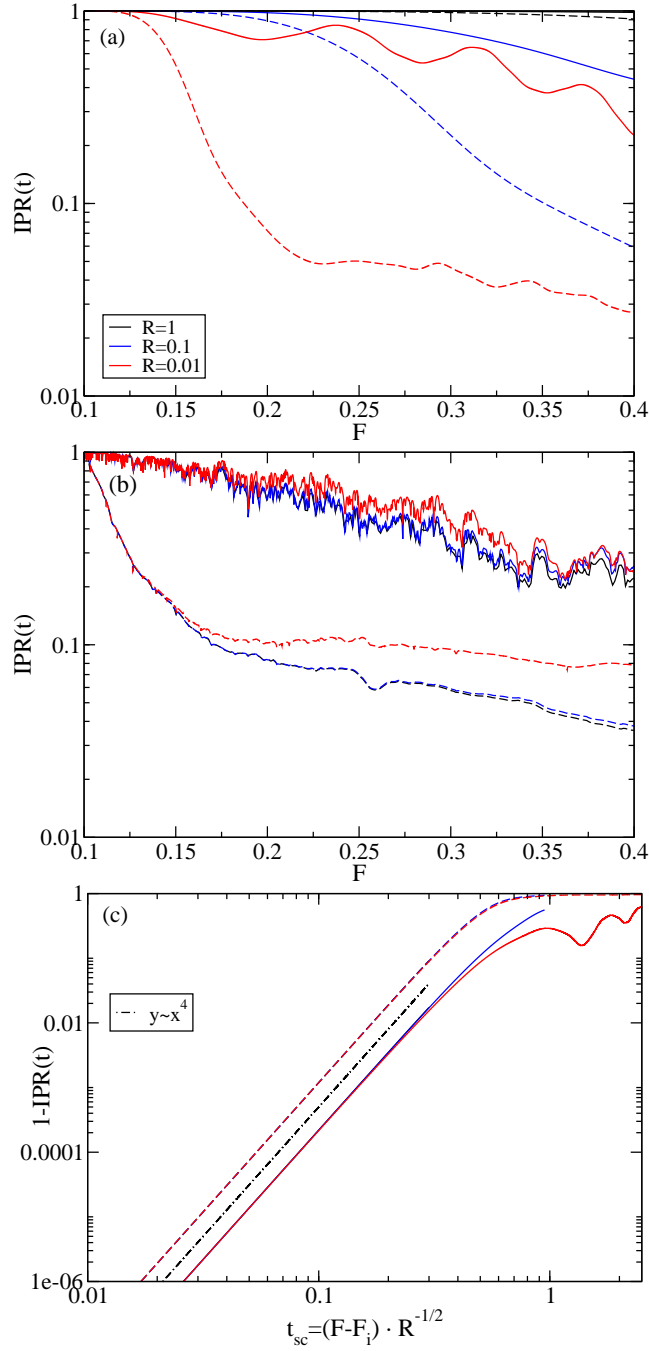
Figure 5.7: Dynamical evolution of the average IPR, Eq. (5.2), as a function of the tilt F, for various rates R, Eq. (5.5). The initial and final values of the tilt are given by $F_i = 0.1$ and $F_f = 0.4$, respectively. The average is taken over a set of solitonic (solid lines) and irregular initial states (dashed lines) that are marked in the spectrum in Fig. 5.6. We monitor the IPR in both, (a) the initial (fixed) eigenbasis and (b) the instantaneous eigenbasis. In the case of the fixed eigenbasis, also $1 - \text{IPR}(t)$ is plotted, versus the scaled time $t_{sc} = t\sqrt{R}$ in panel (c). The dash-dotted line has slope four, and is drawn to guide the eye.

[40], we expect a super-Gaussian decay

$$P(t) \sim \exp[-R^2 t^4] \tag{5.8}$$

for linearly driven chaotic systems. This suggests a scale invariance of $P(t)$ and therefore of the IPR with respect to the scaled time $t_{sc} = t\sqrt{R}$. This can indeed be observed in Fig. 5.7 (c), where the same behavior is found for both sets of initial states. However, the absolute decay is again much smaller for the solitonic states. Furthermore, for a very small driving rate $R = 0.01$, the IPR exhibits oscillations around $t_{sc} = 1$, as also observable in Fig. 5.7 (a). These oscillations are likely to result from the regularity of the integrable part of the spectrum.

5.3 Generating mechanism

In the previous subsection, we numerically confirmed the dynamical stability of the solitonic states, as suggested by their parametric level evolution. In the following, we identify the mechanism responsible for their stability and, furthermore, we discuss the reason for their destruction for increasing values of the tilt F.

In order to understand why the solitonic states, distinguished by the fact that the majority of atoms are located on one lattice site, are eigenstates of the system in the chaotic regime at all, remember the evolution of the parametric level dynamics with increasing tunneling coupling J (Fig. 3.6 of Sec. 3.2.2): For $J = 0$, the system's eigenstates are Wannier-Fock states and there is no coupling between any two levels, as obvious from Figs. 3.6 (a). Increasing J then couples individual levels, leading to avoided crossings between them, see Figs. 3.6 (b), (c) and 5.1. However, the stronger a state is localized on the lattice, the less it is affected by the tunneling term, since its energy is dominated by the contribution from the onsite interaction. In particular, this implies that states where all particles are located on a single lattice site remain basically unaffected for values of J where less localized states are already modified considerably, and thus they remain approximate eigenstates of the Hamiltonian.

The existence of eigenstates of a many-body quantum system with all particles localized close to each other, despite the presence of repulsive interactions U, was experimentally first demonstrated for pairs of atoms [200]. Beyond that, theoretical investigations [101, 148, 192] also revealed the existence of three-body bound states [145, 178, 189]. Such repulsively-bound many-particle states are formed as a consequence of the energy mismatch between onsite interaction and maximal kinetic energy that can be realized in the lowest energy band of the lattice. That is, due to the (strongly) repulsive onsite interaction, the energy of the bound states lies above the rest of the spectrum, *i.e.*, they are energetically isolated.

In contrast, a striking feature of the solitonic states is their appearance in the chaotic regime of the Hamiltonian and the fact that they run through the *irregular bulk* of the spectrum. That is, their energies lie in the same interval as the energies of the chaotic eigenstates, and energetic isolation can be ruled out as a possible generating mechanism. In fact, we do observe that energetically allowed transitions between solitonic eigenstates and states from the chaotic bulk are strongly suppressed. In order to understand this, consider the following: A change of the static field F induces transitions between the eigenstates of the system. The time-independent part of the transition amplitude T_{fi} from some initial state $|\psi_i\rangle$ to some final state $|\psi_f\rangle$, is given by the corresponding matrix element of the center-of-mass operator $\sum_{l=1}^{L} \tilde{l}\hat{n}_l$, which is proportional to the static term in the Hamiltonian (2.26),

$$T_{fi} = \langle\psi_f| \sum_{l=1}^{L} \tilde{l}\hat{n}_l |\psi_i\rangle. \tag{5.9}$$

As shown above, in the case of an irregular eigenstate, the atoms are basically distributed over the entire lattice, whereas a special characteristic of the solitonic states is the localization of the majority of particles on one particular lattice site. Thus, the solitonic eigenstates are "close" to eigenstates of the center-of-mass operator. That is, for $|\psi_i\rangle$ being a solitonic state, we can approximately write $\sum_{l=1}^{L} \tilde{l}\hat{n}_l |\psi_i\rangle \propto |\psi_i\rangle$, while for non-solitonic states this is not the case. As a result, the transition amplitude T_{fi} between a solitonic state and a chaotic state becomes very small since both are system eigenstates. Physically, the transition from a solitonic to an irregular state requires the relocation of essentially all atoms on the lattice. However, both, simultaneous tunneling of several atoms and the movement of a single atom over more than one lattice site, correspond to higher-order-processes in the Bose-Hubbard Hamiltonian and are therefore suppressed for typical lattice configurations. The observed localization of the bosons on individual lattice sites in a solitonic state hence induces a suppression of energetically allowed transitions, leading to solely tiny avoided crossings with states from the chaotic bulk, that leave the solitons' slope essentially unaffected.

Our above discussion illustrates the mechanism responsible for the appearance and robustness of the solitonic states. Let us now discuss the major reason for their destruction with increasing tilt (see Fig. 5.4). Under the assumption that a given solitonic state can be approximated by a Fock state of the form $|\ldots,0,n,0,\ldots\rangle$, it follows that a first-order tunneling process only couples it to the state $|\ldots,0,n-1,1,0,\ldots\rangle$. Quite generally we find that such states are also (to a good approximation) system eigenstates and, since they show similar features as the solitonic states, we refer to them as *solitonic states of second order*. For the case of three particles, such states have also been analyzed in the literature [178]. In the simplest approximation, one can treat the interplay between a solitonic state of first and second order as a two-level system of Fock states. In this approach, the irregular bulk is completely neglected, since transitions are strongly suppressed as explained
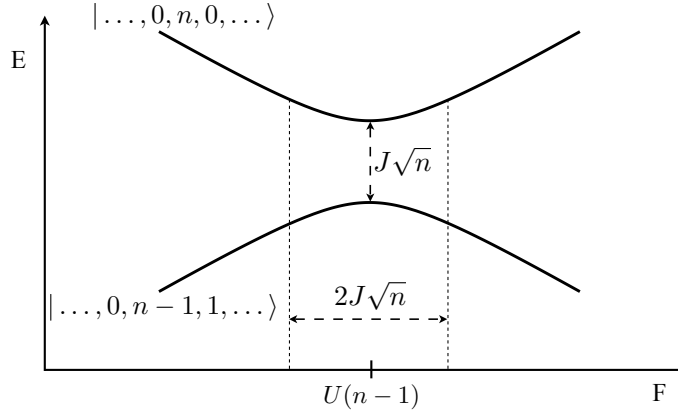
Figure 5.8: Schematic diagram of the avoided crossing between the states $|\ldots,0,n,0,\ldots\rangle$ and $|\ldots,0,n-1,1,0,\ldots\rangle$. For vanishing tunneling coupling $J=0$, the energies would coincide at $F = U(n-1)$. For non-vanishing tunneling coupling, an avoided crossing of width $\Delta F = 2J\sqrt{n}$ emerges.

above. For vanishing tunneling coupling $J = 0$, the energies of the states $|\ldots,0,n,0,\ldots\rangle$ and $|\ldots,0,n-1,1,0,\ldots\rangle$ would coincide only at $F = U(n-1)$.[4] This is however far outside the parameter regime where the solitonic states exist, see Fig. 5.4 and Fig. 5.5. When we take into account the tunneling coupling, an avoided crossing emerges, as depicted schematically in Fig. 5.8. The energy difference between the two states is then

$$\Delta E = \sqrt{(U(n-1)-F)^2 + (J\sqrt{n})^2}\,, \tag{5.10}$$

and, consequently, the avoided crossing has a width $\Delta F = 2J\sqrt{n}$. This affects the stability of the solitonic states for tilts larger than a critical value

$$F_c \simeq U(n-1) - J\sqrt{n}\,, \tag{5.11}$$

what, for the parameter values used here, corresponds to $F_c \simeq 0.27$. From Fig. 5.4 and Fig. 5.5 we see that this is indeed where the solitonic states start to dissolve. We thus conclude that the coupling to solitonic states of second order is the dominant mechanism for the destruction with increasing tilt.

We have verified the existence of solitonic states also for larger particle numbers (see, *e.g.*, Fig. 3.6 (c) and Fig. 3.7 (b) that show the spectrum for $n = 4$ bosons in a lattice of $L = 5$ sites) and even for filling factors $n/L > 1$. Note that the difference in the interaction

---

[4]Note that first-order tunneling in principle also couples the state $|\ldots,0,n,0,\ldots\rangle$ to the state $|\ldots,0,1,n-1,0,\ldots\rangle$, where the energies coincide at $F = -U(n-1)$. However, since we consider a tilting of the lattice around the central lattice site, the spectrum is symmetric and we restrict our analysis to positive values of F.

energy $U(n-1)$ between two solitons of first and second order increases linearly with the total number of bosons and, moreover, also transitions to chaotic states are increasingly suppressed since more and more particles have to undergo tunneling processes in order to transform a solitonic to a chaotic state. Thus, the stability of the solitonic states is expected to be enhanced with increasing particle number. Furthermore, for large boson numbers, one can construct a mean-field phase space for the Bose-Hubbard Hamiltonian, assuming $Un = const.$ (see, *e.g.*, [58, 73, 92, 93]). In this context, the solitonic states should be identifiable with regular islands in the mixed phase space. Semiclassical arguments then guarantee the existence of quantum mechanical eigenstates which are localized within these islands, and which are only weakly coupled to the states living in the chaotic sea [27].

However, three-body interactions, that are not described by the Bose-Hubbard Hamiltonian, can become a non-negligible effect when more and more particles are located on one and the same lattice site. Such three-body collisions may result in the formation of untrapped molecules leading to additional decay channels [50, 122] for solitonic states, which eventually can limit the maximum number of atoms participating in such a state. However, if the effective interaction is kept constant in an experiment, *i.e.*, $Un/(JL) = const.$, this problem can be avoided. Current experiments with $n = 500$ atoms in a double well potential [205] reach effective interactions of $Un/(JL) \approx 3$, which is about an order of magnitude larger than the values we considered above. Thus, the robust structures identified here provide an appealing approach for the experimental preparation of stable quantum many-body states, which typically becomes increasingly challenging with growing particle number.

5.4 Conclusion

In summary, we have identified regular structures within the chaotic regime of the tilted Bose-Hubbard Hamiltonian [181, 182]. Those are characterized by energy levels that feature a simple linear dependence on a system parameter, namely the strength of the tilt, over a sizable interval. The associated eigenstates are termed *solitonic* states and keep their shape under changes of the tilt. They are strongly localized on the lattice and couple only weakly to states from the chaotic bulk. We have found that the stability of the solitonic eigenstates becomes particularly manifest in a dynamical evolution where the lattice is driven non-adiabatically by linearly sweeping the tilt. That is, solitonic eigenstates exhibit very robust localization properties over a wide range of the driving rate and of the tilt. Furthermore, we have shown that neither Stark localization nor energetic isolation [200] can explain the robustness of these states, which is rather due to a subtle interplay of interaction and tunneling dynamics.

The localization on the lattice represents an appealing signature for the soliton's experi-

mental detection in terms of modern microscopy techniques in optical lattices [10]. Thus, the solitonic states are excellent candidates for coherent control, since – in contrast to basically all the non-solitonic states – they are robust under changes of external conditions.

6 Irreversible decay of Bloch oscillations

In Chapter 4 we demonstrated that a chaotic many-particle spectrum implies inefficient numerical simulations of many-body quantum systems. In the present chapter, we focus on the many-particle dynamics itself, instead of its simulability. The experimentally studied phenomena of ultracold atoms in optical lattices include Landau-Zener tunneling between different bands of the periodic potential [46, 94, 102, 106, 137, 174, 204], macroscopic self-trapping of the Bose-Einstein condensate on a single site due to interatomic interactions [8], quench dynamics, where one system parameter, like, *e.g.*, the interaction strength, is suddenly changed [33, 109, 155], and Bloch oscillations [4, 12, 65, 83, 133], which arise under the influence of a static tilt. We choose this latter example (which has been studied in great detail) to investigate how the spectral properties of the system influence the Bloch oscillations and, in turn, what we can infer about the system from the characteristics of the oscillations. More precisely, we want to establish a relation between the spectral statistics of the interacting many-particle system and the decay of the Bloch oscillations.

In the following, we give an introduction to the theory of Bloch oscillations and discuss their experimental realization. Thereafter, the different regimes of oscillations will be investigated in the framework of the tilted Bose-Hubbard Hamiltonian. In Secs. 6.3 and 6.4, we focus on the fast and irreversible decay of the oscillations in the chaotic regime which we will directly relate to the spectral properties of the many-body Hamiltonian.

6.1 Introduction to Bloch oscillations

Bloch oscillations are a genuine quantum phenomenon, that relies on the wave nature of particles. They result from the interplay of a periodic potential and an external static field, and were first described for single particles, in the quantum theory of electrical conductivity in crystal lattices, by Bloch and Zener [16, 203]. In order to appreciate the counter intuitive quantum dynamics of a single particle in a periodic potential, imagine for a moment a classical particle in such a setup, *e.g.*, a table tennis ball in one of the wells of an egg carton [180]. This system constitutes a classical analog to the quantum system we consider in the following. If the device is tilted under the influence of gravitation, the particle will remain in its initial position until a certain critical angle is reached. Thereupon, it will fall out of its well and slide down the potential since it is subject to a constant acceleration due to gravity.
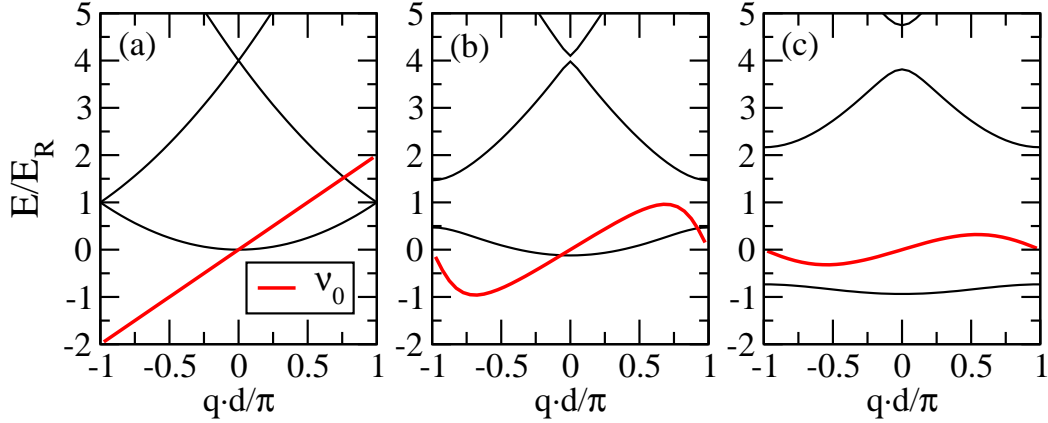
Figure 6.1: Band energies $E_q^{(\eta)}/E_R$ of a 1D periodic potential $V(x) = V_0 \sin^2(k_l x)$ (compare Fig. 2.3), in units of the photopn recoil energy E_R (black lines), and mean velocity v_0, Eq. (6.2), in the fundamental band (thick red lines). Shown is (a) the free particle case $V_0 = 0$, (b) the case of a shallow potential $V_0/E_R = 2$, and (c) the case of a deep potential with $V_0/E_R = 10$.

In the quantum case, the situation is dramatically different: As explained in Sec. 2.2.2, the energy of a single quantum particle that is confined in an (optical) periodic potential of the form $V(x) = V_0 \sin^2(k_l x)$, Eq. (2.6), is determined by the band structure, depicted in Fig. 6.1. In such a setting, both the energies $E_q^{(\eta)}$ and the eigenstates $|\phi_q^{(\eta)}\rangle$ are labeled by the discrete *band index* η and the continuos *quasimomentum* $q \in [-\pi/d, \pi/d]$, where d is the spacing between neighboring sites of the lattice. Due to the periodicity of the spectrum, q can be confined to the first Brillouin zone, and we restrict our analysis to 1D lattices.

Under application of a constant external force $f \geq 0$, a given Bloch state $|\phi_{q(t=0)}^{(\eta)}\rangle$ evolves in time (up to a phase factor) to the state $|\phi_{q(t)}^{(\eta)}\rangle$, where

$$q(t) = q(0) + ft. \tag{6.1}$$

The mean velocity associated with the state $|\phi_q^{(\eta)}\rangle$, is given by [9]

$$v_\eta(q) = \frac{dE_q^{(\eta)}}{dq}. \tag{6.2}$$

Hence, for a nonvanishing potential depth $V_0 \neq 0$, the velocity of a particle that is initially prepared in the state $|\phi_{q(0)}^{(\eta)}\rangle$, oscillates in time, with zero mean[1] (see Fig. 6.1 (b) and (c)).

---

[1]This is only true if the external force f is weak enough not to induce transition to other bands. The corresponding conditions on the system parameters have been discussed in Sec. 2.4, and can readily be satisfied in experiments with ultracold atoms in optical lattices.

This is in striking contrast to the free particle case $V_0 = 0$, where the force induces a constant acceleration and the velocity is a linear function of time, as we illustrate in Fig. 6.1 (a).[2]

As pointed out above, the spectrum is periodic and thus it is sufficient to consider the quasimomentum within the first Brillouin zone. Consequently, it flips from $q = \pi/d$ to $q = -\pi/d$ when the right zone edge is reached and the dynamics induced by an external force F is periodic in time, where the periodicity is given by the Bloch period[3]

$$T_B = \frac{2\pi}{F} \,. \tag{6.3}$$

Here we again set $F = fd$ (compare Sec. 2.4). As a consequence of the velocity's oscillatory behavior around zero mean, also oscillations in real space occur. Hence, in the single-particle case, which we consider in this introductory section, not net current along a perfect lattice can be induced by applying a static field. The extent of the oscillations on the lattice is given by Δ_η/F, where Δ_η is the energy width of the band under consideration, *i.e.*, the stronger the static field, the smaller the oscillations in real space [87]. At first sight surprising, this behavior can qualitatively be understood from the fact that the time spent to traverse the first Brillouin zone is given by the Bloch period T_B. As a consequence, for strong fields, the particle has less time to travel along the lattice in one direction before the velocity changes its sign and the particle returns. Thus, the amplitude of the oscillations in real space is reduced.

Bloch oscillations are a single-particle interference phenomenon that relies on the coherence of the wave function. Therefore, scattering between particles or deviations from the potential's perfect periodicity due to impurities can change the situation dramatically: They induce a decoherence in the time-evolution of the wave function, which, in turn, leads to a dephasing of the oscillations. In the present work, we do not treat impurities (disordered systems) but restrict ourselves to the description of interactions between the particles, which already lead to a plethora of different dynamical regimes as we will see in Sec. 6.2.

In principle, the easiest way to realize a periodic potential plus an additional static field in a quantum system, is to apply an electric field gradient along a crystal. However, since in such systems the typical electron-phonon scattering time is much shorter than the Bloch period, Bloch oscillations could never be observed in natural crystals. Due to the rapid decoherence of the wave function, in such systems, the static field rather induces a directed

---

[2]Note that for $V_0 = 0$, the energy of the particle is given by the energy-momentum parabola of the free particle and no periodic band structure emerges. Consequently, the (real) momentum cannot be restricted to the first Brillouin zone. In Fig. 6.1 (a) we, however, choose this depiction in order to highlight the difference to the case of a particle trapped inside a periodic potential with $V_0 \neq 0$.

[3]The Bloch period has already been introduced in Sec. 2.4.1 where we found that it describes the periodicity of the transformed, time-dependent Bose-Hubbard Hamiltonian with periodic boundary conditions $\hat{H}_p(t)$, Eq. (2.34).

current along the lattice [9], as used habitually in everyday life when the application of a voltage to a metal leads to an electric current. Nevertheless, Bloch oscillations were by now observed in a variety of systems, ranging from semiconductor superlattices [123, 131, 188, 190], where the larger spatial period leads to much shorter Bloch periods (see Eq. (6.3)), to Bloch oscillations of photons in temperature-tuned waveguide arrays [55, 142, 143, 176] and acoustic waves in layered and elastic structures [84, 161].

Another possibility to experimentally realize Bloch oscillations are engineered, clean systems like ultracold bosons in tilted optical lattices. Here, deviations from the perfect periodicity are virtually negligible and various experiments were performed, see for example [4, 12, 46, 133, 137]. Since in such systems all the parameters can be tuned very sensitively[4] (see Sec. 2.3.1), also the role of interactions was investigated, see for example [65, 67, 83]. Moreover, also Bloch oscillations of ultracold fermions in optical lattices, where an admixture of bosons causes a decay of the formerly perfect oscillations, and leads to directed transport along the lattice, were studied [140]. In such systems, the separation of timescales between the bosonic and the fermionic degrees of freedom allows to treat the bosons as a bath and, consequently, a master equation for the fermionic density matrix can be derived [151].

6.1.1 Experimental realization with ultracold bosons in optical lattices

A detailed experimental investigation of Bloch oscillations of ultracold bosons in optical lattices was performed by Gustavsson *et al.* in 2008 [65, 83]. In this work, a Bose-Einstein condensate of Cesium atoms was adiabatically loaded in the lowest band of a vertical optical lattice, where a vertical magnetic field gradient that causes an upward force, so-called magnetic levitation [191], was used to support the condensate against gravity. In addition, a bias magnetic field could be tuned in order to control the interaction strength between the atoms by means of a Feshbach resonance [96, 122]. After switching off the magnetic levitation field, the atoms were let to evolve in the lattice under the influence of gravitation, for variable holding times. Finally, the confinement was turned off, in order to determine the momentum distribution by a time-of-flight measurement, see for example Ref. [18].

Fig. 6.2 shows the measured momentum distribution of the condensate within different Bloch cycles, for minimal interactions between the atoms. In each panel (a)-(d), the distribution traverses the first Brillouin zone once. Initially, it features narrow peaks (a), that get broadened as time elapses, (b)-(d). However, the precise control of the interatomic interactions allowed to realize $U \approx 0$ and, consequently, the dephasing of the oscillations,

---

[4]This also includes the degree of disorder in the system, which we do not consider in the present work.
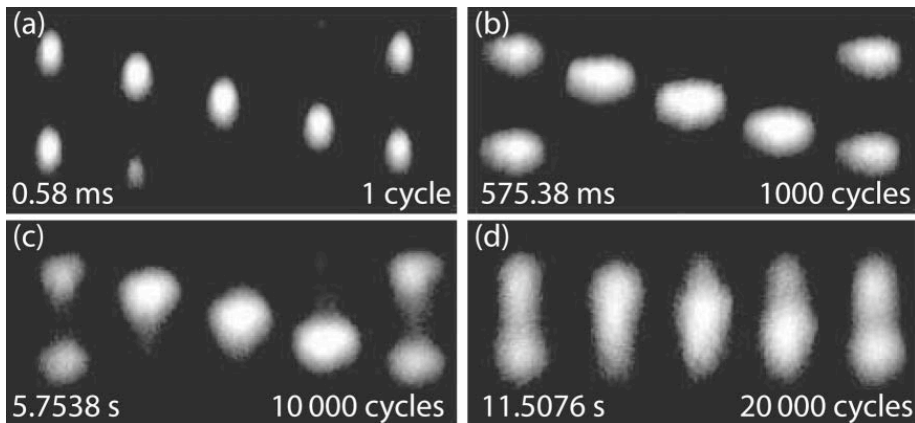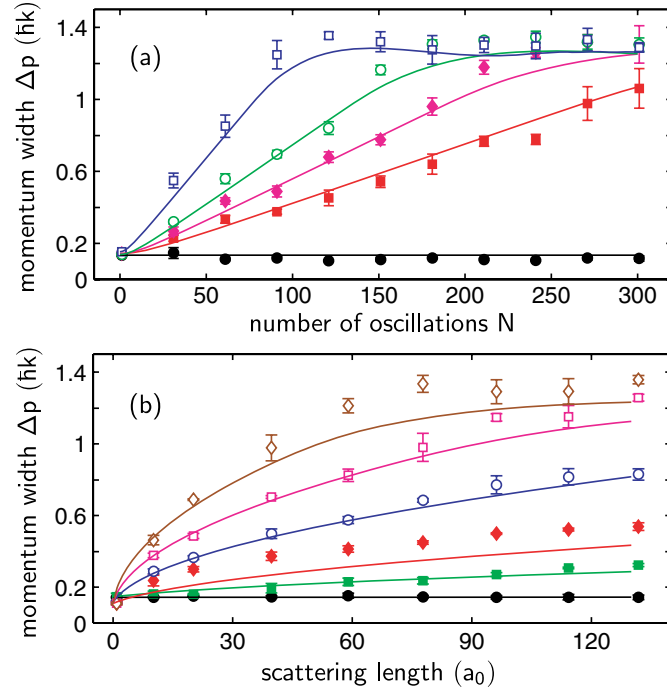
Figure 6.2: Bloch oscillations of a Bose-Einstein condensate of Cesium atoms with minimal inter-actions, in a vertical optical lattice under the influence of gravitation, taken from [83]. Each panel shows the time evolution of the condensate's momentum distribution within one Bloch cycle, where the different columns within the panels correspond to pictures taken after different holding times. Displayed are (a) the first, (b) the 1000th, (c) the 10 000th, and (d) the 20 000th Bloch cycle.

measured by the width of the momentum distribution Δp, was strongly suppressed. This allowed to follow more than 20 000 cycles.

In a second step, the influence of the interaction strength on the dephasing of the oscil-lations was investigated. Fig. 6.3 (a) shows Δp as a function of the number of completed Bloch oscillations, for different values of the interaction strength, controlled by the scatter-ing length a_s, while Fig. 6.3 (b) depicts Δp versus a_s for different evolution times. Both figures immediately reveal that the strength of the interactions is directly reflected in the broadening of the momentum distribution, *i.e.*, stronger interactions lead to more rapid de-phasing.

In the experiment discussed above, a condensate of about $n \approx 5 \times 10^4$ atoms was loaded into $L = 40$ to 65 lattice sites, depending on the initial vertical extent of the atomic cloud. Thus, the average filling factor was of the order $n/L \approx 10^3$. For such high values of n/L, one can expect mean-field[5] calculations to reproduce the experimental observations. Indeed, nu-merical calculations solving the one-dimensional Gross-Pitaevskii equation in the presence of an optical lattice [166], that are depicted by solid lines in Fig. 6.3, show nice agreement with the experimental data. In our study, we are interested in the quantum regime, *i.e.*, systems with few bosons and filling factors of approximately one, where few-particle ef-fects are important. Consequently, the experimental findings of Ref. [83] can only provide a first impression of the different regimes of Bloch oscillations of ultracold atoms in optical

---

[5]For a short introduction to the mean-field approach see Sec. 2.5.

Figure 6.3: Dephasing of the Bloch oscillations of a Bose-Einstein condensate of Cesium atoms (compare Fig. 6.2), measured by the width of the momentum distribution Δp, taken from [83]. In panel (a), Δp is plotted against the number N of Bloch cycles, for different interaction strengths, given by the scattering length a_s, in units of the Bohr radius a_0 ($a_s/a_0 = 0, 25, 50, 100$ and 300 from bottom to top). Panel (b) shows Δp as a function of the scattering length a_s, in units of a_0, for a fixed number of Bloch cycles ($N = 1, 25, 50, 100, 150$ and 200 from bottom to top). Solid lines represent mean-field calculations obtained from the discrete Gross-Pitaevskii equation.

lattices. In general, however, we cannot expect them to agree with results within the Bose-Hubbard model, which we want to use to infer knowledge on the statistical properties of the spectrum.

6.2 Regimes of Bloch oscillations in the tilted Bose-Hubbard Hamiltonian

In order to characterize Bloch oscillations in the tilted Bose-Hubbard Hamiltonian, we have to utilize suitable observables in real space and in momentum space. In analogy with the

experiment, we analyze, on the one hand, the center of mass of the bosons on the lattice

$$x(t) = \frac{1}{n} \langle \psi(t) | \sum_{l=1}^{L} \tilde{l} \, \hat{n}_l | \psi(t) \rangle, \tag{6.4}$$

which, according to the definition of the tilted Bose-Hubbard Hamiltonian in Sec. 2.4, can take the values $x \in [-L/2, L/2 - 1]$ for even L, and $x \in [-(L-1)/2, (L-1)/2]$ for odd L. On the other hand, we study the mean velocity

$$v(t) = \frac{1}{n} \frac{d}{dq} \langle \psi(t) | \hat{H} | \psi(t) \rangle, \tag{6.5}$$

which lies within the interval $[-J, J]$. Here $|\psi(t)\rangle$ is the many-body wave function and, due to its many-body character as opposed to the single-particle case of Eq. (6.2), we have to normalize with the particle number n. Instead of (6.5) we can also write

$$v(t) = \frac{1}{n} \langle \psi(t) | \hat{V} | \psi(t) \rangle, \tag{6.6}$$

where the velocity operator[6] is given by

$$\hat{V} = \frac{d}{dq} \hat{H}. \tag{6.7}$$

In the case of the linear lattice with Dirichlet boundary conditions, *i.e.*, when considering the Hamiltonian $\hat{H}$, Eq. (2.26), this leads to

$$\hat{V} = \frac{J}{2i} \sum_{l=1}^{L-1} (\hat{a}_{l+1}^\dagger \hat{a}_l - h.c.), \tag{6.8}$$

while in the case of periodic boundary conditions, *i.e.*, when considering the Hamiltonian $\hat{\tilde{H}}_p(t)$, Eq. (2.34), one obtains

$$\hat{V} = \hat{V}(t) = \frac{J}{2i} \sum_{l=1}^{L} (\hat{a}_{l+1}^\dagger \hat{a}_l \, e^{iFt} - h.c.). \tag{6.9}$$

Note that in complete analogy to the definitions of the Hamiltonians $\hat{H}$ and $\hat{\tilde{H}}_p(t)$, expression (6.8) contains one less term than expression (6.9) since the sum only runs up to $L - 1$ instead of L (see also discussion on p. 15).

---

[6]Expression (6.7) for the velocity operator can straight forwardly be evaluated when considering the Hamiltonian in momentum representation. The latter is obtained with the help of the transformations $\hat{a}_l^\dagger = 1/\sqrt{L} \sum_{j=1}^{L} e^{-i\kappa_j l} \hat{a}_{\kappa_j}^\dagger$, where $\kappa_j = 2\pi \cdot (j-1)/L$ (compare Sec. 2.4.1.1), see, *e.g.*, [150].

As in the experiment [83], we consider as initial states the ground state of the untilted Bose-Hubbard Hamiltonian ($F = 0$), for various values of the onsite interaction U and, without loss of generality, for fixed tunneling coupling $J = 1$. We then monitor the dynamics that arise after the lattice is suddenly tilted to a constant field strength F.

In the present section, we will give an overview on the plethora of dynamical behaviors that arise in the different parameter regimes, and also discuss once again the role of periodic or Dirichlet boundary conditions. We start with the non-interacting case $U = 0$, before we turn to interacting bosons, that define the scope of the subsequent analysis. If not stated otherwise, the data are obtained for a system composed of $n = 7$ bosons on $L = 7$ lattice sites.

6.2.1 Noninteracting bosons

In the noninteracting case $U = 0$, we effectively have to deal with a single-particle situation which makes this regime especially suited to work out the influence of the applied boundary conditions on the dynamical quantities. In Fig. 6.4 we plot the velocity $v(t)$ (upper row) and the center of mass $x(t)$ (lower row), where time is given in units of the Bloch period $T_B = 2\pi/F$, for periodic (blue dashed lines) and Dirichlet boundary conditions (solid black lines), and different values of the static field strength $F = 0.1, 1$, and 10.

For periodic boundary conditions, we observe perfect Bloch oscillations of the velocity $v(t)$, in excellent agreement with experimental findings, see for example [65, 83]. As expected from Eqs. (6.1) and (6.2), we find that the tilt F only changes the velocity with which the the Brillouin zone is traversed. Hence, upon rescaling time with the Bloch period, the dynamics is independent of the static field strength, since the oscillations are now identical in all three cases. It may come as a surprise that the corresponding center of mass $x(t)$ equals zero for all times. This behavior is a result of the initial state we consider here: The ground state of the untilted Hamiltonian has vanishing quasimomentum[7] $\kappa = 0$ and is completely delocalized over the lattice. As a consequence, its center of mass vanishes, $x(t = 0) = 0$. A localization in real space, which is the prerequisite for oscillations of the center of mass, requires a superposition of states with different values of quasimomentum. As discussed in Sec. 2.4.1.1, the tilted Hamiltonian $\hat{\tilde{H}}_p(t)$, Eq. (2.34), does not couple blocks of different quasimomenta and hence no oscillations in real space can occur. This argument holds irrespective of the interaction strength U, and thus there will be no oscillations of the center of mass $x(t)$, also when $U \neq 0$. Nevertheless, the temporal behavior of the velocity $v(t)$ can be studied, and we will not further comment on $x(t)$.

While, for periodic boundary conditions, the lattice is effectively infinite and boundary

---

[7]As discussed in Sec. 2.4.1.1, we again refer to the discrete quasimomentum that appears in a finite lattice as κ instead of q.
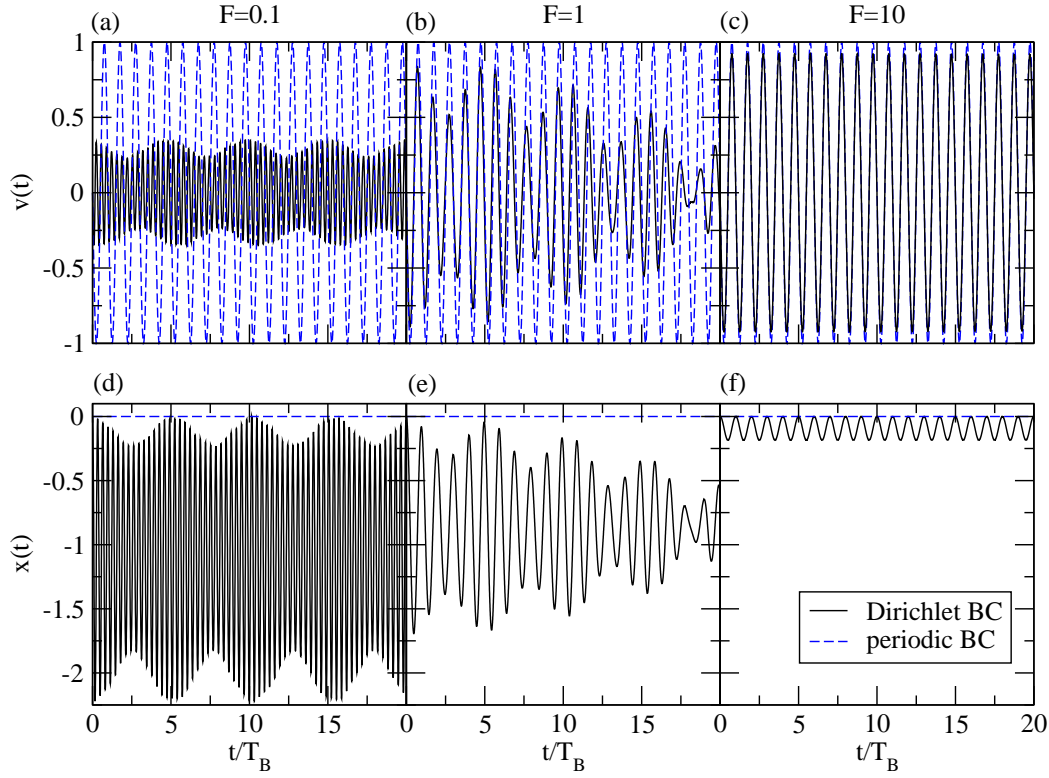
Figure 6.4: Mean velocity $v(t)$, Eq. (6.6), (upper row), and center of mass of the bosons on the lattice $x(t)$, Eq. (6.4), (lower row) as a function of time, in units of the Bloch period t/T_B, for $n = 7$ bosons on $L = 7$ lattice sites, with tunneling coupling $J = 1$. Here, the dynamics of noninteracting bosons, $U = 0$, is shown for different values of the static field strength, $F = 0.1$ (left column), 1 (middle column), 10 (right column), both for Dirichlet boundary conditions (black solid lines) and periodic boundary conditions (blue dashed lines).

effects do not occur, in the case of Dirichlet boundary conditions the finiteness of the lattice can play an important role during time evolution. As a consequence, the behavior of the mean velocity $v(t)$ and of the center of mass $x(t)$ strongly depends on the static field strength F. In order to understand this, recall that the amplitude of the oscillations in real space is proportional to $1/F$. For a large tilt, $F = 10$ (Fig. 6.4 (c) and (f)), the extent of the oscillations $\Delta x_{F=10} \approx 0.185$ is sufficiently small compared to the length of the lattice, that stretches from $x = -3$ to 3 for the lattice with $L = 7$ lattice sites we consider here, and the boundaries are not probed during the dynamics. Consequently, perfect oscillations both in real and momentum space[8] occur. For $F = 1$ ((b) and (e)), we would expect $\Delta x_{F=1} \approx 1.85$ in

---

[8]The reduction of the amplitude of the velocity's oscillations, as compared to the case of periodic boundary conditions, stems from the definition of the velocity operator $\hat{V}$, Eq. (6.8), that contains one term less than
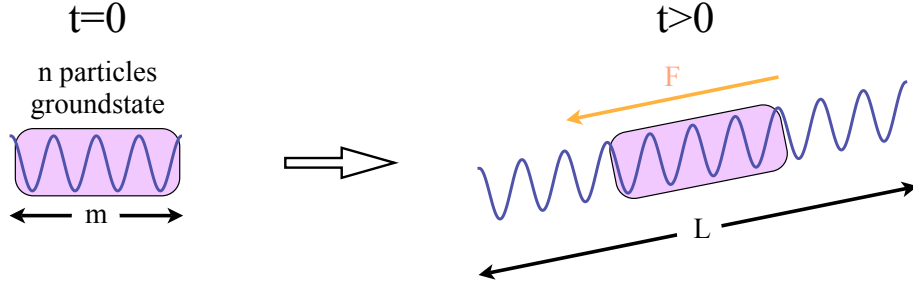
Figure 6.5: Schematic diagram of an initial configuration that avoids finite size effects. At $t = 0$ the ground state of a sublattice with $m < L$ sites is prepared. During the dynamics ($t > 0$), the bosons are then let to evolve within the original (larger) lattice.

an infinite lattice, and therefore the dynamics is considerably modified by boundary effects. For an even smaller tilt, $F = 0.1$ ((a) and (d)), we would expect $\Delta x_{F=0.1} \approx 18.5$ and thus, in the small system we consider here, the oscillations are strongly distorted (note also the different frequency components in the dynamics).

To summarize, we find that, when starting from the ground state of the untilted lattice, perfect Bloch oscillations in the velocity $v(t)$ are obtained for periodic boundary conditions, irrespective[9] of the static field strength F, as expected from theory [16, 203] and experimental results [65, 83]. This behavior directly reflects the regularity of the system's spectral structure for $U = 0$, as discussed in Secs. 3.2 and 3.3. For Dirichlet boundary conditions, perfect Bloch oscillations are only observed for large tilts. Since we will later need to study Bloch oscillations in lattices with Dirichlet boundary conditions for smaller values of the static field F, we have to adjust the number of lattice sites and the shape of the initial state such that the boundaries are not probed during the dynamics. One possibility is to consider as initial state the ground state of a smaller, untilted sublattice with $m < L$ lattice sites, which is then placed into the original lattice before applying the tilt, as depicted schematically in Fig. 6.5. Specifically, we always choose the initial configuration such that the m sites that are occupied at $t = 0$ are shifted upward on the larger, tilted lattice instead of being placed in the middle. This choice guarantees that the atoms, which fulfill Bloch oscillations in downward direction (see Fig. 6.4, lower row), do not reach the boundaries of the lattice during the dynamical evolution. When we want to relate the dynamics to the spectral statistics of the system, we then have to evaluate the *effective spectrum*, *i.e.*, that part of the spectrum that actually contributes to the dynamics. If F is large enough such that

---

the corresponding operator for periodic boundary conditions (6.9).

[9]The maximal magnitude of the static field F we can consider is, however, limited by the single-band approximation, see Sec. 2.4.

the atoms do not spread over the lattice as time evolves, this means that *m* instead of *L* is the physically relevant quantity (compare discussion on p. 58 in Sec. 4.2.2). The approach of Fig. 6.5 also closely resembles the typical experimental setup, where the atoms are initially held in a dipole trap which determines the initial extent of the atomic cloud, and which is turned off at the beginning of the experimental procedure, see, *e.g.*, reference [83].

6.2.2 Interacting bosons

In the case of nonvanishing interactions between the bosons, the situation changes dramatically. Depending on the interaction strength U, there exist different regimes of Bloch oscillations, as we briefly elaborate on in the following. Our primary interest resides in the case of intermediate interaction strengths, where the underlying energy level statistics is chaotic. This regime will be thoroughly discussed in the remainder of this chapter.

6.2.2.1 Weak interactions

For weak interactions, we choose $U = 0.1$, the system is still regular in terms of its level statistics (see Sec. 3.3). However, the Bloch oscillations are already strongly modified as evident from Fig. 6.6. Quite generally, we observe a decay of the oscillations, where the exact behavior depends on the strength of the static field: the larger F, the weaker the decay.

For small and intermediate tilts, $F = 0.1, 1$, the interactions induce a dephasing which, however, does not completely destroy the periodicity of the system's dynamics. For strong tilts, $F \gg J$, a second, interaction-induced time-period T_U appears [112]. It can be derived explicitly by treating the atom-atom interaction as a perturbation, and is given by

$$T_U = \frac{F}{U} \cdot T_B.$$ (6.10)

Consequently, for $F = 10$, $v(t)$ and $x(t)$ (Fig. 6.6 (c) and (f)) are expected to exhibit a beating signal, with periodicity $T_U = 100 \cdot T_B$. Since here we only depict the dynamics up to $t = 20 \cdot T_B$, this additional oscillation is not resolved. Note however, that the observed decay of the oscillations stems exactly from the appearance of the new period T_U, as we have verified by running simulations for longer times.

Analogously to the case of noninteracting bosons, for Dirichlet boundary conditions and $F = 0.1, 1$, the dynamics are again significantly affected by the finiteness of the lattice.

6.2.2.2 Intermediate interactions

For intermediate interactions, we choose $U = 1$, the system is chaotic as long as the tilt is not too strong, *i.e.*, $F < 1.3$ (see Sec. 3.3), and in this regime the dynamical behavior shown
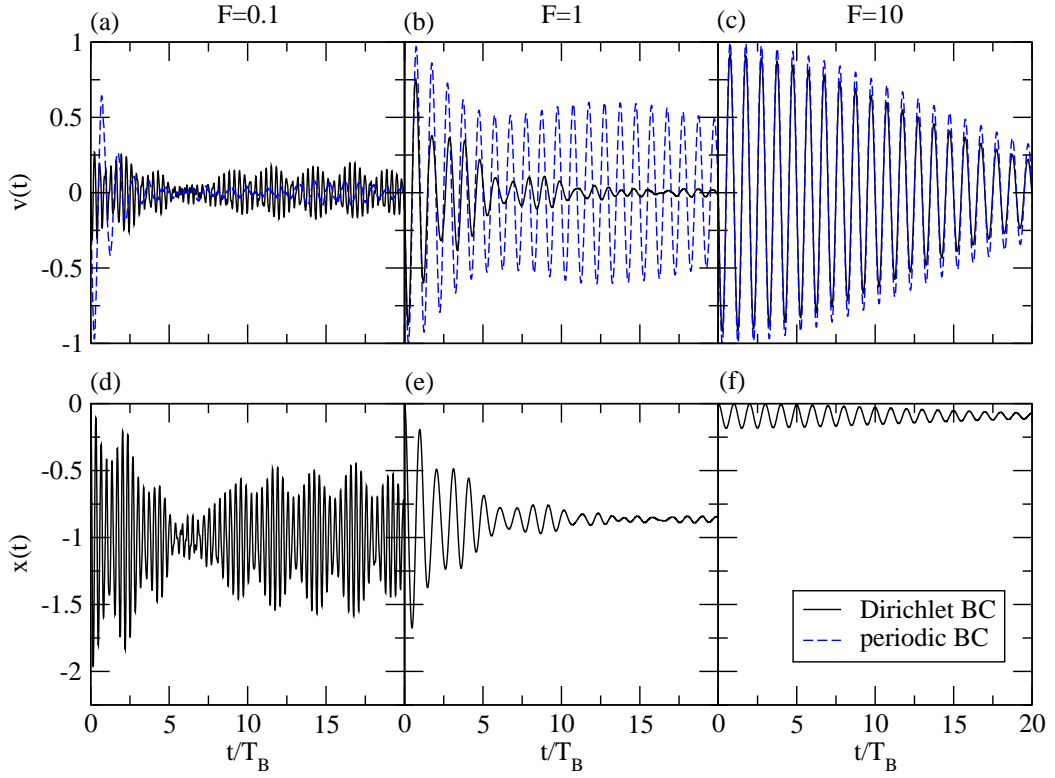
Figure 6.6: Same as Fig. 6.4 for weakly interacting bosons, $U = 0.1$. In the case of periodic boundary conditions we do not show $x(t)$ since it vanishes for all times, see the discussion on p. 84.

in Fig. 6.7 is strikingly different. For small and intermediate static fields (left and middle column), the Bloch oscillations show a fast and irreversible decay. For $F = 1$, we can observe this behavior in the velocity $v(t)$ for both periodic and Dirichlet boundary conditions (Fig. 6.7 (b)), with no qualitative and only little quantitative difference. Inspection of the associated center of mass dynamics (Fig. 6.7 (e)) reveals the reason for this behavior: The oscillations in real space decay before the atoms can finish even one single Bloch cycle, *i.e.*, they do not have time to probe the finite size of the lattice before reaching the equilibrium state. For $F = 0.1$, periodic boundary conditions lead to qualitatively the same behavior as found already for $F = 1$ (Fig. 6.7 (a)). However, in the case of Dirichlet boundary conditions, we again observe a strong influence of the edges of the system (Fig. 6.7 (a), (d)). The origin of this fast and irreversible decay of the Bloch oscillations in the chaotic regime of the Bose-Hubbard Hamiltonian will be discussed in detail in Secs. 6.3 and 6.4.

For strong tilts $F = 10$, the system becomes regular again and the interaction-induced period T_U, Eq. (6.10), leads to a beating signal with periodicity $T_U = 10 \cdot T_B$ (Fig. 6.7 (c) and (f)).
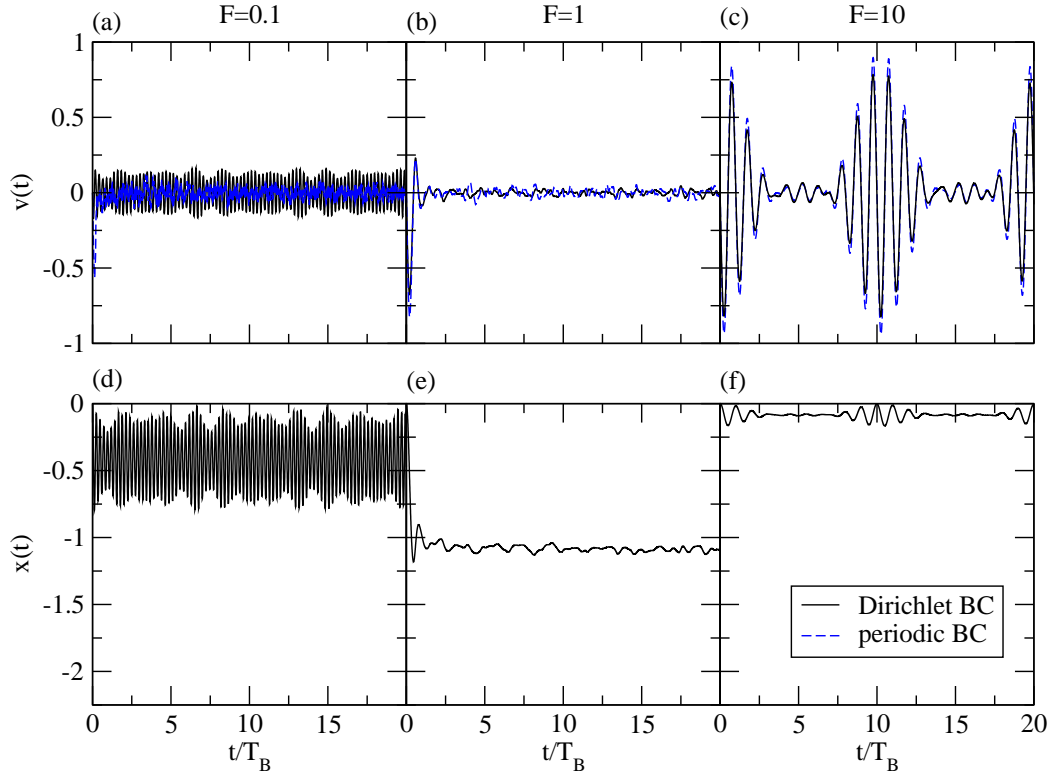
Figure 6.7: Same as Fig. 6.4, for intermediate interaction strength $U = 1$.

6.2.2.3 Strong interactions

In the case of strong interactions $U = 10$, the system is regular, independently of the tilt, and its eigenstates are well approximated by Wannier-Fock states. As a consequence, the mobility of the bosons is strongly suppressed, as can be observed for $F = 0.1$ and 1 (Fig. 6.8 (a), (d) and (b), (e)), where both velocity and center of mass are essentially constant as time elapses.

In contrast, for $F = 10$, we observe oscillations of $v(t)$ and $x(t)$ (Fig. 6.8 (c), (f)) with a periodicity that is approximately five times the Bloch period. It thus *differs* from the interaction-induced period $T_U = F/U \cdot T_B$, Eq. (6.10), that equals the Bloch period for the parameters considered here and that was observed for $U = 1$ and $F = 10$ in Fig. 6.7 (c), (f). The presently observed oscillations occur deep in the Mott insulating regime, and are related to a resonance between the onsite energy U and the static field F, as depicted schematically in Fig. 6.9. In Ref. [113] a resonant approximation that takes into account a limited number of Wannier-Fock basis states is used to explain the observed dynamics. Furthermore, the authors analyze the quasienergy spectrum of the system that can be obtained from an effec-
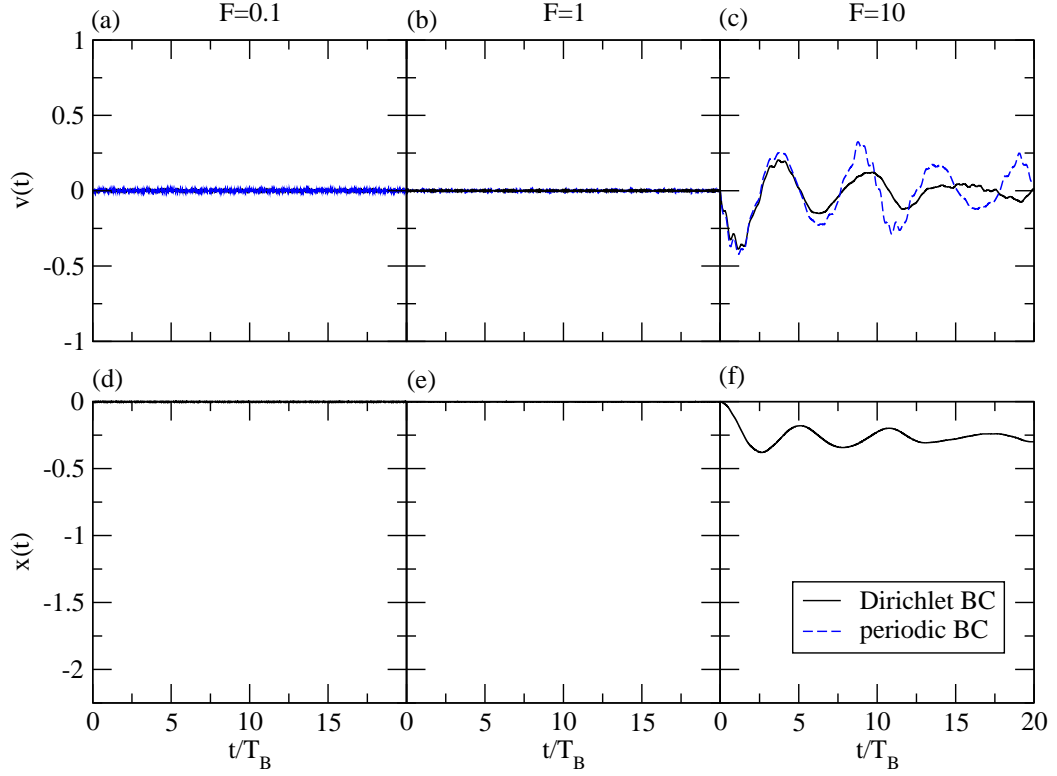
Figure 6.8: Same as Fig. 6.4, for strongly interacting bosons, $U = 10$.

tive Hamiltonian as given in Ref. [158]. However, the main features of the dynamics are already captured by a simple two-level approximation, as we will discuss in the following.

For strong interactions, the ground state of the untilted lattice, which constitutes the initial state in the dynamics shown here, is quite well approximated by a Fock state with exactly one particle on each lattice site. Moreover, for $F = U$, any Fock state of the form $|\ldots, 1, 1, \ldots\rangle$ is energetically degenerate with the state $|\ldots, 2, 0, \ldots\rangle$, where the two states differ solely on the two given sites. We then make a two-level approximation, only considering the two Fock states $|1, 1\rangle$ and $|2, 0\rangle$ that describe two neighboring lattice sites (see Fig. 6.9). After a simple calculation, we find that an avoided crossing with energy gap

$$\Delta E = \sqrt{(U - F)^2 + 2J^2} \tag{6.11}$$

emerges (compare Eq. (5.10)). We thus expect oscillations between the two states, with periodicity $T_{res} = 2\pi/\Delta E$ which, in units of the Bloch period, is given by

$$T_{res} = \frac{F}{\Delta E} \cdot T_B. \tag{6.12}$$
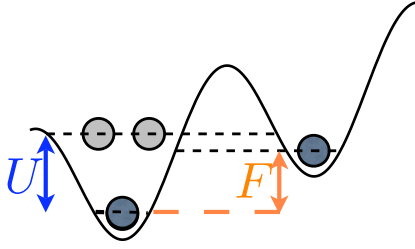
Figure 6.9: Schematic diagram of two ultracold bosons in two neighboring sites of a tilted optical lattice, described by the tilted Bose-Hubbard Hamiltonian $\hat{H}$, Eq. (2.26). For $F = U$, the state where both particles are located in the lower lattice site (light grey) and the state with one particle per site (dark grey) are energetically degenerate.

For fixed tunneling coupling, the frequency depends on the *detuning* $U - F$ and on the static field strength F. Exemplary values of the theoretically expected period T_{res} are given, for $U = 10$ and $J = 1$, in Table 6.1.

To compare our theoretical expectations with numerical data, the dynamics of the center of mass $x(t)$ is shown for $n = 2$ bosons in a lattice with $L = 11$ sites in Fig. 6.10 (a), for $U = 10$, $J = 1$, and $F = 8, 10, 12$. Such as to guarantee that boundary effects are negligible during the dynamics, we initially prepare the n bosons in the ground state of a lattice with $m = n$ sites, placed into the larger lattice, with Dirichlet boundary conditions, before applying the tilt (compare Fig. 6.5). The location of the smaller lattice within the large lattice is chosen such that at $t = 0$ the two uppermost sites of the tilted lattice are empty (see also discussion on p. 86). The numerical values $T_{num}^{n=2}$ are given in Table 6.1, and we find excellent agreement with the theoretical data obtained from the simple two-level approximation.

One might wonder whether this also holds for larger particle numbers. In order to answer this question, we plot $x(t)$ for $n = 5$ bosons, for the same parameters as used above, in Fig. 6.10 (b). Here, the initial state is again the ground state of the bosons in a lattice with $m = n$ sites. We find that, in this case, the numerics (given in Table 6.1) deviate from the theoretical expectations, an that the difference is largest at resonance, *i.e.*, for equal values

F	$T_{res}[T_B]$	$T_{num}^{n=2}[T_B]$	$T_{num}^{n=5}[T_B]$
8	3.27	3.21	2.63
10	7.07	7.05	5.17
12	4.90	4.91	4.38

Table 6.1: Resonance induced period for different strengths of the static field F with $U = 10$ and $J = 1$. Shown are theoretical vales T_{res}, Eq. (6.12), obtained from a simple two-level approximation, and numerical values $T_{num}^{n=2}$, for $n = 2$, and $T_{num}^{n=5}$, for $n = 5$ particles. The initial states are the ground states of n bosons in a lattice with $m = n$ sites, which is then placed into a tilted lattice of total length $L = 11$, such that at $t = 0$ the two uppermost sites of the tilted lattice are empty (see also discussion on p. 86). All periods are given in units of the Bloch period T_B.
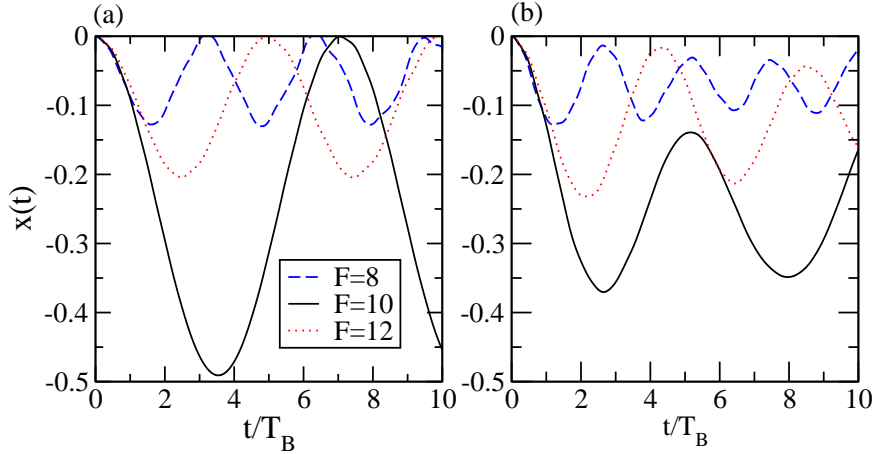
Figure 6.10: Center of mass $x(t)$, Eq. (6.4), of n bosons on a lattice of length $L = 11$ under a variable static tilt F as a function of time, in units of the Bloch period t/T_B, for (a) $n = 2$ and (b) $n = 5$, with $J = 1$ and $U = 10$. The initial state is in both cases the ground state of the bosons in $m = n$ sites of an untilted lattice, placed into the larger lattice with L sites, and Dirichlet boundary conditions (see also Fig. 6.5 and discussion on page 86).

of the tilt and of the interaction strength, $F = U$. Furthermore, the amplitude of the oscillations decays in time. That is, for particle numbers $n > 2$, more resonant states have to be considered in order to reproduce the exact dynamics of the system. Moreover, the decay of the oscillations can then be related to the quasienergy spectrum of the system, as done in Ref. [113]. Note, however, that the periodicity for $n = 7$ bosons in $L = 7$ lattice sites with periodic boundary conditions and $F = 10$ (Fig. 6.8 (c) and (f)) is basically identical to the periodicity observed for $n = 5$ bosons with $F = 10$. We therefore expect the corrections to saturate quickly with growing particle number.

In summary, we have seen that ultracold bosons in tilted optical lattices, described by the tilted Bose-Hubbard Hamiltonian, feature rich dynamics that depend on the relative strength of the control parameters J, U, and F.[10] Those range from perfect Bloch oscillations for vanishing interactions [65, 83], to an irreversible and fast decay when onsite interaction and tunneling coupling are comparable and the underlying spectral structure is chaotic [114, 115]. In the case of dominant static fields and weak interactions, an additional interaction-induced period T_U, Eq. (6.10), appears [112]. For strong static fields and strong interactions, another frequency T_{res} can be observed [113] that results from resonant oscillations between

---

[10]Note that here we did not investigate the role of the filling factor n/L. It, however, also strongly influences the dynamics and analogous behavior between systems with different filling factors can only be expected for fixed scaled interaction strength $U \cdot n/L$, see also Sec. 3.3.

different Wannier-Fock states.

While we focus on Bloch oscillations that emerge when the system is initially prepared in the untilted Hamiltonian's ground state, recently Bloch oscillations for initially localized states of interacting bosons were investigated in Refs. [54, 105]. Here, the authors consider initial states where all n particles are located on one single lattice site which, for large interaction strengths, yields an oscillation period $T = T_B/n$. The origin of this period can be understood by considering the case of two particles [105]: For $U > J$, the many-particle spectrum decomposes into two distinct parts that do not overlap. Those correspond to the noninteracting part, which excludes double occupancy of the lattice sites, and the interacting part, which is characterized by double occupancy. While the former features the equidistant spacing F, the latter has the equidistant spacing $2F$, which is the cost of moving two particles from a given site to a neighboring site. When both particles are initially located on the same site, the initial state strongly overlaps with the interacting part of the spectrum what leads to the period $T = 2\pi/(2F) = T_B/2$.

In the following, we concentrate on the chaotic regime of the Hamiltonian, and relate the rapid and irreversible decay of the oscillations directly to the spectral properties of the many-body system. We discuss two different approaches in order to explain this behavior: The first approach relies on the adiabatic spectrum (see Sec. 3.2.3), whereas the second approach is based on the tilted Bose-Hubbard Hamiltonian and considers the distribution of the velocity operator's matrix elements $V_{n,m}$, weighted with the matrix elements of the initial density matrix ρ_0.

6.3 Approach 1: Adiabatic spectrum

In a first attempt to explain the decay of Bloch oscillations in the chaotic regime, we study the adiabatic spectrum of the tilted Bose-Hubbard Hamiltonian, *i.e.*, the time-dependent spectrum that arises when the Hamiltonian is transformed to the interaction representation with respect to the static field, see Sec. 3.2.3. Specifically, we investigate how the population of the initially prepared ground state *diffuses* in the spectrum via repeated Landau-Zener transitions [121, 203], what leads to a dephasing of the characteristic Bloch oscillations. This concept of energy diffusion was originally applied [135, 198] to the quantum mechanical description of dissipation in finite-size, chaotic systems, as we will discuss in the following. Thereafter, we will apply the general formalism to our specific case, the adiabatic spectrum of the Bose-Hubbard Hamiltonian, and discuss the validity of the approach in this context.
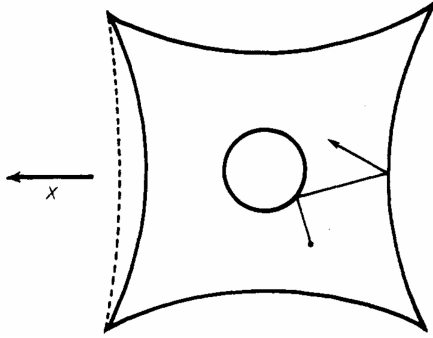
Figure 6.11: Billiard region with a variably shaped boundary, described by the parameter X, taken from [198]. The system can be considered as a driven system, where $\dot{X}$ is associated with the "velocity" of the driving. The cavity is assumed to be chaotic such as to assure that the dynamics is irregular, even in absence of the driving of the wall.

6.3.1 Adiabatic theory of driven quantum systems

Consider a chaotic, classical dynamical system, with a total Hamiltonian $\mathcal{H}(Q,P;X)$ which not only depends on a set of canonical variables Q and P, but furthermore on an additional parameter X which might, in principle, be time dependent, *i.e.*, $X = X(t)$. This situation is found in a broad variety of real physical systems, ranging from nuclear to atomic and mesoscopic physics [198, 199]. As an example, consider the model depicted in Fig. 6.11 where a particle is trapped inside an enclosure. In mesoscopic physics, such systems are often called *billiards* and can be realized with quantum dots [129]. Here, $X(t)$ is associated with the deformation of the left wall which has a mass that is huge compared to the particle's mass. Consequently, the backaction of the system dynamics on $X(t)$ is weak. The model can be thought of as a driven system, with $\dot{X}(t)$ the "velocity" of the driving. We assume the cavity to be chaotic, such as to assure that the motion is irregular, even in absence of the driving of the wall. In the context of (periodic) driving one can then ask, for instance, how energy is pumped into the system.

Quantum mechanically, this scenario translates to a finite-size system with energy eigenvalues controlled by the external parameter X, also referred to as *macroscopic variable*. Again, we assume the system to be chaotic (in the spectral sense, see Sec. 3.1), irrespective of the exact value of the parameter. Consequently, when X is varied, the energy levels undergo various avoided crossings, as depicted schematically in Fig. 6.12 (a) and discussed in detail in Sec. 3.1.1. In the following, we consider the exemplary billiard system depicted in Fig. 6.11, thereby following Wilkinson's scheme [198]. The energy levels of the system are assumed to be occupied by a large number of noninteracting fermions up to the Fermi energy E_F, *i.e.*, the system is initially in its ground state.

When the gap ΔE between two adjacent energy levels is sufficiently small, there is a finite probability P for a particle to make a transition to a formerly unoccupied state, see Fig. 6.12 (b). In the limit where the rate of change $\dot{X}$ of the external parameter is very small,

(a)

(b)
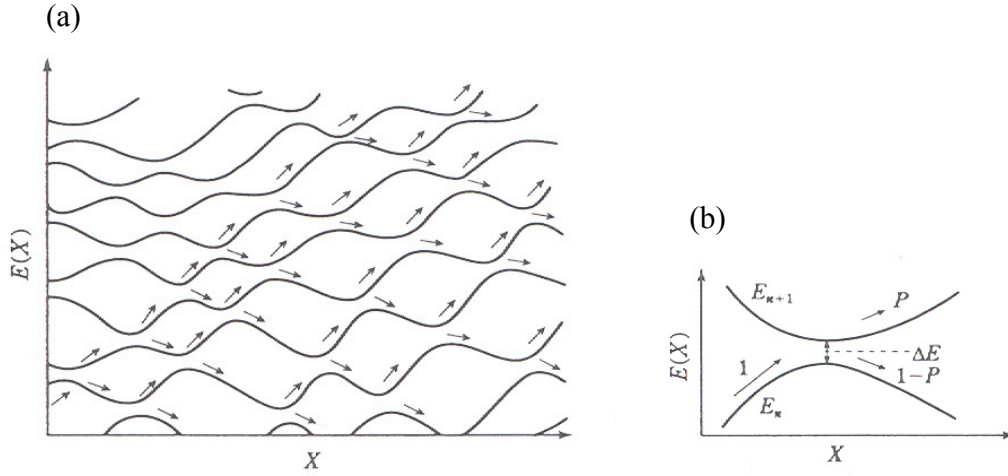
Figure 6.12: (a) Schematic diagram of the parametric level evolution of the energy spectrum of a quantum-chaotic system under changes of some external parameter X, and (b) magnification around one of the avoided crossings, taken from Ref. [135]. Transitions between neighboring levels are indicated by arrows and the corresponding probability is given by P, Eq. (6.13).

this mechanism can be described by Landau-Zener theory [121, 203].[11] The transition probability is then given by

$$P = \exp\left(-\frac{\pi}{2}\frac{\Delta E^2}{A\,|\dot{X}|}\right),\tag{6.13}$$

where A is the relative slope of the two levels under consideration and we have set $\hbar = 1$. Since the system is initially in its ground state, such transitions lead to an increase of the system's energy. This, in turn, induces a damping of the driving motion since the energy of the whole system (that consists of the quantum system and the degree of freedom associated with the macroscopic dynamical variable $X(t)$) is assumed to be conserved. In other words, the diffusion in the microscopic quantum system's energies (Fig. 6.12) is interpreted as the quantum-mechanical origin of a "frictional force" on the macroscopic dynamical variable $X(t)$ [135, 198]. The mechanism of dissipation by Landau-Zener transitions was first suggested by Hill and Wheeler in 1953, in the context of a collective model for nuclei [89].

This description of the damping process is only valid when the gap size ΔE of those avoided crossings at which there is a significant probability to make a transition is much smaller than the mean level spacing Δ, *i.e.*,

$$\Delta E \ll \Delta.\tag{6.14}$$

---

[11]Landau-Zener theory was also applied in Sec. 2.4, to determine the validity of the single-band approximation, within the framework of the tilted Bose-Hubbard Hamiltonian.

In order to obtain a condition on the maximal driving rate $|\dot{X}|$, we assume that the typical transition probability at an avoided crossing is given by $P = e^{-1}$. From Eq. (6.13) this amounts to

$$\frac{\pi}{2} \frac{\overline{\Delta E}^2}{\overline{A}\,|\dot{X}|} = 1\,, \tag{6.15}$$

where $\overline{\Delta E}$ and $\overline{A}$ correspond to the average over the gap sizes ΔE and relative slopes A, taken over all avoided crossings in the spectrum. Together with Eq. (6.14), this yields

$$\overline{A}\,|\dot{X}| \ll \Delta^2\,. \tag{6.16}$$

If the latter condition is not satisfied, transitions between levels that are not nearest neighbors can occur.

When passing slowly through many avoided crossings, the rate of excitation $\mathcal{R}$, i.e., the probability per unit time that a particle makes a transition to a neighboring state, is determined by the distribution $N(A, \Delta E)$ of relative slopes A and gap sizes ΔE via

$$\mathcal{R} = \dot{X} \int\limits_0^\infty dA \int\limits_0^\infty d\Delta E\, N(A, \Delta E) \exp\left(-\frac{\pi}{2} \frac{\Delta E^2}{A\,|\dot{X}|}\right). \tag{6.17}$$

Here $N(A, \Delta E)dA\,d\Delta E$ is the number of avoided crossings encountered per unit length, with relative slopes in the interval $[A, A+dA]$, and gap sizes in the interval $[\Delta E, \Delta E + d\Delta E]$.

If random matrix theory (see Chapter 3) is applicable, the distribution $N(A, \Delta E)$ should be a universal function [198] that fulfills $N(A, \Delta E) \propto P(\Delta E) \cdot P'(A)$. The distribution $P(\Delta E)$ is then determined by the nearest-neighbor level-spacing distribution $P(s)$ that was introduced in Sec. 3.1, while $P'(A)$ is related to the matrix elements of the operator $(\partial \hat{H}/\partial X)$ which also satisfy the statistical hypothesis of random matrix theory. Based on the above, one can then show [198] that, for $\dot{X} = const.$, the transition rate is given by

$$\mathcal{R} \propto |\dot{X}|^{(\nu+2)/2}\,, \tag{6.18}$$

with $\nu = 1$ for GOE and $\nu = 2$ for GUE statistics, and thus it depends on the universality class of the underlying Hamiltonian.

6.3.2 Diffusion in the adiabatic spectrum

How could the adiabatic theory of driven quantum systems be of help to explain the decay of Bloch oscillations? In order to understand this, remember the transformed, time-dependent Hamiltonian $\hat{\tilde{H}}_p(t)$, Eq. (2.34). It contains a time-dependent phase factor of the form e^{iFt} and, consequently, can be considered as the Hamiltonian of a periodically driven system
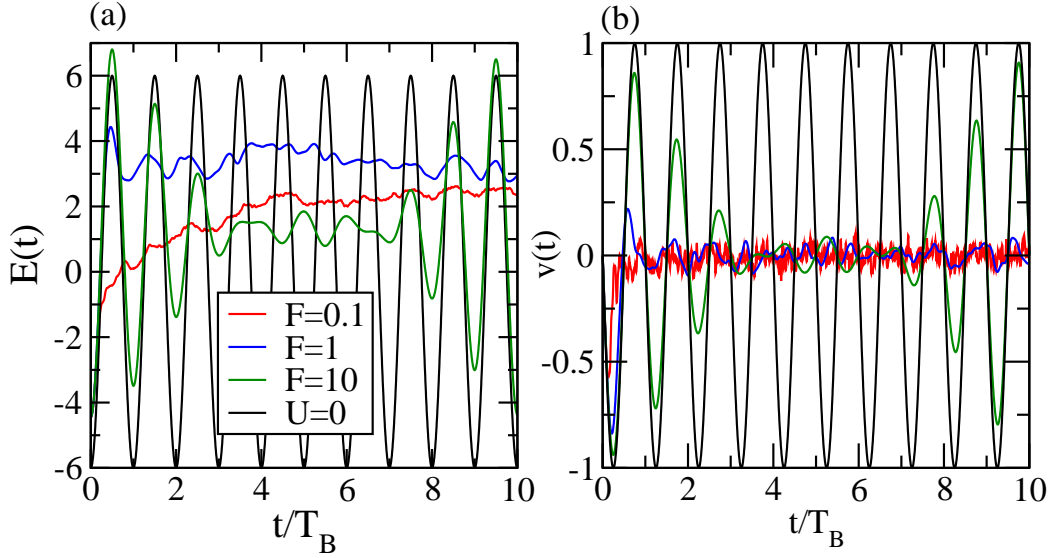
Figure 6.13: (a) Energy $E(t)$, Eq. (6.19), and (b) velocity $v(t)$, Eq. (6.6), for $n = 6$ bosons on $L = 7$ sites with periodic boundary conditions, plotted versus time, in units of the Bloch period t/T_B. The parameters are $U = J = 1$ and $F = 0.1$ (red), 1 (blue), and 10 (green), and the initial state is the untilted Hamiltonian's ground state. The data for noninteracting particles, $U = 0$, are also shown, for comparison (black).

where the *constant* tilt F defines the *driving rate*. This should not be confused with our analysis in Chapter 5, where we considered the parametric evolution of the tilted Bose-Hubbard Hamiltonian $\hat{H}$, Eq. (2.26), as a function of the tilt F and a driving of the system in the form of a linearly *time-dependent* tilt, *i.e.*, $F(t) = F_i + Rt$ (see Eq. (5.4)).

Let us illustrate how the decay of the Bloch oscillations is reflected in the temporal behavior of the energy

$$E(t) = \langle \psi(t) | \hat{\bar{H}}_p(t) | \psi(t) \rangle . \tag{6.19}$$

In Fig. 6.13, we plot $E(t)$ and $v(t)$ versus time, in units of the Bloch period t/T_B, for periodic boundary conditions, $J = U = 1$, and various field strengths F. For comparison, we also show data for noninteracting particles. We find that velocity and energy behave essentially analogous: For $U = 0$, they feature perfect Bloch oscillations which get distorted for $U \neq 0$. In the latter case, the dynamical behavior depends on the strength of the driving F, as already discussed in Sec. 6.2. The main difference between $v(t)$ and $E(t)$ is given by the phase shift of $\pi/2$ between them. This is rooted in the definition of the velocity which is given by the derivative of the energy, compare Eq. (6.5). That is, while the initial value of the energy $E(t = 0)$ corresponds to its minimum value, *i.e.*, the ground state energy of the system, the velocity starts at $v(t = 0) = 0$ and oscillates around zero. Apart from that, $v(t)$
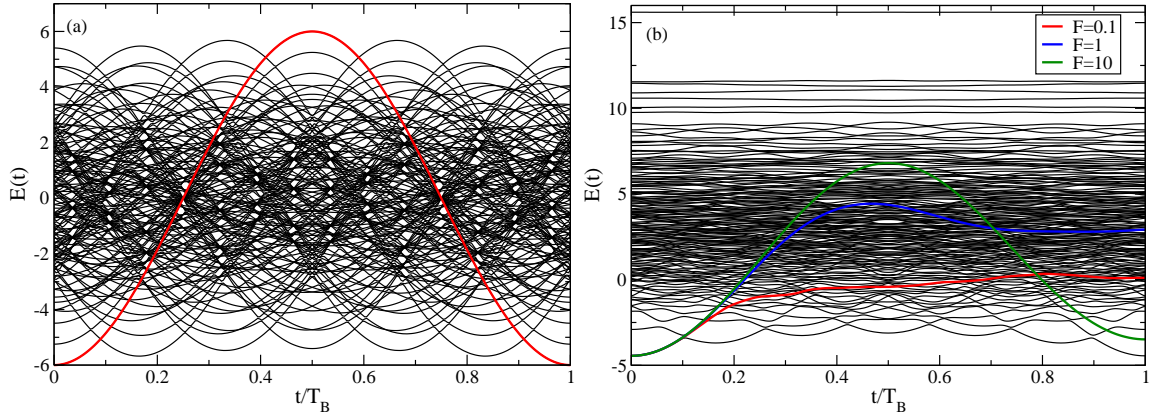
Figure 6.14: Adiabatic spectrum of the time-dependent Hamiltonian $\hat{\bar{H}}_p(t)$, Eq. (2.34), with quasi-momentum $\kappa = 0$, for $n = 6$ on $L = 7$ sites, for (a) $U = 0$, $J = 1$, and (b) $U = J = 1$. The energy $E(t)$, Eq. (6.19), of the system, initially prepared in the ground state, is plotted in color on top of the spectrum. While for $U = 0$ the driving rate F is irrelevant for the dynamics, the behavior strongly depends on F in the case of interacting bosons as indicated for $F = 0.1$ (red line), 1 (blue line), and 10 (green line), compare Fig. 6.13 (a).

and $E(t)$ behave qualitatively similarly.

How is the observed behavior of the Bloch oscillations related to the adiabatic spectrum? The answer is given in Fig. 6.14, where we plot the energy $E(t)$ of the system, initially prepared in its ground state (compare Fig. 6.13 (a)), on top of the adiabatic spectrum with quasimomentum $\kappa = 0$.[12] For (a) noninteracting particles, the spectrum consists of perfectly crossing straight lines and, hence, individual energy levels are not coupled. As a result, no transitions between any two levels occur, and the system's temporal behavior is dictated by the evolution of the initially populated energy level, irrespective of the driving rate F. Thus, in the case of the ground state considered here, we can observe perfect Bloch oscillations.

For (b) interacting particles, the situation changes: The energy levels undergo numerous avoided crossings, and, consequently, transitions between neighboring levels are possible. Also the driving rate F is now of crucial importance. In the case of weak driving $F = 0.1$, only few transitions occur, and the energy stays close to the ground state energy during the dynamics. In this regime, Bloch oscillations cannot be observed (compare Fig. 6.13) since only states in the lower part of the spectrum get occupied during the dynamics. Increasing

---

[12]Due to the translational invariance of the system with periodic boundary conditions, the Hamiltonian decomposes into blocks with distinct quasimomenta κ, and dimensions $\mathcal{N}_\kappa$. Since the ground state lies within the $\kappa = 0$ block, we solely consider the corresponding part of the spectrum here. For further details, and a plot of the adiabatic spectrum of a smaller system where the individual energy levels can be resolved, see Secs. 2.4.1.1 and 3.2.3, respectively.

the driving rate leads to more and more transitions, and for $F = 1$ the system features (decaying) Bloch oscillations. For strong driving, $F = 10$, the diabatic regime is reached, where the system is forced across the avoided crossings and almost perfect oscillations occur, that are solely modified by an additional beating which we already discussed in Sec. 6.2.

We thus see how populations of individual eigenstates of the adiabatic spectrum of $\hat{\bar{H}}_p(t)$ can be redistributed over neighboring levels. Depending on the driving and on the coupling between the levels, *i.e.*, on the size and width of the avoided crossings, an initially localized state will therefore spread and get distributed amongst the levels as time evolves. This spreading is then reflected in the energy $E(t)$, Eq. (6.19), as we observed in Fig. 6.14. In this context, the rate of excitation $\mathcal{R}$, Eq. (6.17), tuns into

$$\mathcal{R} = \frac{F}{2\pi} \int\limits_0^\infty dA \int\limits_0^\infty d\Delta E \, N(A, \Delta E) \exp\left(-\pi^2 \frac{\Delta E^2}{AF}\right), \qquad (6.20)$$

where we have identified $X = Ft/(2\pi) = t/T_B$ and, consequently, $\dot{X} = F/(2\pi)$. As discussed in Sec. 3.2.3, the distribution $N(A, \Delta E)$ of the avoided crossings' widths and corresponding relative slopes depends on the strength of the Hamiltonian's parameters J and U, and has to be extracted numerically from the adiabatic spectrum.

Given the scenarios shown in Fig. 6.14 (b), the question arises for which driving rates F the approach of Wilkinson might be applicable, *i.e.*, whether one of the above cases fulfills the slowness condition (6.16). We thus estimate the largest rate F for which (6.16) still holds. In the simplest approximation, the mean level spacing is given by

$$\Delta = \frac{E_{max} - E_{min}}{\mathcal{N}_{\kappa_0}} \approx 0.12, \qquad (6.21)$$

where $\mathcal{N}_{\kappa_0} = 132$ is the dimension of the $\kappa = 0$ subspace (see Sec. 2.4.1.1), and E_{max} and E_{min} are the largest and smallest energy eigenvalues that appear in the spectrum.[13] Furthermore, we find that the average gap size, taken over all avoided crossings, is given by $\overline{\Delta E} \approx 0.055$, and the average over the relative slopes yields $\overline{A} \approx 4.65$. Consequently, condition (6.14) is reasonably satisfied, and condition (6.16) results in $F \ll 0.02$. That is, Wilkinson's approach of adiabatic driving can only be applied to tilting strengths that fulfill $F \ll 0.02$. However, for such small tilts, decaying Bloch oscillations are not observed in the chaotic regime.

The above discussion is corroborated by Fig. 6.15, which is a zoom of Fig. 6.14 (b) around the first avoided crossing encountered by the many-particle ground state, at $t/T_B =$

---

[13] We actually do not take into account the uppermost level which lies well separated above the rest of the spectrum and thus does not couple to states from the bulk, as obvious from Fig. 6.14 (b).
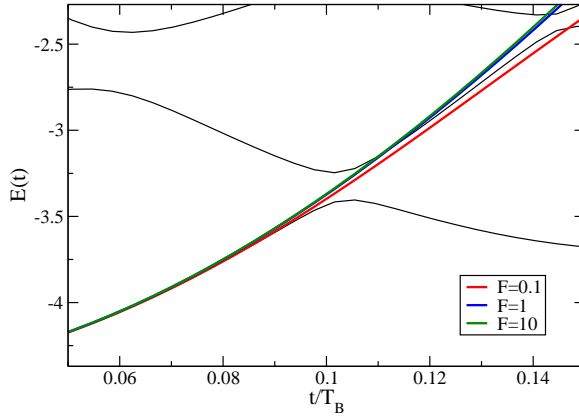
Figure 6.15: Zoom into the adiabatic spectrum of Fig. 6.14 (b), and the energy $E(t)$ in the vicinity of the first avoided crossing between the many-particle ground state and the first excited state, at $t/T_B \approx 0.1$.

0.1. We find that even for weak driving $F = 0.1$, where the system does not feature Bloch oscillations yet, almost the entire population makes a transition to the second level. That is, we are still far from being in the adiabatic regime where Landau-Zener theory is applicable. For $F = 1$ and 10, the situation is even worse: The energy of the system after passing the first avoided crossing lies already above the second energy level. It is thus immediately evident that a local two-level approximation is not applicable here and couplings between non-neighboring levels have to be taken into account.

We conclude that the adiabatic theory of driven quantum systems does not apply in the current context. Instead, one could use time-dependent perturbation theory, *i.e.*, *linear response theory* à la Kubo and Greenwood [38, 76, 119, 198], to calculate the spreading in the energy spectrum. In this formalism, the fine structure of the spectrum, *i.e.*, the distribution of gaps ΔE and slopes A is no longer the relevant quantity. Rather, what matters is the shape of the perturbation operator that usually is a banded matrix [66]. Its bandwidth[14] then determines the maximal distance in energy at which levels are coupled in first order processes. Since the bandwidth is typically much larger than the mean level spacing Δ, distant levels are coupled for fast driving. Here, we do not further pursue this approach since we are interested in how the statistical properties of the Hamiltonian are reflected in the decay of the Bloch oscillations.

---

[14]The bandwidth of the perturbation operator is inversely proportional to the correlation time of the underlying classical (mean-field) dynamics, see for example Refs. [38, 93, 198].

6.4 Approach 2: Statistical analysis of the velocity operator

In this section we develop a method that will allow us to relate the decay rate of the Bloch oscillations to the statistical properties of the tilted Bose-Hubbard Hamiltonian. It is based on the distribution of the velocity operator's matrix elements $V_{n,m}$, weighted with the initial density matrix ρ_0. This distribution closely resembles the *local density of states* (LDoS).

In the following, we first introduce the LDoS and its relation to the survival probability and to the Bloch oscillations. Then, we define and investigate the joint frequency distribution of the velocity operator and of the initial density matrix, which we finally connect to the decay rate of the Bloch oscillations and the spectral statistics of the Bose-Hubbard Hamiltonian. Although our main interest resides in the chaotic spectral regime, we will perform a parametric analysis with respect to the interaction strength.

6.4.1 Local density of states

Consider again a Hamiltonian that depends on a set of control parameters $\{X\}$. As opposed to the discussion in Sec. 6.3.1, we assume the parameters to be time independent and now focus on the eigenstates of the system, and not only on its eigenenergies. As the parameters $\{X\}$, and thus the Hamiltonian, change, also the corresponding instantaneous eigenstates evolve and undergo structural changes. This is reflected in the LDoS which is defined as

$$D_m(E) = \sum_{n=1}^{\mathcal{N}} P(m|n)\,\delta(E - E_n),\qquad(6.22)$$

with the kernel

$$P(m|n) = |\langle m(\{X\})|n(\{X'\})\rangle|^2.\qquad(6.23)$$

Here, $|m(\{X\})\rangle$ represents an *unperturbed* eigenstate of the Hamiltonian $\hat{H}_0$ that corresponds to the parameter set $\{X\}$, *i.e.*,

$$\hat{H}_0|m(\{X\})\rangle = E_{0,m}|m(\{X\})\rangle,\qquad(6.24)$$

$|n(\{X'\})\rangle$ is an eigenstate of the *perturbed* Hamiltonian $\hat{H}$ characterized by $\{X'\}$,

$$\hat{H}|n(\{X'\})\rangle = E_n|n(\{X'\})\rangle,\qquad(6.25)$$

and $\mathcal{N}$ is the Hilbert-space dimension. When interpreted as a function of n for fixed m, the kernel $P(m|n)$ is the projection of a single state $|m\rangle$ on the basis $\{|n\rangle\}$, as illustrated
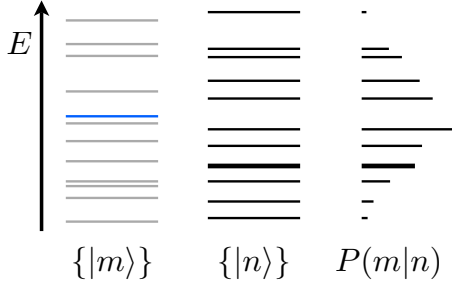
Figure 6.16: Schematic representation of the kernel $P(m|n)$, Eq. (6.23), that appears in the local density of states $D_m(E)$, Eq. (6.22). It describes the projection of an unperturbed eigenstate $|m\rangle$ (blue level) on the eigenbasis $\{|n\rangle\}$ of the perturbed Hamiltonian.

in Fig. 6.16. That is, the LDoS describes the representation of an eigenstate of the unperturbed Hamiltonian $\hat{H}_0$ in the eigenbasis of the perturbed Hamiltonian $\hat{H}$,[15] and thus it characterizes that part of the spectrum which is relevant for the state under consideration. This property makes the LDoS useful in many contexts, since, in general, the details of the entire spectrum are not important. This will be illustrated in the next section, where we consider the time evolution of the so-called *survival probability*.

In the case of the tilted Bose-Hubbard Hamiltonian $\hat{H}$, Eq. (2.26), the set of parameters $\{X\}$ is given by J, U, and F. For example, in Sec. 3.2.2 we saw that, for fixed $U = 0$, the eigenstates change from Bloch to Wannier-Fock states as F is increased from zero. Since we here consider the time evolution of the untilted Hamiltonian's ground state under the action of the tilted Hamiltonian, it is natural to identify the unperturbed Hamiltonian with $\hat{H}_0 = \hat{H}_J + \hat{H}_U$, and the perturbed Hamiltonian with $\hat{H} = \hat{H}_0 + \hat{H}_F$.

To avoid the problem of a time-dependent eigenbasis, we stick to the time-independent Hamiltonian (2.26). Consequently, we apply Dirichlet boundary conditions in the dynamics which, depending on the strength of the static field F, can induce boundary effects, as we have seen in Sec. 6.2. However, as discussed on p. 86, this intricacy can be overcome by choosing as initial state $|\psi_0\rangle$ the ground state of a smaller, untilted sublattice with $m < L$ sites (see Fig. 6.5). In the following, the location of the smaller lattice within the large lattice is always chosen such that at $t = 0$ the two uppermost sites of the tilted lattice are empty. We have checked that this choice guarantees that boundary effects can be neglected for all the parameter sets discussed in the remainder of this chapter.

Since this initial state $|\psi_0\rangle$ is not an eigenstate of the untilted, large lattice, in the following we refer to the LDoS in a more general way. That is, we consider the representation of

---

[15]If interpreted as a function of m, $P(m|n)$ yields the shape of a perturbed eigenstate $|n\rangle$ in the unperturbed basis $\{|m\rangle\}$. For chaotic systems, both cases have been thoroughly studied [31, 38, 39, 41, 72, 91, 196], even for a (three-site) Bose-Hubbard system [90, 92, 93].

$|\psi_0\rangle$ in the eigenbasis of the tilted Hamiltonian $\hat{H}$, *i.e.*,

$$D(E) = \sum_{n=1}^{\mathcal{N}} |\langle \psi_0 | n \rangle|^2 \, \delta(E - E_n) . \tag{6.26}$$

This can also be written as

$$D(E) = \sum_{n=1}^{\mathcal{N}} \rho_{0n,n} \, \delta(E - E_n) , \tag{6.27}$$

where

$$\rho_0 = |\psi_0\rangle \langle \psi_0| , \tag{6.28}$$

is the initial density matrix. That is, the coefficients of the LDoS are given by the diagonal elements of the initial density matrix in the representation of the Hamiltonian $\hat{H} = \hat{H}_0 + \hat{H}_F$ that generates the dynamics.

In the upper row of Fig. 6.17, we illustrate the evolution of the LDoS $D(E)$ for fixed $J = F = 1$, and various interaction strengths U. We find that U strongly affects the structure of the LDoS: For vanishing interactions $U = 0$, it features equidistant peaks, which get broadened as U increases to $U = 0.1$. For even stronger interactions, $U = 1$ and $U = 3$, the regular structure is washed out completely, and the LDoS features numerous peaks of different heights and spacings.

6.4.1.1 Relation to the survival probability and the mean velocity

How do these structural changes manifest in the system dynamics? In order to answer this, it is useful to recall that the LDoS is tightly connected to an important dynamical quantity, the *survival probability*

$$P(t) = |\langle \psi_0 | \psi(t) \rangle|^2 , \tag{6.29}$$

which quantifies the overlap of the time-evolved state

$$|\psi(t)\rangle = \hat{U}(t) |\psi_0\rangle \tag{6.30}$$

with the initial state $|\psi_0\rangle$. When expressing the time-evolution operator $\hat{U}(t)$ in the eigenbasis of the Hamiltonian $\hat{H}$ that generates the dynamics as

$$\hat{U}(t) = \sum_{n=1}^{\mathcal{N}} e^{-iE_n t} |n\rangle \langle n| , \tag{6.31}$$

we easily see that $P(t)$ can also be written as

$$
P(t) = \left| \sum_{n=1}^{\mathcal{N}} e^{-iE_n t} \langle \psi_0 | n \rangle \langle n | \psi_0 \rangle \right|^2
$$

$$
= \left| \sum_{n=1}^{\mathcal{N}} e^{-iE_n t} |\langle \psi_0 | n \rangle|^2 \right|^2 = \left| \sum_{n=1}^{\mathcal{N}} e^{-iE_n t} \rho_{0n,n} \right|^2 \tag{6.32}
$$

$$
= \left| \int_{-\infty}^{\infty} dE \, e^{-iEt} D(E) \right|^2 ,
$$

where in the last line we used the definition (6.26) of the LDoS. Thus, the survival probability is the modulus squared of the Fourier transform of the LDoS, or, in other words, the Fourier transform of the LDoS provides us with the so-called *survival probability amplitude*. It is therefore evident that the different structures of $D(E)$ as observed in Fig. 6.17 (top row) imply fundamentally distinct temporal behavior of $P(t)$, Fig. 6.17 (middle row). Specifically, we find that the equidistant comb structure for $U = 0$ leads to perfectly periodic dynamics, corresponding to undisturbed Bloch oscillations of the bosons as discussed in Sec. 6.2.1. That is, the particles oscillate on the lattice, and return to their initial configuration at integer multiples l of the Bloch period T_B. Consequently, the survival probability has its maxima at $t = l \cdot T_B$, *i.e.*, $P(l \cdot T_B) = 1$. For nonvanishing interactions $U \neq 0$, the periodicity is distorted and the resulting dynamics ranges from a decay of the oscillations within a few Bloch periods for $U = 0.1$, to their immediate destruction for $U = 1$, and a complete suppression for $U = 3$.

Our ultimate goal is not to describe $P(t)$, but to understand the decay of the Bloch oscillations that is encoded in the velocity $v(t)$ (or likewise in the center of mass $x(t)$) from the statistical properties of the Hamiltonian. The question thus is whether or not the LDoS alone carries sufficient information to do so. The answer is given already in the bottom row of Fig. 6.17, where we depict the velocity, investigated in Sec. 6.2, for the very same system as above. For $U = 0$, $v(t)$ and $P(t)$ behave completely analogously, that is they are periodic with T_B. For nonvanishing interactions, however, the behavior differs, although both quantities feature a decay of the oscillations. For example, for $U = 0.1$, the decay observed in $v(t)$ is less rapid and we can still observe oscillations after an evolution time $t = 4 \cdot T_B$, where $P(t)$ has fully decayed. That is, in general, survival probability and velocity do not behave analogously and, consequently, the LDoS does not provide us with the complete information that is needed to understand the Bloch oscillations' decay.

In the following, we investigate the equations describing the velocity in more detail, in order to understand how the behavior of $v(t)$ is reflected in the statistical properties of the Hamiltonian.
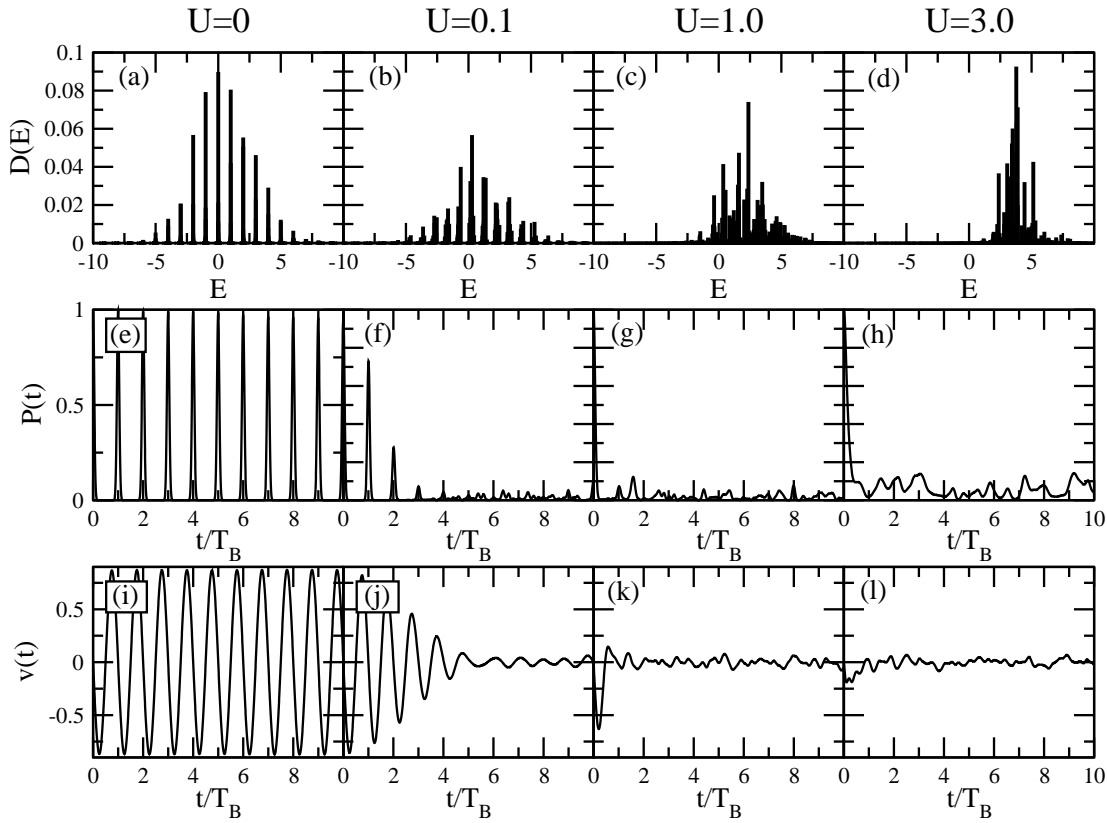
Figure 6.17: Top: local density of states $D(E)$, Eq. (6.26), middle: survival probability $P(t)$, Eq. (6.29), and bottom: mean velocity $v(t)$, Eq. (6.6), for different interaction strengths $U = 0$, 0.1, 1, and 3 (from left to right). The initial state $|\psi_0\rangle$ is the ground state of $n = 5$ particles in $m = 5$ lattice sites, and the tunneling coupling is $J = 1$. The strength of the static field is given by $F = 1$ and the tilted system on which we propagate $|\psi_0\rangle$ has $L = 11$ sites. The LDoS is depicted as a function of the energy E, and survival probability and mean velocity are plotted versus time, in units of the Bloch period t/T_B.

6.4.2 Reformulation of the mean velocity

We use expressions (6.30) and (6.31) for the time-evolved state $|\psi(t)\rangle$, to rewrite the mean velocity $v(t)$, Eq. (6.6), of the bosons on the lattice as

$$
\begin{aligned}
v(t) &= \langle\psi(t)|\hat{V}|\psi(t)\rangle \\
&= \sum_{n,n'=1}^{\mathcal{N}} e^{-i(E_{n'}-E_n)t}\langle n'|\psi_0\rangle\langle\psi_0|n\rangle\langle n|\hat{V}|n'\rangle \\
&= \sum_{n,n'=1}^{\mathcal{N}} e^{-i(E_{n'}-E_n)t}\langle n'|\rho_0|n\rangle\langle n|\hat{V}|n'\rangle \\
&= \sum_{n,n'=1}^{\mathcal{N}} e^{-i(E_{n'}-E_n)t}\rho_{0n',n}V_{n,n'} \\
&= \sum_{n,n'=1}^{\mathcal{N}} e^{-i\Delta E_{n',n}\cdot t}\left(\rho_0\circ V^T\right)_{n',n}.
\end{aligned}
\tag{6.33}
$$

Here, ρ_0 and V are the matrix representations of the initial density matrix and of the velocity operator in the eigenbasis of the tilted Hamiltonian that generates the dynamics. V^T is the transpose of the matrix V, and $\rho_0\circ V^T$ denotes the (entrywise) Hadamard product of ρ_0 and V^T. We thus see that the time dependence of the mean velocity is determined by the *differences* between all contributing eigenenergies of the system,

$$
\Delta E_{n',n} = E_{n'} - E_n\,,
\tag{6.34}
$$

i.e., the *distances* between all the peaks of the LDoS. The corresponding coefficients are given by the matrix elements of the initial density matrix ρ_0, weighted with the elements of the velocity operator's transpose V^T. That is, as opposed to the survival probability (6.32), where the dynamical behavior is solely determined by the LDoS, here, we also have to consider the matrix elements of the velocity operator.

To develop some intuition of how ρ_0 and V evolve under changes of the interaction strength and to better understand the importance of the weighting, we depict ρ_0 (top row), V (middle) and $\rho_0\circ V^T$ (bottom) for different values of U, in Fig. 6.18. Shown are the absolute values of the matrix elements for $n=3$ bosons in a lattice of length $L=6$. We choose this relatively small system with Hilbert-space dimension $\mathcal{N}=56$, Eq. (2.39), in order to be able to resolve the individual elements of the matrices. Here, the initial state is the ground state of the $n=3$ bosons in $m=3$ lattice sites. The axes are chosen such that in each panel the upper left corner corresponds to the smallest, and the lower right corner to the largest eigenenergy of the system.
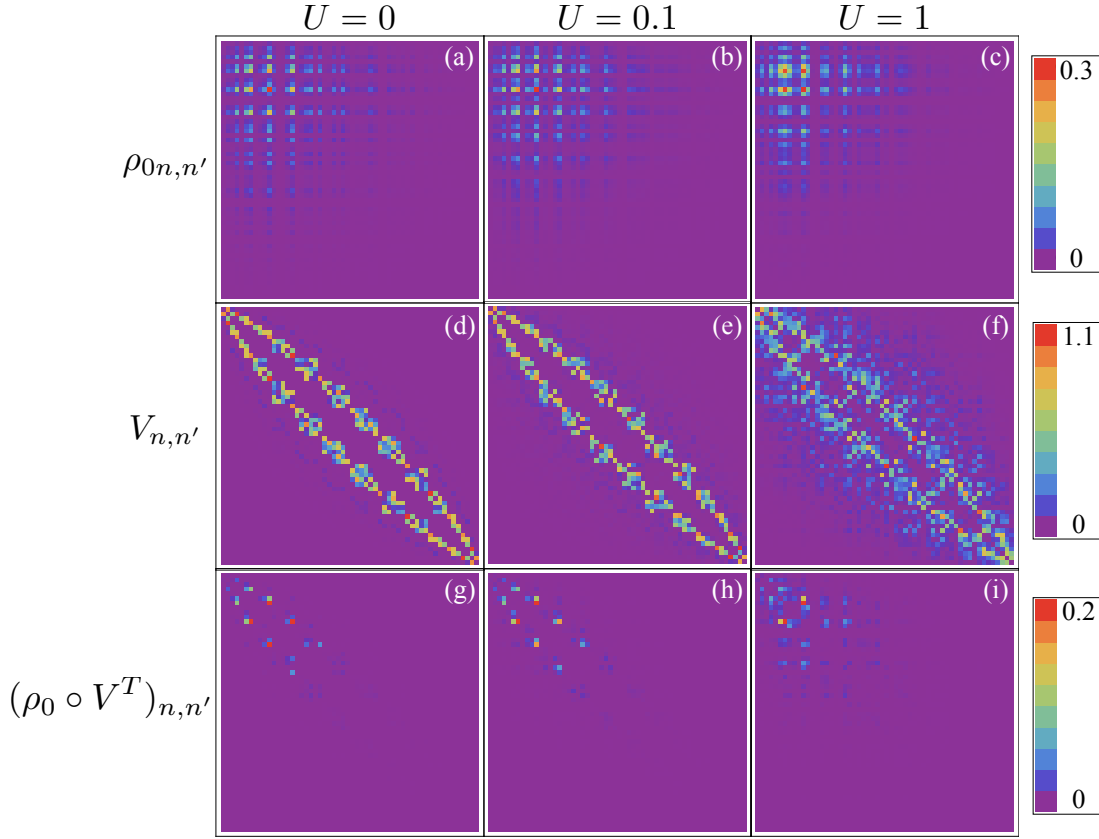
Figure 6.18: Top: initial density matrix ρ_0, Eq. (6.28), middle: velocity operator V, Eq. (6.6), and bottom: Hadamard product $\rho_0 \circ V^T$, in the eigenbasis of the tilted Bose-Hubbard Hamiltonian $\hat{H}$, Eq. (2.26). Shown are the absolute values of the matrix elements for $n = 3$ bosons in a lattice of length $L = 6$, with Hilbert-space dimension $\mathcal{N} = 56$, Eq. (2.39). The initial state is the ground state of the $n = 3$ bosons in $m = 3$ lattice sites. The tunneling coupling and the static field strength are $J = F = 1$, and the onsite interaction takes the values $U = 0, 0.1$, and 1 (from left to right). The axes are chosen such that in each panel the upper left corner corresponds to the smallest and the lower right corner to the largest eigenenergy of the system.

We observe that ρ_0 is only weakly affected by the interaction strength. This is due to our choice of the initial state, which is the ground state of the smaller, untilted system where the interaction strength is the same as in the larger, tilted system. As a consequence, changes in the eigenbasis are only induced by the tilt F. For the parameters considered here, those changes are relatively small and thus the representation of ρ_0 in the tilted Hamiltonian's eigenbasis only slightly depends on U. The situation is different for very strong interactions $U \gg 1$, since in this regime the (Fock) initial state is almost an eigenstate of the tilted

Hamiltonian, and ρ_0 reduces to a matrix which is essentially zero apart from one spot.

On the contrary, V is significantly modified under variations of U since the operator itself is independent of the interaction strength and does not commute with $\hat{H}_U$. For $U = 0$ and small F, the tilted Hamiltonian's eigenbasis is closest to the Bloch basis, and the representation of the velocity operator $\hat{V}$ in this basis has only relatively few nonzero elements that form two off-diagonal bands. This regular structure gets washed out with increasing inter-particle interaction and we find that V is smeared out in the Hamiltonian's eigenbasis for $U = 1$. This can be understood from the evolution of the eigenbasis with increasing U (compare Sec. 2.3.2): the larger the onsite interaction, the more the eigenstates approach Wannier-Fock states, and, consequently, the broader V. We also note that the diagonal elements $V_{n,n}$ vanish independently of U. This results from the definition of the operator $\hat{V}$, Eq. (6.8), which implies that all its matrix elements are purely imaginary, together with the requirement of selfadjointness, which every physical observable has to satisfy.

Combination of both matrices ρ_0 and V leads to the joint distribution of matrix elements $\rho_0 \circ V^T$. We observe that the weighting plays an important role: While the structure of the matrix, *i.e.*, whether or not it is smeared out in the Hamiltonian's eigenbasis, is determined by the velocity operator, the initial density matrix restricts the number of coefficients that need to be taken into account. It is thus evident that the weighting of ρ_0 with V^T in $v(t)$ will significantly influence the dynamical behavior of the mean velocity. Moreover, since V is given in the eigenbasis of the Hamiltonian that generates the dynamics, it contains all the spectral information on the system.

In order to obtain a deeper understanding of the velocity's temporal behavior, we further simplify expression (6.33). In a first step, we use the fact that all diagonal elements are zero, *i.e.*, $V_{n,n} = 0 \ \forall \ n$, and split the sum into two contributions with either only positive (first term) or only negative frequencies $\Delta E_{n',n}$ (second term)

$$v(t) = \sum_{n'=1}^{\mathcal{N}} \sum_{n=n'+1}^{\mathcal{N}} e^{-i\Delta E_{n',n}\cdot t} \left(\rho_0 \circ V^T \right)_{n',n} + \sum_{n=1}^{\mathcal{N}} \sum_{n'=n+1}^{\mathcal{N}} e^{-i\Delta E_{n',n}\cdot t} \left(\rho_0 \circ V^T \right)_{n',n}. \quad (6.35)$$

This can be rewritten as

$$v(t) = \sum_{n'=1}^{\mathcal{N}} \sum_{n=n'+1}^{\mathcal{N}} e^{-i\Delta E_{n',n}\cdot t} \left(\rho_0 \circ V^T \right)_{n',n} + \sum_{n'=1}^{\mathcal{N}} \sum_{n=n'+1}^{\mathcal{N}} e^{-i\Delta E_{n,n'}\cdot t} \left(\rho_0 \circ V^T \right)_{n,n'}, \quad (6.36)$$

where, in the second term, we have exchanged the summation indices n and n'. From the definition of $\Delta E_{n',n}$, Eq. (6.34), we have $\Delta E_{n',n} = -\Delta E_{n,n'}$. Moreover, since ρ_0 is real while V is purely imaginary, we also know that

$$\left(\rho_0 \circ V^T \right)_{n',n} = i \Im \left[\left(\rho_0 \circ V^T \right)_{n',n} \right], \quad (6.37)$$

where $\Im$ denotes the imaginary part. Since ρ_0 is orthogonal and V is selfadjoint, this implies

$$-(\rho_0 \circ V)_{n',n} = (\rho_0 \circ V^T)_{n',n} = (\rho_0 \circ V^T)^*_{n,n'} = -(\rho_0 \circ V)^*_{n,n'}. \qquad (6.38)$$

Consequently, we can write

$$v(t) = -\sum_{n'=1}^{\mathcal{N}} \sum_{n=n'+1}^{\mathcal{N}} e^{-i\Delta E_{n',n} \cdot t} (\rho_0 \circ V)_{n',n} - \sum_{n'=1}^{\mathcal{N}} \sum_{n=n'+1}^{\mathcal{N}} e^{i\Delta E_{n',n} \cdot t} (\rho_0 \circ V)^*_{n',n}, \qquad (6.39)$$

where now both sums only include positive frequencies, *i.e.*, we have $\Delta E_{n',n} > 0$ for all considered combinations of n and n'. Expression (6.39) is equivalent to

$$v(t) = -2\,\Re \left[\sum_{n'=1}^{\mathcal{N}} \sum_{n=n'+1}^{\mathcal{N}} e^{-i\Delta E_{n',n} \cdot t} (\rho_0 \circ V)_{n',n} \right], \qquad (6.40)$$

where $\Re$ denotes the real part. A change of the summation indices such that only one index remains leads to

$$v(t) = -2\,\Re \left[\sum_{k=1}^{N} e^{-i\Delta E_k \cdot t} (\rho_0 \circ V)_k \right], \qquad (6.41)$$

where the sum now runs up to $N = (\mathcal{N}^2 - \mathcal{N})/2$. Substituting Eqs. (6.37) and (6.38) results in

$$v(t) = -2 \sum_{k=1}^{N} \sin(\Delta E_k \cdot t)\, \Im\left[(\rho_0 \circ V)_k \right]. \qquad (6.42)$$

Consequently, the mean velocity can also be written as

$$v(t) = -2\,\Im \left[\int_0^\infty d\Delta E\, e^{-i\Delta E t} G_{\rho_0 V}(\Delta E) \right], \qquad (6.43)$$

where, in close analogy to the LDoS $D(E)$, Eq. (6.26), we define the distribution of frequencies as

$$G_{\rho_0 V}(\Delta E) = \sum_{k=1}^{N} \Im\left[(\rho_0 \circ V)_k \right] \delta(\Delta E - \Delta E_k). \qquad (6.44)$$

That is, $v(t)$ is uniquely defined by the Fourier transform[16] of the frequency distribution $G_{\rho_0 V}(\Delta E)$, which will be investigated in detail in Sec. 6.4.3.

---

[16]Note that as opposed to Eq. (6.32), where the integral stretches from $-\infty$ to ∞, here we only consider an integration from 0 to ∞ since all frequencies ΔE appearing in the frequency distribution $G_{\rho_0 V}(\Delta E)$ are strictly positive, $\Delta E > 0$.

6.4.2.1 Relation to the survival probability

An analogous expression can be found for the survival probability $P(t)$, if we first rewrite Eq. (6.32) as

$$
\begin{aligned}
P(t) &= \left| \sum_{n=1}^{\mathcal{N}} e^{-iE_n t} \langle \psi_0 | n \rangle \langle n | \psi_0 \rangle \right|^2 \\
&= \sum_{n,n'=1}^{\mathcal{N}} e^{-i(E_{n'} - E_n)t} \langle n' | \psi_0 \rangle \langle \psi_0 | n \rangle \langle n | \psi_0 \rangle \langle \psi_0 | n' \rangle \\
&= \sum_{n,n'=1}^{\mathcal{N}} e^{-i\Delta E_{n',n} t} \rho_{0n',n} \rho_{0n,n'} \, .
\end{aligned}
\tag{6.45}
$$

This closely resembles expression (6.33) and, in complete analogy to the procedure above, it can be recast in the form

$$
P(t) = \sum_{n=1}^{\mathcal{N}} \rho_{0n,n}^2 + 2\Re \left[\int_0^\infty d\Delta E \, e^{-i\Delta E t} G_{\rho_0}(\Delta E) \right] ,
\tag{6.46}
$$

where we define

$$
G_{\rho_0}(\Delta E) = \sum_{k=1}^{N} (\rho_0 \circ \rho_0)_k \, \delta(\Delta E - \Delta E_k) \, .
\tag{6.47}
$$

Comparing expression (6.43) for the velocity to Eq. (6.46), we find that $v(t)$ and $P(t)$ can be expressed such that they have the same functional structure. While the former is given by the imaginary part of the Fourier transform of the corresponding frequency distribution $G_{\rho_0 V}(\Delta E)$, the latter is given by the real part of the Fourier transform of $G_{\rho_0}(\Delta E)$. In addition, the survival probability contains a time-indendent term, which stems from the diagonal contributions of the initial density matrix and is nothing else but the inverse participation ratio (IPR) defined in Eq. (5.2). In the case of the velocity, this term also appears, as $(\rho_0 \circ V)_{n,n}$, but vanishes exactly since V has a vanishing diagonal.

In analogy to $G_{\rho_0 V}(\Delta E)$ and $G_{\rho_0}(\Delta E)$, we define the distribution

$$
G_V(\Delta E) = \sum_{k=1}^{N} \Im [V_k] \, \delta(\Delta E - \Delta E_k) \, ,
\tag{6.48}
$$

which does not correspond to any dynamical quantity. However, since $G_{\rho_0 V}(\Delta E)$ is obtained from $G_{\rho_0}(\Delta E)$ by simply replacing one of the ρ_0 in expression (6.47) by V, it provides valuable insight whether ρ_0 or V dominates the frequency distribution of interest, $G_{\rho_0 V}(\Delta E)$.
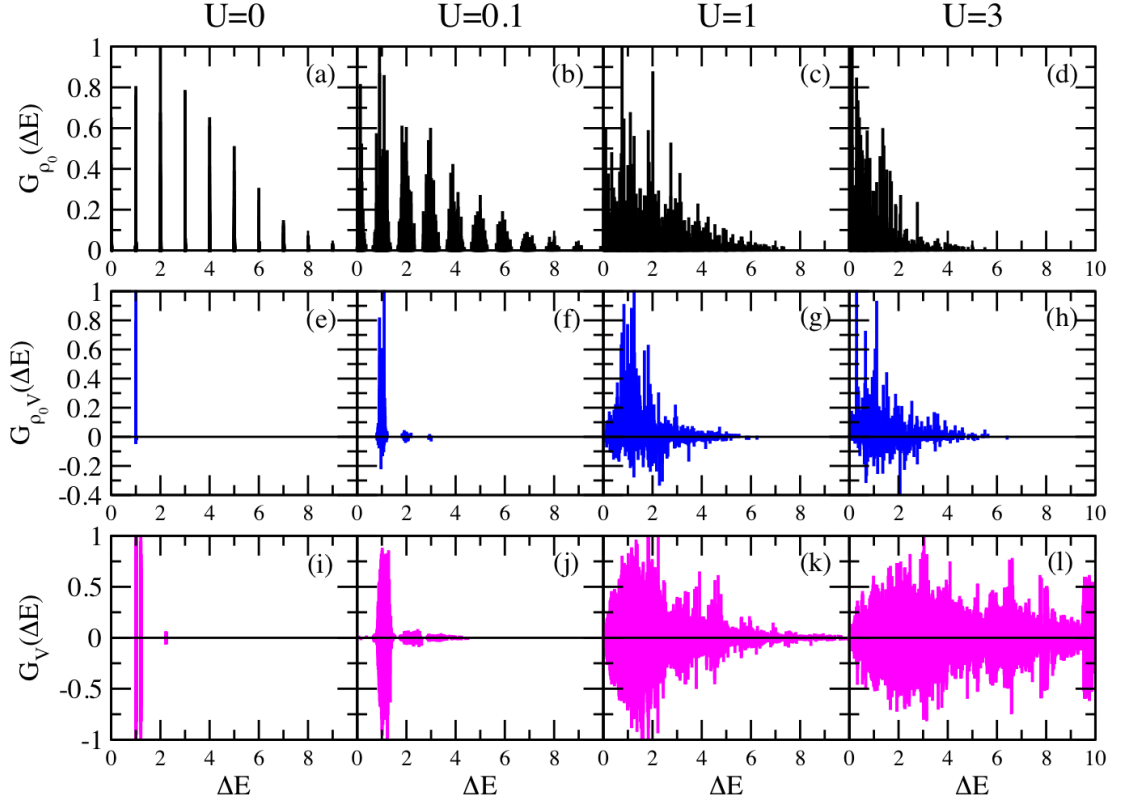
6.4.3 Frequency distributions

In Fig. 6.18, we have already witnessed the importance of weighting ρ_0 with V^T which enters the expression for the velocity $v(t)$. In the following, we will analyze the corresponding frequencies by investigating the distributions $G_{\rho_0}(\Delta E)$, Eq. (6.47), $G_{\rho_0 V}(\Delta E)$, Eq. (6.44), and $G_V(\Delta E)$, Eq. (6.48), where the former two dictate the time evolution of the survival probability and the velocity, respectively.

Fig. 6.19 shows all three distributions as a function of ΔE, for the interaction strengths $U = 0, 0.1, 1$ and 3. Before we discuss details of the distributions, we note that in the case of $G_{\rho_0}(\Delta E)$ (top row), all coefficients are strictly positive, since $(\rho_0 \circ \rho_0)_k = \rho_{0k}^2$. On the contrary, $G_{\rho_0 V}(\Delta E)$ (middle) and $G_V(\Delta E)$ (bottom), can turn negative, since the matrix elements of ρ_0 and V enter only linearly. In order to understand the implications thereof on the Bloch oscillations, consider the following: As obvious from expression (6.42), the contributions of two coefficients with amplitudes $a_k = -a_j$ and identical frequencies $\Delta E_k = \Delta E_j$ cancel exactly. In contrast, if only positive (or, likewise, only negative) coefficients are involved, a vanishing velocity requires a dephasing of the individual contributions which can only result from (incommensurate) frequencies.

Note that, in the distribution $G_{\rho_0 V}(\Delta E)$, that determines the temporal behavior of the velocity $v(t)$, positive coefficients always dominate the distribution. Negative coefficients are only relevant for strong interactions U, what corresponds to a regime where Bloch oscillations are completely suppressed, even for very short times, see Fig. 6.17 (l). We also note again that the distribution $G_V(\Delta E)$, which has as many negative as positive coefficients, does not have any immediate meaning for the dynamics of the system. Since eventually we want to study the integrated frequency distributions (see Sec. 6.4.3.1), in the following, we consider the absolute values of the distributions that are depicted in Fig. 6.20, and do not discuss Fig. 6.19 in more detail.

For noninteracting particles, $U = 0$, we observe a sharp, peaked structure of all three frequency distributions, what implies that only a limited number of well-defined frequencies contribute to the dynamics. Specifically, all frequencies in $|G_{\rho_0}(\Delta E)|$ fulfill the condition $\Delta E = l$, where $l \in \mathbb{N}$ and, consequently, the fundamental period $T = 2\pi/\Delta E = 2\pi$ is identical to the Bloch period T_B.[17] As a consequence, the survival probability $P(t)$ is expected to be periodic with T_B, with a strong suppression of the amplitude at times $t \neq l \cdot T_B$, due to the admixture of higher harmonics. In the case of $|G_{\rho_0 V}(\Delta E)|$, only one peak with frequency $\Delta E = 1$ appears, and from Eq. (6.42) we thus expect the velocity to feature perfect,

---

[17]Note that here we choose $F = 1$ for the static field strength. However, completely analogous behavior is also found for $F \neq 1$, if the distributions are plotted as a function of $\Delta E/F$, what corresponds to measuring time in units of the Bloch period, *i.e.*, t/T_B. We then have $\Delta E/F = l$, with $l \in \mathbb{N}$, and the fundamental period again corresponds to the Bloch period $T_B = 2\pi/F$.

Figure 6.19: Top: frequency distribution $G_{\rho_0}(\Delta E)$, Eq. (6.47), middle: $G_{\rho_0 V}(\Delta E)$, Eq. (6.44), and bottom: $G_V(\Delta E)$, Eq. (6.48), for the same system parameters as in Fig. 6.17, and again $U = 0, 0.1$, 1, and 3, as a function of ΔE. The distributions are normalized, such that the highest peak for each interaction strength equals 1.

sinusoidal Bloch oscillations. These findings are in *perfect* agreement with our dynamical observations of Fig. 6.17 (e) and (i). The distribution $|G_V(\Delta E)|$ is dominated by two peaks at positions $\Delta E = 1$ and $\Delta E \approx 1.2$. However, as discussed above, $|G_{\rho_0}(\Delta E)|$ only has contributions at integer multiples of $\Delta E = 1$, and, consequently, only the former peak can also be found in $|G_{\rho_0 V}(\Delta E)|$. Vice versa, all frequencies $\Delta E \neq 1$ that appear in $|G_{\rho_0}(\Delta E)|$, are suppressed in $|G_{\rho_0 V}(\Delta E)|$, since $|G_V(\Delta E)|$ singles out the contribution at $\Delta E = 1$.

For nonvanishing but weak interactions, $U = 0.1$, the formerly perfect peaks in the distributions are broadened. Although $|G_V(\Delta E)|$ again singles out the contribution of $|G_{\rho_0}(\Delta E)|$ around $\Delta E = 1$ (*i.e.*, $|G_{\rho_0 V}(\Delta E)|$ is still dominated by the velocity operator) now also frequencies that slightly deviate from the inverse Bloch period $2\pi/T_B$ contribute to the dynamics. This causes a dephasing of the oscillations over time, as we observed in Fig. 6.17 (f) and (j).
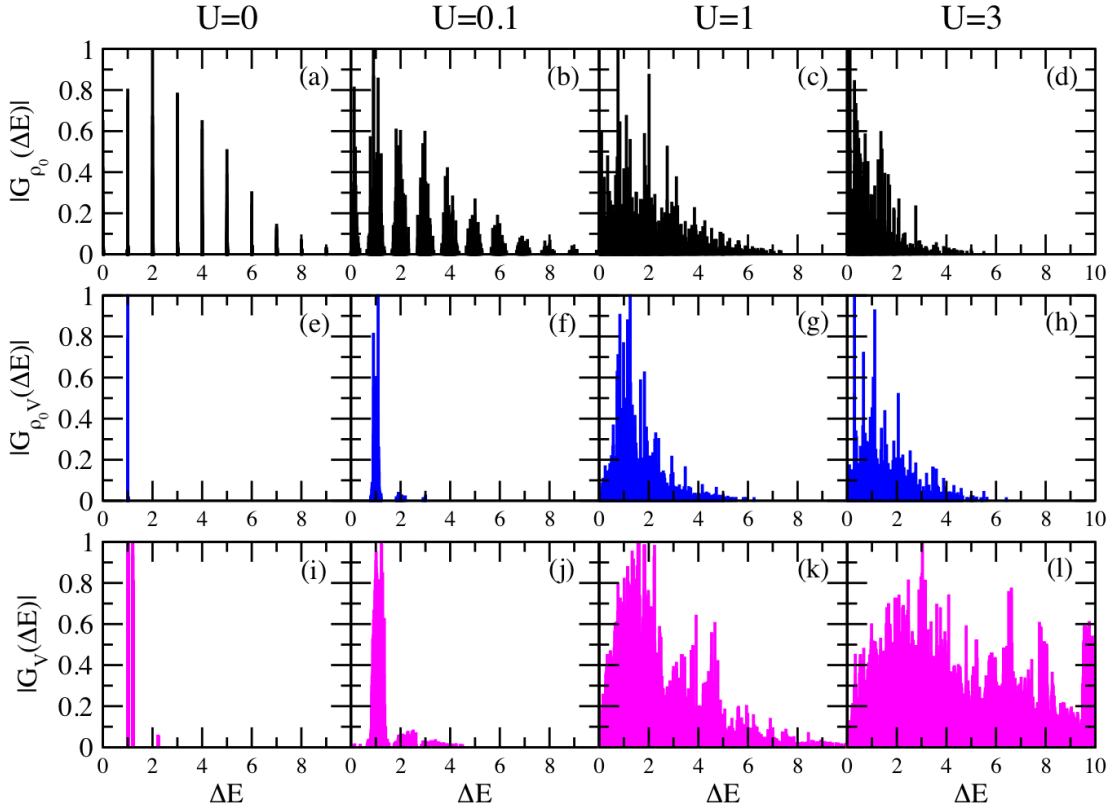
Figure 6.20: Absolute values of the frequency distributions $G_{\rho_0}(\Delta E)$, Eq. (6.47), $G_{\rho_0 V}(\Delta E)$, Eq. (6.44), and $G_V(\Delta E)$, Eq. (6.48), for the same system parameters as used in Figs. 6.17 and 6.19.

In the case of stronger interactions, $U = 1$, all three frequency distributions are broadly distributed, over a large frequency range, and single peaks can hardly be resolved. Note that the shape of $|G_{\rho_0 V}(\Delta E)|$ is no longer dominated by $|G_V(\Delta E)|$, and the three distributions strongly resemble each other. Only the suppression of $|G_{\rho_0 V}(\Delta E)|$ at small values of ΔE results from the vanishing diagonal of the velocity operator. In this regime, many frequencies contribute to the dynamics equally, leading to a rapid and irreversible dephasing of the Bloch oscillations (compare Fig. 6.17 (g) and (k)).[18]

For even stronger interactions, $U = 3$, the situation is similar. Moreover, now $|G_{\rho_0 V}(\Delta E)|$ rather resembles $|G_{\rho_0}(\Delta E)|$, since $|G_V(\Delta E)|$ is completely smeared out. Note that now also the negative contributions to $G_{\rho_0 V}(\Delta E)$ start to get relevant, see Fig. 6.19 (h), leading to a

---

[18]In a strict sense, for a finite number of coefficients in $G_{\rho_0 V}(\Delta E)$, irreversible dephasing of the Bloch oscillations can only be expected for incommensurate frequencies. While we did not analyze the incommensurability, we note that the revival time can, in any case, be expected to be arbitrarily large if sufficiently many distinct frequencies contribute to the dynamics.
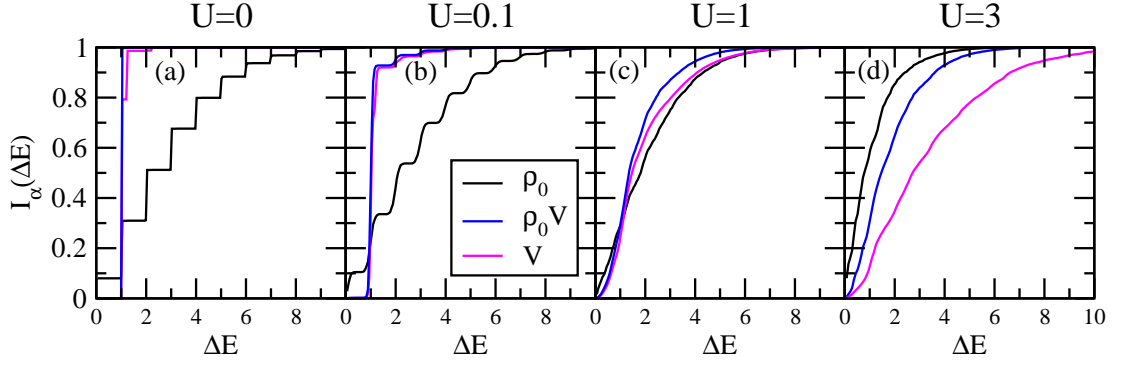
Figure 6.21: Integrated frequency distributions $I_{\rho_0}(\Delta E)$ (black), $I_{\rho_0 V}(\Delta E)$ (blue) and $I_V(\Delta E)$ (magenta), corresponding to the distributions shown in Fig. 6.20. The $I_\alpha(\Delta E)$ are defined in Eq. (6.49).

complete suppression of oscillations in $P(t)$ and $v(t)$ (see Fig. 6.17 (h) and (l)).

6.4.3.1 Integrated distributions

As mentioned above, we now consider the integrated distributions

$$I_\alpha(\Delta E) = \frac{1}{N_I} \int\limits_0^{\Delta E} dE' \, |G_\alpha(\Delta E')|, \qquad (6.49)$$

where α stands for either ρ_0, $\rho_0 V$, or V, and the normalization N_I is chosen such that $I_\alpha(\Delta E \to \infty) = 1$. The $I_\alpha(\Delta E)$ have the advantage that they resolve data points that are degenerate in frequency, and allow to directly extract certain properties of the distributions such as their widths and the median, both of which will be important in the following discussion. All three integrated distributions $I_{\rho_0}(\Delta E)$, $I_{\rho_0 V}(\Delta E)$, and $I_V(\Delta E)$ are shown in Fig. 6.21, for the same physical situation as assumed in Fig. 6.20, and we briefly discuss their relation to the distributions $|G_\alpha(\Delta E)|$, before turning to a quantitative analysis.

For (a) noninteracting particles, $U = 0$, we observe a sharp step structure that reflects the peaks of Fig. 6.20 (first column). Note that, as observed above, in this regime $I_{\rho_0 V}(\Delta E)$ is well approximated by $I_V(\Delta E)$. For (b) $U = 0.1$, the steps in the distributions are rounded off, reflecting the broadening of the peaks in the second column of Fig. 6.20. Again, $I_{\rho_0 V}(\Delta E)$ is dominated by the integrated distribution $I_V(\Delta E)$. For (c) stronger interactions, $U = 1$, the step structure is completely lost, and many different frequencies contribute. This corresponds to the broad distributions we observed in Fig. 6.20 (third column), where single peaks are essentially not resolved any more. Note that now, all three integrated distributions are almost identical and, in particular, $I_{\rho_0 V}(\Delta E)$ is no longer dominated by $I_V(\Delta E)$.
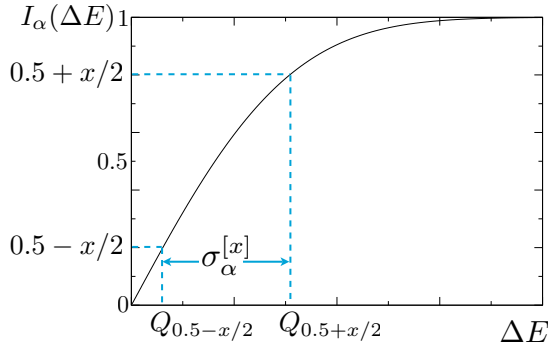
Figure 6.22: Definition of the width $\sigma_\alpha^{[x]}$ of the integrated frequency distribution $I_\alpha(\Delta E)$ via the quantiles $Q_{0.5+x/2}$ and $Q_{0.5-x/2}$. Here, $x \in [0, 1]$ quantifies the fraction of the distribution that is considered.

The situation is similar in the case (d) of even stronger interactions, $U = 3$, where, however, $I_V(\Delta E)$ and $I_{\rho_0}(\Delta E)$ have exchanged their character, *i.e.*, the former is now much broader that the latter. Furthermore, for such strong interactions, $I_{\rho_0 V}(\Delta E)$ rather resembles $I_{\rho_0}(\Delta E)$.

6.4.3.2 Width of the integrated distributions

In order to quantify our above statements, we also consider the widths of the distributions

$$\sigma_\alpha^{[x]} = Q_{0.5+x/2} - Q_{0.5-x/2}, \tag{6.50}$$

which we define via the quantiles $Q_{0.5+x/2}$ and $Q_{0.5-x/2}$, where $x \in [0, 1]$, as depicted schematically in Fig. 6.22. With this definition, $\sigma_\alpha^{[x]}$ is the frequency width in ΔE that accounts for the central $100 \cdot x\%$ of the distribution $I_\alpha(\Delta E)$. In the following, we refer to the width $\sigma_{\rho_0 V}^{[x]}$ of the distribution $I_{\rho_0 V}(\Delta E)$ as Γ, since it constitutes an important dynamical quantity.

We show $\sigma_\alpha^{[x]}$ for all three integrated distributions with $x = 0.6$, as a function of $U \cdot n/m$, on a double-logarithmic scale in Fig. 6.23 (a). Since we fix $x = 0.6$, we can skip the label $[x]$, *i.e.*, instead of $\sigma_\alpha^{[0.6]}$ we simply write σ_α in the following.[19] The system is again defined as in Fig. 6.17, however, we also vary the particle number, *i.e.*, consider the ground states of $n = 4$, $n = 5$, and $n = 6$ particles in a lattice with $m = 5$ sites as initial states. The scaling of the x-axis is chosen as suggested by the analysis in Sec. 3.3, where we had found universal spectral behavior of the Bose-Hubbard system for fixed effective onsite interaction $U \cdot n/L$. We find that this scaling is also applicable here, since for different particle numbers n, the widths σ_α of the three distributions behave completely analogously. As discussed on p. 87,

---

[19]Although we restrict our discussion to $x = 0.6$, we have verified that our findings also hold for other choices, as long as x is mall enough to resolve the structure of the integrated distribution. This threshold is approximately given by $x \lesssim 0.7$.

we here use the number of initially occupied sites m rather than the total number of lattice sites L, which is chosen large such as to avoid numerical artifacts. This choice is justified since, for $F = 1$, the particles hardly spread over the lattice and, consequently, m is the physically relevant quantity.

The fact that, depending on the interaction strength, $I_{\rho_0 V}(\Delta E)$ can either be approximated by $I_{\rho_0}(\Delta E)$ or by $I_V(\Delta E)$ is also reflected in the widths σ_α of the distributions. Specifically, we find that for $U \cdot n/m \leq 0.4$, Γ is basically identical to σ_V. In this regime,[20] Γ grows with increasing interaction strength. For $0.4 \leq U \cdot n/m \leq 2$, the situation changes and the widths σ_α of all three distributions are comparable. For even stronger interactions $U \cdot n/m \geq 2$, we find that σ_V keeps increasing, while Γ has saturated and is now limited by σ_{ρ_0}. This can be understood from the behavior of V and ρ_0 under changes of the interaction strength that we discussed in Sec. 6.4.2 (see, in particular, Fig. 6.18). There we had found that ρ_0 is almost unaffected by changes of U, while V gets smeared out with increasing interaction strength and, consequently, its width σ_V increases.

Naturally, the question to ask is what distinguishes the different regimes we identified above? To answer this, we plot in Fig. 6.23 (b) the deviation Δ^2, Eq. (3.19), of the tilted Bose-Hubbard Hamiltonian's nearest-neighbor level-spacing distribution from universal statistics[21], as a function of the scaled onsite interaction strength $U \cdot n/m$, on a semi-logarithmic scale. In analogy to the scaling with n/m instead of n/L discussed just above, we consider for this analysis the effective spectrum (see also p. 87). In the specific example considered here, this means that we investigate the spectral statistics of $n = 4$, 5, and 6 bosons on a tilted lattice with 5 sites.

We find that for $U \cdot n/m \leq 0.4$, all three considered realizations are regular, since the deviation from Poissonian statistics is small. This exactly corresponds to the regime where Γ is identical to the width of $I_V(\Delta E)$, which is determined by the velocity operator in the eigenbasis of the tilted Hamiltonian. On the contrary, for $0.4 \leq U \cdot n/m \leq 2$, we find that the different realizations are best described by chaotic level statistics, since here the deviation from GOE statistics is small. As pointed out above, in this parameter regime, all three integrated frequency distributions $I_\alpha(\Delta E)$ closely resemble each other, and, consequently, also the widths σ_α are comparable. For $U \cdot n/m \geq 2$, the level-spacing distribution once more changes its character and the system turns regular again. In this regime, the distribution $I_{\rho_0 V}(\Delta E)$, and in particular its width, is well described by $I_{\rho_0}(\Delta E)$.

In summary, we have found that in the regular regime of the Hamiltonian, the distribution $I_{\rho_0 V}(\Delta E)$, which dictates the temporal behavior of the velocity, is either dominated by the

---

[20]For very weak interactions, the width Γ is usually overestimated, *i.e.*, the actual values lie below the ones depicted in Fig. 6.23 (a). This stems from the finite binning of ΔE, what is most critical for very steep integrated distributions $I_\alpha(\Delta E)$, that arise for small U and $\alpha = \rho_0 V$, V.

[21]For a thorough discussion of universal spectral statistics see Chapter 3.
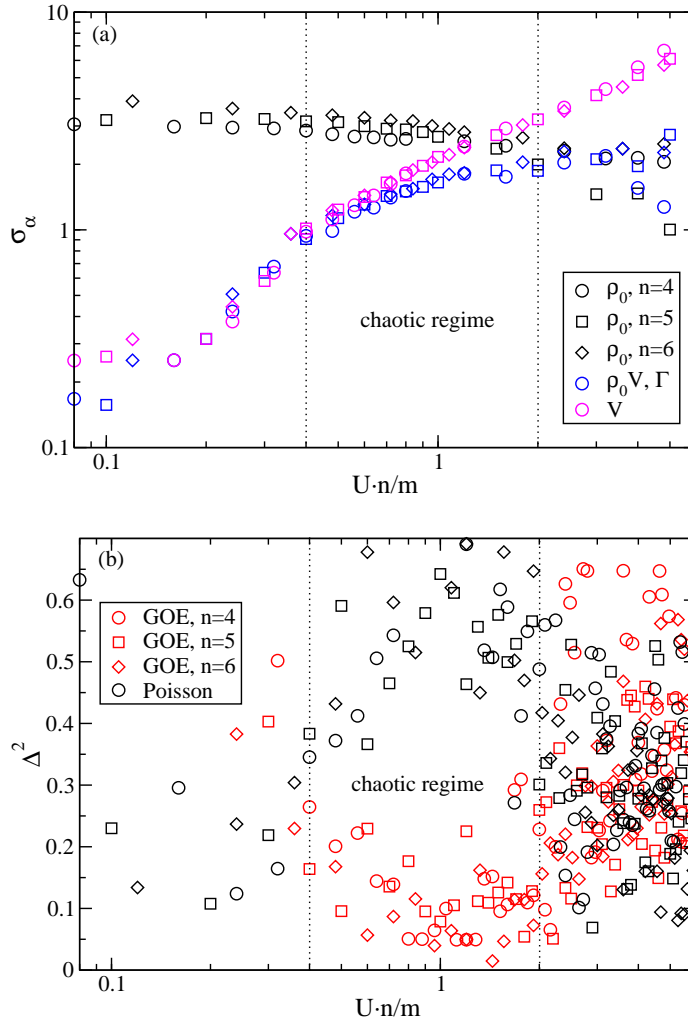
Figure 6.23: (a) Width σ_α, Eq. (6.50), of the integrated frequency distribution $I_{\rho_0}(\Delta E)$, Eq. (6.47), (black symbols), $I_{\rho_0 V}(\Delta E)$, Eq. (6.44), (blue symbols), and $I_V(\Delta E)$, Eq. (6.48), (magenta symbols), as a function of the scaled interaction $U \cdot n/m$, on a double-logarithmic scale. (b) Deviation Δ^2, Eq. (3.19), of the effective spectrum's nearest neighbor level spacing distribution from universal GOE, *i.e.*, chaotic, statistics (red symbols) and from universal Poissonian, *i.e.*, regular, statistics (black symbols), also as a function of $U \cdot n/m$, on a semi-logarithmic scale. The parameters are chosen as in Fig. 6.17. In addition to the case of $n = 5$ particles (squares), also data for $n = 4$ (circles) and $n = 6$ (diamonds) particles are shown, with red and black symbols again referring to the deviation from GOE and Poissonian statistics. Vertical dotted lines indicate the transitions between regular and chaotic level statistics.
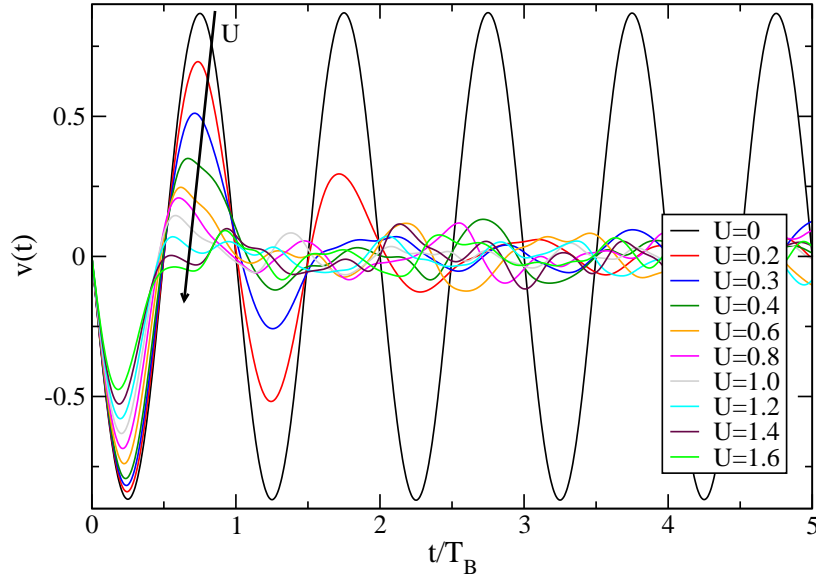
Figure 6.24: Mean velocity $v(t)$, Eq. (6.6), as a function of time, in units of the Bloch period T_B, for $n = m = 5$, $L = 11$, and various interaction strengths U (see legend). The tunneling coupling and the static field strength are $J = F = 1$.

initial density matrix ρ_0 (for very small interactions), or by the velocity operator $\hat{V}$ (for sufficiently large interactions). In contrast, in the chaotic regime both operators contribute equally, and thus knowledge of both quantities is needed in order to determine the exact shape of the distribution.

Since the mean velocity $v(t)$ is uniquely determined by the Fourier transform of $G_{\rho_0 V}(\Delta E)$, see Eq. (6.43), we expect the *statistical* features discussed above to directly relate to the *dynamical* behavior of the Bloch oscillations. In the following, we thus quantify the Bloch oscillations' decay and investigate how it reflects the spectral properties of the Hamiltonian. More precisely, we will show that a large width Γ of the frequency distribution $I_{\rho_0 V}(\Delta E)$ implies a rapid decay of the oscillations, expressed by a large *decay constant*.

6.4.4 Quantifying the decay of the Bloch oscillations

We now return to the *dynamical* behavior of the Bloch oscillations discussed in Sec. 6.2.2. In Fig. 6.24, we plot the mean velocity $v(t)$, Eq. (6.6), as a function of time, in units of the Bloch period T_B, for various interaction strengths U, fixed $J = F = 1$, $n = m = 5$, and $L = 11$. In general, we find that the larger U, the faster the decay. More precisely, whereas for weak interactions, $U < 0.4$, the dynamics appears damped periodic, for $U > 0.4$ already the second extremum is considerably distorted. Furthermore, for the strongest interactions
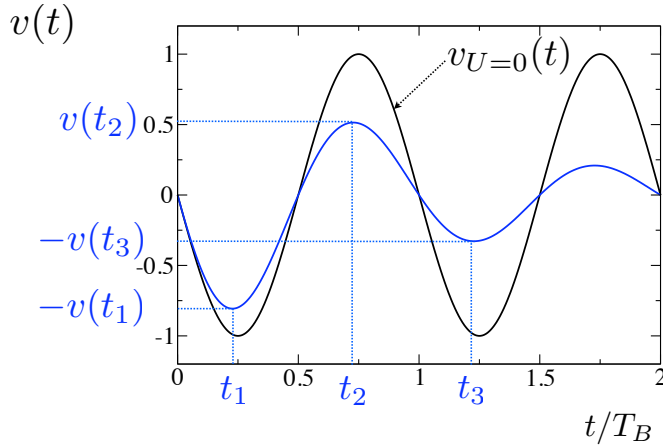
Figure 6.25: Definition of the velocity's extremal amplitudes $v(t_1)$, $v(t_2)$, and $v(t_3)$ used to extract the decay constant of the Bloch oscillations γ, see Eq. (6.52). The black line $v_{U=0}(t)$ corresponds to vanishing interaction strength.

depicted here ($U = 1.6$), the oscillatory behavior is almost completely suppressed and only the first excursion of $v(t)$ is significantly larger than the residual fluctuations[22]. We also observe a shift of the extrema of $v(t)$ to shorter times with increasing interaction strength, what will be investigated in Secs. 6.4.4.1 and 6.4.5.1.

To quantify the decay of the Bloch oscillations, we first seek a qualitative characterization of the dynamical behavior. As suggested by Ref. [28], we assume an exponentially decaying envelope

$$v(t) = v_{U=0}(t)\,e^{-\gamma \cdot t}, \qquad (6.51)$$

where $v_{U=0}(t)$ is the velocity that results for vanishing interaction strength (black line in Fig. 6.24[23]), and $\gamma > 0$ is the *decay constant*. We then define γ_k by fitting to the velocity's k-th extremum $v(t_k)$, at time t_k (see also the schematic diagram in Fig. 6.25), as

$$\gamma_k = -\ln\left(\frac{v(t_k)}{v_{U=0}(t_k)}\right) \cdot \frac{1}{t_k}. \qquad (6.52)$$

If the γ_k obtained from different extrema $v(t_k)$ of the numerical data are identical, the Bloch oscillations decay exponentially as a function of time.

Fig. 6.26 (a) shows γ_1 (red symbols), γ_2 (green symbols), and γ_3 (black symbols) for the same system parameters as in Fig. 6.23, again as a function of the scaled interaction

---

[22]The magnitude of the asymptotic fluctuations depends inversely on the Hilbert-space dimension, and is thus smaller for larger systems.

[23]Note that in Fig. 6.24 the amplitude of the velocity's oscillations for $U = 0$ is smaller than one. As we already pointed out above, this results from the definition of the velocity operator $\hat{V}$ for Dirichlet boundary conditions, Eq. (6.8). For periodic boundary conditions (6.9) the amplitude equals one. For other aspects of the temporal behavior of $v_{U=0}(t)$ see Appendix B.
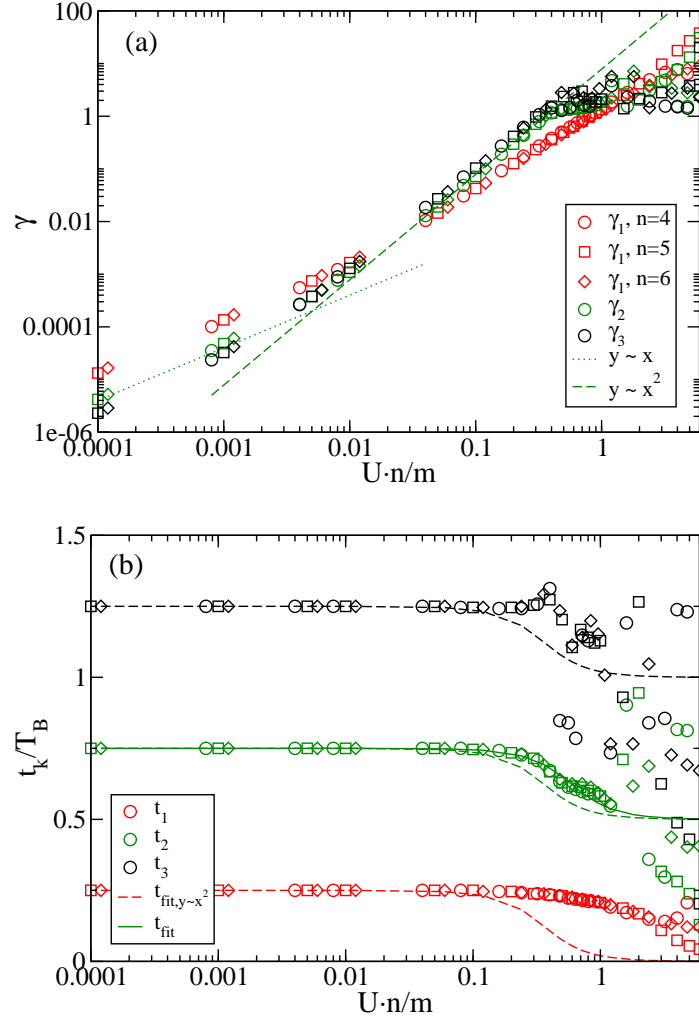
Figure 6.26: (a) Decay constant γ and (b) times t_k of the oscillations' extrema as a function of the scaled interaction strength $U \cdot n/m$, on a logarithmic scale. The system parameters are chosen as in Fig. 6.23. Here, γ_1 and t_1 (red symbols), γ_2 and t_2 (green symbols), and γ_3 and t_3 (black symbols) correspond to the first, the second, and the third extremum of $v(t)$, see Fig. 6.25 and definition (6.52). In panel (a), the dotted and dashed lines correspond to $y \sim x$ and $y \sim x^2$, respectively. The latter is obtained from a fit to γ_2 in the interval $0.04 \leq U \cdot n/m \leq 0.4$, see Eq. (6.53). In panel (b), the dashed lines correspond to the times $t_{fit,y \sim x^2}$ obtained by inserting the quadratic fit (6.53) in Eq. (6.54), and the solid green line t_{fit} represents a fit of the functional form (6.54) to the numerical data t_2, see Eq. (6.55).

strength[24] $U \cdot n/m$, on a double-logarithmic scale. As expected from the data in Fig. 6.24, we find that all three values increase with $U \cdot n/m$, *i.e.*, the stronger the interactions, the faster the oscillations are destroyed. We also reconfirm that the appropriate scaling of the interaction strength is provided by n/m. For $U \cdot n/m > 1.2$, the data scatter erratically and also Bloch oscillations can hardly be observed at all (see Figs. 6.17 (l) and 6.24). Consequently, for such strong interactions, the definition of a decay constant is not meaningful.

Interestingly, while γ_2 and γ_3 show the same functional behavior for $U \cdot n/m \leq 0.4$, γ_1 deviates significantly. That is, we observe some transient behavior before the velocity's dynamics can properly be described (from the second extremum onwards) by expression (6.51). Hence, the Bloch oscillations do not feature a simple exponential decay. In the following, we will not investigate the short-time behavior, expressed by γ_1, in more detail. We rather focus on the different regimes that can be distinguished in the functional dependence of γ_2 and γ_3 on $U \cdot n/m$, which imply qualitatively distinct dynamics.

We observe that the two decay rates γ_2 and γ_3 feature a transition from linear to quadratic increase at $U \cdot n/m \approx 5 \cdot 10^{-3}$, as highlighted by the dotted and dashed lines in Fig. 6.26 (a). While the former is simply drawn to guide the eye,[25] the latter represents a polynomial fit to the numerical data γ_2 in the interval $0.04 \leq U \cdot n/m \leq 0.4$ and corresponds to

$$\gamma_2 = 7.84 \cdot (U \cdot n/m)^2 \,. \tag{6.53}$$

The observed increase suggests that for $U \cdot n/m < 5 \cdot 10^{-3}$, first-order perturbation theory in $U \cdot n/m$ can be used to explain the oscillations' decay, whereas for $U \cdot n/m > 5 \cdot 10^{-3}$, second-order contributions are dominant. For $U \cdot n/m \geq 0.4$, the quadratic increase breaks down and, furthermore, γ_2 and γ_3 start to deviate from each other. This behavior again reflects that already the second and, even more so, the third extremum of $v(t)$, is considerably distorted in this parameter regime (see Fig. 6.24), what we will discuss in more detail in Sec. 6.4.5.

6.4.4.1 Temporal shift of the velocity's extrema

As pointed out above, the decay of the oscillations is also reflected in a temporal shift of the velocity's extrema that we further quantify in the following. In order to obtain an expression for this shift as a function of the decay constant, we assume perfect sinusoidal oscillations in the case of vanishing interactions, *i.e.*, $v_{U=0}(t) = -v_0 \sin(t/T_B)$, what yields

---

[24]Note that, in contrast to Fig. 6.23, here also data for very weak interactions, *i.e.*, down to $U \cdot n/m = 10^{-4}$, are shown, in order to develop an intuition of the Bloch oscillations' dependence on the interaction strength.

[25]Since we are mainly interested in the chaotic regime of the Hamiltonian that corresponds to larger values of the interaction strength, we do not investigate the regime of very weak interactions $U \cdot n/m < 5 \cdot 10^{-3}$ in great detail. We thus do not have enough data points for a reliable fit.

a good approximation to the dynamics in the current context (see also Appendix B). A simple calculation starting from Eq. (6.51) then leads to

$$t_k = (\arctan(1/\gamma) + (k-1) \cdot 0.5) \cdot T_B. \tag{6.54}$$

For noninteracting particles with $\gamma = 0$, we thus have $t_1 = 0.25 \cdot T_B$, $t_2 = 0.75 \cdot T_B$, and $t_3 = 1.25 \cdot T_B$.

The numerical values of t_1, t_2, and t_3 are shown in units of the Bloch period T_B, as a function of $U \cdot n/m$ in Fig. 6.26 (b). We find that, as discussed above, for $U \cdot n/m > 0.1$ the extrema are shifted to shorter times as U increases, while for smaller scaled interaction strengths no shift occurs. Here, the dashed lines $t_{fit, y \sim x^2}$ are obtained by inserting the quadratic fit (6.53) in expression (6.54). As expected already from the data for the decay constants depicted in Fig. 6.26 (a), t_1 deviates significantly from the theoretical curve for $U \cdot n/m > 0.1$, *i.e.*, as soon as a shift can be observed. In contrast, t_2 behaves qualitatively consistently with the theoretical expectation, and even features the same functional dependence. It does, however, not follow the curve $t_{fit, y \sim x^2}$, but is best described by the fit t_{fit} obtained by choosing

$$\gamma = 2.89 \cdot (U \cdot n/m)^2 \tag{6.55}$$

in Eq. (6.54) (solid green line). That is, the second extremum is shifted less than expected. The time corresponding to the third extremum t_3 again differs strongly from the fit $t_{fit, y \sim x^2}$ (for $U \cdot n/m > 0.1$) and also does not exhibit the functional behavior (6.54). This once more reflects the strong deviations from periodic behavior as found in Fig. 6.24, and the consequent deviations between γ_2 and γ_3 for $U \cdot n/m \geq 0.4$.

To summarize, we have found that the Bloch oscillation feature a more complicated temporal behavior than the simple exponential decay of expression (6.51). However, for $U \cdot n/m < 1.2$, γ_2 provides a suitable quantity to characterize the velocity's dynamics as it captures the main features, *i.e.*, the decay of the oscillations and the temporal shift of the extrema. We will thus use it in the following, in order to relate the Bloch oscillations' decay to the spectral structure of the Hamiltonian and, eventually, establish a connection between the decay constant and the statistics of the velocity operator, expressed by the width Γ.

6.4.5 Decay of Bloch oscillations and statistics of the velocity operator

In Fig. 6.27 (a) we plot the decay constant γ_2 and the width Γ, extracted from the integrated distribution $I_{\rho_0 V}(\Delta E)$, as a function of the scaled interaction strength $U \cdot n/m$, on a double-logarithmic scale, for the same system parameters as in Fig. 6.23. Taking into account the
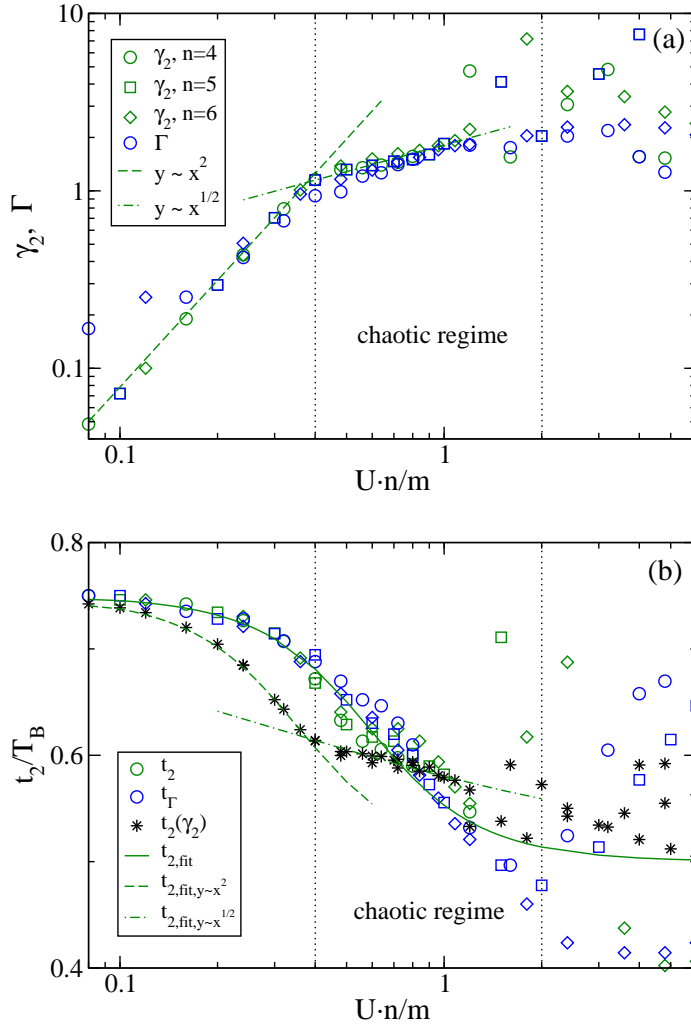
Figure 6.27: Relation between the decay of the Bloch oscillations and the statistics of velocity operator. Panel (a) depicts the decay constant γ_2, (green symbols) and the width Γ of the distribution $I_{\rho_0 V}(\Delta E)$ (blue symbols), compare Fig. 6.23 (a), as a function of the scaled interaction strength $U \cdot n/m$, on a double-logarithmic scale. Dashed and dashed-dotted lines correspond to $y \sim x^2$ and $y \sim x^{1/2}$, and represent fits to γ_2 in the intervals $0.04 \leq U \cdot n/m \leq 0.4$, Eq. (6.53), and $0.4 \leq U \cdot n/m \leq 1.2$, Eq. (6.56), respectively. Panel (b) shows the time t_2 of the second extremum (green symbols), again as a function of the scaled interaction strength $U \cdot n/m$, on a semi-logarithmic scale. In addition, the time t_Γ (blue symbols), Eq. (6.58), extracted from the median of the distribution $I_{\rho_0 V}(\Delta E)$, and the time $t_2(\gamma_2)$ (black stars), obtained from inserting the numerical values of γ_2 into Eq. (6.54), are shown. The fitted times $t_{2,fit}$ (green solid line), $t_{2,fit,y \sim x^2}$ (green dashed line), and $t_{2,fit,y \sim x^{1/2}}$ (green dashed-dotted line) again represent fits to the numerical data (compare Fig. 6.26). The system parameters are chosen as in Fig. 6.23, and vertical dotted lines indicate the transitions between regular and chaotic level statistics of the underlying tilted Bose-Hubbard Hamiltonian.

overestimation of Γ for small values of $U \cdot n/m$, that we discussed in Sec. 6.4.3.2, we find that γ_2 and Γ are proportional to each other as long as $U \cdot n/m < 1.2$. For larger interaction strengths, the proportionality $\gamma_2 \sim \Gamma$ breaks down, and both data sets scatter strongly. We note again that, in this regime, Bloch oscillations are almost completely suppressed (see Fig. 6.17 (l) and Fig. 6.24) and, accordingly, negative coefficients are relevant in the frequency distribution $G_{\rho_0 V}(\Delta E)$ (see discussion in Sec. 6.4.3). Consequently, both the concept of a decay constant γ and the definition of the width Γ are problematic, and a linear relation cannot be expected.

In detail, depending on the scaled interaction strength, two different regimes can be distinguished: For $U \cdot n/m \leq 0.4$, we find that both quantities increase quadratically with $U \cdot n/m$. This is highlighted by the dashed line with slope two that is obtained from a fit to γ_2, Eq. (6.53). As indicated by the vertical dotted lines, in this regime the underlying spectral structure is regular. When increasing the interaction strength to $U \cdot n/m \geq 0.4$, the quadratic behavior breaks down and, simultaneously, the system turns chaotic. In this regime, a power-law fit to γ_2 (dashed-dotted line) yields

$$\gamma_2 = 1.82 \cdot (U \cdot n/m)^{1/2}. \tag{6.56}$$

While the origin of this power law remains open, we can exclude second-order perturbation theory to capture the features of the dynamics.

The linear relation $\gamma_2 \sim \Gamma$ is exactly what we expect, since, according to (6.43), the velocity $v(t)$ can be obtained from the frequency distribution $G_{\rho_0 V}(\Delta E)$ with the help of a Fourier transformation. Consequently, the width Γ provides a measure for the decay of the Bloch oscillations expressed by γ_2 and vice versa.

6.4.5.1 Temporal shift of the extrema and median of the frequency distribution

One might wonder whether also the shift of the oscillations' extrema to smaller times with increasing interaction strength is reflected in the frequency distribution $I_{\rho_0 V}(\Delta E)$? In order to answer this, we define

$$T_\Gamma = \frac{2\pi}{\Delta E_m}, \tag{6.57}$$

where ΔE_m is the median of the distribution $G_{\rho_0 V}(\Delta E)$, i.e., $I_{\rho_0 V}(\Delta E_m) = 0.5$. Such as to compare it to the numerically obtained time of the second extremum t_2, which in the case of a perfect sinusoidal oscillation would be reached at $0.75 \cdot T_B$, we also introduce

$$t_\Gamma = 0.75 \cdot T_\Gamma. \tag{6.58}$$

In Fig. 6.27 (b) we plot the time t_2 of the second extremum, in units of the Bloch period T_B, as a function of the scaled interaction strength $U \cdot n/m$, for the same system parameters

as in Fig. 6.23. We find that for $U \cdot n/m < 1.2$, t_2 (green symbols) is well approximated by t_Γ (blue symbols), where the agreement is best in the regular regime $U \cdot n/m < 0.4$. That is, the frequency distribution $G_{\rho_0 V}(\Delta E)$ also provides a tool to describe the shift of the oscillations' extrema to shorter times with increasing interaction strength, and vice versa.

As in Fig. 6.26, we also show the fitted times $t_{2,fit}$ (solid line), and $t_{2,fit,y\sim x^2}$ (dashed line), and, furthermore, the time $t_{2,fit,y\sim x^{1/2}}$ (dashed-dotted line), obtained by inserting the fit (6.56) in Eq. (6.54). Moreover, we plot the time $t_2(\gamma_2)$ (black stars), obtained from inserting the numerical values of γ_2 into Eq. (6.54). The latter again affirms that the two fits in Fig. 6.27 (a) yield good approximations to the numerical data γ_2. However, as already seen in Fig. 6.26 (b), $t_2(\gamma_2)$ overestimates the temporal shift as compared to what we observe in the dynamics.

6.5 Conclusion

In the present chapter, we investigated Bloch oscillations of ultracold bosons in tilted optical lattices and found that they sensibly depend on the strength of the interatomic interactions. We defined a measure both for the distribution of relevant frequencies and for the oscillations' decay rate and found that the two quantities are proportional to each other over a wide range of the interaction strength. Most importantly, they exhibit a characteristic transition from quadratic to square root behavior at the same point that denotes the border between the regular and the chaotic regime of the Bose-Hubbard Hamiltonian.

Specifically, for fixed and comparable tunneling coupling and static field strength, we found that for weak interactions, where the system is regular, the frequency distribution is dominated by the velocity operator, and the decay of the oscillations can be well described by an exponential envelope. In this regime, the decay constant increases quadratically with the interaction strength. This scaling breaks down and is replaced by a distinct behavior with increasing interactions when entering the chaotic regime, although the decay of the oscillations is still exponential. In this regime, also the frequency distribution changes its character: It is no longer dominated by the velocity operator, but also the initial density matrix has to be considered. The situation changes once more for even larger interactions, where the system turns regular again. Here, Bloch oscillations do not occur since the amplitude is basically completely suppressed and the two measures for the distribution of relevant frequencies and for the oscillations' decay rate cannot be properly defined. For even larger interactions, different, resonance-induced oscillations occur.

The decay of the oscillations is also reflected in a shift of the extrema of $v(t)$ to shorter times, with increasing interaction strength, and we also identified traces of this behavior in the distribution of the relevant frequencies.

For the values of the interaction strength investigated here, the so-called dynamical instability may play an important role in the experiment and lead to a rapid destruction of the condensate, see for example [29, 45, 62, 201] and references therein. It is well described by mean-field theory and is not accounted for in the Bose-Hubbard model.[26] However, if the tunneling coupling is kept sufficiently small, the effect of the dynamical instability can be strongly suppressed. This renders an experimental realization of the discussed scenario feasible, since the parameters that define the dynamics can be essentially controlled at will [77, 125, 134].

In conclusion, we have found that the statistics of the underlying Hamiltonian directly relate to the behavior of the Bloch oscillations of ultracold bosons in optical lattices. That is, when the spectral regime is known, we can infer how the Bloch oscillations will behave. More importantly, also the reverse holds: the Bloch oscillations provide a tool to probe distinct spectral regimes of the system. More precisely, when observing an exponential decay where the decay constant grows quadratically with the scaled interaction strength, the system is regular. If the decay is exponential but the corresponding decay constant is proportional to the square root of the interactions, we know that we are in the chaotic regime. This provides us with a sensitive tool to probe the system's spectral structure, a venture that is hard to realize in many-body quantum systems.[27]

---

[26]Recently it was shown that dynamical instability can be related to Bogoliubov's depletion of the condensate in the framework of the Bose-Hubbard Hamiltonian [117].

[27]Spectroscopy of ultracold bosons has been applied to measure excitation spectra in the superfluid and the Mott insulating regime where distinct characteristic features could be detected [108, 170]. However, single energy levels could not be resolved, what is the prerequisite to directly detect universal spectral statistics. Recently, a matter-wave scattering approach was proposed to detect the spectral structure of the Bose-Hubbard system in Ref. [95].

7 Conclusions

In this thesis, we studied interacting ultracold bosons in tilted optical lattices. Since we focussed on genuine quantum effects, we investigated systems that consist of relatively few sites with filling factors of the order of one. For the mathematical description, we thus applied the tilted Bose-Hubbard Hamiltonian, the simplest nontrivial quantum many-body model that accounts for the competing interplay of interaction and kinetic energy. This competition induces complexity in the system which, on the spectral level, is reflected in chaotic level dynamics, *i.e.*, spectral chaos. Our key focus lied on the implications of the latter, which we discussed from three different perspectives: We investigated how the numerical simulability of the system is affected by the underlying spectral structure, identified robust states that survive within the chaotic regime of the Hamiltonian, and determined the spectral origin of the Bloch oscillations' decay.

The basis for these investigations was the precise knowledge of the system's spectral properties. In a first step, we thus identified spectrally chaotic and regular regimes in the tilted Bose-Hubbard Hamiltonian, employing methods from random matrix theory. Based on an energy argument, we performed a scaling analysis of the different contributions in the Bose-Hubbard Hamiltonian and found that the system is chaotic for comparable strengths of the tunneling coupling J and the scaled onsite interaction $U \cdot n/L$, as long as the static field does not dominate the system. We thus verified that different realizations of the system, concerning the number of bosons and of lattice sites, are equivalent in terms of their spectral structure if the Hamiltonian's parameters are chosen according to the found scaling. We numerically verified our predictions for various system sizes, spanning a large range of the Hilbert-space dimension, and determined the critical field strength that marks the transition point between chaotic and regular spectral statistics as the static field strength F increases.

Based on numerical simulations employing the time-dependent density matrix renormalization group algorithm, we showed that, at the transition from regular to chaotic spectral statistics, the possibility to efficiently simulate the system breaks down. This manifests in a broad distribution of dynamically generated Schmidt coefficients, what precludes the possibility of an effective basis truncation and leads to a highly unfavorable scaling of the numerical resources with the Hilbert-space dimension. Since chaoticity implies universal-

ity, expressed for example in universal spectral statistics, we stress that our results obtained via the tilted Bose-Hubbard system can be directly carried over to generic many-body quantum systems. Moreover, as universal level statistics, in turn, imply universal properties of the associated eigenstates, our findings can be expected to hold for renormalization algorithms in general.

Deep in the chaotic regime of the Bose-Hubbard Hamiltonian, we identified robust structures, reflected in straight lines in the spectrum, that are dynamically stable against perturbations. We confirmed this robustness by ramping up the tilt of the lattice, linearly in time, and found that the *solitonic* eigenstates associated with the above, stable spectral structures are strongly localized on the lattice. We showed that both Stark localization and energetic isolation can be ruled out as generating mechanism. The stability of these states is rather induced by a subtle interplay of interaction and tunneling dynamics, and relies on their weak coupling to the chaotic background.

In the last chapter, we turned to the dynamics of ultracold bosons in optical lattices and investigated the impact of the inter-particle interaction on the Bloch oscillations induced by the static tilt. Here, we focussed on the fast and irreversible decay of the oscillations in the chaotic regime of the Bose-Hubbard Hamiltonian. In order to establish a relation between the oscillations' dynamical decay and spectral quantities of the system, we followed two different approaches: The first one relied on the adiabatic theory of driven quantum systems, which we applied to the spectrum of the transformed, time-dependent Bose-Hubbard Hamiltonian. We showed that a fundamental prerequisite of this approach, namely the adiabaticity of the driving, is not fulfilled in the system at hand, what renders it inapplicable to describe the decay of the Bloch oscillations. The second approach which we developed in this work, is based on the statistics of the velocity operator. We defined a measure for both, the distribution of relevant frequencies, and for the oscillations' decay rate, and found that they are proportional to each other over a wide range of interaction strengths. Most importantly, these two quantities exhibit a characteristic crossover in their functional dependence on the interaction strength, at exactly the same point where the transition between the regular and the chaotic regime of the Bose-Hubbard Hamiltonian occurs.

In summary, we elucidated how the dynamics of ultracold bosons in optical lattices is determined by the underlying spectral structure of the Bose-Hubbard Hamiltonian. On the one hand, we showed how the onset of spectral chaos substantially hinders an efficient numerical treatment of the system, what makes it hard to reliably predict its behavior. On the other hand, we identified two distinct signatures of the Hamiltonian's spectral structure that are appealing for an experimental realization with state-of-the-art techniques: The *soli-*

tonic states are excellent candidates for coherent control since they are dynamically stable against external perturbations. The decay of the Bloch oscillations, in turn, provides us with a sensitive tool to probe the system's spectral structure by measuring readily accessible dynamical quantities, such as the velocity or the center of mass of the bosons on the lattice.

In this thesis, we focussed on genuine *quantum* effects that are observed in the limit of few particles on the lattice. In the literature, also systems with large particle numbers and filling factors have been intensely studied via the mean-field Gross-Pitaevskii equation, which represents the *classical* limit of ultracold bosons in optical lattices. These two well-established limits, together with the ever increasing experimental precision in the preparation and in the measurement, render the system an ideal candidate for a *quantitative* understanding of the quantum-to-classical transition, one of the fundamental questions in physics.

A Unfolding spectra

In general, the distribution of spacings $S_i = E_{i+1} - E_i$ between neighboring energy levels E_i, where the E_i are ordered such that $E_{i+1} - E_i \geq 0$, depends on the specific form of the underlying Hamiltonian. In fact, the S_i averaged over i, in a band of width ε around some central energy E, are given by the inverse of the smoothed density of states

$$\overline{d}(E) = \frac{1}{2\varepsilon} \int\limits_{E-\varepsilon}^{E+\varepsilon} d(E)\mathrm{d}E. \tag{A.1}$$

Here, the density of states

$$d(E) = \sum_i \delta(E - E_i), \tag{A.2}$$

is a string of delta peaks at positions E_i, corresponding to the eigenenergies of the system. The spacings S_i then fluctuate around the mean level spacing $\Delta(E) = 1/\overline{d}(E)$, and the corresponding cumulative density

$$\overline{N}(E) = \int\limits_{-\infty}^{E} \overline{d}(E')\mathrm{d}E' \tag{A.3}$$

counts the (smoothed) number of states with an energy less than E.

In order to obtain a level-spacing distribution that is independent of the specific form of the underlying Hamiltonian, the spectrum needs to be unfolded, *i.e.*, the system-specific density of states has to be normalized out. To this end the energy levels E_i are replaced by a new set of numbers

$$e_i = \overline{N}(E_i), \tag{A.4}$$

which, by definition, have an average spacing of one. We can thus think of them as a set of normalized energies with smoothed density $\overline{d}(E) = 1$. Defining

$$s_i = e_{i+1} - e_i, \tag{A.5}$$

the probability that $s \leq s_i \leq s + \mathrm{d}s$ for any i, is then given by the distribution $P(s)$ via $P(s)\mathrm{d}s$, and has been found to be universal for a broad class of systems [74].

Also different unfolding procedures have been established, which are however equivalent to the method presented here [85]. In particular, the definition (A.5) is equivalent to the expression for the normalized level spacing $s_i = (E_{i+1} - E_i)/\Delta(E)$, Eq. (3.1), that we discussed in Sec. 3.1.

B Dynamics of initially localized states

In Chapter 6 of this thesis we focus on Bloch oscillations that emerge when the system is initially prepared in the untilted Hamiltonian's ground state. However, when applying Dirichlet boundary conditions, finite size effects can significantly influence the dynamics as we discuss in Sec. 6.2. In order to avoid those effects, we also consider as initial states the ground states of smaller, untilted sublattices with $m < L$ lattice sites, which are then placed within the original lattice before applying the tilt. This procedure is depicted schematically in Fig. 6.5. In the following, we investigate how the Bloch oscillations are influenced by this choice and, more precisely, we discuss its impact on the oscillations' amplitude.

In Fig. B.1 (a) we depict the velocity $v(t)$, Eq. (6.6), as a function of time in units of the Bloch period T_B, for $n = 5$ noninteracting particles in $L = 11$ lattice sites. We set the tunneling coupling and the static field strength to $J = F = 1$, and vary the number of initially populated sites m. The initial configuration is always chosen to be the ground state of the $n = 5$ bosons in m lattice sites, which is placed into the tilted lattice with L sites at $t = 0$, such that the two uppermost sites are empty (see also discussion on page 86). We find that at $t = 0$, the velocity vanishes for all the initial states $|\psi_0\rangle$ considered here, i.e.,

$$v(t = 0) = \langle\psi_0|\hat{V}|\psi_0\rangle = 0.$$ (B.1)

This results from the symmetry of the initial states with respect to the central populated lattice site, which stems from the translational invariance of the untilted lattice. The subsequent behavior for $t > 0$ then depends on the choice of initially populated sites.

For $m = 1$ (black line), $|\psi_0\rangle$ is given by a Wannier-Fock state $|\mathbf{n}\rangle$, Eq. (2.22), where all particles are located on one and the same lattice site. This state constitutes an eigenstate of the Hamiltonian for $J = 0$ and $U \neq 0$ and, thus, it is orthogonal to the eigenstates of the system we consider here. For such states, not only the velocity but also its derivative initially equals zero, i.e., $v(t = 0) = \dot{v}(t = 0) = 0$. As time elapses, the atoms spread on the lattice and Bloch oscillations emerge. After a (short) transient time, the oscillations feature the expected periodicity[1] described by T_B while the amplitude still increases. For $m > 1$, the system immediately features Bloch oscillations. However, as particularly evident from the red line that corresponds to $m = 2$, the oscillations' amplitude increases as a function

---

[1]Note that, here, we consider localized states of noninteracting bosons. In the case of strong interactions, it was shown that the period of the oscillations scales as the inverse number of particles [54, 105].
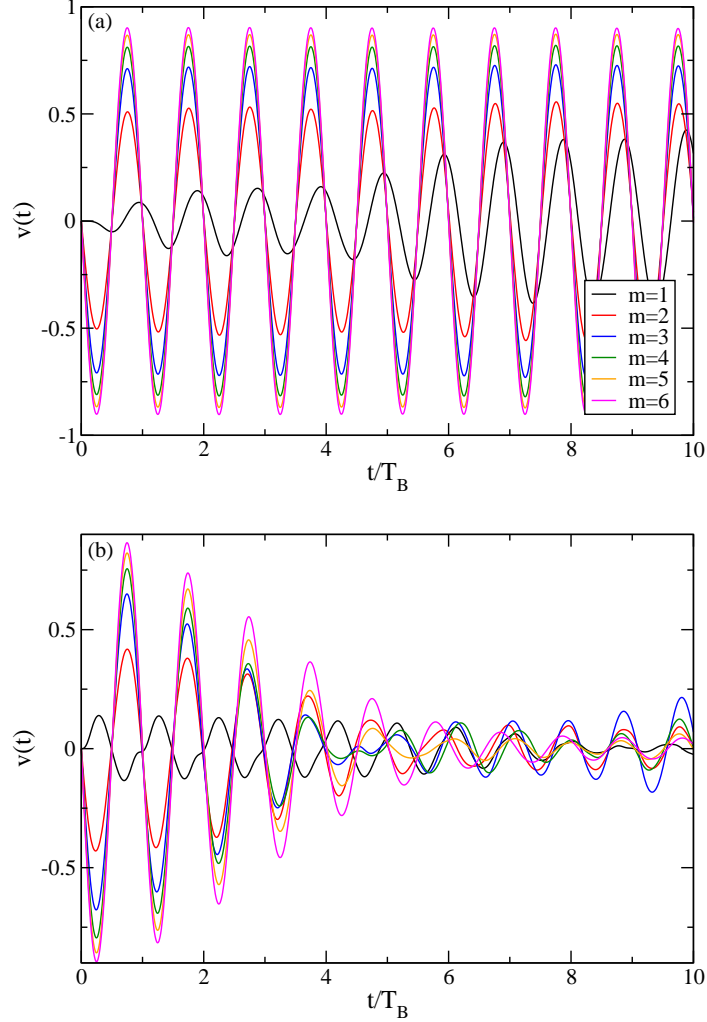
Figure B.1: Mean velocity $v(t)$, Eq. (6.6), as a function of time in units of the Bloch period T_B, for $n = 5$ particles in $L = 11$ lattice sites. The tunneling coupling and the static field strength are set to $J = F = 1$ and the onsite interaction is given by (a) $U = 0$ and (b) $U = 0.1$. The initial states correspond to the ground states of the particles within a smaller sublattice with m lattice sites (compare Fig. 6.5) and the different colors correspond to different choices of m as indicated by the legend. The initial configuration is always chosen such that at $t = 0$ the two uppermost sites of the tilted lattice are empty (see also discussion on page 86).

of time. This behavior again stems from the spreading of the initially localized particles. In general, we find that the larger m, the larger the initial amplitude of the oscillations and, consequently, the smaller the amplitude's increase as a function of time. Moreover, the amplitude saturates quickly as the number of initially populated sites is increased. Note that the saturation value is smaller than one, what results from the definition of the velocity operator $\hat{V}$ for Dirichlet boundary conditions, Eq. (6.8). In the case of periodic boundary conditions (6.9) the amplitude equals one.

Strictly speaking, the oscillations thus do not simply feature a sinusoidal behavior but rather resemble[2]

$$v_{U=0}(t) = -v_0 \, e^{\alpha \cdot t} \, \sin(t/T_B) \,, \tag{B.2}$$

where $0 < \alpha \ll 1$. However, as m increases, α quickly tends to zero and the assumption of perfect sinusoidal oscillations is justified.

Introducing interactions between the particles leads to a decay of the oscillations as time evolves. This can be observed in Fig. B.1 (b) for weak interactions $U = 0.1$. The behavior is, however, counteracted by the initial spreading discussed above and, consequently, for very small $U \ll 1$, it is possible that the amplitude still increases as a function of time. In order to quantify the interaction induced decay (see Sec. 6.4.4), we thus have to relate the behavior of $v(t)$ for $U \neq 0$ to $v_{U=0}(t)$ as done in Eq. (6.52).

---

[2]Note that for $m = 1$, we also have to introduce a phase shift φ_0.

Bibliography

[1] Akatsuka, T., Takamoto, M., and Katori, H. Optical lattice clocks with non-interacting bosons and fermions. *Nat. Phys.* **4**, 954 (2008).

[2] Álvaro Perales and Vidal, G. Entanglement growth and simulation efficiency in one-dimensional quantum lattice systems. *Phys. Rev. A* **78**, 042337 (2008).

[3] Amico, L., Osterloh, A., and Cataliotti, F. Quantum Many Particle Systems in Ring-Shaped Optical Lattices. *Phys. Rev. Lett.* **95**, 063201 (2005).

[4] Anderson, B. P. and Kasevich, M. A. Macroscopic Quantum Intereference from Atomic Tunnel Arrays. *Science* **282**, 1686 (1998).

[5] Anderson, M. H., Ensher, J. R., Matthews, M. R., Wieman, C. E., and Cornell, E. A. Observation of Bose-Einstein Condensation in a Dilute Atomic Vapor. *Science* **269**, 198 (1995).

[6] Anderson, P. W. Absence of Diffusion in Certain Random Lattices. *Phys. Rev.* **109**, 1492 (1958).

[7] Andrews, M. R., Townsend, C. G., Miesner, H.-J., Durfee, D. S., Kurn, D. M., and Ketterle, W. Observation of Interference Between Two Bose Condensates. *Science* **275**, 637 (1997).

[8] Anker, T., Albiez, M., Gati, R., Hunsmann, S., Eiermann, B., Trombettoni, A., and Oberthaler, M. K. Nonlinear Self-Trapping of Matter Waves in Periodic Potentials. *Phys. Rev. Lett.* **94**, 020403 (2005).

[9] Ashcroft, N. W. and Mermin, N. D. *Solid State Physics*. Harcourt College Publishers (1976).

[10] Bakr, W. S., Gillen, J. I., Peng, A., Fölling, S., and Greiner, M. A quantum gas microscope for detecting single atoms in a Hubbard-regime optical lattice. *Nature* **462**, 74 (2009).

[11] Bakr, W. S., Peng, A., Tai, M. E., Ma, R., Simon, J., Gillen, J. I., Fölling, S., Pollet, L., and Greiner, M. Probing the Superfluid-to-Mott-Insulator Transition at the Single-Atom Level. *Science* **329**, 547 (2010).

[12] Ben Dahan, M., Peik, E., Reichel, J., Castin, Y., and Salomon, C. Bloch oscillations of atoms in an optical potential. *Phys. Rev. Lett.* **76**, 4508 (1996).

[13] Bernstein, L. J. The three-waveguide nonlinear directional coupler: the center waveguide excitation. *Optics Communications* **94**, 406 (1992).

[14] Berry, M. V. and Tabor, M. Level clustering in the regular spectrum. *Proc. R. Soc. Lond. A* **356**, 375 (1977).

[15] Billy, J., Josse, V., Zuo, Z., Bernard, A., Hambrecht, B., Lugan, P., Clement, D., Sanchez-Palencia, L., Bouyer, P., and Aspect, A. Direct observation of Anderson localization of matter waves in a controlled disorder. *Nature* **453**, 891 (2008).

[16] Bloch, F. Über die Quantenmechanik der Elektronen in Kristallgittern. *Z. Phys.* **52**, 555 (1929).

[17] Bloch, I. Quantum coherence and entanglement with ultracold atoms in optical lattices. *Nature* **453**, 1016 (2008).

[18] Bloch, I., Dalibard, J., and Zwerger, W. Many-body physics with ultracold gases. *Rev. Mod. Phys.* **80**, 885 (2008).

[19] Bodyfelt, J. D., Hiller, M., and Kottos, T. Engineering fidelity echoes in Bose-Hubbard Hamiltonians. *Europhys. Lett.* **78**, 50003 (2007).

[20] Bogoliubov, N. N. On the Theory of Superfluidity. *J. Phys. (USSR)* **11**, 23 (1947).

[21] Bohigas, O., Giannoni, M. J., and Schmit, C. Characterization of Chaotic Quantum Spectra and Universality of Level Fluctuation Laws. *Phys. Rev. Lett.* **52**, 1 (1984).

[22] Bose, S. N. Plancks Gesetz und Lichtquantenhypothese. *Z. Phys.* **26**, 178 (1924).

[23] Bradley, C. C., Sackett, C. A., Tollett, J. J., and Hulet, R. G. Evidence of Bose-Einstein Condensation in an Atomic Gas with Attractive Interactions. *Phys. Rev. Lett.* **75**, 1687 (1995).

[24] Brody, T. A. A statistical measure for the repulsion of energy levels. *Lettere Al Nuovo Cimento* **7**, 482 (1973).

[25] Brody, T. A., Flores, J., French, J. B., Mello, P. A., Pandey, A., and Wong, S. S. M. Random-matrix physics: spectrum and strength fluctuations. *Rev. Mod. Phys.* **53**, 385 (1981).

[26] Bruder, C., Fazio, R., and Schön, G. The Bose-Hubbard model: from Josephson junction arrays to optical lattices. *Ann. Phys.* **14**, 566 (2005).

[27] Buchleitner, A., Delande, D., and Zakrzewski, J. Non-dispersive wave packets in periodically driven quantum systems. *Phys. Rep.* **368**, 409 (2002).

[28] Buchleitner, A. and Kolovsky, A. R. Interaction-Induced Decoherence of Atomic Bloch Oscillations. *Phys. Rev. Lett.* **91**, 253002 (2003).

[29] Burger, S., Cataliotti, F. S., Fort, C., Minardi, F., Inguscio, M., Chiofalo, M. L., and Tosi, M. P. Superfluid and Dissipative Dynamics of a Bose-Einstein Condensate in a Periodic Optical Potential. *Phys. Rev. Lett.* **86**, 4447 (2001).

[30] Casati, G., Chirikov, B. V., and Guarneri, I. Energy-Level Statistics of Integrable Quantum Systems. *Phys. Rev. Lett.* **54**, 1350 (1985).

[31] Casati, G., Chirikov, B. V., Guarneri, I., and Izrailev, F. M. Band-random-matrix model for quantum localization in conservative systems. *Phys. Rev. E* **48**, R1613 (1993).

[32] Cataliotti, F. S., Burger, S., Fort, C., Maddaloni, P., Minardi, F., Trombettoni, A., Smerzi, A., and Inguscio, M. Josephson Junction Arrays with Bose-Einstein Condensates. *Science* **293**, 843 (2001).

[33] Cazalilla, M. A. and Rigol, M. Focus on Dynamics and Thermalization in Isolated Quantum Many-Body Systems. *New J. Phys.* **12**, 055006 (2010).

[34] Chefles, A. Nearest-neighbour level spacings for the non-periodic discrete Schrödinger equation. *J. Phys. A.* **29**, 4515 (1996).

[35] Chirikov, B. V. A universal instability of many-dimensional oscillator systems. *Phys. Rep.* **52**, 263 (1979).

[36] Chu, S. Nobel Lecture: The manipulation of neutral particles. *Rev. Mod. Phys.* **70**, 685 (1998).

[37] Cladé, P., de Mirandes, E., Cadoret, M., Guellati-Khélifa, S., Schwob, C., Nez, F., Julien, L., and Biraben, F. Determination of the Fine Structure Constant Based on

Bloch Oscillations of Ultracold Atoms in a Vertical Optical Lattice. *Phys. Rev. Lett.* **96**, 033001 (2006).

[38] Cohen, D. Chaos and Energy Spreading for Time-Dependent Hamiltonians, and the Various Regimes in the Theory of Quantum Dissipation. *Ann. Phys.* **283**, 175 (2000).

[39] Cohen, D. and Heller, E. J. Unification of perturbation theory, random matrix theory, and semiclassical considerations in the study of parametrically dependent eigenstates. *Phys. Rev. Lett.* **84**, 2841 (2000).

[40] Cohen, D. and Kottos, T. Quantum-Mechanical Nonperturbative Response of Driven Chaotic Mesoscopic Systems. *Phys. Rev. Lett.* **85**, 4839 (2000).

[41] Cohen, D. and Kottos, T. Parametric dependent Hamiltonians, wave functions, random matrix theory, and quantal-classical correspondence. *Phys. Rev. E* **63**, 036203 (2001).

[42] Cohen-Tannoudji, C. *Atomic Motion in Laser Light*. North Holland (1992).

[43] Cohen-Tannoudji, C. N. Nobel Lecture: Manipulating atoms with photons. *Rev. Mod. Phys.* **70**, 707 (1998).

[44] Cornell, E. A. and Wieman, C. E. Nobel Lecture: Bose-Einstein condensation in a dilute gas, the first 70 years and some recent experiments. *Rev. Mod. Phys.* **74**, 875 (2002).

[45] Cristiani, M., Morsch, O., Malossi, N., Jona-Lasinio, M., Anderlini, M., Courtade, E., and Arimondo, E. Instabilities of a Bose-Einstein condensate in a periodic potential: an experimental investigation. *Opt. Express* **12**, 4 (2004).

[46] Cristiani, M., Morsch, O., Müller, J. H., Ciampini, D., and Arimondo, E. Experimental properties of Bose-Einstein condensates in one-dimensional optical lattices: Bloch oscillations, Landau-Zener tunneling, and mean-field effects. *Phys. Rev. A* **65**, 063612 (2002).

[47] Cruzeiro-Hansson, L., Feddersen, H., Flesch, R., Christiansen, P. L., Salerno, M., and Scott, A. C. Classical and quantum analysis of chaos in the discrete self-trapping equation. *Phys. Rev. B* **42**, 522 (1990).

[48] Daley, A. *Manipulation and Simulation of cold atoms in optical lattices*. Ph.D. thesis, Leopold-Franzens-Universität Innsbruck (2005).

[49] Daley, A. J., Kollath, C., Schollwöck, U., and Vidal, G. Time-dependent density-matrix renormalization-group using adaptive effective Hilbert spaces. *J. Stat. Mech.* **4**, p04005 (2004).

[50] Dalfovo, F., Giorgini, S., Pitaevskii, L. P., and Stringari, S. Theory of Bose-Einstein condensation in trapped gases. *Rev. Mod. Phys.* **71**, 463 (1999).

[51] Damski, B., Zakrzewski, J., Santos, L., Zoller, P., and Lewenstein, M. Atomic Bose and Anderson Glasses in Optical Lattices. *Phys. Rev. Lett.* **91**, 080403 (2003).

[52] Davis, K. B., Mewes, M. O., Andrews, M. R., van Druten, N. J., Durfee, D. S., Kurn, D. M., and Ketterle, W. Bose-Einstein Condensation in a Gas of Sodium Atoms. *Phys. Rev. Lett.* **75**, 3969 (1995).

[53] de Filippo, S., Fusco Girard, M., and Salerno, M. Avoided crossing and nearest-neighbour level spacings for the quantum DST equation. *Nonlinearity* **2**, 477 (1989).

[54] Dias, W. S., Nascimento, E. M., Lyra, M. L., and de Moura, F. A. B. F. Frequency doubling of Bloch oscillations for interacting electrons in a static electric field. *Phys. Rev. B* **76**, 155124 (2007).

[55] Dreisow, F., Szameit, A., Heinrich, M., Pertsch, T., Nolte, S., Tünnermann, A., and Longhi, S. Bloch-Zener Oscillations in Binary Superlattices. *Phys. Rev. Lett.* **102**, 076802 (2009).

[56] Dyson, F. J. Statistical Theory of the Energy Levels of Complex Systems. I. *J. Math. Phys.* **3**, 140 (1962).

[57] Eilbeck, J. C. and Johansson, M. *The discrete nonliner Schrödinger equation – 20 years on. Proc. of the 3rd Conf. Localization and Energy Transfer in Nonlinear System.* World Scientific, New Jersey (2003).

[58] Eilbeck, J. C., Lomdahl, P. S., and Scott, A. C. The discrete self-trapping equation. *Physica D* **16**, 318 (1985).

[59] Einstein, A. Quantentheorie des einatomigen idealen Gases. *Sitzungsber. Preuss. Akad. Wiss., Phys. Math. Kl.* page 261 (1924).

[60] Einstein, A. Quantentheorie des einatomigen idealen Gases. Zweite Abhandlung. *Sitzungsber. Preuss. Akad. Wiss., Phys. Math. Kl.* page 3 (1925).

[61] Evers, F. and Mirlin, A. D. Anderson transitions. *Rev. Mod. Phys.* **80**, 1355 (2008).

[62] Fallani, L., De Sarlo, L., Lye, J. E., Modugno, M., Saers, R., Fort, C., and Inguscio, M. Observation of Dynamical Instability for a Bose-Einstein Condensate in a Moving 1D Optical Lattice. *Phys. Rev. Lett.* **93**, 140406 (2004).

[63] Fallani, L., Lye, J. E., Guarrera, V., Fort, C., and Inguscio, M. Ultracold atoms in a disordered crystal of light: Towards a bose glass. *Phys. Rev. Lett.* **98**, 130404 (2007).

[64] Fannes, M., Nachtergaele, B., and Werner, R. F. Finitely Correlated States On Quantum Spin Chains. *Commun. Math. Phys.* **144**, 443 (1992).

[65] Fattori, M., D'Errico, C., Roati, G., Zaccanti, M., Jona-Lasinio, M., Modugno, M., Inguscio, M., and Modugno, G. Atom Interferometry with a Weakly Interacting Bose-Einstein Condensate. *Phys. Rev. Lett.* **100**, 080405 (2008).

[66] Feingold, M. and Peres, A. Distribution of matrix elements of chaotic systems. *Phys. Rev. A* **34**, 591 (1986).

[67] Ferrari, G., Poli, N., Sorrentino, F., and Tino, G. M. Long-Lived Bloch Oscillations with Bosonic Sr Atoms and Application to Gravity Measurement at the Micrometer Scale. *Phys. Rev. Lett.* **97**, 060402 (2006).

[68] Feynman, R. P. Forces in Molecules. *Phys. Rev.* **56**, 340 (1939).

[69] Feynman, R. P. Simulating Physics with Computers. *International Journal of Theoretical Physics* **21**, 467 (1982).

[70] Finlayson, N. and Stegeman, G. I. Spatial switching, instabilities, and chaos in a three-waveguide nonlinear directional coupler. *App. Phys. Lett.* **56**, 2276 (1990).

[71] Fisher, M. P. A., Weichman, P. B., Grinstein, G., and Fisher, D. S. Boson localization and the superfluid-insulator transition. *Phys. Rev. B* **40**, 546 (1989).

[72] Flambaum, V. V., Gribakina, A. A., Gribakin, G. F., and Kozlov, M. G. Structure of compound states in the chaotic spectrum of the ce atom: Localization properties, matrix elements, and enhancement of weak perturbations. *Phys. Rev. A* **50**, 267 (1994).

[73] Franzosi, R. and Penna, V. Chaotic behavior, collective modes, and self-trapping in the dynamics of three coupled Bose-Einstein condensates. *Phys. Rev. E* **67**, 046227 (2003).

[74] Giannoni, M.-J., Voros, A., and Zinn-Justin, J. (editors). *Chaos and Quantum Physics*. North-Holland, Amsterdam (1991).

[75] Glück, M., Kolovsky, A. R., and Korsch, H. J. Wannier–Stark resonances in optical and semiconductor superlattices. *Phys. Rep.* **366**, 103 (2002).

[76] Greenwood, D. A. The Boltzmann Equation in the Theory of Electrical Conduction in Metals. *Proc. Phys. Soc.* **71**, 585 (1958).

[77] Greiner, M. and Fölling, S. Optical lattices. *Nature* **453**, 436 (2008).

[78] Greiner, M., Mandel, O., Esslinger, T., Hänsch, T. W., and Bloch, I. Quantum phase transition from a superfluid to a Mott insulator in a gas of ultracold atoms. *Nature* **415**, 39 (2002).

[79] Grifoni, M. and Hänggi, P. Driven quantum tunneling. *Phys. Rep.* **304**, 229 (1998).

[80] Grimm, R., Weidemüller, M., and Ovchinnikov, Y. Optical dipole traps for neutral atoms. *Adv. At. Mol. Opt. Phys.* **42**, 95 (2000).

[81] Gross, E. P. Structure of a Quantized Vortex in Boson Systems. *Il Nuovo Cimento* **20**, 454 (1961).

[82] Gross, E. P. Hydrodynamics of a Superfluid Condensate. *J. Math. Phys.* **4**, 195 (1963).

[83] Gustavsson, M., Haller, E., Mark, M. J., Danzl, J. G., Rojas-Kopeinig, G., and Nägerl, H.-C. Control of Interaction-Induced Dephasing of Bloch Oscillations. *Phys. Rev. Lett.* **100**, 080404 (2008).

[84] Gutiérrez, L., Díaz-de Anda, A., Flores, J., Méndez-Sánchez, R. A., Monsivais, G., and Morales, A. Wannier-Stark Ladders in One-Dimensional Elastic Systems. *Phys. Rev. Lett.* **97**, 114301 (2006).

[85] Haake, F. *Quantum Signatures of Chaos*. Springer (2004).

[86] Hagley, E. W., Deng, L., Kozuma, M., Wen, J., Helmerson, K., Rolston, S. L., and Phillips, W. D. A well-collimated quasi-continous atom laser. *Science* **283**, 1706 (1999).

[87] Hartmann, T., Keck, F., Korsch, H. J., and Mossmann, S. Dynamics of Bloch oscillations. *New J. Phys.* **6**, 2 (2004).

[88] Heinzner, P., Huckleberry, A., and Zirnbauer, M. Symmetry classes of disordered fermions. *Communications in Mathematical Physics* **257**, 725 (2005).

[89] Hill, D. L. and Wheeler, J. A. Nuclear Constitution and the Interpretation of Fission Phenomena. *Phys. Rev.* **89**, 1102 (1953).

[90] Hiller, M. *Parametric Bose-Hubbard Hamiltonians: Quantum Dissipation, Irreversibility, and Pumping*. Ph.D. thesis, Georg-August-Universität zu Göttingen (2007).

[91] Hiller, M., Cohen, D., Geisel, T., and Kottos, T. Wavepacket dynamics, quantum reversibility, and random matrix theory. *Ann. Phys.* **321**, 1025 (2006).

[92] Hiller, M., Kottos, T., and Geisel, T. Complexity in parametric Bose-Hubbard Hamiltonians and structural analysis of eigenstates. *Phys. Rev. A* **73**, 061604(R) (2006).

[93] Hiller, M., Kottos, T., and Geisel, T. Wave-packet dynamics in energy space of a chaotic trimeric Bose-Hubbard system. *Phys. Rev. A* **79**, 023621 (2009).

[94] Holthaus, M. Bloch oscillations and Zener breakdown in an optical lattice. *J. Opt. B* **2**, 589 (2000).

[95] Hunn, S., Hiller, M., Buchleitner, A., Cohen, D., and Kottos, T. Inelastic chaotic scattering on a Bose-Einstein condensate. *arXiv:1010.2092* (2010).

[96] Inouye, S., Andrews, M. R., Stenger, J., Miesner, H.-J., Stamper-Kurn, D. M., and Ketterle, W. Observation of Feshbach resonances in a Bose-Einstein condensate. *Nature* **392**, 151 (1998).

[97] Izrailev, F. M. Quantum localization and statistics of quasienergy spectrum in a classically chaotic system. *Phys. Lett. A* **134**, 13 (1988).

[98] Izrailev, F. M. Simple models of quantum chaos: Spectrum and eigenfunctions. *Phys. Rep.* **196**, 299 (1990).

[99] Jaksch, D., Bruder, C., Cirac, J. I., Gardiner, C. W., and Zoller, P. Cold Bosonic Atoms in Optical Lattices. *Phys. Rev. Lett.* **81**, 3108 (1998).

[100] Jaksch, D. and Zoller, P. The cold atom Hubbard toolbox. *Ann. Phys.* **315**, 52 (2005).

[101] Jin, L., Chen, B., and Song, Z. Coherent shift of localized bound pairs in the Bose-Hubbard model. *Phys. Rev. A* **79**, 032108 (2009).

[102] Jona-Lasinio, M., Morsch, O., Cristiani, M., Malossi, N., Müller, J. H., Courtade, E., Anderlini, M., and Arimondo, E. Asymmetric Landau-Zener Tunneling in a Periodic Potential. *Phys. Rev. Lett.* **91**, 230406 (2003).

[103] Ketterle, W. Nobel lecture: When atoms behave as waves: Bose-Einstein condensation and the atom laser. *Rev. Mod. Phys.* **74**, 1131 (2002).

[104] Ketzmerick, R. Fractal conductance fluctuations in generic chaotic cavities. *Phys. Rev. B* **54**, 10841 (1996).

[105] Khomeriki, R., Krimer, D. O., Haque, M., and Flach, S. Interaction-induced fractional Bloch and tunneling oscillations. *Phys. Rev. A* **81**, 065601 (2010).

[106] Kling, S., Salger, T., Grossert, C., and Weitz, M. Atomic Bloch-Zener Oscillations and Stückelberg Interferometry in Optical Lattices. *Phys. Rev. Lett.* **105**, 215301 (2010).

[107] Klümper, A., Schadschneider, A., and Zittartz, J. Matrix Product Ground States for One-Dimensional Spin-1 Quantum Antiferromagnets. *Europhys. Lett.* **24**, 293 (1993).

[108] Kollath, C., Iucci, A., Giamarchi, T., Hofstetter, W., and Schollwöck, U. Spectroscopy of ultracold atoms by periodic lattice modulations. *Phys. Rev. Lett.* **97**, 050402 (2006).

[109] Kollath, C., Läuchli, A. M., and Altman, E. Quench Dynamics and Nonequilibrium Phase Diagram of the Bose-Hubbard Model. *Phys. Rev. Lett.* **98**, 180601 (2007).

[110] Kollath, C., Roux, G., Biroli, G., and Läuchli, A. M. Statistical properties of the spectrum of the extended Bose–Hubbard model. *J. Stat. Mech.* **2010**, p08011 (2010).

[111] Kolmogorov, A. N. Logical Basis for Information Theory and Probability Theory. *IEEE Trans. Inf. Theory* **14**, 662 (1968).

[112] Kolovsky, A. R. New Bloch Period for Interacting Cold Atoms in 1D Optical Lattices. *Phys. Rev. Lett.* **90**, 213002 (2003).

[113] Kolovsky, A. R. Bloch oscillations in the Mott-insulator regime. *Phys. Rev. A* **70**, 015604 (2004).

[114] Kolovsky, A. R. and Buchleitner, A. Floquet-Bloch operator for the Bose-Hubbard model with static field. *Phys. Rev. E* **68**, 056213 (2003).

[115] Kolovsky, A. R. and Buchleitner, A. Multiparticle quantum chaos in tilted optical lattices. *J. Mod. Opt.* **51**, 999 (2004).

[116] Kolovsky, A. R. and Buchleitner, A. Quantum chaos in the Bose-Hubbard model. *Europhys. Lett.* **68**, 632 (2004).

[117] Kolovsky, A. R., Korsch, H. J., and Graefe, E.-M. Bloch oscillations of Bose-Einstein condensates: Quantum counterpart of dynamical instability. *Phys. Rev. A* **80**, 023617 (2009).

[118] Kolovsky, A. R., Ponomarev, A. V., and Korsch, H. J. Damped Bloch oscillations of cold atoms in optical lattices. *Phys. Rev. A* **66**, 053405 (2002).

[119] Kubo, R. A general expression for the conductivity tensor. *Can. J. Phys.* **34**, 1274 (1956).

[120] Kubotani, H., Adachi, S., and Toda, M. Exact Formula of the Distribution of Schmidt Eigenvalues for Dynamical Formation of Entanglement in Quantum Chaos. *Phys. Rev. Lett.* **100**, 240501 (2008).

[121] Landau, L. D. On the motion of electrons in a crystal lattice. *Phys. Z. Sowjetunion* **3**, 884 (1933).

[122] Leggett, A. J. Bose-Einstein condensation in the alkali gases: Some fundamental concepts. *Rev. Mod. Phys.* **73**, 307 (2001).

[123] Leo, K., Bolivar, P. H., Brüggemann, F., Schwedler, R., and Köhler, K. Observation of Bloch oscillations in a semiconductor superlattice. *Solid State Commun.* **84**, 943 (19992).

[124] Letokhov, V. S. Doppler line narrowing in a standing light wave. *JETP Letters* **7**, 272 (1968).

[125] Lewenstein, M., Sanpera, A., Ahufinger, V., Damski, B., Sen, A., and Sen, U. Ultracold atomic gases in optical lattices: mimicking condensed matter physics and beyond. *Adv. Phys.* **56**, 243 (2007).

[126] Li, J., Yu, Y., Dudarev, A. M., and Niu, Q. Interaction broadening of Wannier functions and Mott transitions in atomic BEC. *New J. Phys.* **8**, 154 (2006).

[127] Lichtenberg, A. and Lieberman, M. *Regular and Stochastic Motion*. Springer (1983).

[128] Madroñero, J., Ponomarev, A., Carvalho, A., Wimberger, S., Viviescas, C., Kolovsky, A., Hornberger, K., Schlagheck, P., Krug, A., and Buchleitner, A. Quantum chaos, transport and control – in quantum optics. *Adv. At. Mol. Opt. Phys.* **53**, 33 (2006).

[129] Marcus, C. M., Rimberg, A. J., Westervelt, R. M., Hopkins, P. F., and Gossard, A. C. Conductance fluctuations and chaotic scattering in ballistic microstructures. *Phys. Rev. Lett.* **69**, 506 (1992).

[130] Mehta, M. L. *Random Matrices*. Elsevier Academic Press, 3rd edition (2004).

[131] Mendez, E. E., Agulló-Rueda, F., and Hong, J. M. Stark Localization in GaAs-GaAlAs Superlattices under an Electric Field. *Phys. Rev. Lett.* **60**, 2426 (1988).

[132] Mewes, M.-O., Andrews, M. R., Kurn, D. M., Durfee, D. S., Townsend, C. G., and Ketterle, W. Output coupler for bose-einstein condensed atoms. *Phys. Rev. Lett.* **78**, 582 (1997).

[133] Morsch, O., Müller, J. H., Cristiani, M., Ciampini, D., and Arimondo, E. Bloch Oscillations and Mean-Field Effects of Bose-Einstein Condensates in 1D Optical Lattices. *Phys. Rev. Lett.* **87**, 140402 (2001).

[134] Morsch, O. and Oberthaler, M. Dynamics of Bose-Einstein condensates in optical lattices. *Rev. Mod. Phys.* **78**, 179 (2006).

[135] Nakamura, K. and Harayama, T. *Quantum Chaos & Quantum Dots*. Oxford University Press (2004).

[136] Nielsen, M. A. and Chuang, I. L. *Quantum Computation and Quantum Information*. Cambridge University Press (2000).

[137] Niu, Q., Zhao, X.-G., Georgakis, G. A., and Raizen, M. G. Atomic Landau-Zener Tunneling and Wannier-Stark Ladders in Optical Potentials. *Phys. Rev. Lett.* **76**, 4504 (1996).

[138] Orzel, C., Tuchman, A. K., Fenselau, M. L., Yasuda, M., and Kasevich, M. A. Squeezed States in a Bose-Einstein Condensate. *Science* **291**, 2386 (2001).

[139] Ott, E. *Chaos in Dynamical Systems*. Cambridge University Press, 2nd edition (2002).

[140] Ott, H., de Mirandes, E., Ferlaino, F., Roati, G., Modugno, G., and Inguscio, M. Collisionally Induced Transport in Periodic Potentials. *Phys. Rev. Lett.* **92**, 160601 (2004).

[141] Pechukas, P. Distribution of Energy Eigenvalues in the Irregular Spectrum. *Phys. Rev. Lett.* **51**, 943 (1983).

[142] Pertsch, T., Dannberg, P., Elflein, W., Bräuer, A., and Lederer, F. Optical Bloch Oscillations in Temperature Tuned Waveguide Arrays. *Phys. Rev. Lett.* **83**, 4752 (1999).

[143] Peschel, U., Pertsch, T., and Lederer, F. Optical Bloch oscillations in waveguide arrays. *Opt. Lett.* **23**, 1701 (1998).

[144] Pethick, C. J. and Smith, H. *Bose-Einstein Condensation in Dilute Gases*. Cambridge University Press, 2nd edition (2008).

[145] Petrosyan, D., Schmidt, B., Anglin, J. R., and Fleischhauer, M. Quantum liquid of repulsively bound pairs of particles in a lattice. *Phys. Rev. A* **76**, 033606 (2007).

[146] Phillips, W. D. Nobel Lecture: Laser cooling and trapping of neutral atoms. *Rev. Mod. Phys.* **70**, 721 (1998).

[147] Pichler, H., Daley, A. J., and Zoller, P. Nonequilibrium dynamics of bosonic atoms in optical lattices: Decoherence of many-body states due to spontaneous emission. *Phys. Rev. A* **82**, 063605 (2010).

[148] Piil, R. and Mølmer, K. Tunneling couplings in discrete lattices, single-particle band structure, and eigenstates of interacting atom pairs. *Phys. Rev. A* **76**, 023607 (2007).

[149] Pitaevskii, L. P. Vortex Lines in an Imperfect Bose Gas. *Sov. Phys. JETP* **13**, 451 (1961).

[150] Ponomarev, A. V. *Dynamics of cold Fermi atoms in one-dimensional optical lattices*. Ph.D. thesis, Albert-Ludwigs-Universität Freiburg (2008).

[151] Ponomarev, A. V., Madronero, J., Kolovsky, A. R., and Buchleitner, A. Atomic Current across an Optical Lattice. *Phys. Rev. Lett.* **96**, 050404 (2006).

[152] Prosen, T. and Žnidarič, M. Is the efficiency of classical simulations of quantum dynamics related to integrability? *Phys. Rev. E* **75**, 015202 (2007).

[153] Rey, A. M. *Ultracold bosonic atoms in optical lattices*. Ph.D. thesis, University of Maryland (2004).

[154] Roati, G., D'Errico, C., Fallani, L., Fattori, M., Fort, C., Zaccanti, M., Modugno, G., Modugno, M., and Inguscio, M. Anderson localization of a non-interacting Bose–Einstein condensate. *Nature* **453**, 895 (2008).

[155] Roux, G. Finite-size effects in global quantum quenches: Examples from free bosons in an harmonic trap and the one-dimensional Bose-Hubbard model. *Phys. Rev. A* **81**, 053604 (2010).

[156] Russell, J. S. *Report on waves*. Fourteenth meeting of the British Association for the Advancement of Science, York (1844).

[157] Sachdev, S. *Quantum Phase Transitions*. Cambridge University Press (1999).

[158] Sachdev, S., Sengupta, K., and Girvin, S. M. Mott insulators in strong electric fields. *Phys. Rev. B* **66**, 075128 (2002).

[159] Salomon, C., Dalibard, J., Aspect, A., Metcalf, H., and Cohen-Tannoudji, C. Channeling atoms in a laser standing wave. *Phys. Rev. Lett.* **59**, 1659 (1987).

[160] Salzman, W. R. Quantum mechanics of systems periodic in time. *Phys. Rev. A* **10**, 461 (1974).

[161] Sanchis-Alepuz, H., Kosevich, Y. A., and Sánchez-Dehesa, J. Acoustic Analogue of Electronic Bloch Oscillations and Resonant Zener Tunneling in Ultrasonic Superlattices. *Phys. Rev. Lett.* **98**, 134301 (2007).

[162] Schmidt, E. Zur Theorie der linearen und nichtlinearen Integralgleichungen. *Math. Annal.* **63**, 433 (1907).

[163] Schollwöck, U. The density-matrix renormalization group. *Rev. Mod. Phys.* **77**, 259 (2005).

[164] Schuch, N., Wolf, M. M., Verstraete, F., and Cirac, J. I. Entropy Scaling and Simulability by Matrix Product States. *Phys. Rev. Lett.* **100**, 030504 (2008).

[165] Sherson, J. F., Weitenberg, C., Endres, M., Cheneau, M., Bloch, I., and Kuhr, S. Single-atom-resolved fluorescence imaging of an atomic Mott insulator. *Nature* **467**, 68 (2010).

[166] Smerzi, A. and Trombettoni, A. Nonlinear tight-binding approximation for Bose-Einstein condensates in a lattice. *Phys. Rev. A* **68**, 023613 (2003).

[167] Spielman, I. B., Phillips, W. D., and Porto, J. V. Mott-Insulator Transition in a Two-Dimensional Atomic Bose Gas. *Phys. Rev. Lett.* **98**, 080404 (2007).

[168] Stöckmann, H.-J. *Quantum Chaos: an introduction*. Cambridge University Press (2006).

[169] Stöckmann, H.-J. and Stein, J. "Quantum" chaos in billiards studied by microwave absorption. *Phys. Rev. Lett.* **64**, 2215 (1990).

[170] Stöferle, T., Moritz, H., Schori, C., Köhl, M., and Esslinger, T. Transition from a Strongly Interacting 1D Superfluid to a Mott Insulator. *Phys. Rev. Lett.* **92**, 130403 (2004).

[171] Suzuki, M. Fractal decomposition of exponential operators with applications to many-body theory and Monto Carlo simulations. *Phys. Lett. A* **146**, 319 (1990).

[172] Suzuki, M. General theory of fractal path integrals with applications to many-body theories and statistical physics. *J. Math. Phys.* **32**, 400 (1991).

[173] Takamoto, M., Hong, F.-L., Higashi, R., and Katori, H. An optical lattice clock. *Nature* **435**, 321 (2005).

[174] Tayebirad, G., Zenesini, A., Ciampini, D., Mannella, R., Morsch, O., Arimondo, E., Lörch, N., and Wimberger, S. Time-resolved measurement of Landau-Zener tunneling in different bases. *Phys. Rev. A* **82**, 013633 (2010).

[175] Trombettoni, A. and Smerzi, A. Discrete Solitons and Breathers with Dilute Bose-Einstein Condensates. *Phys. Rev. Lett.* **86**, 2353 (2001).

[176] Trompeter, H., Pertsch, T., Lederer, F., Michaelis, D., Streppel, U., Bräuer, A., and Peschel, U. Visual Observation of Zener Tunneling. *Phys. Rev. Lett.* **96**, 023901 (2006).

[177] University of Innsbruck. Atom traps worldwide. http://www.uibk.ac.at/exphys/ultracold/atomtraps.html (2007).

[178] Valiente, M., Petrosyan, D., and Saenz, A. Three-body bound states in a lattice. *Phys. Rev. A* **81**, 011601 (2010).

[179] Venzl, H., Daley, A. J., Mintert, F., and Buchleitner, A. Statistics of Schmidt coefficients and the simulability of complex quantum systems. *Phys. Rev. E* **79**, 056223 (2009).

[180] Venzl, H. and Phillips., W. D. The Quantum Lattice. Nature Video: Missions in Space Time. http://www.nature.com/video/lindau/index.html (2008).

[181] Venzl, H., Zech, T., Oleś, B., Hiller, M., Mintert, F., and Buchleitner, A. Robust states of ultra-cold bosons in tilted optical lattices. *arXiv:1012.4167* (2010).

[182] Venzl, H., Zech, T., Oleś, B., Hiller, M., Mintert, F., and Buchleitner, A. Solitonic eigenstates of the chaotic Bose–Hubbard Hamiltonian. *Appl. Phys. B: Lasers and Optics* **98**, 647 (2010).

[183] Verstraete, F. and Cirac, J. I. Renormalization algorithms for Quantum-Many Body Systems in two and higher dimensions. *arXiv:cond-mat/0407066* (2004).

[184] Verstraete, F. and Cirac, J. I. Matrix product states represent ground states faithfully. *Phys. Rev. B* **73**, 094423 (2006).

[185] Verstraete, F., García-Ripoll, J. J., and Cirac, J. I. Matrix Product Density Operators: Simulation of Finite-Temperature and Dissipative Systems. *Phys. Rev. Lett.* **93**, 207204 (2004).

[186] Vidal, G. Efficient Classical Simulation of Slightly Entangled Quantum Computations. *Phys. Rev. Lett.* **91**, 147902 (2003).

[187] Vidal, G. Efficient Simulation of One-Dimensional Quantum Many-Body Systems. *Phys. Rev. Lett.* **93**, 040502 (2004).

[188] Voisin, P., Bleuse, J., Bouche, C., Gaillard, S., Alibert, C., and Regreny, A. Observation of the Wannier-Stark Quantization in a Semiconductor Superlattice. *Phys. Rev. Lett.* **61**, 1639 (1988).

[189] Wang, L., Hao, Y., and Chen, S. Quantum dynamics of repulsively bound atom pairs in the Bose-Hubbard model. *Eur. Phys. J. D* **48**, 229 (2008).

[190] Waschke, C., Roskos, H. G., Schwedler, R., Leo, K., Kurz, H., and Köhler, K. Coherent submillimeter-wave emission from Bloch oscillations in a semiconductor superlattice. *Phys. Rev. Lett.* **70**, 3319 (1993).

[191] Weber, T., Herbig, J., Mark, M., Nägerl, H.-C., and Grimm, R. Bose-Einstein Condensation of Cesium. *Science* **299**, 232 (2003).

[192] Weiss, C. and Breuer, H.-P. Photon-assisted tunneling in optical lattices: Ballistic transport of interacting boson pairs. *Phys. Rev. A* **79**, 023608 (2009).

[193] White, S. R. Density matrix formulation for quantum renormalization groups. *Phys. Rev. Lett.* **69**, 2863 (1992).

[194] White, S. R. Density-matrix algorithms for quantum renormalization groups. *Phys. Rev. B* **48**, 10345 (1993).

[195] White, S. R. and Feiguin, A. E. Real-Time Evolution Using the Density Matrix Renormalization Group. *Phys. Rev. Lett.* **93**, 076401 (2004).

[196] Wigner, E. P. Characteristic Vectors of Bordered Matrices with Infinite Dimensions. *Ann. Math.* **62**, 548 (1955).

[197] Wigner, E. P. Characteristic Vectors of Bordered Matrices with Infinite Dimensions II. *Ann. Math.* **65**, 203 (1957).

[198] Wilkinson, M. Statistical aspects of dissipation by Landau-Zener transitions. *J. Phys. A: Math. Gen.* **21**, 4021 (1988).

[199] Wilkinson, M. *Supersymmetry and Trace Formulae: Chaos and Disorder*, chapter Parametric Random Matrices: Static and Dynamic Applications, pages 369–399. Kluwer Academic / Plenum Publishers, New York (1999).

[200] Winkler, K., Thalhammer, G., Lang, F., Grimm, R., Denschlag, J. H., Daley, A. J., Kantian, A., Büchler, H. P., and Zoller, P. Repulsively bound atom pairs in an optical lattice. *Nature* **441**, 853 (2006).

[201] Wu, B. and Niu, Q. Superfluidity of Bose–Einstein condensate in an optical lattice: Landau–Zener tunnelling and dynamical instability. *New J. Phys.* **5**, 104 (2003).

[202] Zakrzewski, J., Buchleitner, A., and Delande, D. Nondispersive wave packets as solitonic solutions of level dynamics. *Z. Phys. B* **103**, 115 (1997).

[203] Zener, C. A Theory of the Electrical Breakdown of Solid Dielectrics. *Proc. R. Soc. Lond. A* **145**, 523 (1934).

[204] Zenesini, A., Ciampini, D., Morsch, O., and Arimondo, E. Observation of Stückelberg oscillations in accelerated optical lattices. *arXiv:1010.2413* (2010).

[205] Zibold, T., Nicklas, E., Gross, C., and Oberthaler, M. K. Classical Bifurcation at the Transition from Rabi to Josephson Dynamics. *Phys. Rev. Lett.* **105**, 204101 (2010).

[206] Zirnbauer, M. R. Riemannian symmetric superspaces and their origin in random-matrix theory. *J. Math. Phys.* **37**, 4986 (1996).

[207] Zwerger, W. Mott–Hubbard transition of cold atoms in optical lattices. *J. Opt. B* **5**, S9 (2003).

[208] Zyss, J. and Ledoux, I. Nonlinear Optics in Multipolar Media: Theory and Experiments. *Chem. Rev.* **94**, 77 (1994).